

Ministry of Education and Science of the Russian Federation
Saint Petersburg National Research University of Information
Technologies, Mechanics, and Optics

NANOSYSTEMS:
PHYSICS, CHEMISTRY, MATHEMATICS

2017, volume 8(6)

Наносистемы: физика, химия, математика

2017, том 8, № 6



NANOSYSTEMS:

PHYSICS, CHEMISTRY, MATHEMATICS

ADVISORY BOARD MEMBERS

Chairman: V.N. Vasiliev (*St. Petersburg, Russia*),
V.M. Buznik (*Moscow, Russia*); V.M. Ievlev (*Voronezh, Russia*), P.S. Kop'ev (*St. Petersburg, Russia*), N.F. Morozov (*St. Petersburg, Russia*), V.N. Parmon (*Novosibirsk, Russia*),
A.I. Rusanov (*St. Petersburg, Russia*),

EDITORIAL BOARD

Editor-in-Chief: I.Yu. Popov (*St. Petersburg, Russia*)

Section Co-Editors:

Physics – V.M. Uzdin (*St. Petersburg, Russia*),
Chemistry, material science – V.V. Gusarov (*St. Petersburg, Russia*),
Mathematics – I.Yu. Popov (*St. Petersburg, Russia*).

Editorial Board Members:

V.M. Adamyan (*Odessa, Ukraine*); O.V. Al'myasheva (*St. Petersburg, Russia*);
A.P. Alodjants (*Vladimir, Russia*); S. Bechta (*Stockholm, Sweden*); J. Behrndt (*Graz, Austria*);
M.B. Belonenko (*Volgograd, Russia*); V.G. Bepalov (*St. Petersburg, Russia*); J. Brasche (*Clausthal, Germany*);
A. Chatterjee (*Hyderabad, India*); S.A. Chivilikhin (*St. Petersburg, Russia*); A.V. Chizhov (*Dubna, Russia*);
A.N. Enyashin (*Ekaterinburg, Russia*), P.P. Fedorov (*Moscow, Russia*); E.A. Gudilin (*Moscow, Russia*);
V.K. Ivanov (*Moscow, Russia*), H. Jónsson (*Reykjavik, Iceland*); A.A. Kiselev (*Madison, USA*); Yu.S. Kivshar (*Canberra, Australia*);
S.A. Kozlov (*St. Petersburg, Russia*); P.A. Kurasov (*Stockholm, Sweden*); A.V. Lukashin (*Moscow, Russia*);
V.A. Margulis (*Saransk, Russia*); I.V. Melikhov (*Moscow, Russia*); G.P. Miroshnichenko (*St. Petersburg, Russia*);
I.Ya. Mittova (*Voronezh, Russia*); H. Neidhardt (*Berlin, Germany*); V.V. Pankov (*Minsk, Belarus*); K. Pankrashkin (*Orsay, France*);
A.V. Ragulya (*Kiev, Ukraine*); V. Rajendran (*Tamil Nadu, India*); A.A. Rempel (*Ekaterinburg, Russia*);
V.Ya. Rudyak (*Novosibirsk, Russia*); D. Shoikhet (*Karmiel, Israel*); P. Stovicek (*Prague, Czech Republic*);
V.M. Talanov (*Novocherkassk, Russia*); A.Ya. Vul' (*St. Petersburg, Russia*); A.V. Yakimansky (*St. Petersburg, Russia*), V.A. Zagrebnoy (*Marseille, France*).

Editors:

I.V. Blinova; A.I. Popov; A.I. Trifanov; E.S. Trifanova (*St. Petersburg, Russia*),
R. Simoneaux (*Philadelphia, Pennsylvania, USA*).

Address: University ITMO, Kronverkskiy pr., 49, St. Petersburg 197101, Russia.

Phone: +7(812)232-67-65, **Journal site:** <http://nanojournal.ifmo.ru/>,

E-mail: popov1955@gmail.com

AIM AND SCOPE

The scope of the journal includes all areas of nano-sciences. Papers devoted to basic problems of physics, chemistry, material science and mathematics inspired by nanosystems investigations are welcomed. Both theoretical and experimental works concerning the properties and behavior of nanosystems, problems of its creation and application, mathematical methods of nanosystem studies are considered.

The journal publishes scientific reviews (up to 30 journal pages), research papers (up to 15 pages) and letters (up to 5 pages). All manuscripts are peer-reviewed. Authors are informed about the referee opinion and the Editorial decision.

CONTENT

PHYSICS

- M.A. Gorlach, A.P. Slobozhanyuk
Nonlinear topological states in the Su-Schrieffer-Heeger model 695
- S.Y. Liashko, H. Jónsson, V.M. Uzdin
Calculations of switching field and energy barrier for magnetic islands with perpendicular anisotropy 701
- A. Mallaiah, G.N. Swamy, K. Padmapriya
1-bit and 2-bit comparator designs and analysis for quantum-dot cellular automata 709
- M.A. Pyataev, A.V. Shorokhov, N.N. Khvastunov, K.R. Vlasov, V.D. Krevchik, M.B. Semenov, K.N. Alekseev, F.V. Kusmartsev
Amplification of electromagnetic radiation in a superlattice placed in a tilted magnetic field 717
- K. Sukuta, M. Van den Bossche, A. Pedersen, H. Jónsson
Nanocluster structure deduced from AC-STEM images coupled to theoretical modelling 723
- A.V. Shibaev, O.E. Philippova
Viscoelastic properties of new mixed wormlike micelles formed by a fatty acid salt and alkylpyridinium surfactant 732
- A.V. Shorokhov, N.S. Prudskikh, M.B. Semenov, V.D. Krevchik, M.A. Pyataev, S.E. Golovatyuk, Tian-Rong Li, Yu-Hua Wang
Kinetic coefficients of semiconductor superlattices in high-frequency electromagnetic fields 740
- S.M. Vlasov, P.F. Bessarab, V.M. Uzdin, H. Jónsson
Instantons describing tunneling between magnetic states at finite temperature 746

CHEMISTRY AND MATERIAL SCIENCE

- A.L. Popov, A.B. Shcherbakov, N.M. Zholobak, A.Ye. Baranchikov, V. K. Ivanov
Cerium dioxide nanoparticles as third-generation enzymes (nanozymes) 760
- A. Ganguly, S.S. Nath, G. Gope, M. Choudhury
CdS quantum dot sensitized zinc oxide based solar cell with aluminum counter electrode 782

N.S. Kozhevnikova, A.S. Vorokh, O.I. Gyrdasova, I.V. Baklanova, A.N. Titov, M.V. Kuznetsov Synthetic pathway of a Cu₂ZnSnS₄ powder using low temperature annealing of nanostructured binary sulfides	787
G.A. Lyubas Generation of laser radiation by nanostructured solid active elements with selective optical nanoresonators formed in nanoporous aluminum oxide films	793
D.I. Petukhov, Ar.A. Eliseev, A.A. Poyarkov, A.V. Lukashin, An.A. Eliseev Porous polypropylene membrane contactors for dehumidification of gases	798
R.V. Shalayev, V.N. Varyukhin, A.M. Prudnikov, <u>A.I. Linnik</u> , V.V. Syrotkin Role of carbon in the formation of the structure and magnetic properties of Ni@CN_x nanoclusters under reactive magnetron deposition	804
M.S. Swapna, S. Sankararaman Fractal analysis – a surrogate technique for material characterization	809
A.A. Valeeva, M.G. Kostenko Stable Ti₉O₁₀ nanophase grown from nonstoichiometric titanium monoxide TiO_y nanopowder	816
P.A. Morozova, D.I. Petukhov Preparation of Au/TiO₂/Ti memristive elements via anodic oxidation	823
P.P. Fedorov, M.N. Mayakova, V.A. Maslov, A.E. Baranchikov, V.K. Ivanov, A.A. Pynenkov, M.A. Uslamina, K.N. Nishchev The solubility of sodium and potassium fluorides in strontium fluoride	830
P.Yu. Vanina, A.A. Naberezhnov, A.A. Sysoeva, V.I. Nizhankovskii, B. Nacke Phase diagram for K_(1-x)(NH₄)_(x)H₂PO₄ (x = 0 – 0.15) solid solutions embedded into magnetic glasses	835
Information for authors	839

Nonlinear topological states in the Su–Schrieffer–Heeger model

M. A. Gorlach, A. P. Slobozhanyuk

ITMO University, Kronverkskiy, 49, St. Petersburg, 197101, Russia

m.gorlach@metalab.ifmo.ru, a.slobozhanyuk@metalab.ifmo.ru

PACS 42.50.Ct, 42.70.Qs

DOI 10.17586/2220-8054-2017-8-6-695-700

Topological photonics offers unique functionalities in light manipulation at the nanoscale by means of the so-called topological states which are robust against various forms of disorder. One of the simplest one-dimensional models supporting topological states is the Su–Schrieffer–Heeger model. In this paper, we review the physics of the Su–Schrieffer–Heeger model and its nonlinear counterparts exhibiting self-induced, tunable and many-particle edge states. We discuss the robustness of these states, highlighting their rich potential for nanophotonic and quantum optics applications.

Keywords: topological states, nanophotonics, Su–Schrieffer–Heeger model.

Received: 10 November 2017

Revised: 3 December 2017

1. Introduction

Research interest in topological photonics that has recently emerged [1–3], is largely driven by the unprecedented possibilities provided by the topological states of light. Such topological states are immune to backscattering on structure imperfections or sharp bends exhibiting a vast range of unusual properties including, for instance, unidirectional spin-locked propagation [1–3].

Very recently, the quest for tunable topological states has given rise to the *nonlinear topological photonics*, which offers even broader spectrum of opportunities including soliton-like [4–6], self-induced [7, 8], tunable [7] and many-particle [9, 10] topological states.

Possibly the simplest model of the topological states in one-dimensional systems is provided by the well-celebrated Su–Schrieffer–Heeger model (SSH) [11, 12], which was investigated and realized in various contexts including electronic [11, 12], photonic [13–19], plasmonic [20–23], polaritonic [24] and mechanical [25] systems. Though initially the SSH model was applied to explain charge transfer in polymer molecules, it can be also used for describing the physics of artificial photonic and plasmonic structures. In photonic and plasmonic contexts, the SSH model can be implemented with the array of nearest-neighbor coupled cavities with the two alternating tunneling constants as depicted in Fig. 1(a). Plasmonic realization of the SSH model [21–23] allows one to achieve a nanoscale confinement of the edge mode which, however, is subject to the losses inherent to metals. On the contrary, the SSH model based on the all-dielectric platform [15, 16, 18] is almost loss-free but has worse confinement of light.

Note also that the SSH-type model can be implemented with a zigzag array of identical nanoparticles [15, 18–20, 23]. In such geometry, the vector eigenmode problem can be decomposed into two scalar problems, each of which has SSH type. This system can be based on plasmonic [20, 23] or all-dielectric [15, 18, 19] platforms that utilize electric dipole [20, 23], magnetic dipole [19] or magnetic quadrupole [15, 18] resonances of the constituent particles. Topological states in the described model emerge only for the specific range of zigzag angles [15, 19].

In this paper, we review the physics of the Su–Schrieffer–Heeger model and its nonlinear generalizations especially focusing on the edge states, their robustness and topological characterization. As we highlight, even such simple model features quite rich physics thus paving a route to the novel nanophotonic applications.

2. Topological states in the linear SSH model

The Hamiltonian of the SSH model in the linear case reads:

$$\hat{H} = \omega_0 \sum_m \hat{n}_m - J_1 \sum_m \left[\hat{a}_{2m}^\dagger \hat{a}_{2m-1} + \hat{a}_{2m-1}^\dagger \hat{a}_{2m} \right] - J_2 \sum_m \left[\hat{a}_{2m}^\dagger \hat{a}_{2m+1} + \hat{a}_{2m+1}^\dagger \hat{a}_{2m} \right], \quad (1)$$

where \hat{a}_m^\dagger and \hat{a}_m are creation and annihilation operators for the photon in m^{th} cavity, $\hat{n}_m = \hat{a}_m^\dagger \hat{a}_m$, $J_{1,2}$ are so-called tunneling amplitudes, and ω_0 is cavity eigenfrequency.

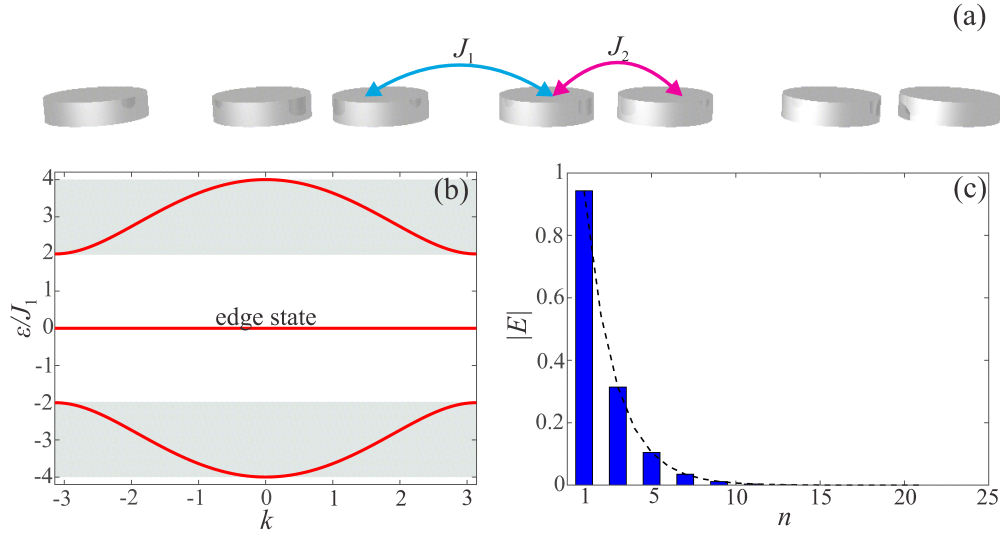


FIG. 1. (a) Array of coupled cavities described by the Su–Schrieffer–Heeger (SSH) model. (b) Energy bands (shaded) and edge states in the SSH model. (c) Field distribution for the the edge state in the SSH array of $N = 21$ coupled resonator. Calculations are performed for $J_2/J_1 = 3$

Note that the Hamiltonian commutes with the total number of particles $\hat{N} = \sum_m \hat{n}_m$. Therefore, the total number of photons in the array is conserved. First, we consider single-photon excitations. The wave function can be searched in the form:

$$|\psi_1\rangle = \sum_m \alpha_m \hat{a}_m^\dagger |0\rangle, \quad (2)$$

where $|0\rangle$ presents the ground state of the system, and coefficients α_m are the probability amplitudes to observe a photon in m^{th} cavity of the array. The eigenvalue equation $\hat{H} |\psi\rangle = (\varepsilon + \omega_0) |\psi\rangle$ yields the system of linear equations for the probability amplitudes α_m :

$$\varepsilon \alpha_1 = -J_1 \alpha_2, \quad (3)$$

$$\varepsilon \alpha_{2m+1} = -J_2 \alpha_{2m} - J_1 \alpha_{2m+2}, \quad (4)$$

$$\varepsilon \alpha_{2m} = -J_1 \alpha_{2m-1} - J_2 \alpha_{2m+1}, \quad (5)$$

where $m = 1, 2, \dots$. Quite importantly, exactly the same equations (3)–(5) are obtained in the classical limit when the number of photons is sufficiently large. In the latter case, α_m denotes electric field amplitude in m^{th} cavity. Such correspondence allows one to investigate the physics of the SSH model in fully classical setups, including electronic [11, 12], photonic [13–19], plasmonic [20–23], polaritonic [24] and mechanical [25] systems. The bulk energy spectrum of the SSH model is found from Eqs. (4)–(5) using the translational symmetry of the infinite array:

$$\alpha_{2m-1} = a e^{ikm}, \quad \alpha_{2m} = b e^{ikm}, \quad -\pi < k < \pi. \quad (6)$$

The result reads:

$$\varepsilon = \pm \sqrt{J_1^2 + J_2^2 + 2J_1 J_2 \cos k}. \quad (7)$$

The energy bands of the SSH model with the ratio $J_2/J_1 = 3$ are depicted in Fig. 1(b).

However, the SSH model supports not only bulk states Eq. (7), but also the edge state. To illustrate this, we consider a semi-infinite array and apply the full system of equations Eqs. (3)–(5), where Eq. (3) plays the role of the boundary condition. Straightforward calculation yields that the edge state exists under the condition $J_1 < J_2$ (i.e. the edge state emerges at the weak link edge), it has the energy $\varepsilon_{\text{edge}} = 0$ and the field distribution $\alpha_2 = \alpha_4 = \dots = \alpha_{2m} = \dots = 0$, $\alpha_{2m-1} = a e^{ikm}$ for $m = 1, 2, \dots$ with $e^{ik} = -J_1/J_2$. The field distribution for the edge state of the SSH model is shown in Fig. 1(c). If the array is terminated by weak links from both edges, two degenerate edge states appear.

Most remarkably, this edge state features some robustness with respect to the various forms of disorder. For instance, the eigenfrequencies of the resonators or tunneling amplitudes in the array can be randomly modulated

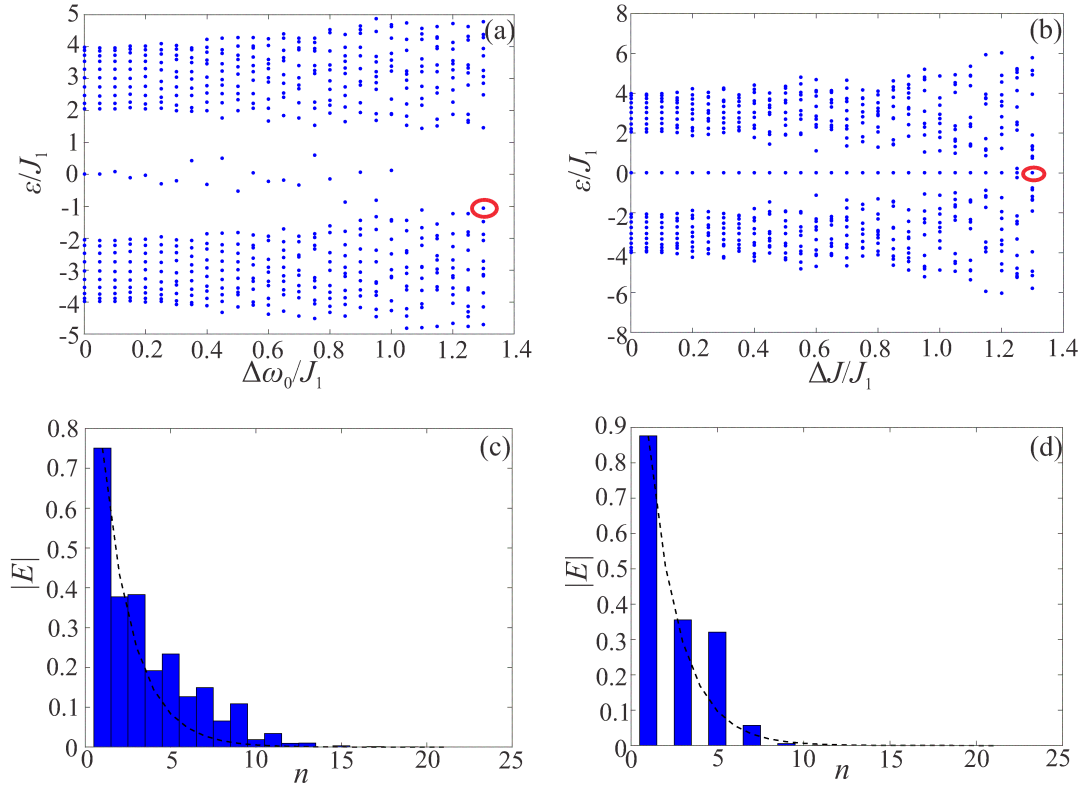


FIG. 2. Energy bands (a,b) and edge states (c,d) in the SSH model with $J_2/J_1 = 3$ when the disorder is introduced into the resonator eigenfrequencies (a,c) or into the tunneling amplitudes (b,d). $\Delta\omega_0$ and ΔJ are the standard deviations for the resonator eigenfrequency and tunneling amplitude, respectively. $|E|$ is the field amplitude inside the resonator

with the dispersion $\Delta\omega_0^2$ and ΔJ^2 , respectively. However, the edge state still persists even though the associated field distribution exhibits some distortions. This important property is further illustrated in Fig. 2.

Furthermore, the very existence of the edge state can be linked to the bulk properties of the system. To elucidate this point, we outline the calculation of the Zak phase [26]:

$$\gamma = \int_{-\pi}^{\pi} i \left\langle u_k \left| \frac{\partial u_k}{\partial k} \right. \right\rangle dk, \quad (8)$$

where $|u_k\rangle$ is the periodic part of the wave function. Since the unit cell contains only two cavities, the periodic part reads $|u_k\rangle = (a, b)^T$. With this unit cell choice, J_1 is an intracell tunneling amplitude, and J_2 is an intercell tunneling constant. The Zak phase is gauge-independent quantity defined modulo 2π that can take two values: $\gamma = 0$ for $J_1 > J_2$ and $\gamma = \pi$ for $J_1 < J_2$. Thus, the existence of the edge state is related to the nonzero Zak phase when the edge link is chosen to be the intracell tunneling constant. Note also that the Zak phase depends on the unit cell choice: if J_2 is considered as an intracell tunneling amplitude, the result for the Zak phase will be the opposite.

3. Nonlinear SSH models

The SSH model allows a number of interesting generalizations to the nonlinear domain. Here we will consider two nonlinear systems supporting edge states: classical nonlinear SSH array with the tunneling constants depending on intensity [7,8], and the SSH model in quantum two-particle regime with the effective photon-photon interaction [9,10].

An intuitive way to introduce the tunability in the SSH array of cavities is to make some of the tunneling constants intensity-dependent. The authors of Ref. [7] suggested a specific form of nonlinearity: $J_2^{2m,2m+1} = J_2 + \alpha (|E_{2m}|^2 + |E_{2m+1}|^2)$, $J_1 = \text{const}$, where E_m is the field amplitude in m^{th} resonator. For the zero mode intensity (measured by $A^2 = |E_1|^2 + |E_2|^2$), the system was chosen to be in the trivial regime $J_1 > J_2$ without any

edge states. However, with an increase of the intensity, the system undergoes a topological transition due to the growth of intercell coupling strength [7]. Such self-induced topological transition is illustrated in Fig. 3(a). Even though the fact of topological transition is suggested by the linear SSH model, the properties of the topological edge state which appears [Fig. 3(b)] strongly differ from its linear counterpart. The reason is that the effective tunneling amplitudes $J_2^{2m,(2m+1)}$ in the edge state become dependent on the index m due to the mode decay away from the array edge.

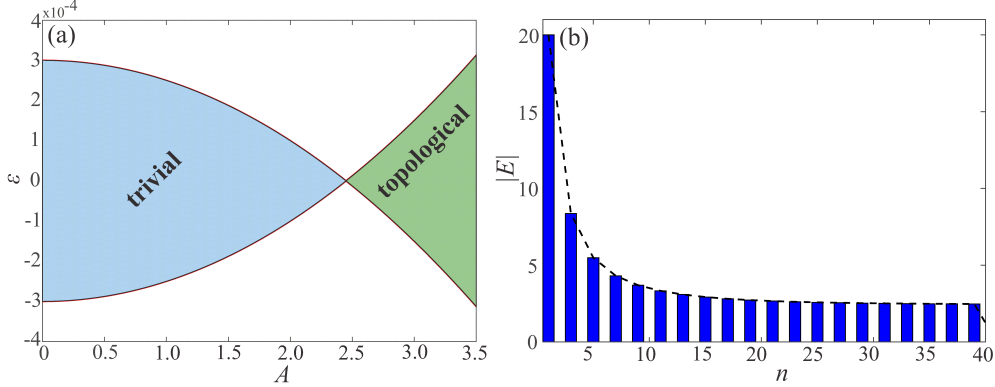


FIG. 3. Self-induced topological transitions and edge states in the nonlinear SSH model with the intercell coupling coefficient depending on intensity. (a) Transition from the trivial regime to the topological one happening due to the intensity increase. (b) Field distribution for the self-induced edge state calculated for $J_1 = 2.3 \cdot 10^{-3}$, $J_2 = 2.0 \cdot 10^{-3}$ and $\alpha = 5.0 \cdot 10^{-5}$

Another interesting system is the two-particle SSH model described by the Bose-Hubbard Hamiltonian [9,10]:

$$\hat{H} = \omega_0 \sum_m \hat{n}_m + U \sum_m \hat{n}_m (\hat{n}_m - 1) - J_1 \sum_m [\hat{a}_{2m}^\dagger \hat{a}_{2m-1} + \hat{a}_{2m-1}^\dagger \hat{a}_{2m}] - J_2 \sum_m [\hat{a}_{2m}^\dagger \hat{a}_{2m+1} + \hat{a}_{2m+1}^\dagger \hat{a}_{2m}]. \quad (9)$$

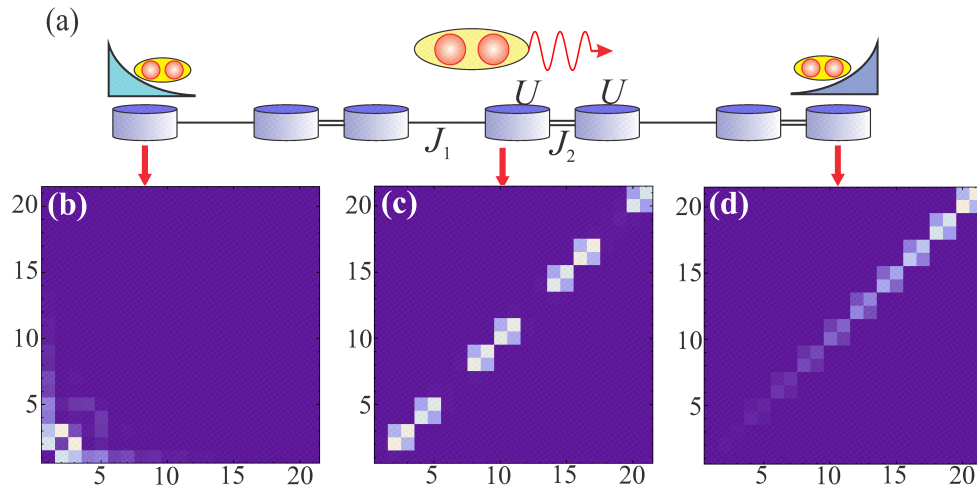


FIG. 4. Two-photon bound bulk and edge states in the SSH array described by Bose-Hubbard model with $J_2/J_1 = 5.0$, $U/J_1 = 8.0$. (a) The schematic of the two-photon bound states. (b,d) Probability distribution for the two-photon edge states localized at the edges of the array with smaller (b) and greater (d) tunneling amplitudes. (c) Probability distribution for the two-photon bulk bound states (doublons). x and y axes show the coordinates of the first and second photon, respectively

The U term takes into account Kerr-type nonlinearity of the medium inside the resonators. This nonlinearity induces effective photon-photon interactions and gives rise to the photon binding (Fig. 4(a,c)). Quite counter-intuitive, bound photon pairs (doublons) emerge even in the case of repulsive nonlinearity ($U > 0$) [27,28] and can appear in the continuum of weakly interacting two-photon states [29,30]. In the case of the simple array with $J_1 = J_2$, the doublon edge states are not possible [31,32]. However, in the SSH geometry, the edge states of bound photon pairs can appear not only at the edge with the weak tunneling link (Fig. 4(b)), as in the single-particle case, but also at the edge with the strong tunneling link (Fig. 4(d)) [10] which is a distinctive feature of the two-particle interacting problem. The latter edge states were argued to be topological [10].

4. Discussion and conclusions

Despite its conceptual simplicity, the Su–Schrieffer–Heeger model provides qualitatively correct description of the diverse physical phenomena related to electronic, photonic, plasmonic, polaritonic and mechanical systems. In the context of topological states, the most important feature of the SSH model is the emergence of the edge state which has the topological nature being robust against various forms of disorder. This topological state has been observed in a series of experiments with various systems either at the edge of the array or at the domain wall of the two SSH arrays with the different dimerizations.

Nonlinear generalizations of the SSH model feature even more exciting physics. Besides the tunability of the edge states, it becomes possible to realize self-induced topological transitions, soliton-like and many-particle edge states. Quantum topological states can be promising candidates for the variety of quantum optics and quantum information applications including the implementation of qubits and NOON states for quantum precision measurements.

We anticipate that the nonlinear topological SSH-type models which are currently under active investigation can shed new light onto the design of the novel types of nonlinear topological insulators.

Acknowledgements

This work was supported by the Russian Science Foundation (Grant No. 16-19-10538).

References

- [1] Lu L., Joannopoulos J.D., Soljačić M. Topological photonics. *Nature Photonics*, 2014, **8** (5), P. 821–829.
- [2] Lu L., Joannopoulos J.D., Soljačić M. Topological states in photonic systems. *Nature Physics*, 2016, **12** (7), P. 626–629.
- [3] Khanikaev A.B., Shvets G. Two-dimensional topological photonics, *Nature Photonics*, 2017, **11**, P. 763–773.
- [4] Leykam D., Chong Y.D. Edge solitons in nonlinear-photonic topological insulators. *Physical Review Letters*, 2016, **117** (14), P. 143901.
- [5] Chen B.G., Upadhyaya N., Vitelli V. Nonlinear conduction via solitons in a topological mechanical insulator. *Proceedings of the National Academy of Sciences of the United States of America*, 2014, **111** (36), P. 13004–13009.
- [6] Gulevich D.R., Yudin D., et al. Exploring nonlinear topological states of matter with excitation-polaritons: Edge solitons in kagome lattice. *Scientific Reports*, 2017, **7** (1), P. 1780.
- [7] Hadad Y., Khanikaev A.B., Alu A. Self-induced topological transitions and edge states supported by the nonlinear staggered potentials. *Physical Review B*, 2016, **93** (15), P. 155112.
- [8] Hadad Y., Vitelli V., Alu A. Solitons and Propagating Domain Walls in Topological Resonator Arrays. *ACS Photonics*, 2017, **4** (8), P. 1974–1979.
- [9] Di Liberto M., Recati A., Carusotto I., Menotti C. Two-body physics in the Su–Schrieffer–Heeger model. *Physical Review A*, 2016, **94** (6), P. 062704.
- [10] Gorlach M.A., Poddubny A.N. Topological edge states of bound photon pairs. *Physical Review A*, 2017, **95** (5), P. 053866.
- [11] Su W.P., Schrieffer J.R., Heeger A.A. Solitons in polyacetylene. *Physical Review Letters*, 1979, **42** (25), P. 1698–1701.
- [12] Heeger A.J., Kivelson S., Schrieffer J.R., Su W.P. Solitons in conducting polymers. *Reviews of Modern Physics*, 1988, **60** (3), P. 781–850.
- [13] Malkova N., Hromada I., et al. Observation of optical Shockley-like surface states in photonic superlattices. *Optics Letters*, 2009, **34** (11), P. 1633–1635.
- [14] Schomerus H. Topologically protected midgap states in complex photonic lattices. *Optics Letters*, 2013, **38** (11), P. 1912–1914.
- [15] Slobozhanyuk A.P., Poddubny A.N., et al. Subwavelength topological edge states in optically resonant dielectric structures. *Physical Review Letters*, 2015, **114** (12), P. 123901.
- [16] Poli C., Bellec M., et al. Selective enhancement of topologically induced interface states in a dielectric resonator chain. *Nature Communications*, 2015, **6**, P. 7710.
- [17] Blanco-Redondo A., Andonegui I., et al. Topological Optical Waveguiding in Silicon and the Transition between Topological and Trivial Defect States. *Physical Review Letters*, 2016, **116** (16), P. 163901.
- [18] Slobozhanyuk A.P., Poddubny A.N., et al. Enhanced photonic spin Hall effect with subwavelength topological edge states. *Laser & Photonic Reviews*, 2016, **10** (4), P. 656–664.
- [19] Kruk S., Slobozhanyuk A., et al. Edge States and Topological Phase Transitions in Chains of Dielectric Nanoparticles. *Small*, 2017, **13** (11), P. 1603190.
- [20] Poddubny A., Miroshnichenko A., Slobozhanyuk A., Kivshar Y. Topological Majorana States in Zigzag Chains of Plasmonic Nanoparticles. *ACS Photonics*, 2014, **1** (2), P. 101–105.

- [21] Ling C.W., Xiao M., et al. Topological edge plasmon modes between diatomic chains of plasmonic nanoparticles. *Optics Express*, 2015, **23** (3), P. 2021–2031.
- [22] Cheng Q., Pan Y., Wang Q., Li T., Zhu S. Topologically protected interface mode in plasmonic waveguide arrays. *Laser & Photonics Reviews*, 2015, **9** (4), P. 392–398.
- [23] Sinev I.S., Mukhin I.S., et al. Mapping plasmonic topological states at the nanoscale. *Nanoscale*, 2015, **7** (28), P. 11904–11908.
- [24] St-Jean P., Goblot V., et al. Lasing in topological edge states of a one-dimensional lattice. *Nature Photonics*, 2017, **11** (10), P. 651–656.
- [25] Kane C.L., Lubensky T.C. Topological boundary modes in isostatic lattices. *Nature Physics*, 2014, **10**, P. 39–45.
- [26] Zak J. Berry's Phase for Energy Bands in Solids. *Physical Review Letters*, 1989, **62** (23), P. 2747–2750.
- [27] Winkler K., Thalhammer G., et al. Repulsively bound atom pairs in an optical lattice. *Nature*, 2006, **441** (7095), P. 853–856.
- [28] Valiente M., Petrosyan D. Two-particle states in the Hubbard model. *Journal of Physics B*, 2008, **41** (16), P. 161002.
- [29] Zhang J.M., Braak D., Kollar M. Bound states in the continuum realized in the one-dimensional two-particle Hubbard model with an impurity. *Physical Review Letters*, 2012, **109** (11), P. 116405.
- [30] Zhang J.M., Braak D., Kollar M. Bound states in the one-dimensional two-particle Hubbard model with an impurity. *Physical Review A*, 2013, **87** (12), P. 023613.
- [31] Pinto R.A., Nguenang J.P., Flach S. Boundary effects on quantum q-breathers in a Bose-Hubbard chain. *Physica D*, 2009, **238** (5), P. 581–588.
- [32] Longhi S., Della Valle G. Tamm-Hubbard surface states in the continuum. *Journal of Physics: Condensed Matter*, 2013, **25** (23), P. 235601.

Calculations of switching field and energy barrier for magnetic islands with perpendicular anisotropy

S. Y. Liashko^{1,2}, H. Jónsson^{2,3}, V. M. Uzdin^{1,4}

¹ITMO University, Kronverkskiy, 49, St. Petersburg, 197101, Russia

²Science Institute and Faculty of Physical Sciences, Univ. of Iceland 107 Reykjavik, Iceland

³Center for Nonlinear Studies, Los Alamos, NM 87545, USA

⁴St. Petersburg State University, St. Petersburg, 198504, Russia

serjfv@gmail.com, hj@hi.is, v_uzdin@mail.ru

DOI 10.17586/2220-8054-2017-8-6-701-708

Calculations of the magnetic field required to reverse the magnetization of islands with out-of-plane anisotropy are carried out using a model describing nucleation followed by rapid domain wall motion. The calculations are based on an extension of the Stoner–Wohlfarth model where thermal activation is taken into account as well as the applied magnetic field. The calculated switching field distribution (SFD) is compared with recently reported experimental measurements of de Vries *et al.* [New J. Phys. 19, 093019 (2017)] on circular 220 nm CoPt islands. The measured results can be closely reproduced by choosing appropriate values of two parameters, the nucleation volume, and the effective anisotropy. Both the position of SFD peaks and their width at high and low temperature, 300 K and 10 K, are amply described using the same set of parameter values for a given island, while there is a large difference between islands with weak and strong magnetic anisotropies. There is no need to introduce the temperature dependence of the activation energy at zero field. This is in contrast with the estimates obtained from the so-called diamond model used by de Vries *et al.* in their data analysis where multiple adjustable parameters are introduced, and a three- to fourfold change in the zero field activation energy is invoked.

Keywords: activation volume, pre-exponential factor, magnetic islands, activation energy, rate theory, spin ice.

Received: 14 November 2017

Revised: 19 November 2017

1. Introduction

A large research effort has over the past decades been dedicated to studies of small magnetic particles. Advances in the technology for fabricating such particles of various forms, such as powder samples and ferrofluids, as well as ordered arrangements of magnetic particles have allowed a wide range of interesting experiments. As a result, new physical phenomena have been discovered and technological advances made, such as high anisotropy nanoparticles [1], single-domain magnetic dots [2] and devices for spin manipulation [3]. There is a large potential for such materials in new applications from high-density data storage and logic devices to magnetic sensors. New applications are constantly found, for example in medicine for transportation of chemical substances or transfer of energy to defined target regions in biological systems, both for diagnostics and therapeutics.

One of the most important issues is the description of the magnetization reversal processes in such systems. The bulk magnetic material consists of multiple regions with homogeneous magnetization – domains which are separated by domain walls. The structure and the shape of the domains are strongly dependent on the combination of exchange, magnetostatic and anisotropy energy. If one would decrease the volume of the magnetic system, the size of the domains and the width of the domain walls would also tend to decrease. If the size of the magnetic particles is decreased sufficiently, the formation of the domain wall becomes unfavorable, and only a single magnetic domain is found within the particles [4]. This critical size depends on the saturation magnetization, the exchange energy between the spins and the anisotropy energy. For spherical particles, the critical diameter is on the order of 10–800 nm [5]. For example, the critical diameters of Fe and Co particles have been estimated to be 15 nm and 35 nm, respectively, while for SmCo₅ an estimate of 750 nm has been given [6].

Even if the particles have a single magnetic domain, there can be variations in magnetic properties within the particle due to impurities, changes in elemental composition and due to the shape of the particle. As a result, the anisotropy and exchange energy, for example, can vary in different regions of the particle. A reversal of the magnetization in the presence of an applied field can start in regions where the spins can be more easily flipped and then propagate rapidly from there throughout the particle. The field required to reverse the magnetization, the switching field H_{sw} , is then strongly affected by imperfections in the particle that lower the activation energy for spin flips. Experiments on continuous [7] as well as patterned [8] magnetic devices including random access

memory devices [9] have been interpreted successfully in terms of such a nucleation and propagation mechanism for magnetization reversal. The switching field is then largely determined by the volume of the critical nucleus, which in turn determines the activation energy for the magnetization reversal.

Even carefully prepared samples of thin magnetic films on non-magnetic surfaces and magnetic islands patterned from such films have been found to have a wide distribution of nucleation volumes [10–12]. For example, experiments on Co/Pd islands as large as $5\ \mu\text{m}$ [12] have shown that the switching field distribution (SFD) of patterned islands is a reflection of the spatial variation of the nucleation volume of the continuous film from which the islands were formed. The measurements could be described by a model where the continuous film reverses by nucleation of a low anisotropy volume followed by rapid domain wall propagation. While it might be assumed that high exchange coupling in patterned islands would lead to narrow SFD, compared for example to the thin films, this is not what has been found experimentally [12,13]. Experiments, where the angle, θ , between the applied field and the anisotropy axis was varied, showed the well-known $1/\cos\theta$ dependence for the continuous film, consistent with a mechanism where the reversal rate is limited by wall propagation. However, a minimum in the critical field at 45° was found for magnetic islands, consistent with the Stoner–Wohlfarth model [14], which describes the rotation of a single magnetic moment of a homogeneous magnetic particle. This indicates that the rotation of the magnetic moment of the critical nucleus can be described by the Stoner–Wohlfarth model.

In recent experiments, de Vries *et al.* were able to measure the SFDs of individual magnetic islands and found a large variation in the properties of the islands even though the shape and size were the same [15]. In these experiments, the SFD is only a reflection of the stochastic nature of the thermal activation since the measurements are carried out for one island at a time but with repeated sweeps of the magnetic field. The experiments were based on the highly sensitive anomalous Hall effect and were carried out for disk-like islands of 220 nm diameter patterned from a Co/Pt multilayer film. A large difference was found in the maximum field needed to switch the magnetization of different islands, likely due to variations in the thickness and composition of the metallic layers from one island to another. “Weak” islands had, for example, a maximum in the SFD at a field of 84 kA/m while “strong” islands a maximum at 184 kA/m in measurements carried out at 10 K [15]. As the temperature was increased to 300 K, the peaks shifted to the lower field by ca. 50 kA/m and 30 kA/m for weak and strong islands, respectively.

These experiments were analyzed by a so-called diamond model, where the shape of the islands is approximated by a square, and the activation energy is related to the length of a domain wall that starts at one corner and then propagates through the island. Several parameters in the model were adjusted in order to reproduce the experimental measurements, including a fairly strong drop in the saturation magnetization, by 7 %, and the anisotropy constant, by 16 %, as the temperature is increased from 10 K to 300 K. In earlier research, de Vries *et al.* concluded from their analysis that the energy barrier for magnetization reversal in zero field is a factor of three to four lower at 300 K than at 10 K. This is a very large factor and would mean that this fundamental and important parameter could not be obtained from measurements of remagnetization rates over a range in temperature, as is frequently done to establish Arrhenius rate expressions.

In this article, we present calculations using an extended Stoner–Wohlfarth model [16] where the effect of thermal activation has been added and analyze the experimental measurements reported by de Vries *et al.* An analytical expression for the remagnetization rate, both pre-exponential factor, and activation energy is used to evaluate the SFD for both weak and strong islands. By adjusting two parameters in the model, the effective anisotropy constant and the nucleation volume, to reproduce the measured SFD peak positions, the full shape of the SFD at both 10 K and 300 K is found to be in close agreement with the experiments, without the need to vary the values of the parameters with temperature. Contrary to the conclusions described above, we find that a temperature independent energy barrier at zero field can be consistent with the experimental observations of de Vries *et al.* While the saturation magnetization and anisotropy should, of course, vary to some extent with temperature, our results indicate that it is only a small effect.

In the next section, the model is described including the method for calculating the SFDs. The results on the fitting of the peak positions are then described, followed by a comparison with the full shape of the SFDs. Calculated hysteresis loops for weak and strong islands are presented. Finally, the effect of temperature dependence is illustrated and discussed. The article closes with a conclusion section.

2. Model

The calculations are based on an extended Stoner–Wohlfarth model that takes into account thermal fluctuations [16]. This model was recently used to analyze remagnetization in elements of kagome spin ice [17]. In order to mimic the islands measured by de Vries *et al.*, the easy axis is taken to be perpendicular to the surface plane, and the applied magnetic field is directed parallel to the easy axis and opposite to the initial direction of

the magnetization. A schematic of an island and a critical nucleus for the reversal are shown in Fig. 1 along with the coordinate system used. It is chosen in the same way as in ref. [16] for consistency. In the present case, the magnetic moment entering the model represents a critical nucleus for the remagnetization transition, not the total magnetic moment of the island. It is assumed that the remagnetization transition starts in a small region within the island where for some reason it is easier to reverse the magnetic moments. Once the critical nucleus has formed, the domain of reversed magnetization grows quickly. A key parameter of the model is the volume of the nucleus, V , from which the magnetic moment of the nucleus, M , can be obtained by multiplying with the saturation magnetization, M_s , as $M = VM_s$. The other key parameter of the model is the anisotropy constant, K_1 . It represents an effective anisotropy that indirectly takes into account interfacial effects between the nucleus and the rest of the island. The experimental measurements of Thomson *et al.* [12] support the use of such a model to describe remagnetization in magnetic islands that are too large for uniform rotation of all the magnetic moments in the island to be feasible. The parameters V and K_1 are treated as adjustable model parameters.

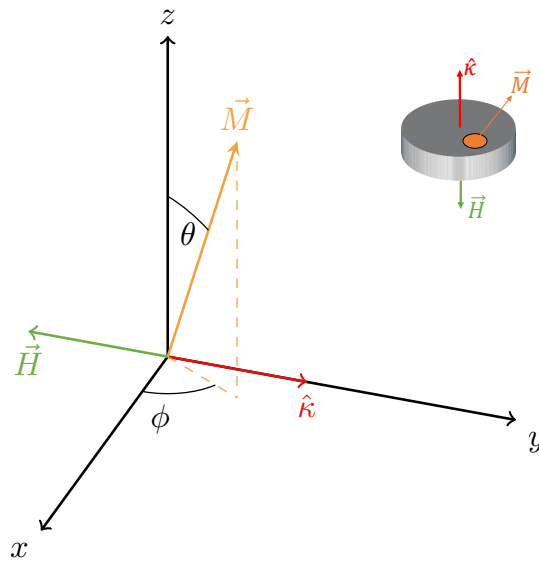


FIG. 1. Schematic representation of a magnetic island and the coordinate system used in the calculations. The out-of-plane anisotropy dominates over the in-plane anisotropy, and the magnetization is pointing along the surface normal, \hat{k} . The external magnetic field, \mathbf{H} , is directed opposite to the initial state magnetization. The model focuses on the magnetic moment of the critical nucleus of the remagnetization transition, \mathbf{M} , pointing in the direction given by θ and ϕ .

For an applied magnetic field, H , pointing in the direction of the out-of-plane anisotropy axis the extended Stoner–Wohlfarth model gives an analytical expression for the rate of magnetization reversals [16]:

$$k_{\parallel}^{HTST} = f_0 e^{-\Delta E/k_B T} = \frac{\gamma K_1 \sqrt{(1-h)(2c-h+1)}}{\pi M_s} \exp \left[-\frac{K_1 V}{k_B T} (1-h)^2 \right], \quad (1)$$

where γ is the gyromagnetic ratio, $h \equiv HM_0/2K_1$, and c is the ratio of the out-of-plane, K_1 , and in-plane, K_2 , anisotropy constants, $c \equiv K_2/K_1$. The value of c does not affect the calculated results significantly and is simply assumed here to be 0.1. This expression can be used to estimate the magnetic field needed to reverse the magnetization at a given temperature and for a given timescale. A similar model has been used to analyze the reversal of magnetization in a spring magnet [18].

In typical experimental measurements, including those of de Vries *et al.*, the magnetic field is increased at a constant rate, $R = \Delta H/\Delta t$ until the magnetization reverses. Since the transition is thermally activated, in addition to being aided by the applied field, the field strength at the point when the reversal occurs varies from one measurement to another. Given the pre-exponential factor, f_0 and activation energy, ΔE , as in the expression for the rate constant above, the probability density for the value of H when the magnetization switches can be

estimated as [19]:

$$p_{sw}(H) = \frac{f_0(H)}{R} \exp\left(-\frac{\Delta E(H)}{k_B T}\right) \times \exp\left[-\frac{1}{R} \int_{-H_{sat}}^{H'} f_0(H') \exp\left(-\frac{\Delta E(H')}{k_B T}\right) dH'\right]. \quad (2)$$

The value of $p_{sw}(H)dH$ gives the probability that the magnetization switching will occur when the field strength is within the interval $[H, H + dH]$ (the first two factors in 2), given the condition that it has not occurred at a smaller value of the field (the last factor in eq 2). This distribution can be compared with a histogram of the switching field in repeated measurements of a single magnetic island, as in the experiments of de Vries *et al.*. The M_s was chosen to have the reported value, $M_s = 829$ kA/m [15]. The islands were estimated to have a diameter of $d = 220$ nm and thickness $t = 20$ nm, giving total volume of $V_{isl} = 760 \cdot 10^3$ nm³, but these dimensions of the islands do not enter the calculations presented here since the focus is on the critical nucleus and its volume rather than the whole island. Only when the ratio of the volume of the nucleus and the total volume of the island is calculated for presentation purposes are the estimated total volume of the islands needed.

Each island is within this model described by the two parameters K_1 and V . Even if all the islands in the array have the same size and round shape, the effective anisotropy and, thereby, nucleation volume can differ significantly, for example, due to variations in the thickness of the metallic layers. Below, a detailed comparison is made between calculations using the model described above and the experimental measurements of de Vries *et al.* on weak and strong islands at a temperature of 10 K and 300 K.

3. Results

The maxima in the SFD at 10 K and at 300 K, H_{10K}^m and H_{300K}^m , were calculated over a range of values for the two model parameters, K_1 and V . The results are shown in Fig. 2. The contour graph shows the value of the difference, $\Delta H^m = H_{10K}^m - H_{300K}^m$, and the two colored curves show the values of K_1 and V that give H_{10K}^m in agreement with the values obtained by de Vries *et al.* for weak and strong islands. The measured shift, ΔH^m , is ca. 50 kA/m for weak islands and 30 kA/m for strong islands. The low-temperature peaks, H_{10K}^m , are largely determined by K_1 but V affects the calculated temperature dependence of the peak positions.

For one particular set of parameters, K_1 and V , the measured values of both H_{10K}^m and H_{300K}^m can be reproduced for each type of island. The peak in the SFD at 10 K is largely determined by the anisotropy parameter and is weakly dependent on the nucleation volume (thus the small slope of the colored lines). The temperature shift, however, depends also on V and the isolines of constant temperature shift in H^m are nearly straight lines with a significant slope.

Figure 3 shows the measured and calculated SFDs. It is evident from the figure that close agreement between the calculated and measured peak positions can be obtained by adjusting the two parameters. The optimal values are $K_1 = 99.28$ kJ/m³ and $V = 0.036V_{isl}$ for strong islands, and $K_1 = 49.46$ kJ/m³ and $V = 0.0067 V_{isl}$ for weak islands.

Not only are the measured peak positions reproduced well, but also the shape of the calculated SFDs is in agreement with the measurements of de Vries *et al.* [15]. Since the width of the SFD peaks is not part of the fitting procedure, this lends strong support for the appropriateness of the present model for this system. Also, it is interesting that this close agreement with the experimental data can be obtained with the same values of K_1 and V over such widely different temperature values, 10 K and 300 K. The shift in peak position and the increased width of the peaks as temperature is increased is accurately described by harmonic transition state theory for magnetic systems [20] on which the extended Stoner–Wohlfarth model is based.

The zero field activation energy obtained from the model using these values of the parameters is 1.6 eV for weak and 17.0 eV for strong islands. The difference is indeed very large, showing that the inhomogeneity is strong. The calculated pre-exponential factors in the rate expression, eqn. (1), at zero field are $3.5 \cdot 10^9$ Hz and for weak and $7.1 \cdot 10^9$ Hz for strong islands. These values are close to what has been assumed for Arrhenius rate expressions in the previous analysis [15,21]. However, in the present approach, these values are obtained from the extended Stoner–Wohlfarth model.

Calculated hysteresis loops for weak and strong islands are shown in Fig. 4. The SFD is used there to produce loops for each type of island representing averages obtained in repeated scans of the applied field. The narrowing of the loops as the temperature is increased from 10 K to 300 K is clearly seen as well as the rounding of the corners due to the stochastic nature of the thermal activation. While the applied field lowers the activation energy the system needs to overcome to reverse the magnetization, the transitions eventually occur due to thermal fluctuations. So, different values of the critical field are obtained in different scans of the field strength.

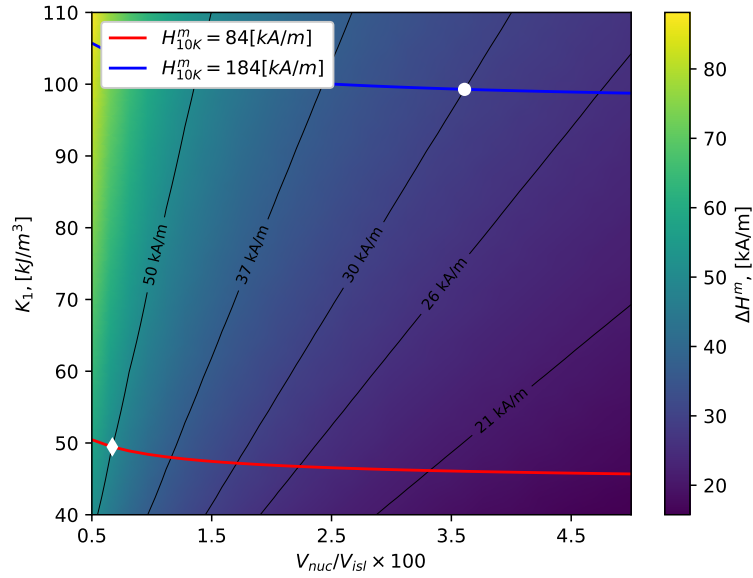


FIG. 2. Contour graph of the calculated shift in SFD peak positions when the temperature is increased from 10 K to 300 K, i.e., $\Delta H^m = H_{10K}^m - H_{300K}^m$, as a function of the two adjustable parameters, the anisotropy constant, K_1 , and the nucleation volume, V (given as the fraction of the total volume $V_{isl} = 760 \cdot 10^3 \text{ nm}^3$). Parameter values that give peak positions at 10 K, i.e., H_{10K}^m in agreement with experimental observations [15] are shown with lines (red for a weak island, blue for a strong island). White diamond and disk identify parameter values that give peak positions in agreement with experiments at both 10 K and 300 K for weak and strong islands, respectively. The figure illustrates how a unique set of the two adjustable parameters can be found in such a way as to obtain agreement between the calculated and measured position of maxima in the SFD.

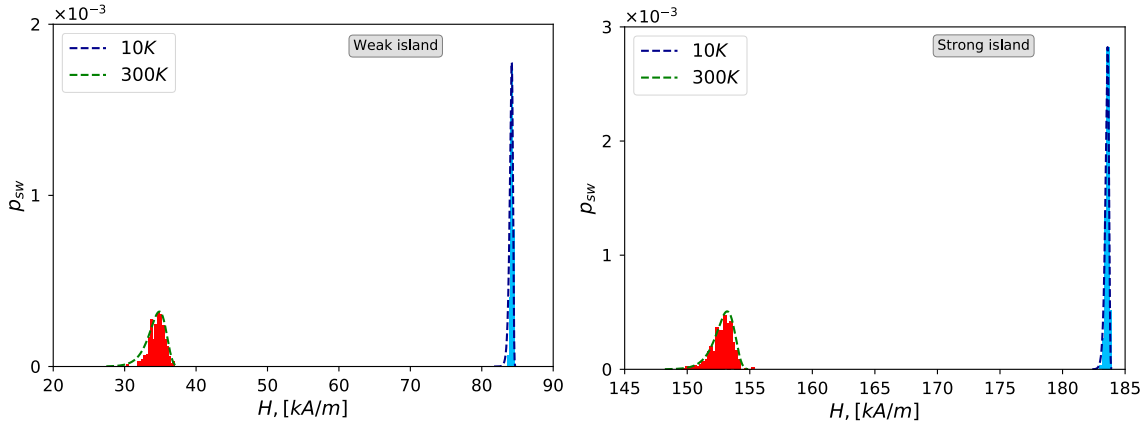


FIG. 3. Comparison of calculated (dashed lines) and measured (histograms) [15] SFDs for weak and strong islands at 10 K and at 300 K. The values of the two parameters, K_1 and V , in the theoretical model were obtained by adjusting the positions of the maxima of the SFD (see Fig. 2), but the shape of the SFDs then turns out to also be in close agreement with the experimental measurements.

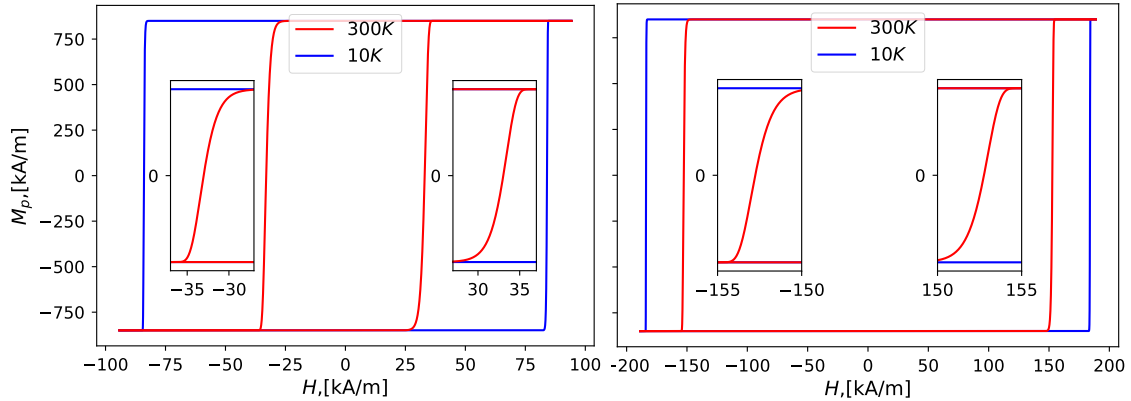


FIG. 4. Calculated hysteresis for a weak (left) and strong (right) island obtained from the calculated SFDs. The insets show on an expanded scale the rounding of the corners due to the stochastic nature of the thermal activation.

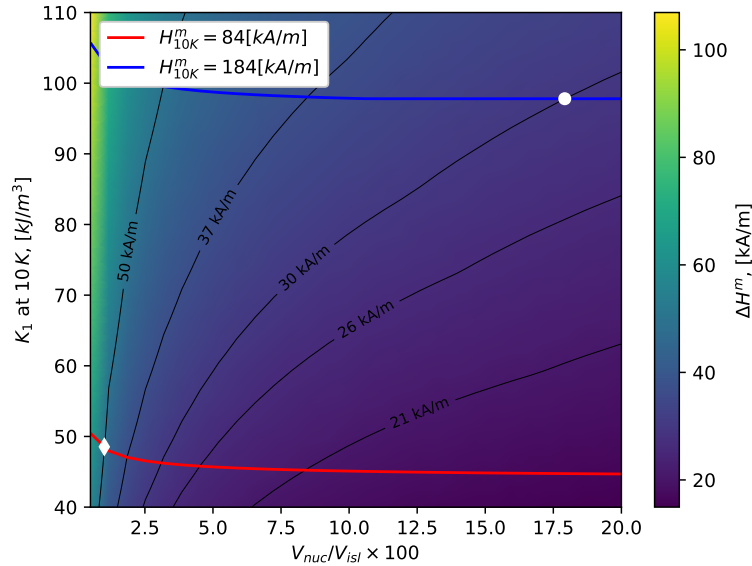


FIG. 5. Contour graph similar to Fig. 2 except here the saturation magnetization, M_s , is assumed to drop by 7 % and the anisotropy constant, K_1 , by 16 % as the temperature is increased from 10 K to 300 K, as estimated by de Vries *et al.* [15]. Parameter values that give peak positions at 10 K, i.e., H_{10K}^m in agreement with experimental observations [15] are shown with lines (red for a weak island, blue for a strong island). The value of the nucleation volume, V , needed to reproduce the shift in SDF peak position as the temperature is increased from 10 K to 300 K is much larger and the contour lines are more curved than when the parameters are temperature independent (see Fig. 2).

It is interesting that such close agreement with the experimental data can be obtained without changing the values of K_1 and V as well as M_s at the two values for the temperature, 10 K to 300 K. There will, of course, be some temperature dependence of these parameters, but the model used here indicates that it should be small. Previous estimates by de Vries *et al.* from their analysis showed a decrease in M_s by about 7 % and a decrease in K_1 by about 16 % as the temperature is increased from 10 K to 300 K [15]. It is indeed possible to reproduce the positions of the peaks in the SFDs with such a strong temperature dependence of these parameter values, but the nucleation volume, V , then needs to become 4 to 5 times larger at 300 K than at 10 K. As a result, the width of the SFD becomes much too narrow, by more than an order of magnitude, in strong disagreement with the experimental measurements. Within the present model, the decrease in the values of K_1 and V as well as M_s must be much smaller than the estimate of de Vries *et al.* in order to reproduce the experimental observations.

4. Conclusion

A simple model based on an extended Stoner–Wohlfarth equation for magnetization reversal in an island where the transition mechanism involves nucleation followed by rapid domain wall motion is found to reproduce well the elegant measurements of de Vries *et al.* [15] of SFDs of individual magnetic islands. The two adjustable parameters in the model, the anisotropy constant and the nucleation volume can be determined from the SFD peak positions at 10 K and 300 K. It is not necessary to include temperature dependence of the parameters. The shape of the SFD is then also found to be in close agreement with the measurements. The conclusion from this analysis of the experimental data is that the activation energy in zero field can be taken to be independent of temperature. This is in contradiction to the conclusion of de Vries *et al.* based on the diamond model, where the zero field activation energy is decreased by a factor of three to four (for weak vs. strong islands) as the temperature is increased from 10 K to 300 K. This represents a large and important difference in the analysis of the experimental data. If indeed the zero field activation energy were to change so much with temperature, the standard methodology for determining activation energy from measurements taken over a wide temperature interval could not be applied when determining this important quantity. Instead, our analysis indicates that the standard approach is applicable and can give a proper characterization of the magnetization reversal transition.

Our analysis does not assume the value of the pre-exponential factor, f_0 , in the rate expression, eqn. (1). Rather, it is obtained from the model. While the magnitude of the pre-exponential factor turns out to be between 10^9 Hz and 10^{10} Hz in the present case, similar to what is often assumed for magnetic transitions, it is important to realize that harmonic transitions state theory has in some cases been found to give quite different values for pre-exponential factors in magnetic reversals (see, for example, [22,23]). In general, it is important to evaluate the pre-exponential factor rather than just to assume some value.

5. Acknowledgements

This work was supported by the Icelandic Research Fund, the Academy of Finland (grant 278260) and the Government of the Russian Federation (grant 074U01).

References

- [1] Sun S., Murray C.B., Weller D., Folks L., Moser A. Monodisperse FePt nanoparticles and ferromagnetic FePt nanocrystal superlattices. *Science*, 2000, **287**(5460), P. 1989–1992.
- [2] Allwood D.A., Xiong G., Faulkner C.C., Atkinson D., Petit D., Cowburn R.P. Magnetic domain-wall logic. *Science*, 2005, **309**(5741), P. 1688–1692.
- [3] Katine J.A., Albert F.J., Buhrman R.A., Myers E.B., Ralph D.C. Current-driven magnetization reversal and spin-wave excitations in Co/Cu/Co pillars. *Physical Review Letters*, 2000, **84**(14), P. 3149.
- [4] Jacobs S., Bean C.P. *Fine Particles, Thin Films and Exchange Anisotropy*. Magnetism vol. III, ed. Rado G.T. and Suhl H. (New York: Academic), 1963, P. 275.
- [5] Zijlstra H. *Permanent magnets, theory*. Handbook of Magnetic Materials, vol. 3, ed. Wohlfarth E.P. (Amsterdam: North-Holland), 1982, P. 37–107.
- [6] Givord D., Lu Q., Rossignol M.F. *Coercivity in hard magnetic materials*. In Science and Technology of Nanostructured Magnetic Materials, Springer US, 1991, P. 635–656.
- [7] Zhu J.G., Peng Y., Laughlin D.E. *Toward an understanding of grain-to-grain anisotropy field variation in thin film media*. IEEE transactions on magnetics, 2005, **41**(2), P. 543–548.
- [8] Terris B.D., Thomson T. Nanofabricated and self-assembled magnetic structures as data storage media. *Journal of physics D: Applied physics*, 2005, **38**(12), P. R199.
- [9] Engel B.N., Akerman J., Butcher B., Dave R.W., DeHerrera M., Durlam M., Slaughter J.M., et al. A 4-Mb toggle MRAM based on a novel bit and switching method. *IEEE Transactions on Magnetism*, 2005, **41**(1), P. 132–136.
- [10] Jang H.J., Eames P., Dahlberg E.D., Farhoud M., Ross C.A. Magnetostatic interactions of single-domain nanopillars in quasistatic magnetization states. *Applied Physics Letters*, 2005, **86**(2), P. 023102.
- [11] Kitade Y., Komoriya H., Maruyama T. Patterned media fabricated by lithography and argon-ion milling. *IEEE transactions on magnetics*, 2004, **40**(4), P. 2516–2518.
- [12] Thomson T., Hu G., Terris B.D. Intrinsic Distribution of Magnetic Anisotropy in Thin Films Probed by Patterned Nanostructures. *Phys. Rev. Lett.*, 2006, **96**, P. 257204.
- [13] Shaw J.M., Rippard W.H., Russek S.E., Reith T., Falco C.M. Origins of switching field distributions in perpendicular magnetic nanodot arrays. *Journal of Applied Physics*, 2007, **101**(2), P. 023909.
- [14] Stoner E.C., Wohlfarth E.P. A mechanism of magnetic hysteresis in heterogeneous alloys. *Phil. Trans. Roy. Soc. A*, 1948, **240**, P. 599–642.
- [15] de Vries J., Bolhuis T., Abelman L. Temperature dependence of the energy barrier and switching field of sub-micron magnetic islands with perpendicular anisotropy. *New J. Phys.*, 2017, **19**, P. 093019.
- [16] Liashko S.Y., Uzdin V.M., Jónsson H. Thermal stability of magnetic states in submicron magnetic islands. *Nanosystems: Physics, Chemistry, Mathematics*, 2017, **8**(5), P. 572–578.
- [17] Liashko S.Y., Jónsson H., Uzdin V.M. The effect of temperature and external field on transitions in elements of kagome spin ice. *New J. Phys.*, 2017, **19**, P. 113008.

- [18] Moskalenko M., Bessarab P.F., Uzdin V.M., Jónsson H. Qualitative Insight and Quantitative Analysis of the Effect of Temperature on the Coercivity of a Magnetic System. *AIP Advances*, 2016, **6**(2), P. 025213.
- [19] Engelen J.B., Delalande M., Le Febre A.J., Bolhuis T., Shimatsu T., Kikuchi N., Abelmann L., Lodder J.C. Thermally induced switching field distribution of a single CoPt dot in a large array. *Nanotechnology*, 2009, **21**(3), P. 035703.
- [20] Bessarab P.F., Uzdin V.M. Jónsson H. Harmonic Transition State Theory of Thermal Spin Transitions. *Phys. Rev. B*, 2012, **85**(18), P. 184409.
- [21] Engelen J.B.C., Delalande M., le Febre A.J., Bolhuis T., Shimatsu T., Kikuchi N., Abelmann L., Lodder J.C. Thermally induced switching field distribution of a single CoPt dot in a large array. *Nanotechnology*, 2010, **21**(3), P. 035703.
- [22] Bessarab P.F., Uzdin V.M. Jónsson H. Size and Shape Dependence of Thermal Spin Transitions in Nanoislands. *Phys. Rev. Lett.*, 2013, **110**(2), P. 020604.
- [23] Ivanov A.A., Bessarab P.F., Uzdin V.M., Jónsson H. Magnetic exchange force microscopy: Theoretical analysis of induced magnetization reversals. *Nanoscale*, 2017, **9**(35), P. 13320–13325.

1-bit and 2-bit comparator designs and analysis for quantum-dot cellular automata

A. Mallaiah¹, G. N. Swamy², K. Padmapriya³

¹Research Scholar, JNTUA, Anthapuramu, A.P, India

²Department of EI&E, VR Siddhartha Engineering College, Vijayawada, A.P, India

³Department of ECE, JNTUK, Kakinada, A.P, India

malli797@gmail.com

PACS 03.65.Xp , 03.67.Hk , 03.67.Lx, 05.60.Gg

DOI 10.17586/2220-8054-2017-8-6-709-716

In PCs, the number of arithmetic operations, the comparator is a vital equipment unit, consisting of complementary metal-oxide-semiconductor (CMOS) technology. Another procedure, referred to as Quantum Cellular Automata (QCA) will supplant the CMOS outlines, having leverage concerning zone, control utilization, and latency. The primary QCA circuits planned with the inverter and majority voter entryways. In this paper, we utilize the clocking method 180 out of phase clock crossover to outline the 1-bit comparator and compare with the current outcomes. The new proposed wire crossing plan lessens the quantity of cells required to configuration, power and area necessities. Additionally, we planned 2-bit comparator having 11 majority gates (voters), 2 number of crossovers with $0.38 \mu\text{m}^2$ area, 203 number of cells. The designed 1-bit comparator contrast and the past outcomes where cells, region, delay demonstrates 53.57 %, 50 % and 33.32 % improvement respectively.

Keywords: QCA design, wire crossing, comparator, Ex OR gate.

Received: 16 November 2017

Revised: 21 November 2017

1. Introduction

A few advanced microchips that have been popularized in the 21-st century incorporate decimal number juggling equipment units. This is a reaction to procuring requests for sophisticated calculations which are necessary for cost-saving and mechanical applications. As the preparing requests approach galactic measurements, the PC business is considering the possible development towards new rising advancements to defeat CMOS limitations for execution speed and wide power scattering on limiting the incorporated circuits [1–4].

The present crucial breaking points in CMOS circuit's calculations and development of quantum mechanical impacts in exponentially as of recently added quantum circuits to another dimensional tending of the electronic group [5,6]. As a consequence, quantum calculation and data remain an appealing territory of research over the most recent few decades [7]. This shows that superior information of quantum mechanics is required.

The innovation of quantum dot cell automata (QCA) proposed by Lent and Tougaw, is plainly becoming one of the developing advances without bounds PCs due to its minor component sizes, ultra-low power utilization, straightforward conceptualization [8,9].

Quantum dot cellular automata are the processing with cell automata confined with varieties of quantum dots. A QCA cell is a Nano shell device ready to encode data by two electron shape. Current advancement of quantum computing continues from numerous viewpoints; quantum circuit's combination is the massive test in the quantum information handling and the improvement of the quantum PC engineering [10].

2. Quantum DOT Cellular Automata (QCA)

2.1. Background: How QCA charge transfer?

A QCA cell can be seen as an arrangement of four charge vessels or “specks”, set in the corners of a square. The cell is pick up accuse of two free electrons which are able to burrow between dots. QCA are exhibited coulomb coupled quantum dot cells. Electrons situated in every cell have characteristic states with characteristic relate charge scattering. The condition of every cell is checked by its significant interaction with adjoining cells [26]. Bury cell barriers entirely repress charge exchange between the cells. The limit condition of last cells which go about as an information and yield cells which rely upon numerous electron frameworks in the composed circuit. Edge cells are controlled by the communication of electrostatic charge. With the computational issue settled one can outline the QCA design of the cells change starting from the earliest stage of electrons to arrangement state. We have watched the electron move in the wire (course of action of cells by adjoining) to perform general calculations.

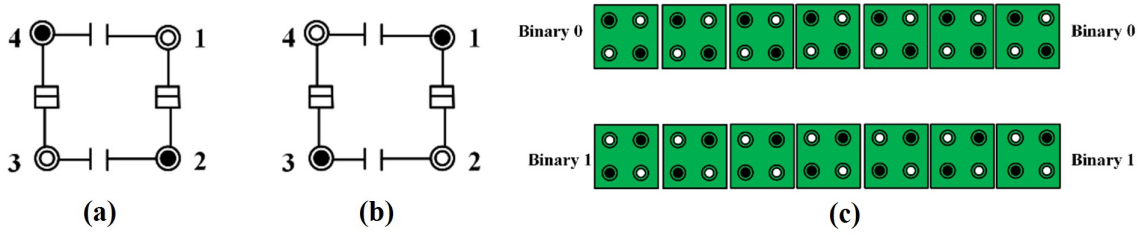


FIG. 1. (a) (b) QCA cell negative polarization denoted as logic “0”; (b) QCA cell with positive polarization denoted as “1”; (c) QCA wire showing charge transfer

A regular illustration of a solitary QCA cell is shown in Fig. 1(a,b). This figure demonstrates that a cell of four quantum dots organized in a square. There are two electrons inside the cell and passage obstructions between adjoining destinations [11, 12]. Burrowing out of the cell is thought to be totally stifled. QCA cell measure was reduced to nuclear measurements. As cell measure diminished the energy part between stationary states increments and the fleeting reaction turns out to be speedier. The close neighbor separation between dots inside a standard cell is 20 nm, the burrowing energy between dots is 0.3 meV.

2.2. Clocking

The timing of QCA, follow the semi adiabatic timing system. This system consists of four stages: switch, hold, release (discharge) and relax (unwind). At first, when the potential energy of the electron is low and the electron isn’t equipped for burrowing between quantum dots, it has a definite extremity. With the start of the switch stage, the potential vitality of electrons begins to rise and toward the finish of this stage the electron achieves its most extreme potential vitality. Amid the hold stage the electron keeps up its greatest potential energy and turns out to be totally delocalized losing its polarity. In the discharge stage the potential energy of the electron begins to decrease and the cell moves incrementally towards a definite polarity. Amid the last stage i.e. the unwind stage the electron keeps up least energy and is excessively powerless, making it impossible to burrow between the dots. Along these lines, the cell achieves a definite extremity. Each QCA engineering involves four clock zones, if not less, each of which contains the above said four clock stages. Each check zone is out of stage with the following check zone as appeared in Fig. 2(a). The different check zones in a QCA design are spoken to by different hues. The shading codes we have utilized is appeared in Fig. 2(b).

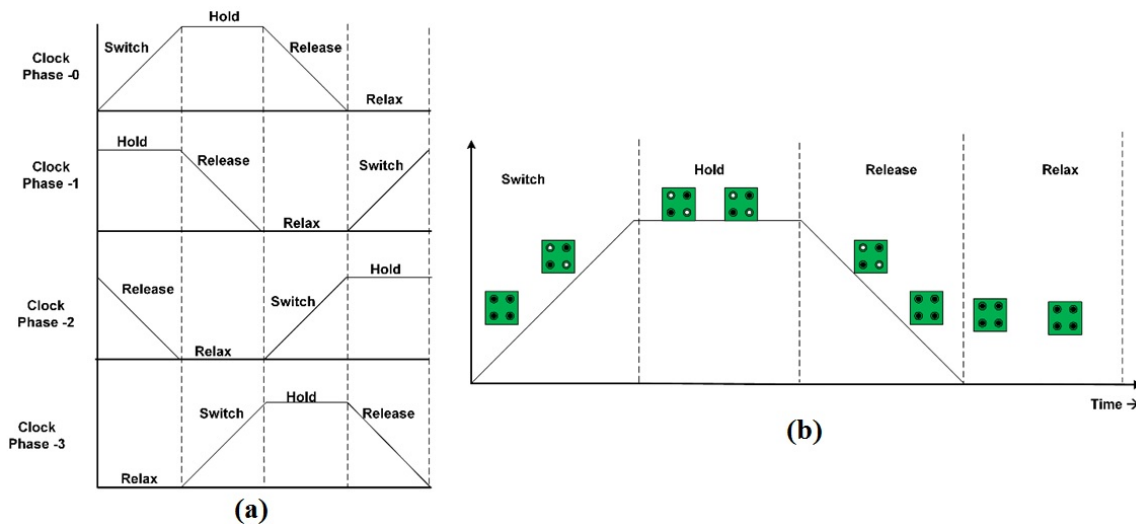


FIG. 2. (a) QCA cell with clocking; (b) Propagating of QCA cell in clock zones

The principle contrast between CMOS configuration circuits and QCA configuration circuits is that in the CMOS, the clock flag controls the circuit yield and states, whereas in QCA, the clock is valuable to exchange the charge information from one cell to next contiguous associated cell. On each clock cycle every cell discharge or evacuates its state and each cell in QCA including info and yield cells are clock controlled [13].

2.3. Wire crossing technique

For efficient design of QCA circuit in a smaller footprint, one area of primary consideration is wire crossing. Wire crossing is vital in QCA based plan and numerous strategies have been proposed to outline an efficient wire crossing, for example, coplanar based and the multilayer based methods, recently. Meanwhile the wire crossing strategies utilizing the control of clock stage have also been proposed [14]. Keeping in mind the end goal to outline the wire crossing using the said procedures, extra undertakings ought to be requested, for example, interpretation or rotation of QCA cells control of clock stage, expansion of bigger and soon. Like this their methods require extra time or spatial intricacy.

i) Coplanar based wire crossing procedure was proposed by Tougaw and Lent is shown in Fig. 3(a) basic geometry of the coplanar based wire crossing system [18, 19]. In this illustration the vertical wire and even wires are transmitting the values of 1 and 0 separately. To actualize this wire crossing the cell of horizontal wire are rotated by 45° . On the off chance that the length of the vertical wire after a crossing point cell is adequate a transmitting value is not influenced by the other wire [14]. Likewise the horizontal wire should consist of an odd number cells, since the property of the rotated cells has an inverter chain that the polarization substitutes heading between neighboring cells. Cells rotated by 45° initiate the extra space between cells. It inherently diminishes the energy partition between the ground state and the primary energized state which debases the execution of such a device as far as highest working temperature, protection from entropy, and least exchanging time [15].

ii) Multilayer-based wire-crossing strategy utilizes a hybrid crossover technique. This approach is similar to that of the coplanar-based method from the perspective of the floor design since it would seem that appearance of two wires crossing. Truth be told, it comprises of the stereoscopic structure. In spite of the fact that this strategy has a few focal points, the noise issue between convergence cells in the hybrid territory is present [6]. There are additionally a few things to consider for plan and recreation forms in QCA Designer, for example, the quantity of layers, crossover and vertical cells [16].

iii) QCA wire crossing is utilizing the different of clock system we consider the idea of QCA clock stage, for instance the information of present clock region is obtained from the past clock region. In this new technique each non-neighboring clock area does not influence the inverse clock area. In this plan wire crossing depends on the distinction of 180° between two nonadjacent clock regions. However in this strategy a bit much of 45° rotation of cells utilized as a part of co planar wire intersection and sub layers courses of action as utilized as a part of multi-layer wire crossing technique the nitty gritty wire crossing information appeared in Fig. 3(b) utilizes an inverse stage wire clock 0 and clock 2 and in Fig. 3(c) utilizes clock 1 and clock 3 wires used to information stream, the convergence cell can be have a place with any of two wires (either clock 0 or clock 2 in Fig. 3(b) and clock 1 or clock 3 in Fig. 3(c)) and there is no interface with each other.

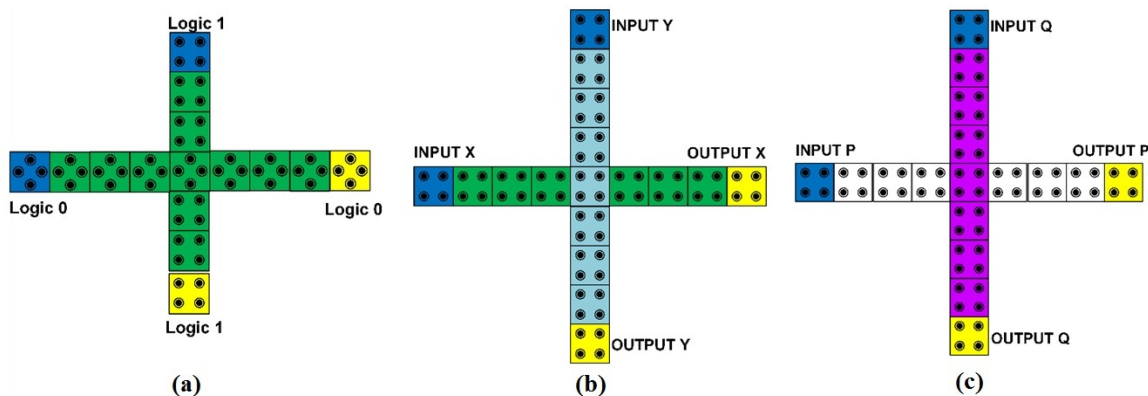


FIG. 3. (a) Co Planar wire crossing; (b) wire crossing using clock 0 and clock 2; (c) wire crossing using clock 1 and clock 3

3. Exclusive OR gate QCA layout

To outline any computerized rationale circuits fundamental entryways AND,OR, NOT and NAND,NOR universal gates are utilized. Notwithstanding that EX-OR additionally utilized for outline of complex circuits like adders, comparators and multipliers so on [17–19].

Here we demonstrated the new format engineering of EX-OR entryway consisting of 13 cells with 1/2 clock delay (Fig. 4). In Table 1, the examination of given EX-OR entryway is demonstrated. This composed EX-OR gate extremely helpful to limit the QCA facilitate format regarding number of cell and clock delay.

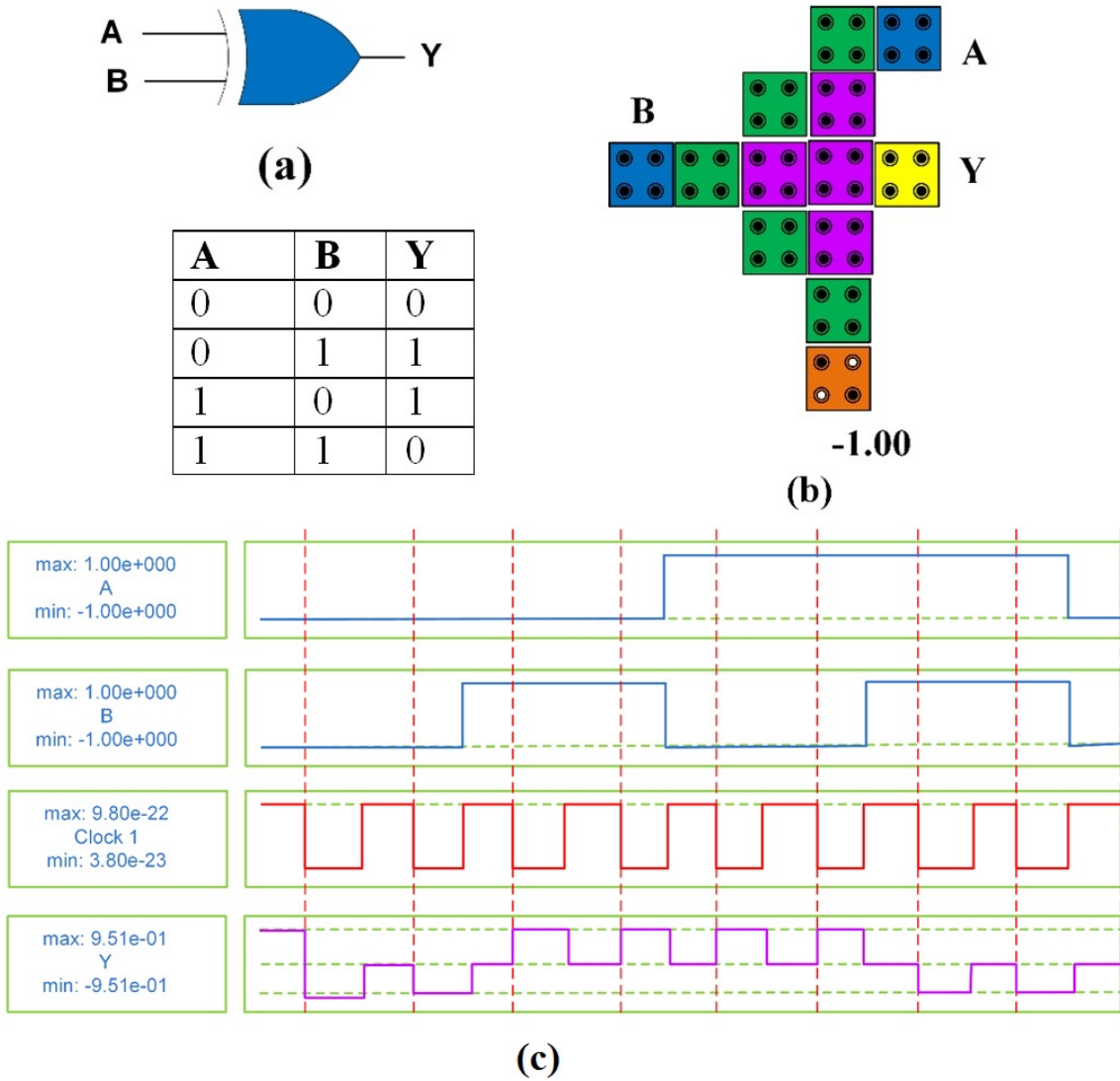


FIG. 4. (a) EX-OR gate symbol and truth table (b) QCA layout Design for a EX-OR gate (c) Simulation waveform

TABLE 1. QCA Ex-OR gate layout comparison analysis

XOR gate in	Area (μm^2)	Delay Clock Cycles	Majority gates count	Number of cells
[20]	0.06	1.25	3	67
[21]	0.02	1	3	32
[22]	0.0233	0.75	4	30
[23]	0.02	0.75	4	28
proposed design	0.01	0.5	1	13

4. Simulation results and discussion

The essential function of a comparator is to regard the magnitude of two binary data to determine their relationship. The EX-NOR gate can be utilized as a fundamental comparator in light of the fact that its output is a 1. On the off chance that the two information bits are equivalent and a 0 if the information bits are not equivalent. we demonstrated 1 bit and 2 bit comparator composed utilizing QCADesign programming with wire crossing uses an inverse clock (180 phase shift) system and actualized with most recent EX-OR entryway. Fig. 5(a,b) demonstrates the 1 bit and 2 bit comparator and planned with fewest number of logic gates. The logic concerns the yield of two bits (A, B) less than ($W1, W2$), equal ($X1, X2$), or greater than ($Y1, Y2$) of 1 bit and 2 bit comparator spoke to with logic condition appeared underneath after streamlined with the K-map.

The logic for a 1 bit comparator outputs is as follows:

$$W1 = A'B, \tag{1}$$

$$X1 = AB + A'B' = A \odot B, \tag{2}$$

$$Y1 = AB'. \tag{3}$$

The logic for a 2 bit comparator outputs is as follows:

$$W2 = A1'A0'B0 + A1'B1 + A0'B1B0 = A1'B1 + (A1 \odot B1)A0'B0, \tag{4}$$

$$X2 = A1'B0'B1'B0' + A1'A0B1'B0 + A1A0B1B0 + A1A0'B1'B0' = (A1 \odot B1)(A0 \odot B0), \tag{5}$$

$$Y2 = A1A0B0' + A1B1' + A0B1'B0' = A1B1' + (A1 \odot B1)A0B0'. \tag{6}$$

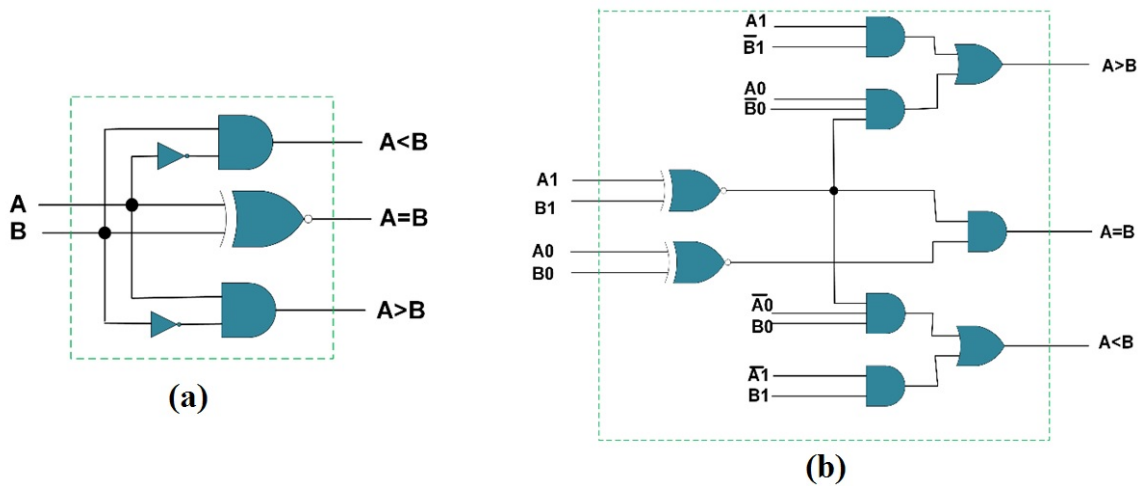


FIG. 5. (a) 1 bit comparator logic circuit; (b) 2 bit comparator logic circuit

TABLE 2. QCA layout analysis of proposed comparators

Name of the comparator		Area (μm^2)	Delay in Clock Cycles	Number of Clock Phases	Number of cells	Wire crossing
1 bit comparator	[24]	0.343	4	16	319	Co-planar
	[25]	0.182	1	4	117	Co-planar
	[26]	0.127	1.25	5	100	Co-planar
	[27]	0.103	1.25	5	95	Multilayer
	Proposed	0.10	0.5	2	60	180 ° clock phase shift
2 bit comparator	Proposed	0.38	1.25	5	203	180 ° clock phase shift

Figure 6(a,b) demonstrates 1 bit comparator and 2 bit comparator planned with no extra assignments, in those outlines we are disposed to utilize consistent coplanar or multilayer wire crossing; here composed circuits utilized 180 clock phase shift wire crossing. Fig. 7 demonstrates the results were obtained with high polarization and less noise. It is regular to assess any QCA circuit as far as the area utilized, clock delay and a number of cells utilized.

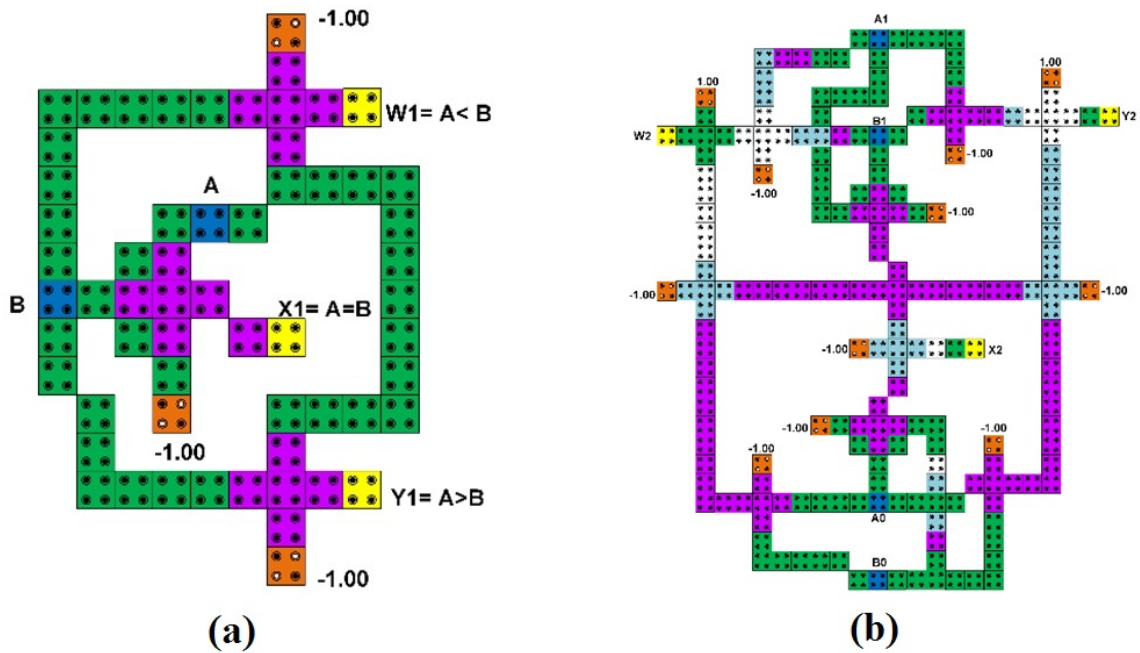


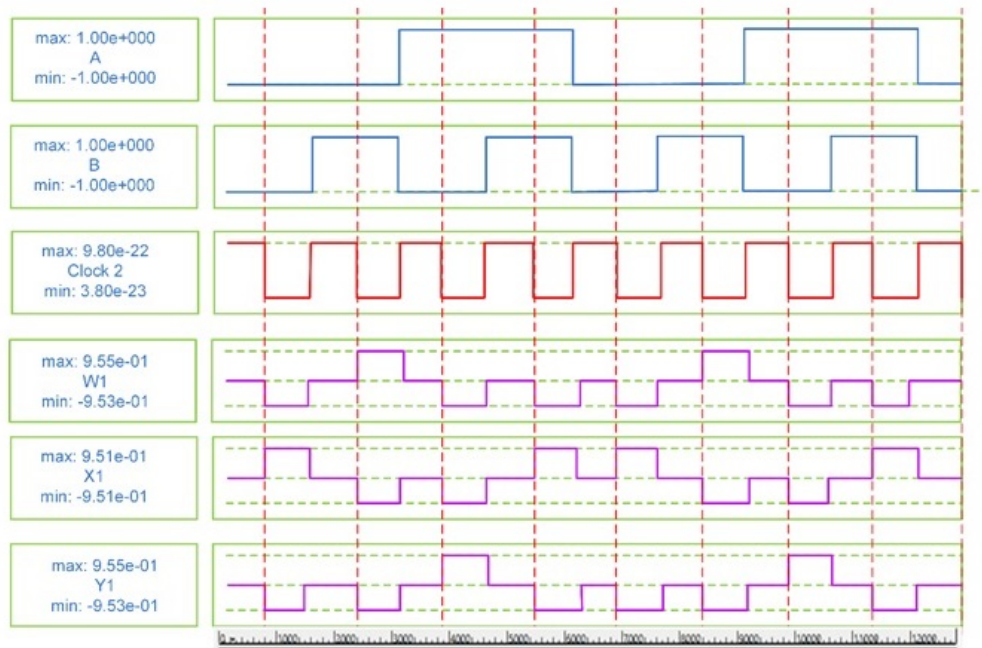
FIG. 6. (a) Proposed 1 bit comparator QCA layout; (b) Proposed 2 bit comparator QCA layout

It has been noted that our designs utilize fewer cells and has less delay. In Table 2, one can see the correlation of past plans and furthermore recorded the proposed 2 bit comparator not compared and the past outlines in light of its inaccessibility in the current literature.

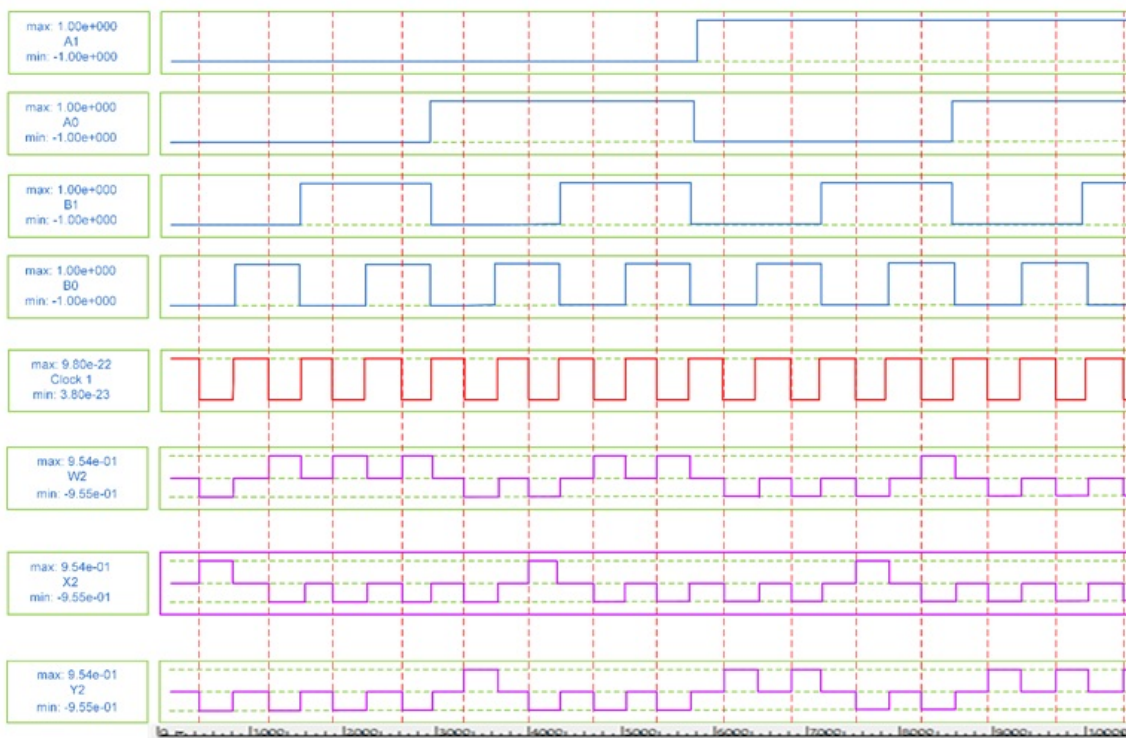
5. Conclusions

The more significant part of QCA combinational circuits with coplanar or multilayer wire crossing it have many-sided outline quality is more. In this paper we proposed a smaller comparator with clock 180 degree wire crossing technique. We composed this QCA design in the QCADesign test system. The proposed 1 bit comparator layout cell count less than 36.84 % of most recent outline and area occupation are less than 2.91 % with delay utilizes just 1/2 clock, whereas the 2 bit comparator possesses range $0.38 \mu\text{m}^2$, cell count 203 with clock delay of 1 1/2.

Generally, QCA circuits have incredibly noteworthy wiring delays for a quick plan in QCA, many-sided quality imperatives are exceptionally basic issues and the outline needs to utilize compositional systems to support the speed considering these limitations. The QCA innovations once realized will probably require a change in the outline rules. These outlines utilized the given particular plan rules, however as in a CMOS plan they can be scaled in a similar manner. This provides a chance to contrast the abnormal state outline engineering and in QCA circuits.



(a)



(b)

FIG. 7. Simulation results of proposed comparators: (a) 1-bit comparator; (b) 2-bit comparator

References

- [1] Walus K., Dysart T., Jullien G., Budiman R. QCADesigner: a rapid design and simulation tool for quantum-dot cellular automata. *IEEE Trans. Nanotechnol.*, 2004, **3**(1), P. 26–29.
- [2] Vetteth A., Walus K., Dimitrov V.S., Jullien G.A. Quantum-dot cellular automata of flip-flops. *Proceedings of the 2003 National Conference on Communications (NCC 2003)*, 2003, P. 368–372.
- [3] Cho H., Swartzlander E.E. Adder and multiplier designs in quantum-dot cellular automata. *IEEE Trans. Comput.*, 2009, **58**(6), P. 721–727.
- [4] Walus K., Schulhof G., Jullien G. Implementation of a simulation engine for clocked molecular QCA, in *IEEE Canadian Conference on Electrical and Computer Engineering (CCECE'06)*, 2006, P. 2128–2131.
- [5] Cho H., Swartzlander E.E. Adder designs and analyses for quantum-dot cellular automata. *IEEE Trans. Nanotechnol.*, 2007, **6**(3), P. 374–383.
- [6] Flood A.H., et al. Whence Molecular Electronics. *Science*, 2004, **306**(5704), P. 2055–2056.
- [7] Heath J.R., Ratner M.A. Molecular Electronics. *Physics Today*, 2003, P. 43–49.
- [8] Chen Y., et al. Nanoscale molecular-switch devices fabricated by imprint lithography. *Applied Physics Letter*, 2003, **82**(10), P. 1610–1612.
- [9] Steuerman D.W., et al. Molecular-Mechanical Switch-Based Solid-State Electrochromic Devices. *Angewandte Chemie International Edition*, 2004, **43**(47), P. 6486–6491.
- [10] Hadley P. Single-Electron Tunneling Devices, AIP conference proceedings 427, 1998, P. 256–270.
- [11] Tahoori M.B., Momenzadeh M., Huang J., Lombardi F. Defects and Faults in Quantum-Dot Cellular Automata. *VLSI Test Symposium (VTS)*, 2004, P. 291–296.
- [12] Berzon D., Fountain T.J. A Memory Design in QCAs Using the SQUARES Formalism. *Proceedings Ninth Great Lakes Symposium on VLSI*, 1999, P. 166–169.
- [13] Orlov A.O., et al. Experimental Demonstration of Clocked Single-electron Switching in Quantum-dot Cellular Automata. *Applied Physics Letters*, 2000, **77**(2), P. 295–297.
- [14] Jiao J., et al. Building Blocking for the Molecular Expression of QCA. Isolation and Characterization of a Covalently Bounded Square Array of two Ferrocenium and Two Ferrocene Complexes.
- [15] Qi H., et al. Molecular Quantum Cellular Automata Cells: Electric Field Driven Switching of a Silicon Surface Bound Array of Vertically Oriented Two-Dot Molecular QCA. *Journal of the Am. Chem. Society*, (JACS Articles), 2003, **125**(49), P. 15250–15259.
- [16] Antonelli D.A., et al. Quantum-Dot Cellular Automata (QCA) Circuit Partitioning: Problem Modeling and Solutions. *Design Automation Conference (DAC)*, 2004, P. 363–368.
- [17] McCluskey E. *Logic Design Principles*, Englewood Cliffs. NJ: Prentice-Hall, 1986.
- [18] Lent C.S., Tougaw P.D., Porod W. Bistable saturation in coupled quantum dots for quantum cellular automata. *Appl. Phys. Lett.*, 1993, **62**, P. 714–716.
- [19] Lent C.S., Tougaw P.D., Porod W., Bernstein G.H. Quantum cellular automata. *Nanotechnology*, 1993, **4**(1), P. 49–58.
- [20] Angizi S., Alkaldy E., Bagherzadeh N., Navi K. Novel robust single layer wire crossing approach for exclusive OR sum of products logic design with quantum-dot cellular automata. *J. Low Power Electron*, 2014, **10**, P. 259–271.
- [21] Sheikhaal S., Angizi S., Sarmadi S., Hossein Moaiyeri M., Sayedsalehi S., Designing efficient QCA logical circuits with power dissipation analysis. *Microelectron. J.*, 2015, **46**, P. 462–471.
- [22] Dallaki H., Mehran M. Novel subtractor design based on quantum-dot cellular automata (QCA) nanotechnology. *Int. J. Nanosci. Nanotechnol.*, 2015, **11**, P. 257–262.
- [23] Singh G., Sarin R.K., Raj B. A novel robust exclusive-OR function implementation in QCA nanotechnology with energy dissipation analysis. *J. Comput. Electron.*, 2016, **15**, P. 455–465.
- [24] Das J.C., De D. Reversible Comparator Design Using Quantum Dot-Cellular Automata. *IETE Journal of Research*, 2016, **62** (3).
- [25] Abdullah-Al-Shafi M., Bahar A.N. Optimized design and performance analysis of novel comparator and full adder in nanoscale. *Cogent Engineering*, 2016, **3** (1).
- [26] Xia Y.-S., Qiu K.-M. Comparator Design Based on Quantum-Dot Cellular Automata, *Journal of Electronics & Information Technology*, 2009, **31**, P. 1517–1520.
- [27] Walus K., Dysart T.J., Jullien G.A., Budiman R.A. QCADesigner: a rapid design and Simulation tool for quantum-dot cellular automata. *IEEE Transactions on Nanotechnology*, 2004, **3**, P. 26–31.

Amplification of electromagnetic radiation in a superlattice placed in a tilted magnetic field

M. A. Pyataev¹, A. V. Shorokhov¹, N. N. Khvastunov², K. R. Vlasov¹, V. D. Krevchik³,
M. B. Semenov³, K. N. Alekseev⁴, F. V. Kusmartsev⁴

¹National Research Mordovia State University, Bolshevistskaya, 68, Saransk, 430005, Russia

²Mordovian State Pedagogical Institute, Studencheskaya, 11 A, Saransk, 430007, Russia

³Penza State University, Krasnaya, 40, Penza, 440026, Russia

⁴Loughborough University, Loughborough, Leicestershire LE11 3TU, UK

pyataevma@gmail.com

PACS 78.67.Pt, 73.21.Cd

DOI 10.17586/2220-8054-2017-8-6-717-722

The interaction of electrons in a superlattice with electromagnetic radiation in presence of static electric and magnetic fields is investigated. The electric field is directed along the superlattice axis while the magnetic field is inclined at an arbitrary angle to the axis of superlattice. It is shown that the dependence of current in the superlattice on electric field in the general case can have several maxima. In some regions of electric and magnetic field values, the absorption coefficient for high frequency electromagnetic radiation can be negative that means the electromagnetic wave will be amplified. We note that negative absorption in the system is possible at some conditions at the region of positive differential conductivity in contrast to classical Bloch oscillator in which amplification takes place in case of negative differential conductivity only. This phenomenon can be used for the design of a terahertz amplifier and generator based on the superlattice.

Keywords: semiconductor superlattice, magnetic field, terahertz radiation.

Received: 6 November 2017

Revised: 13 November 2017

1. Introduction

Semiconductor superlattices are considered promising systems for creation of a compact terahertz radiation amplifier and generator. The idea of using Bloch oscillations in superlattices for the generation of the high-frequency electromagnetic radiation was proposed by Esaki and Tsu [1] more than forty years ago. However, the attempts to create a high-frequency generator based on the phenomenon of Bloch oscillations were not successful. It was shown later that the generation is suppressed by instabilities of space-charge waves in the superlattice in the regime of negative static differential conductivity (SDC). We note that in the case of classical Bloch oscillator the radiation amplification is possible only in the regime of negative SDC. One possible way to overcome this difficulty is the application of a magnetic field. Electron transport in superlattices placed in parallel [2, 3] or perpendicular [4–13] magnetic fields was studied previously. In particular, it was shown recently [15, 16] that the magnetic field applied to the superlattice in a direction perpendicular to the axis can shift the maximum on the static current-voltage characteristics (IV curve) towards the region of higher electric field. At the same time, the absorption coefficient can be negative for high frequencies at electric fields corresponding to positive SDC. That makes possible to achieve amplification of radiation without formation of space-charge wave instabilities. If the superlattice is placed in a tilted magnetic field, then the ballistic electron dynamics becomes more complicated and exhibits chaotic behavior [17–20]. This chaos manifests itself with the appearance of bifurcation points in the parameter space of the system. Various problems associated with the electron transport in the tilted magnetic field have been studied in the last decade [21–23]. The purpose of the present paper is to investigate the possibility of amplification of weak electromagnetic signal by the superlattice placed in both parallel electric and tilted magnetic fields. For this reason, we study absorption of electromagnetic radiation and its relation to the static IV curve.

2. Current and absorption

The schematic view of the investigated system is represented in Fig. 1. The direction of electric field which coincides with the axis of superlattice growth is denoted as x -axis and the magnetic field is inclined on angle θ to the electric field in xz -plane. In addition to constant electric field E_{dc} , we consider small perturbation oscillating with frequency ω and amplitude E_ω . The total electric field is described by the equation:

$$E_x(t) = E_{dc} + E_\omega \cos(\omega t). \quad (1)$$

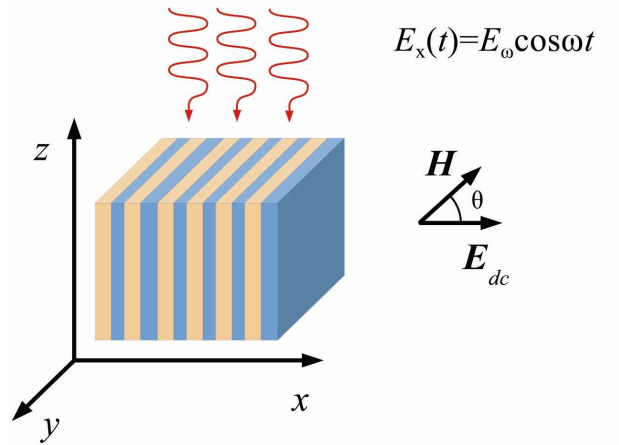


FIG. 1. Schematic representation of the system.

Our main goal is to determine the current produced by this field.

To find the current in the system, we use the semiclassical approximation which is based on the Boltzmann equation for electrons in external fields [15]. The superlattice properties in this approach are taken into account by the miniband dispersion relation for the electrons. In the relaxation-time approximation, the Boltzmann equation can be written in the form:

$$\frac{\partial f}{\partial t} + \frac{1}{\hbar} \left(e\mathbf{E}(t) + \frac{e}{c} \mathbf{v} \times \mathbf{B} \right) \frac{\partial f}{\partial \mathbf{k}} = -\frac{f - f_{eq}}{\tau}, \quad (2)$$

where \mathbf{v} is the electron velocity, τ is the relaxation time, \mathbf{k} is the quasi-wave vector, and $f_{eq}(\mathbf{k})$ is the equilibrium distribution function. In the present study, we consider the case of spatially uniform fields and electron distribution.

The dependence of electron energy on quasi-wave vector in the superlattice is described by the well-known equation from tight-binding approximation:

$$\varepsilon(\mathbf{k}) = -\frac{\Delta}{2} \cos(k_x d) + \frac{\hbar^2(k_y^2 + k_z^2)}{2m}, \quad (3)$$

where d is the superlattice period and Δ is the miniband width.

Based on the method of characteristics, we can represent the distribution function in terms of solutions for ballistic equations of motion for the electrons in the external fields [24]. The equation for quasi-wave vector evolution at the ballistic electron motion has the form:

$$\hbar \dot{\mathbf{k}} = e\mathbf{E}(t) + \frac{e}{c} \mathbf{v}(\mathbf{k}) \times \mathbf{B}. \quad (4)$$

Let $\mathbf{k}^*(t, t_0)$ denotes the solution of Eq. (4) corresponding to the initial condition $\mathbf{k}(t_0) = \mathbf{k}_0$. If we substitute \mathbf{k}^* into Eq. (2) then its left-hand side becomes a total derivative of f with respect to t :

$$\frac{df(\mathbf{k}^*, t)}{dt} = -\frac{f(\mathbf{k}^*, t) - f_{eq}(\mathbf{k}^*)}{\tau}. \quad (5)$$

Then, the steady-state solution of Eq. (2) can be represented in the form:

$$f(\mathbf{k}, t) = \frac{1}{\tau} \int_{-\infty}^t dt_0 f_{eq}(\mathbf{k}^*(t, t_0)) e^{-\frac{t-t_0}{\tau}}, \quad (6)$$

where $\mathbf{k}^*(t, t_0)$ is the solution of Eq. (4) satisfying the condition $\mathbf{k}^*(t, t_0) = \mathbf{k}$ for every t_0 .

The density j of current in x -direction can be represented in terms of the distribution function f by the following equation:

$$j(t) = \frac{2e}{(2\pi)^3} \int d^3\mathbf{k} f(\mathbf{k}, t) v_x(\mathbf{k}), \quad (7)$$

where $v_x = \frac{1}{\hbar} \frac{\partial \varepsilon}{\partial k_x}$ is x -component of the electron velocity, factor $(2\pi)^3$ in the denominator takes into account density of states and factor 2 appears in the numerator for spin. As it follows from Eq. (3) the velocity v_x is given

by:

$$v_x(k_x) = \frac{\Delta d}{2\hbar} \sin(k_x d). \quad (8)$$

Now combining Eqs. (6) and (7) we obtain the following equation for the current:

$$j(t) = \frac{e}{4\pi^3\tau} \int d^3\mathbf{k} f_{eq}(\mathbf{k}) \int_{-\infty}^t dt_0 v_x(\mathbf{k}^*(t, t_0)) e^{-\frac{t-t_0}{\tau}}. \quad (9)$$

In the present study, we consider the case of low temperatures and low electron concentrations N . In this case almost all electron quasi-wave vectors are concentrated at the bottom of miniband near the point $\mathbf{k} = 0$. The equilibrium distribution function in this approximation can be represented as follows [?]:

$$f_{eq} \approx 4N\pi^3\delta(\mathbf{k}), \quad (10)$$

where $\delta(x)$ is the Dirac δ -function.

Let us introduce the dimensionless components of the quasi-wave vector: $K_x = k_x d$, $K_y = k_y d\sqrt{m/m_x}$, and $K_z = k_z d\sqrt{m/m_x}$, where m is electron effective mass in perpendicular direction and $m_x = 2\hbar/d^2\Delta$ is the electron mass in the parallel direction. Then the ballistic equations of motion can be rewritten as follows:

$$\dot{K}_x = \omega_B + \omega_{\perp} K_y + \beta \sin(\omega t), \quad (11)$$

$$\dot{K}_y = -\omega_{\perp} \sin K_x + \omega_{\parallel} K_z, \quad (12)$$

$$\dot{K}_z = -\omega_{\parallel} K_y, \quad (13)$$

where $\omega_B = edE_{dc}/\hbar$ is the Bloch frequency, $\omega_c = eB/mc$ is the cyclotron frequency, $\omega_{\perp} = \omega_c \sin \theta$, $\omega_{\parallel} = \omega_c \cos \theta$ and $\beta = eE_{\omega}d/\hbar$ is the renormalized amplitude of the high-frequency electric field.

To understand various possibilities of quasi-wave vector dynamics from equations (11), (12) and (13), we consider first a few simplified cases. One can see from equations (11) that the parallel magnetic field ($\omega_{\perp} = 0$) does not affect the x component of the quasi-wave vector. In that case, the IV curve of the system has the form obtained by Esaki and Tsu [1].

If the magnetic field is directed parallel to z -axis, then the y coordinate can be separated from others and the system of equations (11)-(13) is decomposed. In this case, the equation for \dot{K}_x can be transformed into the equation of motion for unharmonic pendulum:

$$\ddot{K}_x + \omega_{\perp} \sin K_x = \beta \sin(\omega t). \quad (14)$$

The constant electric field E_{dc} is included into the equations of motions through initial condition:

$$\dot{K}_x(t_0) = \omega_B. \quad (15)$$

As follows from Eq. (14), in the absence of perturbation ($\beta = 0$), there are two regimes of motion for electrons depending on the initial conditions: cyclotron-like oscillations and Bloch type oscillations [4]. In the cyclotron-like regime, the electron quasi-wave vector does not reach the boundary of the first Brillouin zone while in the regime of Bloch type oscillations the quasi-wave vector increases infinitely. If the initial electron quasi-wave vector is zero, then the system undergoes a transition from cyclotron-like oscillations to Bloch type oscillations at the electric field corresponding to condition $\omega_B = 2\omega_c$. In the general case of the inclined magnetic field, there are several bifurcation points and the analytical investigation of the ballistic equations of motion becomes very complicated. In the present study, we have performed numerical solution of the system (11)–(13) and found the dependence of electron quasi-wave vector on time. Then, by equation (9), we have found the time-dependent current in the steady-state regime. After that, we have calculated the absorption as the average dissipation power P in a unit volume by the following equation:

$$P = \frac{1}{T} \int_0^T j(t)E(t)dt, \quad (16)$$

where $T = 2\pi/\omega$ is the period of the small external oscillating field.

3. Results and discussion

Let us consider first the dependence of current on voltage for the case of time independent fields ($E_\omega = 0$). We note that the equations of motion in this case are similar to the equation of motion for an anharmonic pendulum in the field of a plane wave which is the well-known example of a system with chaotic behavior [17, 18]

$$\ddot{K}_z + \omega_{\parallel}^2 K_z = -\omega_{\parallel} \omega_{\perp} \sin\left(\frac{\omega_{\perp}}{\omega_{\parallel}} K_z - \omega_B t + \varphi\right). \quad (17)$$

However, as it follows from Eq. (9), to obtain the current in a dissipative system, one needs to know the values of quasimomentum for a finite period of time (about a few τ) while the chaotic dynamics manifests itself in a very long time. That is why the chaotic dynamics of the systems does not lead to a chaotic behavior of the IV characteristics or absorption. However, bifurcation between different regimes of motion can lead to appearance of a very sharp changes in IV curve.

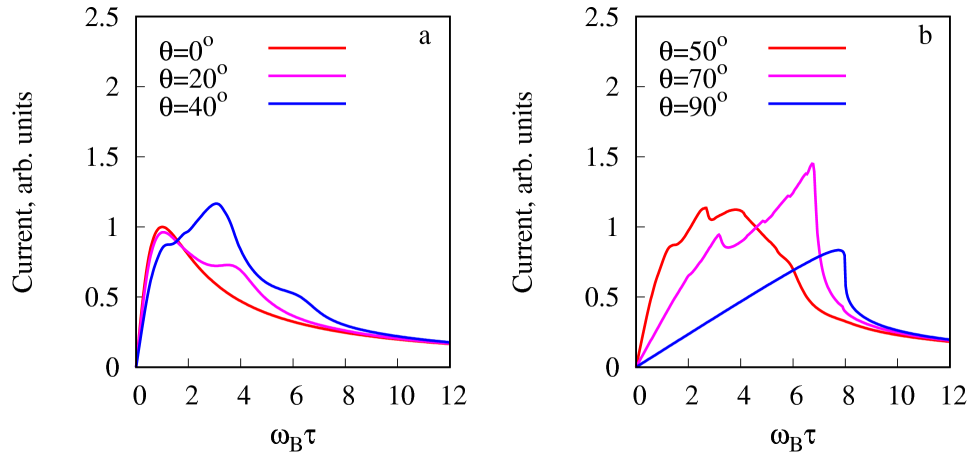


FIG. 2. The dependence of current on the Bloch frequency for various values of angle θ at $\omega_c \tau = 4$.

The dependence of current on the electric field for different inclination angles θ is shown in Fig. 2. One can see from Fig. 2 that the current as a function of electric field has one maximum in the cases of parallel and perpendicular magnetic field. The decrease on the IV curve corresponds to the transition of the transport regime to the Bloch type oscillations. The value of ω_B corresponding to the transition is determined by relation $\omega_B \tau = 1$ in the case of $\theta = 0$ and is close to the value $\omega_B = 2\omega_c$ in the case of $\theta = 90^\circ$. One can see that with increase in angle θ , the position of global maximum on the IV curve is shifted to the region of higher electric fields. Additional peaks occur on the curve in the case of tilted magnetic field due to the appearance of additional bifurcation points in the parameter space. In particular, there is one extra maximum of current at relatively small values of θ (about 20°). Our analysis shows that at electric fields corresponding to the second increase of current, the negative absorption of weak electromagnetic radiation can be obtained. The dependence of absorption coefficient on frequency for this case is shown in Fig. 3. The negative absorption in this case occurs in the region of positive static differential conductivity. Similar results can be obtained in the case of large θ . The dependence of absorption on frequency for $\theta = 80^\circ$ is shown in Fig. 4. One can see from Fig. 4 that the negative absorption at positive differential conductivity can be achieved in the region of electric fields between two local maximums on the IV curve.

4. Conclusion

We have investigated a static current-voltage characteristics and absorption of high-frequency electromagnetic radiation in a semiconductor superlattice in the presence of a parallel electric field and tilted magnetic field. In the cases of parallel and perpendicular magnetic field, the IV curve of the system has one maximum. The positions of maximum on the dependence of current on the Bloch frequency are determined by inverse relaxation time in the parallel field and by doubled cyclotron frequency in perpendicular field. We have shown in the present study that the inclined magnetic field applied to a superlattice can lead to appearance of additional maximums and minimums on the static IV curve. Near the local maximums of the IV curve there are regions of field values in which the static differential conductivity is positive, but the high-frequency absorption coefficient is negative. In this case, the

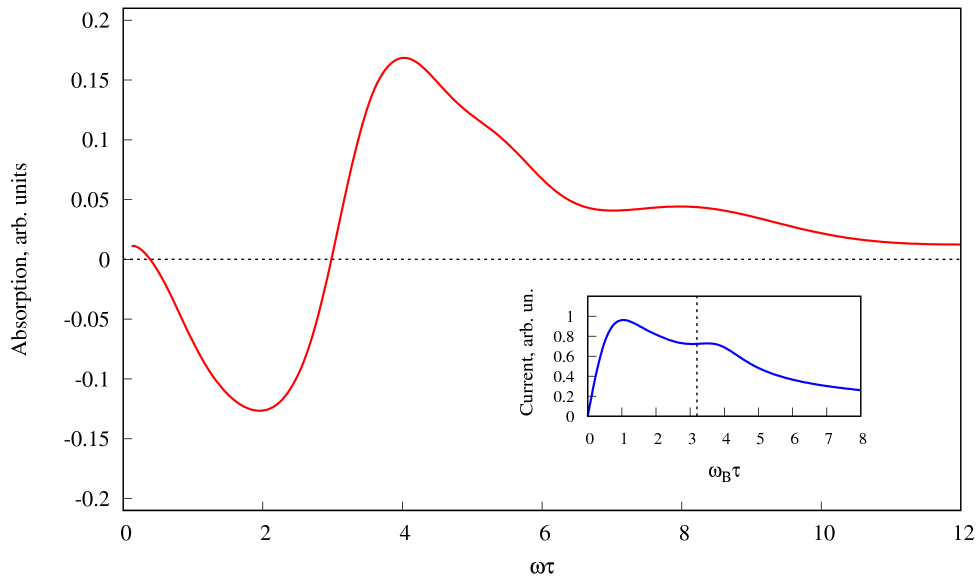


FIG. 3. The dependence of absorption on frequency ω at $\theta = 20^\circ$, $\omega_c\tau = 4$ and $\omega_B\tau = 3.2$. The inset shows the dependence of current on the Bloch frequency (IV curve) for the same parameters. The vertical dashed line marks the Bloch frequency $\omega_B = 3.2/\tau$ which was used for calculation of the absorption. One can see that static differential conductivity is positive at this value of ω_B .

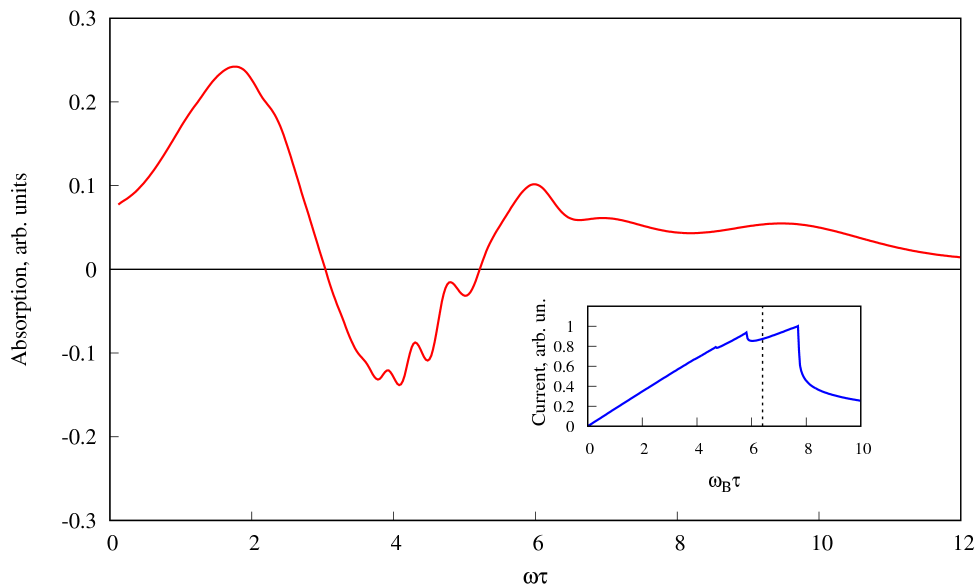


FIG. 4. The dependence of absorption on frequency ω at $\theta = 80^\circ$, $\omega_c\tau = 4$ and $\omega_B\tau = 6.4$. The inset shows the dependence of current on the Bloch frequency (IV curve) for the same parameters. The vertical dashed line marks the Bloch frequency $\omega_B = 6.4/\tau$ which was used for calculation of the absorption. One can see that static differential conductivity is positive at this value of ω_B .

high-frequency radiation can be amplified by the superlattice. At the same time, charge wave instabilities should not appear because of positive SDC. We note that the frequency of radiation which can be generated by the system in this regime is determined by parameters of the superlattice and the value of magnetic field. Our estimations show that for a GaAs/Al_xGa_{1-x}As superlattice with the period $d = 6$ nm, miniband width $\Delta = 60$ meV and magnetic field $B = 2.5$ T the generated frequency is about 1 THz. Hence, such fields configuration can be used in designing of a terahertz generator based on the semiconductor superlattice.

Acknowledgements

This work was supported by the Ministry of Education and Science of the Russian Federation (project no. 3.6321.2017/8.9), and RFBR (project no. 17-02-00969).

References

- [1] Esaki L., Tsu R. Superlattice and negative differential conductivity in semiconductors. *IBM J. Res. Dev.*, 1970, **14**, P. 61.
- [2] Hummel A.B., Bauer T., et al. Influence of a strong magnetic field on the Wannier-Stark states of an electrically biased GaAs/Al_xGa_{1-x}As superlattice. *Phys. Rev. B*, 2003, **67**, 045319-1-10.
- [3] Patane A., Mori N., et al. Magnetic-field-induced suppression of electronic conduction in a superlattice. *Phys. Rev. Lett.*, 2004, **93**, 146801-1-4.
- [4] Bass F.G., Teterov A.P. High-frequency phenomena in semiconductor superlattices. *Phys. Rep.*, 1986, **140** (5), P. 237–322.
- [5] Polyanovskii V.M. Nonlinear conductivity of a semiconductor with a superlattice in a strong magnetic field. *Sov. Phys. Semicond.*, 1980, **14**, P. 718–720.
- [6] Bass F.G., Lykakh V.A., Teterov A.P. Cyclotron resonance in superlattice semiconductor. *Sov. Phys. Semicond.*, 1980, **14**, P. 1372–1376.
- [7] Bass F.G., Zorchenko V.V., Shashora V.I. To the theory of galvanomagnetic and high-frequency phenomena in semiconductors with a superlattice. *Sov. Phys. Semicond.*, 1981, **15**, P. 263–270.
- [8] Sibille A., Palmier J.F., et al. Semi-classical magnetotransport in a superlattice miniband. *Europhys. Lett.*, 1990, **13** (3), P. 279–284.
- [9] Miller D., Laikhtman B. Classical theory of the perpendicular magnetoresistance in superlattice. *Phys. Rev. B*, 1995, **52**, P. 12191–12201.
- [10] Elsholz F., Wacker A., et al. Magnetotransport through semiconductor superlattices. *Phys. Rev. B*, 2001, **63**, 033312-1-4.
- [11] Feil T., Gerl C., Wegscheider W. Transport properties of a shunted surface superlattice in an external magnetic field. *Phys. Rev. B*, 2006, **73**, 125301-1-7.
- [12] Kosevich Yu.A. Anomalous Hall velocity, transient weak supercurrent, and coherent Meissner effect in semiconductor superlattices. *Phys. Rev. B*, 2001, **63**, 205313-1-19.
- [13] Bauer T., Kolb J., et al. Coherent Hall effect in a semiconductor superlattice. *Phys. Rev. Lett.*, 2002, **88**, 086801-1-4.
- [14] Hummel A.B., Blöser C., et al. Electro-optic investigation of the coherent Hall effect in semiconductor superlattices. *Phys. Stat. Sol. (b)*, 2005, **242** (6), P. 1175–1178.
- [15] Hyart T., Mattas J., Alekseev K.N. Model of the influence of an external magnetic field on the gain of terahertz radiation from semiconductor superlattices. *Phys. Rev. Lett.*, 2009, **103**, 117401-1-4.
- [16] Shorokhov A.V., Pyataev M.A., et al. Physical principles of the amplification of electromagnetic radiation due to negative electron masses in a semiconductor superlattice. *JETP Lett.*, 2014, **100** (12), P. 766–770.
- [17] Fromhold T.M., Krokhin A.A., et al. Effects of stochastic webs on chaotic electron transport in semiconductor superlattices. *Phys. Rev. Lett.*, 2001, **87**, 046803-1-4.
- [18] Balanov A.G., Fowler D., et al. Bifurcations and chaos in semiconductor superlattices with a tilted magnetic field. *Phys. Rev. E*, 2008, **77**, 026209-1-13.
- [19] Selskii A.O., Koronovskii A.A., et al. Studying transitions between different regimes of current oscillations generated in a semiconductor superlattice in the presence of a tilted magnetic field at various temperatures. *Tech. Phys. Lett.*, 2015, **41** (8), P. 768–770.
- [20] Selskii A.O., Hramov A.E., et al. Bifurcation phenomena in a semiconductor superlattice subject to a tilted magnetic field. *Phys. Lett. A*, 2016, **380**, P. 98–105.
- [21] Balanov A.G., Greenaway M.T., et al. The effect of temperature on the nonlinear dynamics of charge in a semiconductor superlattice in the presence of a magnetic field. *J. Exp. Theor. Phys.*, 2012, **114** (5), P. 836–840.
- [22] Alexeeva N., Greenaway M.T., et al. Controlling high-frequency collective electron dynamics via single-particle complexity. *Phys. Rev. Lett.*, 2012, **109**, 024102-1-5.
- [23] Balanov A.G., Koronovskii A.A., et al. Space charge dynamics in a semiconductor superlattice affected by tilted magnetic field and heating. *Physics of Wave Phenomena*, 2016, **24** (2), P. 103–107.
- [24] Budd J. Generalized path variable method. *J. Phys. Soc. Japan*, 1963, **18**, P. 142.

Nanostructure deduced from AC-STEM images coupled to theoretical modelling

K. Sukuta¹, M. Van den Bossche¹, A. Pedersen¹, H. Jónsson^{1,2}

¹Science Institute and Faculty of Physical Sciences, University of Iceland, 107 Reykjavík, Iceland

²Center for Nonlinear Studies, Los Alamos, NM 87545, USA

hj@hi.is

DOI 10.17586/2220-8054-2017-8-6-723-731

Determining the atomic structure of nanoclusters is a challenging task and a critical one for understanding their chemical and physical properties. Recently, the high resolution aberration corrected scanning transmission electron microscope (AC-STEM) technique has provided valuable information about such systems, but the analysis of the experimental images has typically been qualitative rather than quantitative. A method is presented for detailed analysis of AC-STEM images combined with theoretical modelling to extract atomic coordinates. An objective function formed by a linear combination of a fit to the two-dimensional AC-STEM image plus an estimate of the cluster's energy for adding information about the third dimension is used in a global optimization algorithm to extract the atomic coordinates. The method is illustrated by analyzing model images generated for the Garzón structure of the Au₅₅ cluster, which is a metastable structure for the embedded atom method (EAM) potential function used here to estimate the total energy. As the method does not rely on the alignment of atom rows in the AC-STEM image, the partially disordered chiral structure of the Au₅₅ can successfully be determined even when a significant level of noise is added to the images.

Keywords: nanocluster, AC-STEM, atomic structure, global optimization, genetic algorithm.

Received: 24 November 2017

Revised: 27 November 2017

1. Introduction

Modern chemistry and condensed matter physics is based on knowing the atomic scale structure of the systems under study. Only after identifying the ordering of the atoms can one reliably assess the various properties such as chemical reactivity. The relationship between structure and function underpins all modern chemical intuition and understanding. Heterogeneous catalysis occurs, for example, on the surface of solids and for a long time a serious hindrance in understanding the catalytic activity was the difficulty in determining the atomic scale structure of solid surfaces. While it is relatively easy to determine atomic ordering in bulk crystals with X-ray scattering, the surface layer of atoms, which can have a significantly different atomic composition and structure than the bulk, gives a too small signal to be 'visible'. With the advent of the scanning tunneling microscope in the early 1980's [1], this problem was largely solved, and since then, there has been an explosion in the study of structure and chemical reactivity of surfaces and a great leap forward in understanding heterogeneous catalysis.

Nanoscale clusters of atoms have shown remarkable catalytic activity. With modern nanotechnology, it is possible to prepare such clusters and deposit them in a non-destructive manner on solid surfaces or into porous solids. It has, for example, been shown that CO oxidation, an important reaction for cleaning exhaust, can occur readily at below room temperature in the presence of Au nanoclusters deposited on a TiO₂ surface if the diameter of the clusters is in the range of 2–3 nm, corresponding to ca. 10³ atoms. For larger as well as smaller clusters, the catalytic activity per site drops dramatically [2]. This and similar observation on other nanocluster catalysts remain puzzling. A consensus on the reason for the strong size dependence of the catalytic activity has not been reached. In other experiments, the catalytic activity of transition metal nanoclusters has been found to depend strongly on preparation conditions and slight variations in composition [3].

A major obstacle for gaining a better understanding of nanocluster catalysis is the lack of information about the atomic structure of the clusters. While, for example, gold crystallizes in the face centered cubic (FCC) structure, small Au clusters can have very different atomic ordering by forming, for example, icosahedral or decahedral structures with fivefold symmetry (see, for example, Ref. [4]) Various theoretical calculations have addressed this problem, using mainly empirical potential functions to describe the interaction between the Au atoms, electronic density functional theory (DFT), or a combinations of both. But, it is extremely hard to search for the optimal structure of such a cluster even if it contains only ca. 10² atoms. Also, it is not clear whether the current approaches to describing the atomic interactions are sufficiently accurate for these unusual systems.

An experimental technique that can provide information about the atomic scale structure of nanoclusters deposited on surfaces has been lacking until the recent development of the aberration-corrected scanning transmission electron microscope (AC-STEM). Based on ideas presented in the late 1990's [5,6], the first such instrument was built in Daresbury in England in 2001 and several such instruments have now been set up at major universities and research laboratories. Publications describing structural determination of nanoclusters and other nanosized systems using AC-STEM have appeared in the past decade, see for example Refs. [7–12].

While the AC-STEM experimental equipment and the refinements of the measured images are highly developed, the analysis of the images in terms of atomic structure of the clusters is still often qualitative. In some cases, a catalog of calculated images based on ideal cluster structures is generated and the measured images then compared to the catalog by eye. This type of analysis is in many cases good enough to determine, for example, which one of the three main categories of structures a measured metallic cluster belongs to: FCC, icosahedra and decahedra. However, more information could be extracted from the images with a quantitative analysis tool. For example, in order to understand catalytic properties, it is important to obtain information about the atomic ordering at the surface of the cluster. The atoms at the surface of a cluster may order in a different way than would be expected from the ordering in the interior, as is well known for the surfaces of crystals.

In this article, we describe an algorithm that can be used to extract atomic coordinates from an AC-STEM image. The method is based on a two-step procedure. First, atomic coordinates in the plane of the AC-STEM image are generated. Then, the image is complemented with an estimate of the energy of the cluster to determine the three-dimensional structure. The algorithm is applied to an analysis of the Au₅₅ cluster. This is an interesting test case for two reasons. Firstly, Garzón and coworkers have carried out extensive studies of this cluster using the Gupta potential and shown that the structure is chiral while being highly disordered [13–15] (see Fig. 2). We will refer to this as the Garzón structure of Au₅₅. Experimental AC-STEM studies have supported this prediction as ca. half of the measured images were found to be consistent with the Garzón structure [16]. The other half of the images were ascribed to higher energy configurations due to thermal energy and electron beam interaction with the clusters but the atomic coordinates of those configurations were not determined. No high symmetry structures were observed. The analysis was based on image simulations using multiple scattering calculations [16].

We choose the Au₅₅ cluster as a demonstration for our method because it is more challenging than a structure where the atoms line up in rows. Furthermore, it is small enough that the globally optimal structure can be found without too much computational effort. Recently, a method for extracting atomic coordinates from AC-STEM images was presented, but it relies on the atoms forming rows and cannot be applied to structures such as the Garzón structure [17]. The estimate of the energy of the cluster is obtained from the embedded atom method (EAM) potential energy function [18] rather than the Gupta potential because EAM predicts a slightly different optimal structure than the Garzón structure. This choice reflects the fact that the energy of a cluster can rarely be calculated to high precision, whether the calculation is based on an empirical potential or DFT. But, when combined with an AC-STEM image the correct structure should be obtained despite errors in the energy. Fig. 1 shows a comparison of the Garzón structure and the optimal structure predicted by the EAM potential. The average difference in atomic coordinates is 0.52 Å. The Garzón structure is metastable for the EAM potential function and is 0.1 eV higher in energy than the global minimum on the EAM energy surface. Nevertheless, the method presented here for analysis of AC-STEM images is able to converge on the atomic coordinates of the Garzón structure even though it relies on an EAM energy estimate.

2. Methodology

The method for extracting atomic coordinates from an AC-STEM image in combination with an estimate of the cluster energy is described in this section. Instead of analyzing an experimental AC-STEM image at this stage, we use for testing and presentation purposes a simulated AC-STEM image for the Garzón structure of the Au₅₅ cluster. We will refer to this as the target image and it is specified by the intensity of pixels in the x - y plane, $I_{tar}(x, y)$. Following Li *et al.*, we assume each of the $N = 55$ atoms is the source of a signal described by a Gaussian [7]:

$$I_{tar}(x, y) = \sum_{i=1}^N \exp\left(\frac{-(x - x_i)^2 + (y - y_i)^2}{2\sigma^2}\right), \quad (1)$$

where x_i, y_i denotes coordinates of atom i . The width of the Gaussian, σ , is chosen to have the value 0.78 Å as was deduced by Li *et al.* from their experimental AC-STEM data on Au nanoclusters [7]. A similar value, 0.8 Å, was deduced by He *et al.* [19].

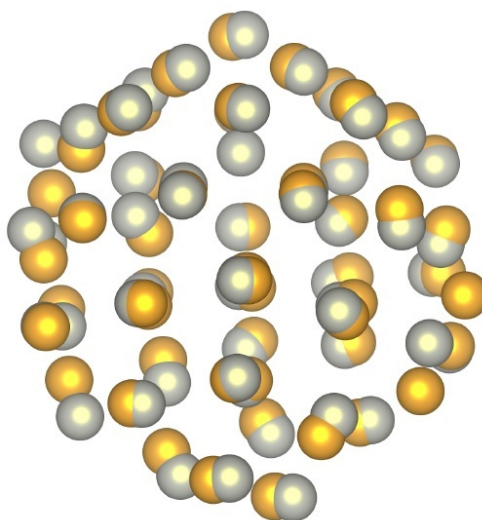


FIG. 1. Comparison of the Garzón structure (the global minimum on the Gupta energy surface) and the EAM optimal structure (the global minimum on the EAM energy surface). The Garzón structure has 0.1 eV higher energy than the EAM optimal structure when the energy is evaluated with the EAM potential. The average difference in the distance between corresponding atoms in the two structures is 0.52 Å.

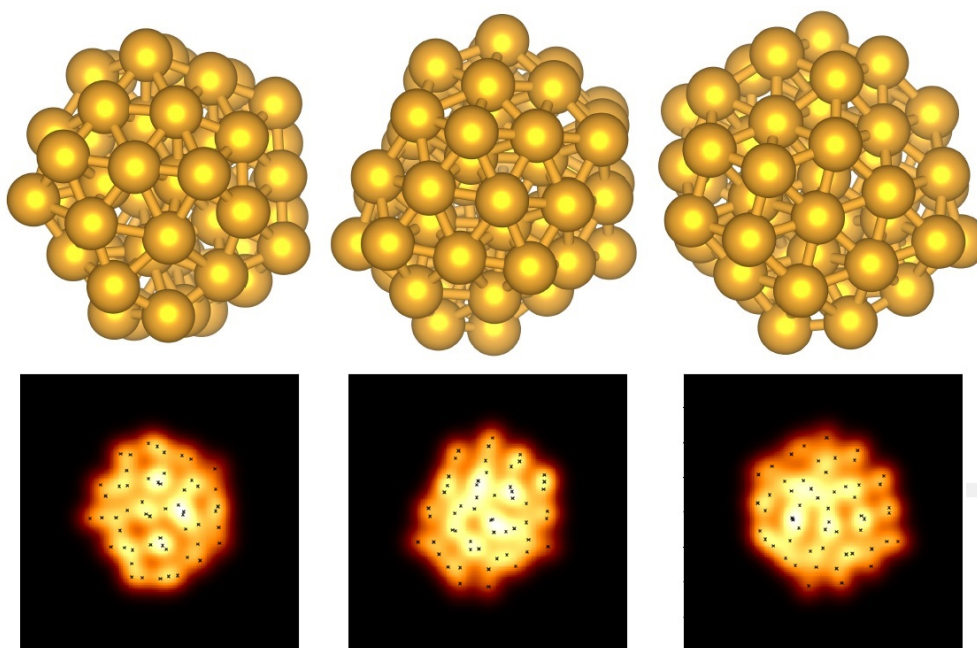


FIG. 2. Three different views of the Garzón structure of a Au_{55} cluster (top), referred to as viewing angle #1, #2 and #3, and simulated AC-STEM images (bottom). The STEM images cover an area of $20 \text{ \AA} \times 20 \text{ \AA}$ and the atomic positions are indicated as black crosses.

Simulated AC-STEM images for three different viewing angles are shown in Fig. 2. Various levels of noise are also added to the images to better emulate experimental data, as described below. The target image is normalized by summing the intensity of all pixels in the image and then dividing the intensity of each pixel with the sum.

The method for generating atomic coordinates from a target image consists of two stages. First, coordinates of the atoms in the plane of the image are generated. This will be referred to as the x - y plane. Then, several three-dimensional structures are created by generating z -coordinates for the atoms and a GA optimization is performed to minimize an objective function constructed from a weighted sum of the difference between target and simulated

images plus an estimate of the potential energy of the cluster. The procedure should, in general, be repeated for different choices of the total number of atoms to find the value that gives best agreement with the target image. The procedure is described in detail in the following paragraphs.

2.1. Generation of x - y coordinates

The first step is to determine (x, y) coordinates for the atoms in such a way that a simulation image, I_{sim} , best fits a target image, I_{tar} (in practice an experimentally measured AC-STEM image, but here the target image is calculated from the Garzón structure in order to have a well-defined test problem).

Each atom, i , located at (x_i, y_i) , makes a contribution to the simulated intensity at a pixel (x, y) given by:

$$I_a(x, y, x_i, y_i) = \frac{1}{2N\pi\sigma^2} \exp\left(\frac{-(x-x_i)^2 + (y-y_i)^2}{2\sigma^2}\right). \quad (2)$$

The normalization is chosen in such a way that the total intensity of N atoms matches the total intensity of the target image. A reasonable estimate for the peak width σ is required. This can be obtained by fitting the width of an isolated feature that is likely to correspond to an isolated atom, or by fitting to the width of a brighter spot corresponding to a column of atoms, if present. Atoms are assigned (x, y) coordinates in the following way. The pixel with highest intensity is selected and the first atom placed at this location in the x - y plane. Then, the contribution of this atom is subtracted from the target intensity. The second atom is placed at the maximum of the reduced target intensity, $I_{tar}(x, y) - I_a(x, y, x_1, y_1)$, etc.

After (x, y) coordinates have been assigned to all N atoms, they are refined by minimizing the difference between the simulated and target images:

$$S_{\text{image}} = \sum_{\text{pixels } p} D(x_p, y_p)^2, \quad (3)$$

$$D(x_p, y_p) = \left(\sum_{i=1}^N I_a(x_p, y_p, x_i, y_i) \right) - I_{\text{tar}}(x_p, y_p). \quad (4)$$

S_{image} represents the sum over all pixels of the difference squared between the simulated and target images. The steepest descent displacement vector for each atom that reduces the discrepancy most rapidly is obtained by differentiating S_{image} with respect to the atomic coordinates. For example, the x -component of the steepest descent vector for atom i is:

$$\frac{\partial S_{\text{image}}}{\partial x_i} = \sum_{\text{pixels } p} 2 D(x_p, y_p) \frac{\partial D(x_p, y_p)}{\partial x_i} \quad (5)$$

$$= \sum_{\text{pixels } p} 2 D(x_p, y_p) \frac{\partial I_a(x_p, y_p, x_i, y_i)}{\partial x_i} \quad (6)$$

$$= \sum_{\text{pixels } p} 2 D(x_p, y_p) I_a(x_p, y_p, x_i, y_i) \left(\frac{x_i - x_p}{\sigma^2} \right). \quad (7)$$

A similar expression applies to the y -components of the coordinates of the atoms.

2.2. Addition of z -coordinates

After (x, y) coordinates have been assigned, the task is to generate a best estimate of the z -coordinates. As an initial estimate, z coordinates are randomly chosen in such a way that the cluster is roughly spherical and no two atoms are too close together. An improved estimate is then generated by defining an objective function that includes the energy of the cluster, E_{pot} , plus the difference in simulated and target images. Here, an EAM potential function constructed by Foiles *et al.* [18] is used to estimate the energy of the cluster, even though it is known not to have the Garzón structure as the global minimum on the energy surface. The combined objective function, Z , is:

$$Z(r_1, r_2, \dots, r_N) = E_{\text{pot}}(r_1, r_2, \dots, r_N) + \chi S_{\text{image}}(r_1, r_2, \dots, r_N). \quad (8)$$

The weighting factor χ is required to bring the potential energy and the image difference on a similar scale. We found it advantageous to start the local minimizations with $\chi = 0$ and to gradually increase this value to $\chi = 100$ eV over the course of the first 50 steps in the local minimization loop.

The potential energy E_{pot} of the nanocluster is estimated using the LAMMPS software [20]. This estimate does not need to be highly accurate, the most important information is in the image, but without some estimate of the optimal distance between atoms it is not possible to assign the z -coordinates. The gradient of the total objective

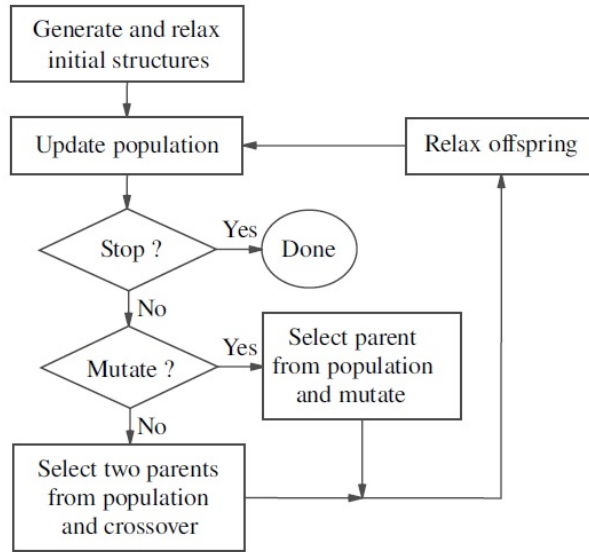


FIG. 3. Flowchart of the genetic algorithm used after a population of cluster structures consistent with the AC-STEM image have been generated.

function then consist of the negative EAM atomic force plus a χ -weighted contribution from the difference in the images, S_{image} .

The full set of coordinates of the atoms in the cluster is refined by local minimization of the objective function (Eq. 8) using the BFGS algorithm [21].

2.3. Genetic algorithm optimization

A global optimization of the atomic coordinates is then carried out by minimizing the objective function, Eqn. (8), using genetic algorithm (GA) tools [22] implemented in the Atomic Simulation Environment (ASE) [23,24]. The outline of the GA used here is shown in Fig. 3. Twenty initial structures are generated as described in the previous subsection. They all have the same x - and y -coordinates for the atoms and the simulated image reproduces well the target image, but they differ in the z -coordinates.

The GA loop starts from a population of lowest energy structures that are also sufficiently distinct, as judged from fingerprint functions (see [25]). New structures are generated either by crossover or mutation (a 25 % mutation probability was used). The required number of parent structures are drawn from the population with a bias towards the more stable and less frequently selected structures (as in Ref. [26]). In the case of crossover, the offspring is produced through standard cut-and-splice pairing of two parent structures [27]. Single-parent mutation can occur in three different ways, as listed in Table 1. The energy of the resulting structure is subsequently minimized using the BFGS algorithm until the largest atomic force drops below 10^{-2} eV/Å. The minimized structure is then added to the list of candidate structures.

3. Results

Figure 4 shows the convergence behavior of the GA calculations for the three orientations of the Garzón structure. In all three cases, the Garzón structure is found with near 100 % success rate within 200 GA steps. On

TABLE 1. The various mutation schemes used in the GA optimization.

Mutation	Probability	Description
Rattle	60 %	Randomly displace the atoms with amplitudes uniformly sampled between 0 and 1.5 Å.
Match	30 %	Force the atomic positions to the initial (x, y) data set after matching using the Hungarian algorithm [28,29].
Squish	10 %	Compress the structure along the z direction.

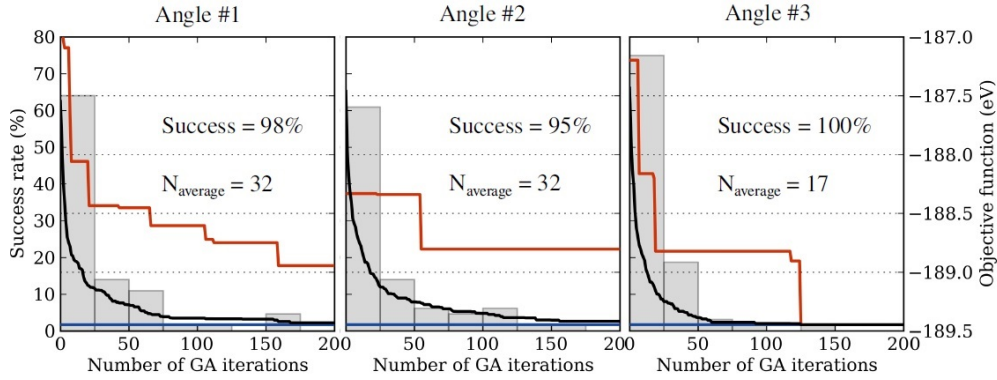


FIG. 4. Hartke graphs of the GA convergence for the three different viewing angles. The statistics are gathered on the basis of 64 independent GA runs. The gray histograms show the distribution of the required number of steps before the Garzón structure is found. The lines represent the evolution of the best-scoring candidating in the best performing (lowest curve) and worst performing (highest curve) runs and the average over the 64 runs (middle curve).

average, circa 30 GA steps are required. A small fraction of the GA runs already finds the GM within the initial population obtained after the first step and random generation of z -coordinates for a near spherical cluster. Such AC-STEM-assisted GA runs tend to converge at a faster rate than regular GA runs without the first step involving only the AC-STEM image fitting. When only the potential energy is used as the objective function, we find the success rate to be only 40 % after 1000 iterations, requiring circa 470 steps on average to find the global minimum on the EAM surface.

Noise is added to the target AC-STEM image by adding random numbers drawn from a Gaussian distribution G centered at zero and with a standard deviation proportional to the local intensity:

$$I_{nois-tar}(x, y) = I_{tar}(x, y) + \eta, \quad (9)$$

where η is a Gaussian random variable obtained from the probability distribution given by

$$G(\eta, \sigma_n) = \frac{1}{\sqrt{2\pi\sigma_n^2}} e^{-\eta^2/2\sigma_n^2}, \quad (10)$$

where $\sigma_n = \beta I_{tar}(x, y)$.

Three different noise levels were used setting the proportionality constant in the width of the Gaussian, β , to 0.1, 0.2 and 0.5, respectively. The resulting images are shown in Fig. 5. At the highest noise level, $\beta = 0.5$, some pixels acquire negative intensities. The added noise is then adequately reduced by subsequent Wiener filtering [30]. The images obtained after such filtering are also shown in Fig. 5, as well as convergence graphs for GA calculations employing the filtered images. When comparing to the data in Fig. 4, it can be concluded that using the noisy but filtered images in the GA optimization only slightly increases the number of steps required to reach convergence. The bottom panel in Fig. 5 confirms that the GM structures obtained using the filtered images agree closely with the reference Garzón structure. This indicates that the method is robust with respect to the presence of noise in the AC-STEM images.

We have also performed tests where the target image is generated from a structure that has been perturbed from the Garzón structure by adding random displacements in the x and y positions, drawn from a uniform distribution $[0, \alpha[$. Such tests effectively correspond to evaluating the relative difficulty of finding an optimal structure which is not close to a local minimum structure of the potential energy surface. The convergence data obtained for maximal displacements of $\alpha = 0.2 \text{ \AA}$, 0.5 \AA and 1.0 \AA are shown in Fig. 6. It can be noted that the convergence speed is reduced, but that fair success rates are still achieved even at the large maximal displacement of 1.0 \AA . The corresponding atomic displacements and changes in the simulated AC-STEM image are illustrated in Fig. 6. We conclude from these tests that it is advisable (though not critically important) to use sufficiently accurate representations of the potential energy surface, such that the real structure is not too distant from a local minimum on the potential energy surface.

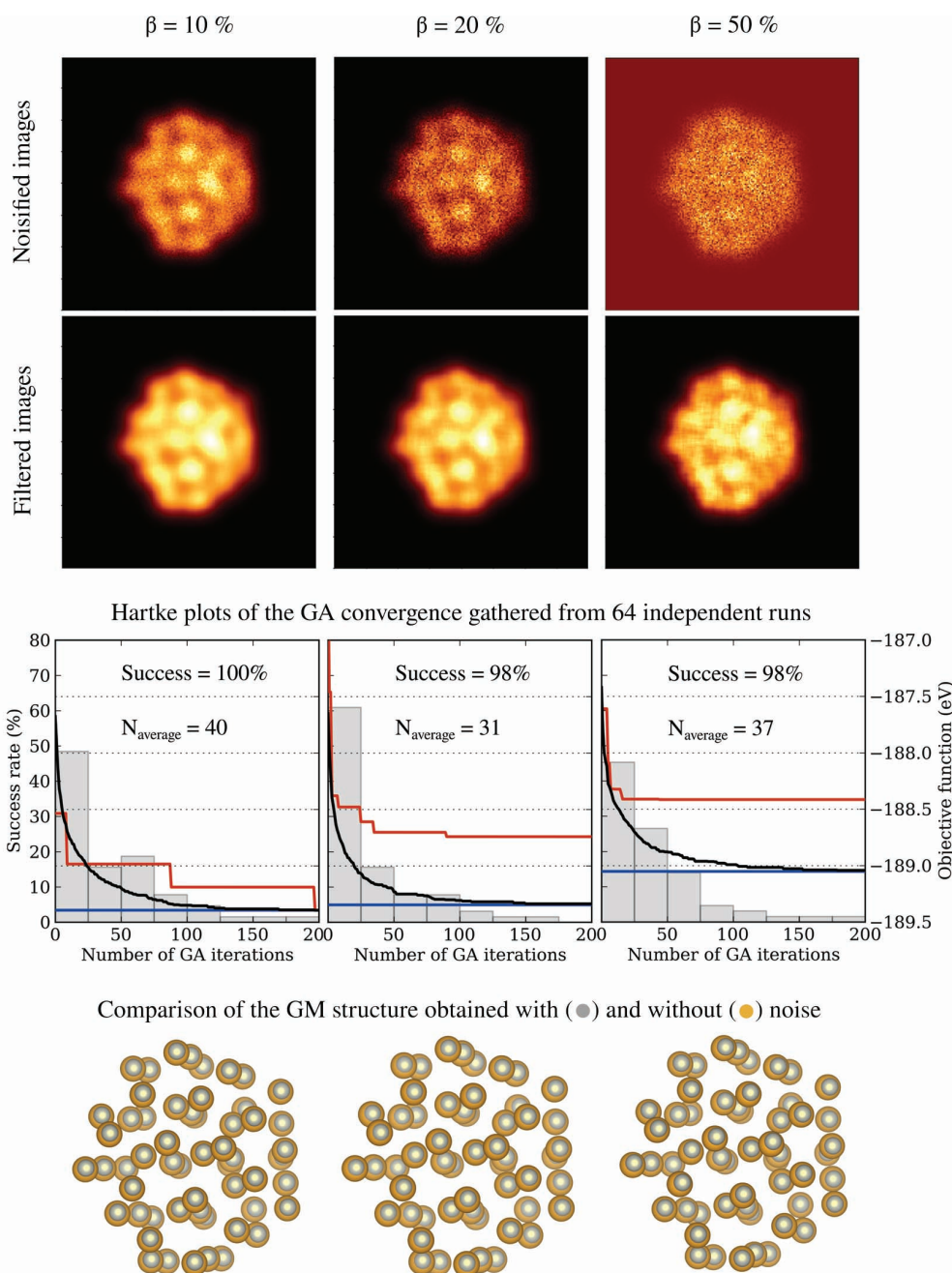


FIG. 5. Top: simulated STEM images with added noise levels (top row) and the corresponding images after Wiener filtering (second row). Center: Hartke graphs showing the convergence of the corresponding GA calculations (bars and lines as in Fig. 4). Bottom: 2-dimensional projections of the Garzón structure (gold) and of the results of the GA calculations with the various noise levels (gray). The latter have been displaced towards the viewer by 0.8 \AA to make it easier to compare the positions in the x - y plane.

4. Discussion

The method presented here for the extraction of atomic coordinates from AC-STEM images supplemented by a method for estimating the cluster energy does not rely on the presence of distinct atomic rows in the AC-STEM image. This is in contrast to the approach by Yu *et al.* [17], where such rows are employed to create the initial population and to apply specific mutations. A second major difference is that we consistently use the total

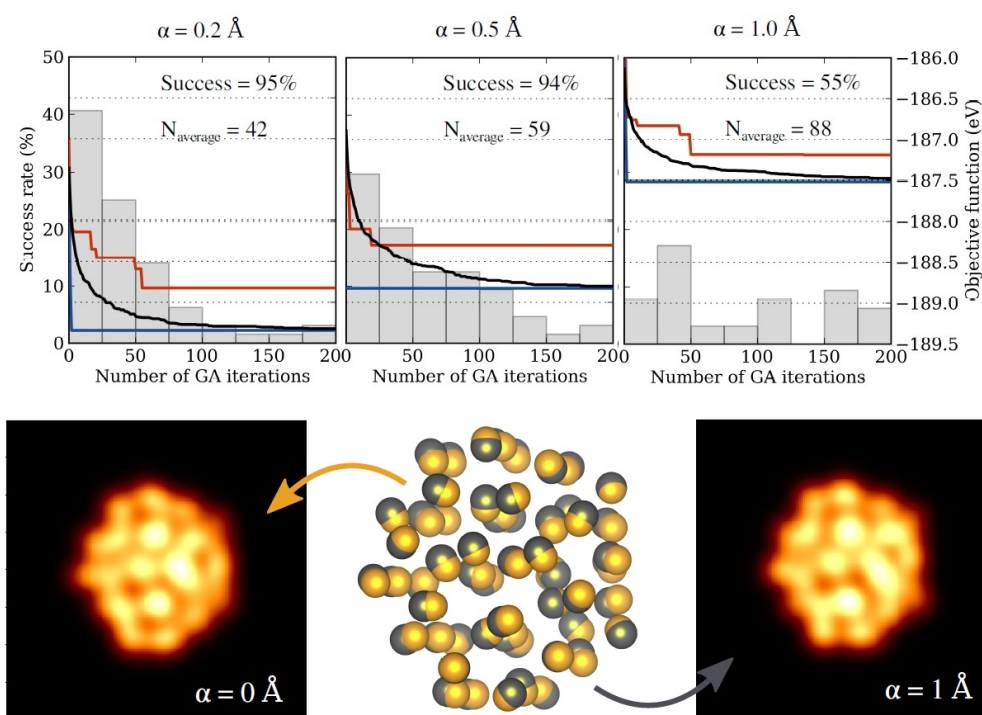


FIG. 6. Top panel: Hartke graphs showing the GA convergence for the three different maximal perturbations from the Garzón structure, α , in the generation of the target image. The histogram and lines are of the same kind as in Fig. 4. Bottom panel, center: Overlay of the structural models of the unperturbed (lighter coloured) and the most strongly perturbed structure ($\alpha = 1.0 \text{ \AA}$) (darker coloured). The atomic radii are 1.5 \AA , for comparison. Bottom panel, left and right: simulated AC-STEM images for the unperturbed Garzón structure and most strongly perturbed structure.

objective function (Eq. 8) throughout the GA run. Yu and coworkers minimize the potential energy during the local optimization and add the image discrepancy term only as a single-point correction after the optimization.

The tests presented here show that it is possible to successfully use an objective function including both the potential energy and an image discrepancy term, even when the experimental AC-STEM image is affected by large noise. The method can be applied to studies of disordered clusters. It should also be able to identify whether the atoms at the surface of the cluster are ordered in a different way than the atoms in the interior, an important aspect for the study of catalytic properties.

5. Acknowledgements

We thank Ignacio Garzón for providing us with the atomic coordinates in the optimal Au_{55} structure deduced from the Gupta potential function. This work was supported by the Icelandic Research Fund and the University of Iceland Doctoral Fund. KS and MVDB gratefully acknowledge computer resources at the University of Iceland Computing Services (Reiknistofnun) and through a SNIC grant at C3SE (Göteborg, Sweden).

References

- [1] Binnig G., Rohrer H., Gerber Ch., Weibel E. Surface studies by scanning tunneling microscopy. *Phys. Rev. Letters*, 1982, **49**(1), P. 57–61.
- [2] Valden M., Lai X., Goodman D.W. Onset of catalytic activity of gold clusters on titania with the appearance of nonmetallic properties. *Science*, 1998, **281**, P. 1647.
- [3] Yamauchi M., Abe R., Tsukuda T., Kato K., Takata M. Highly selective ammonia synthesis from nitrate with photocatalytically generated hydrogen on CuPd/TiO_2 . *J. Am. Chem. Soc.*, 2011, **133**(5), P. 1150–1152.
- [4] Li H., Li L., Pedersen A., Gao Y., Khetrapal N., Jónsson H., Zeng X.C. Magic-number gold nanoclusters with diameter 1 to 3.5 nm: Relative stability and catalytic activity for CO oxidation. *Nano Letters*, 2015, **15**, P. 682.
- [5] Brown L.M. A Synchrotron in a Microscope. *Institute of Physics Conference Series*, 1997, **153**, P. 22.
- [6] Krivanek O.L., Dellby N., Lupini A.R. Towards sub-Å electron beams. *Ultramicroscopy*, 1999, **78**(1-4), P. 1–11.
- [7] Li Z.Y. *al.* Three-dimensional atomic-scale structure of size-selected gold nanoclusters. *Nature*, 2007, **451**(7174), P. 46–48.
- [8] Zhou W., Ross-Medgaarden E.I., Knowles W.V., Wong M. S., Wachs I.E., Kiely C.J., *Nature Chemistry*, 2009, **1**, P. 722.

- [9] Van Aert S., Batenburg K.J., Rossell M.D., Erni R., Van Tendeloo G. Three-dimensional atomic imaging of crystalline nanoparticles. *Nature*, 2011, **470**, P. 374.
- [10] Bals S., Van Aert S., Romero C.P., Lauwaet K., Van Bael M.J., Schoeters B., Partoens B., Yücelen E., Lievens P., Van Tendeloo G., Atomic scale dynamics of ultrasmall germanium clusters. *Nature Communications*, 2012, **3**, P. 897.
- [11] Liu J., Single atom and cluster catalysis: The era of aberration-corrected scanning transmission electron microscopy. *Microscopy and Microanalysis*, 2013, **19** (Suppl. 2), P. 1678.
- [12] Corma A. *et al.*, Exceptional oxidation activity with size-controlled supported gold clusters of low atomicity. *Nature Chemistry*, 2013, **5**, P. 775.
- [13] Garzón I.L., Posada-Amarillas A. Structural and vibrational analysis of amorphous Au₅₅ clusters. *Phys. Rev. B*, 1996, **54**, P. 11796–11802.
- [14] Garzón I.L. *et al.* Lowest Energy Structures of Gold Nanoclusters. *Phys. Rev. Letters*, 1998, **81**, P. 1600–1603.
- [15] Michaelian K., Rendón N., Garzón I.L. Structure and energetics of Ni, Ag, and Au nanoclusters. *Phys. Rev. B*, 1999, **60**(3), P. 2000–2010.
- [16] Wang Z.W., Palmer R.E. Experimental evidence for fluctuating, chiral-type Au₅₅ clusters by direct atomic imaging. *Nanoletters*, 2012, **12**, P. 5510–5514.
- [17] Yu M., Yankovich A.B., Kaczmarowski A., Morgan D., Voyles P.M. Integrated computational and experimental structure refinement for nanoparticles. *ACS Nano*, 2016, **10**(4), P. 4031–4038.
- [18] Foiles S.M., Baskes M.I., Daw M.S. Embedded-atom-method functions for the fcc metals Cu, Ag, Au, Ni, Pd, Pt, and their alloys. *Phys. Rev. B*, 1986, **33**(12), P. 7983–7991.
- [19] He D.S., Li Z.Y., Yuan J. Kinematic HAADF-STEM image simulation of small nanoparticles. *Micron*, 2015, **74**(C), P. 47–53.
- [20] Plimpton S. Fast parallel algorithms for short-range molecular dynamics. *J. Comput. Phys.*, 1995, **117**(1), P. 1–19.
- [21] Head J.D., Zerner M.C. A Broyden-Fletcher-Goldfarb-Shanno optimization procedure for molecular geometries. *Chem. Phys. Lett.*, 1985, **122**(3), P. 264–270.
- [22] Vilhelmsen L.B., Hammer B. Systematic study of Au₆ to Au₁₂ gold clusters on MgO(100) F centers using density-functional theory. *Phys. Rev. Lett.*, 2012, **108**(12), P. 126101(4 pp.).
- [23] Bahn S.R., Jacobsen K.W. An object-oriented scripting interface to a legacy electronic structure code. *Comput. Sci. Eng.*, 2002, **4**(3), P. 56–66.
- [24] Larsen A.H., *et al.* The atomic simulation environment a Python library for working with atoms. *J. Phys.: Condens. Matter*, 2017, **29**(27), P. 273002.
- [25] Lyakhov A.O., Oganov A.R., Stokes H.T., Zhu Q. New developments in evolutionary structure prediction algorithm USPEX. *Comput. Phys. Commun.*, 2013, **184**(4), P. 1172–1182.
- [26] Vilhelmsen L.B., Walton K.S., and Sholl D.S., Structure and mobility of metal clusters in MOFs: Au, Pd, and AuPd clusters in MOF-74. *J. Am. Chem. Soc.*, 2012, **134**(30), P. 12807–12816.
- [27] Daven D.M., Tit N., Morris J. R., Ho K.M. Structural optimization of Lennard-Jones clusters by a genetic algorithm. *Chem. Phys. Lett.*, 1996, **256**(12), P. 195–200.
- [28] Kuhn H.W. The Hungarian method for the assignment problem. *Naval Research Logistics*, 1955, **2**(1-2), P. 83–97.
- [29] Munkres J. Algorithms for the assignment and transportation problems. *J. Soc. Ind. Appl. Math.*, 1957, **5**(1), P. 32–38.
- [30] Kilaas R. Optimal and near-optimal filters in high-resolution electron microscopy. *J. Microsc.*, 1998, **190**(1-2), P. 45–51.

Viscoelastic properties of new mixed wormlike micelles formed by a fatty acid salt and alkyipyridinium surfactant

A. V. Shibaev, O. E. Philippova

Department of Physics, Lomonosov Moscow State University,
Leninskie Gory, 1, bld. 2, Moscow, 119991, Russia

shibaev@polly.phys.msu.ru

PACS 36.20.Ey 47.57.Qk 66.20.Ej 82.70.Gg 83.60.Bc

DOI 10.17586/2220-8054-2017-8-6-732-739

We propose a new combination of an anionic (potassium oleate) and cationic (n-octylpyridinium chloride) surfactants that are able to self-assemble into long cylindrical (wormlike) mixed micelles in water. The solutions have strong viscoelastic properties with viscosity up to 300 Pa·s and elastic modulus around 20 Pa, which are attributed to the formation of an entangled micellar network. We discover that with an increase in the molar ratio of cationic to anionic surfactant, the solutions first increase drastically their viscosity and elasticity due to the growth of micelles in length and formation of the network, but then the rheological parameters slightly decrease, possibly due to micellar branching or shortening. The addition of cationic surfactant also induces the increase of difference between scission energy and micellar electrostatic energy, which is explained both by stronger binding of surfactants within the micelle and decrease of the micellar net charge.

Keywords: surfactant, self-assembly, wormlike micelles, rheology, viscoelastic properties.

Received: 14 November 2017

Revised: 18 November 2017

1. Introduction

Long entangled wormlike micelles of surfactants can impart to aqueous solutions pronounced viscoelastic properties [1–15], which are quite sensitive to external stimuli: ionic strength [2,8], type of salt [11,15], temperature [10], various additives including polymers [6,7] and hydrocarbons [12–14]. Such responsiveness is provided by the self-assembled character of micellar chains formed by weak non-covalent interactions [1,9]. Due to responsive viscoelastic properties the wormlike micellar solutions have found use as thickening agents in a wide range of industrial applications including oil recovery [16,17].

Wormlike micelles can be formed by many common ionic surfactants upon addition of salt [2,8,11,15], which shields the repulsion between similarly charged surfactant heads thus making the cylindrical packing more favorable in comparison with spherical one. Since a wormlike micelle consists of a cylindrical central section and semi-spherical end-caps, the increase of the fraction of cylindrical parts at the expense of the spherical ones suggests the growth of wormlike micelles in length.

An alternative approach to obtain wormlike micelles consists in the use of the mixture of two oppositely charged surfactants [3–7]. In this case, the screening of repulsion is even more effective because cationic and anionic surfactant heads are located in close proximity to each other. However, when the composition approaches equimolarity, such mixtures often have a tendency to precipitate [3,5]. To avoid phase separation, it is necessary to take the surfactants differing significantly in the length of hydrophobic tails [4]. At the same time, the tail of one of the surfactants should not be too short, otherwise it will be unable to tune the formation of long micelles [4]. For instance, in the case of sodium oleate, it was demonstrated that its mixture with n-decyl- (C_{10} TAB) or n-dodecyltrimethylammonium bromide (C_{12} TAB) easily phase separates, whereas n-hexyltrimethylammonium bromide (C_6 TAB) does not induce the formation of long wormlike micelles [4]. Only n-octyltrimethylammonium bromide (C_8 TAB) gives long micelles without phase separation, even at equimolar ratio [4,6,7]. Thus, the search of an optimally oppositely charged surfactant, which can form long wormlike micelles but avoid precipitation, is a significant challenge.

In the present paper, we propose a new surfactant that induces the formation of long wormlike micelles of potassium oleate and study the rheological properties of the micellar solutions at different surfactant mixture ratios.

2. Experimental part

2.1. Materials

Potassium oleate (purity > 98 %) was purchased from TCI, n-octylpyridinium chloride (C₈Pyr, purity > 96 %) was obtained from Chemos GmbH, potassium hydroxide (purity > 98 %) was purchased from Acros. All reagents were used as received. The solutions were prepared in distilled deionized water purified by the Millipore Milli-Q system.

For the preparation of the samples, aqueous stock solutions of potassium oleate and C₈Pyr were first made by dissolving the reagents in water overnight by gentle mixing using a magnetic stirrer. Then, pH of the solutions was adjusted to 11.0±0.1 by adding potassium hydroxide. After that, stock solutions were mixed in appropriate quantities, and the volume was adjusted by adding 10⁻³ M KOH (pH 11.0). The obtained samples were mixed by a magnetic stirrer for 1–2 days and left to equilibrate for several days prior to examination.

2.2. Rheology

In the rheological experiments, a stress-controlled rotational rheometer Physica MCR 301 (Anton Paar, Austria) was used. The details of the measurements are described elsewhere [6,18]. Cone-plate geometry (diameter 50 mm, cone angle 1 °) was used for highly viscous samples (with zero-shear viscosity $\eta_0 > 0.1$ Pa·s). Double gap coaxial cylinders (mean diameter 26.4 mm, height 40 mm, gap 0.42 mm) were used for solutions with lower viscosity ($\eta_0 < 0.1$ Pa·s). Temperature was set at 20.00±0.05 °C by Peltier elements. A specially constructed measurement cell cover was used to prevent solvent evaporation from the sample during measurement. Prior to investigation, highly viscous and viscoelastic samples were kept in the measurement cell for 10 min in order to equilibrate them.

In oscillatory shear tests, the angular frequency dependences of the storage $G'(\omega)$ and loss $G''(\omega)$ moduli were measured. All experiments were performed in the linear viscoelastic regime at the deformation amplitudes (γ) of 0.5–5 %, at which the storage and loss moduli were independent of deformation amplitude. In order to find the range of amplitudes corresponding to linear viscoelasticity, amplitude sweep tests were first performed, in which the frequency was fixed at 10 rad/s and the deformation amplitude was varied from 0.01–100 %. The plateau storage modulus G_0 was determined from the $G'(\omega)$ curves at the frequency ω_{min} where G'' reaches a minimum. The longest relaxation time τ was estimated from the frequency ω_0 where $G'(\omega)$ and $G''(\omega)$ intercept, as $\tau = 1/\omega_0$.

In steady shear tests, the dependences of viscosity on shear rate (flow curves) were measured. Zero-shear viscosity η_0 of shear-thinning samples was found by fitting the data with the Carreau–Yasuda model, and η_0 for low-viscous samples was taken as a value at a plateau at shear rates 1–20 1/s, where viscosity is independent of the applied shear rate.

3. Results and discussion

In this article, we studied the rheological properties of anionic (potassium oleate) and cationic (n-octylpyridinium chloride or C₈Pyr) surfactant mixtures in aqueous solutions. In all experiments, the content of potassium oleate was fixed at 62 mM (2 wt %). This concentration is much higher than its critical micelle concentration (cmc), which equals to ~ 0.9 mM [19], therefore, at this concentration, potassium oleate forms micelles itself in the absence of C₈Pyr. The concentration of C₈Pyr was varied in the range 0–100 mM (0–2.3 wt %), which corresponds to the molar ratios [C₈Pyr] / [potassium oleate] from 0 to 1.6.

At all the molar ratios under study, the solutions were homogeneous and transparent, and no phase separation was observed. This fact indicates that the attraction force between anionic and cationic surfactant molecules, which arises both from electrostatic attraction of their oppositely charged head groups and hydrophobic interaction between alkyl tails, is not too strong to cause precipitation of catanionic complex. Such a precipitation is inherent for surfactants with lower asymmetry in hydrophobic tail length, e.g. for mixtures of sodium oleate with alkyltrimethylammonium bromides with C₁₀ and C₁₂ tails [4]. In our case, no phase separation is seen even at equimolar composition. According to the literature data, high tail length asymmetry and weaker attraction between anionic and short-chain cationic surfactants leads to the incorporation of cationic species into anionic micelles and to the formation of mixed micelles [4].

The rheological properties of mixed anionic / cationic surfactant solutions were studied at different molar ratios [C₈Pyr] / [potassium oleate]. The flow curves are presented in Fig. 1. It is seen that in the absence of C₈Pyr, the viscosity is very low (0.0012 Pa·s) and nearly equal to that of water. At these conditions, spherical potassium oleate micelles are formed, as was shown by literature data [20]. Drastic changes in the rheological behavior are seen upon progressive addition of C₈Pyr (Fig. 1). The viscosity increases by more than 5 orders of magnitude and reaches 300 Pa·s for the molar ratio [C₈Pyr] / [potassium oleate] = 0.5. Also, one can note that at molar ratios 0.4 and higher, the solutions exhibit strong shear-thinning behavior (Fig. 1).

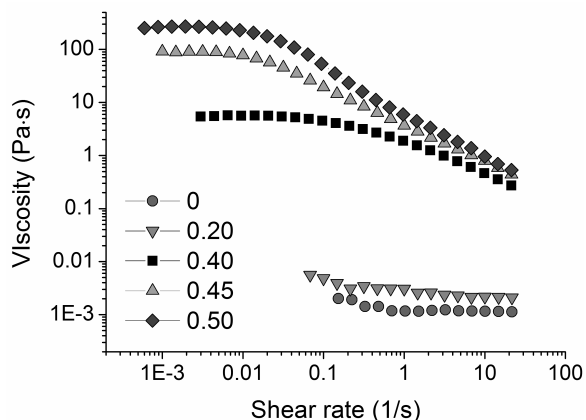


FIG. 1. Flow curves for 62 mM potassium oleate aqueous solutions containing different amounts of C_8Pyr corresponding to molar ratios $[C_8Pyr]/[potassium\ oleate]$: 0 (circles), 0.20 (reverse triangles), 0.40 (squares), 0.45 (triangles), 0.50 (diamonds) at 20 °C

The frequency dependences of the storage (G') and loss (G'') moduli (Fig. 2) show that upon addition of C_8Pyr , the solutions attain strong viscoelastic properties. A well-defined high-frequency elastic plateau appears at $G'(\omega)$ curve, whereas the intercept point ω_0 between $G'(\omega)$ and $G''(\omega)$ curves shifts to lower frequencies (by more than two orders of magnitude), indicating the increase of the terminal relaxation time of the system τ , since $\tau = 1/\omega_0$. These effects can be explained by the progressive incorporation of C_8Pyr molecules into potassium oleate micelles, resulting in the screening of electrostatic repulsions between the charged oleate head groups, which reduces the average distance between them. This leads to the change of molecular packing parameter of surfactant molecules and to the transformation of spherical micelles into cylindrical ones. When the content of C_8Pyr is increased, cylindrical (wormlike) micelles grow in length and form an entangled network, thus imparting high viscosity and viscoelastic properties to the solutions.

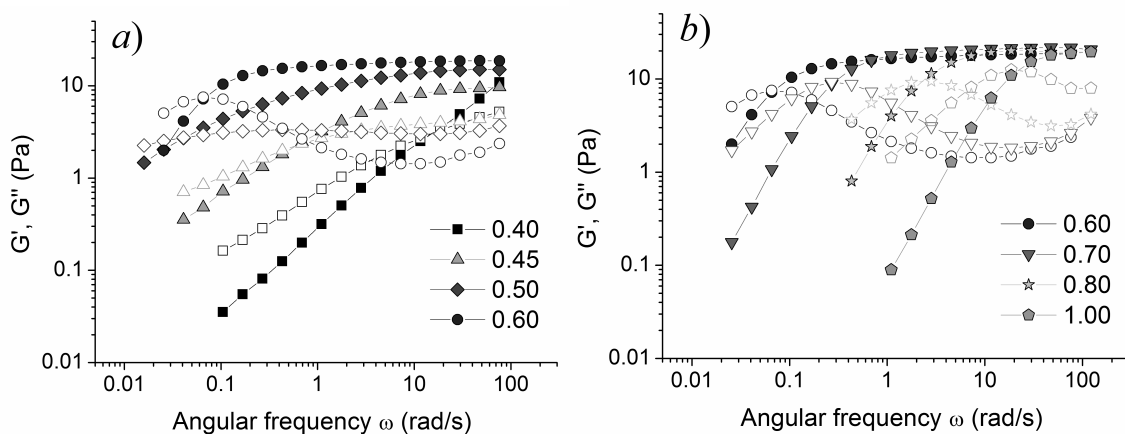


FIG. 2. Frequency dependences of storage G' (filled symbols) and loss G'' (open symbols) moduli for 62 mM potassium oleate aqueous solutions containing different amounts of C_8Pyr corresponding to molar ratios $[C_8Pyr]/[potassium\ oleate]$: 0.40 (squares), 0.45 (triangles), 0.50 (diamonds), 0.60 (circles), 0.70 (reverse triangles), 0.80 (stars), 1.00 (pentagons) at 20 °C

Figures 3 and 4 show the dependences of the rheological parameters (zero-shear viscosity η_0 , relaxation time τ and plateau storage modulus G_0) on C_8Pyr concentration. It can be seen that the viscosity and relaxation time first grow, show a maximum around the molar ratio $[C_8Pyr] / [potassium\ oleate] = 0.5$, and then decrease. Such behavior was observed for many wormlike surfactant micellar systems [4, 8, 20, 21] including anionic / cationic surfactant mixtures [4]. Initial growth was explained by the increase of the length of linear micelles so that the maximum viscosity corresponds to the formation of longest linear wormlike chains. Further decrease of η_0 and τ after the maximum is usually attributed to the formation of branched micelles [9]. However, in mixed anionic / cationic

surfactant systems it may also be due to the shortening of micellar chains as was demonstrated for sodium oleate / C_8 TAB micelles by cryo-transmission electron microscopy [22]. But one should note that the experiments in the last paper [22] were performed at constant total concentration of cationic and anionic surfactants and therefore the amount of long-chain anionic surfactant was decreased as the cationic short-chain surfactant was added, which may favor a decrease of micellar length. In contrast, in the present paper, we keep the anionic surfactant concentration constant. Therefore, one can suppose that for the potassium oleate / C_8 Pyr system under study, both branching and shortening of the micelles can be a reason for the decrease of the rheological parameters after the maximum.

As to the elastic modulus G_0 , it grows at molar ratios up to 0.7 and then stays nearly constant (Fig. 4b). The growth, which mainly occurs in the region of steep viscosity increase, can be attributed to the progressive formation of an entangled network of micelles. Indeed, G_0 is known to be proportional to the number density of entanglements ρ [23]:

$$G_0 \sim \rho kT,$$

where k is the Boltzmann constant, and T is the absolute temperature. In wormlike micellar solutions, there is a wide distribution of micellar lengths, and the solutions contain, in particular, very short micelles. At increasing molar ratio $[C_8\text{Pyr}] / [\text{potassium oleate}]$, the short micelles become longer than the entanglement length and start to contribute to G_0 [24]. At the molar ratio close to 0.7, the micelles become presumably so long that further change of their size does not influence the number of entanglements in the system.

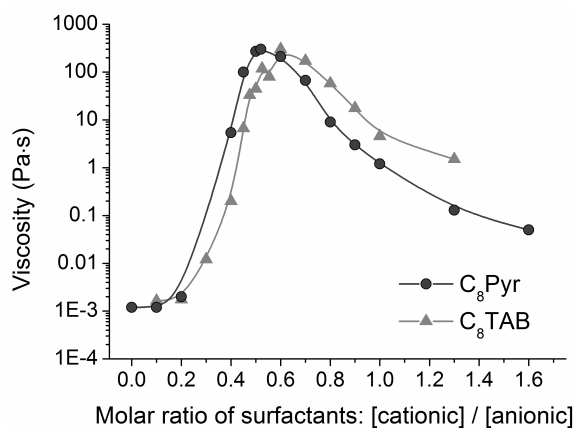


FIG. 3. Dependences of zero-shear viscosity η_0 on the molar ratio [cationic]/[anionic] surfactant for 62 mM aqueous solutions of potassium oleate and different concentrations of C_8 Pyr (circles) or C_8 TAB (triangles) at 20 °C

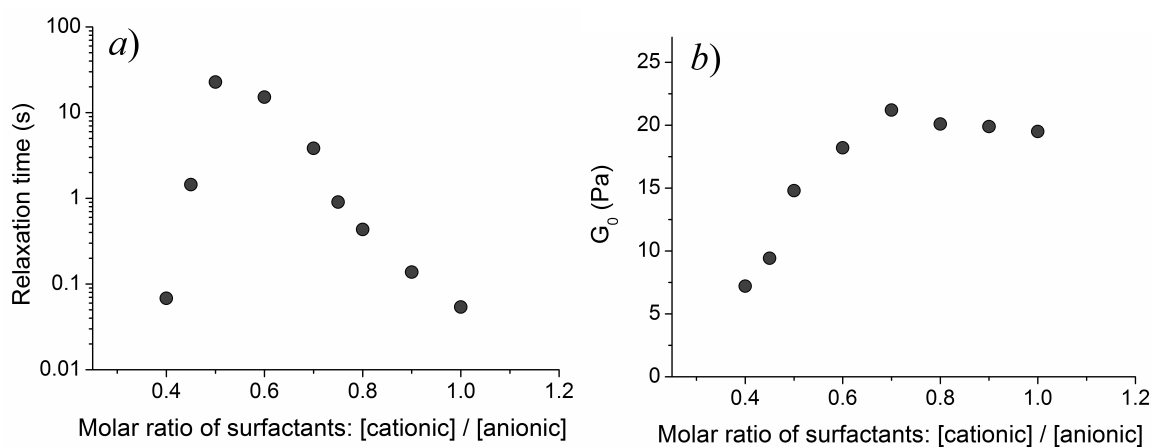


FIG. 4. Dependences of terminal relaxation time τ (a) and plateau storage modulus G_0 (b) on the molar ratio [cationic]/[anionic] surfactant for 62 mM aqueous solutions of potassium oleate and different concentrations of C_8 Pyr at 20 °C

Figure 3 compares the effect of two different cationic surfactants with the same hydrophobic tail length (C8) but different chemical structure of the polar head on the viscosity of mixed anionic / cationic surfactant solutions. It can be seen that both curves are nearly of the same shape with strongly increasing viscosity at low molar ratios, a maximum, and a slight decrease of viscosity at high cationic surfactant concentrations. This means that the chemical structure of the cationic surfactant polar head has minor influence on the behavior of mixed micelles, which is mostly controlled by the length of its hydrophobic tail [4]. However, it is seen that the maximum for C₈Pyr is slightly shifted to lower concentrations compared to C₈TAB, and the difference between C₈Pyr and C₈TAB grows with their increasing concentration after the maximum. This is probably due to more effective screening of electrostatic repulsions by C₈Pyr polar head, in which the charge is more accessible than in C₈TAB, where it is sterically shielded by three methyl groups, or by somewhat higher hydrophobicity of C₈Pyr head group in comparison with C₈TAB. Thus, cationic surfactant with pyridinium polar head allows one to obtain solutions with highest viscosity at lower concentration than its trimethylammonium counterpart.

The results obtained show that the molar ratio of cationic to anionic surfactants in wormlike micelles plays a key role in controlling their rheological properties by tuning the micellar length and morphology. All the experiments in this work were performed without added low molecular weight salt, therefore, electrostatic interactions between anionic and cationic surfactant molecules and the amounts of both negative and positive charges are of the major influence on the behavior of the system. Changing the charge ratio (that is, the molar ratio of cationic to anionic surfactants incorporated into the micelles) should affect two main micellar characteristics: 1) the strength of surfactants binding, which determines the micellar scission energy E_{sc} – the energy needed to break a micelle into two shorter micelles, 2) the net charge of micelles, which controls the micellar electrostatic energy E_e [9]. When a micelle is cut into two pieces, two hemispherical end-cap need to be formed from the cylindrical part, therefore, the scission energy is equal to the difference between the energy of a cylindrical part and spherical end-cap (containing the same amount of surfactant molecules): $E_{sc} = E_{cyl} - E_{sph}$. The higher the scission energy, the more energetically favorable are cylindrical parts compared to spherical end-caps, meaning the formation of longer micelles. On the contrary, higher electrostatic energies result in stronger repulsion between the micelles, thus preventing the formation of longer ones. Therefore, the difference between E_{sc} and E_e controls the mean length of charged micelles L at low ionic strength [9] via the equation:

$$L \sim \varphi^{1/2} \exp((E_{sc} - E_e)/2kT),$$

where φ is the volume fraction of the surfactants, k is the Boltzmann constant, and T is the absolute temperature.

The values of $E_{sc} - E_e$ for C₈Pyr / potassium oleate micelles were estimated from the rheological data. Fig. 5a presents the frequency dependences $G'(\omega)$ and $G''(\omega)$ at different temperatures for the molar ratio $[C_8Pyr]/[potassium\ oleate] = 0.6$. From these dependences the values of the plateau modulus G_0 and the loss modulus at high-frequency minimum G''_{min} were determined, which are related to the average contour length L of micelles by equation [25]:

$$L/l_e \approx G_0/G''_{min},$$

where l_e is the entanglement length. It is argued in the literature that l_e is independent of temperature [26, 27], therefore, $E_{sc} - E_e$ can be determined as a slope of the dependence of $\ln(G_0/G''_{min})$ on $1/T$ (Arrhenius plot). These plots for different $[C_8Pyr] / [potassium\ oleate]$ molar ratios are presented in Fig. 6, and the calculated values of $E_{sc} - E_e$ are given in Fig. 7.

From Fig. 7, it is seen that the difference between scission energy and micellar electrostatic energy increases more than twofold when the molar ratio $[C_8Pyr] / [potassium\ oleate]$ is raised from 0.6 to 0.9. This observation may be explained by two reasons. First, changing the charge ratio between cationic and anionic surfactants may affect the strength of the surfactants' binding. Indeed, incorporation of more cationic species between strongly repelling anionic surfactant polar heads reduces the repulsion between them, thus effectively "binding" them together, which increases the micellar scission energy E_{sc} . Second, the increase of cationic to anionic surfactant molar ratio (when it still remains below unity) reduces the net micellar charge thus lowering the micellar electrostatic energy. Namely, E_e is proportional to $\nu^2 \varphi^{1/2}$, where ν is the effective charge per unit length, and φ is the total surfactant volume fraction [9]; thus, one can estimate that when the molar ratio $[C_8Pyr] / [potassium\ oleate]$ is increased from 0.6 to 0.9, E_e drops by approximately 15 times.

So, the length of the micelles is governed both by scission and electrostatic energy, and temperature. When the solutions are heated, the micellar length decreases, exponentially resulting in reduced viscosity. Typical frequency dependences of the complex viscosity modulus $|\eta^*|$ at different temperatures are presented in Fig. 5b for the molar ratio $[C_8Pyr] / [potassium\ oleate] = 0.6$. It is seen that the low-frequency plateau (representing the viscosity of the system [28]) lowers at heating. From temperature dependence of viscosity the flow activation energy E_a can be

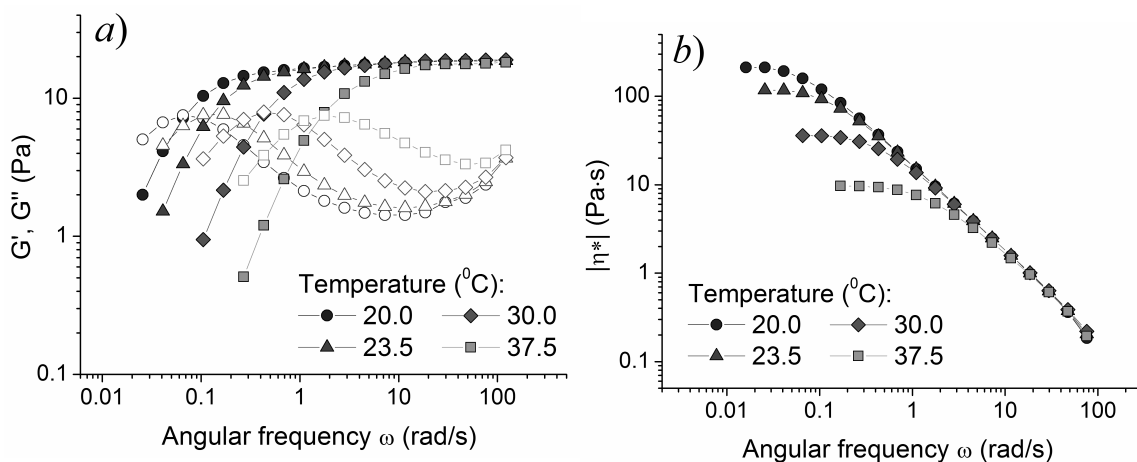


FIG. 5. Frequency dependences of storage G' (filled symbols) and loss G'' (open symbols) moduli (a) and complex viscosity modulus $|\eta^*|$ (b) for 62 mM potassium oleate aqueous solutions in the presence of C₈Pyr (molar ratio [C₈Pyr] / [potassium oleate] = 0.6) at different temperatures (°C): 20 (circles), 23.5 (triangles), 30 (diamonds), 37.5 (squares)

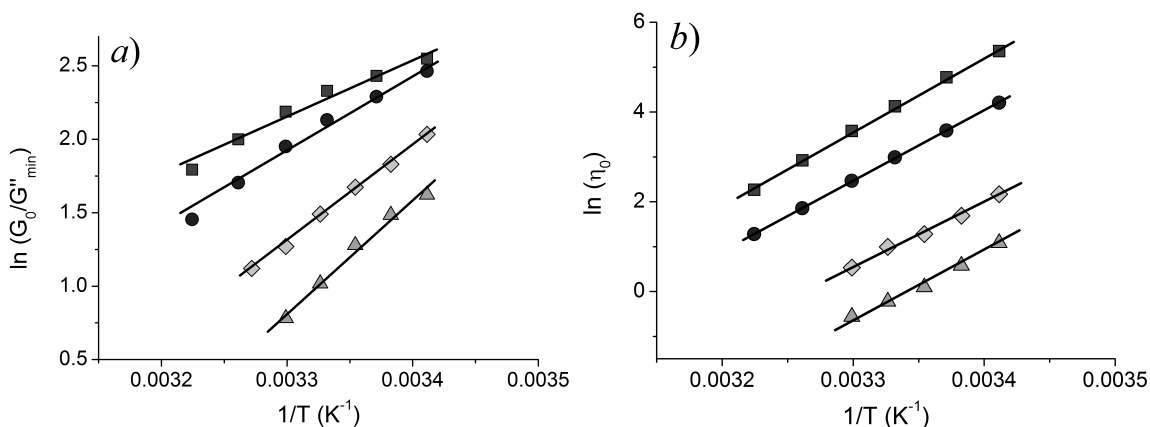


FIG. 6. Dependences of $\ln(G_0/G''_{min})$ (a) and $\ln(\eta_0)$ (b) on $1/T$ for 62 mM potassium oleate aqueous solutions in the presence of different amounts of C₈Pyr corresponding to molar ratios [C₈Pyr] / [potassium oleate]: 0.6 (squares), 0.7 (circles), 0.8 (diamonds), 0.9 (triangles)

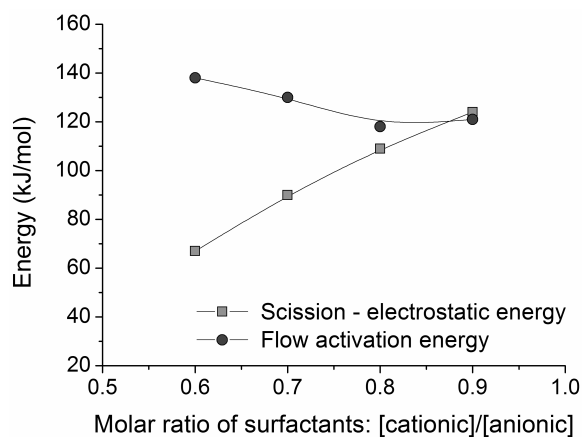


FIG. 7. Dependences of the difference between scission energy and electrostatic energy $E_{sc} - E_e$ (a) and flow activation energy E_a (b) on the molar ratio [cationic]/[anionic] surfactant for 62 mM aqueous solutions of potassium oleate and different concentrations of C₈Pyr at 20 °C

estimated according to the equation [29]:

$$\eta \sim \exp(E_a/kT).$$

The values of E_a determined from the Arrhenius plots $\ln \eta$ vs $1/T$ (Fig. 6b) at different C₈Pyr content are presented in Fig. 7. They are similar to the values reported in literature for different surfactant systems [30,31]. From Fig. 7 it is seen that E_a does not significantly change upon variation of C₈Pyr content indicating that the responsiveness of viscous properties of mixed wormlike micellar solutions to heating is almost unaltered by their composition.

4. Conclusions

In this paper, new mixed wormlike micelles consisting of anionic fatty acid salt surfactant and cationic surfactant from the alkylpyridinium family were prepared and investigated. It was discovered that at moderate surfactant concentrations (about 3 wt % total surfactant) the solutions have high viscosity (5 magnitude higher than the viscosity of water) and strong viscoelasticity, which was explained by the formation of an entangled network of wormlike micelles due to incorporation of a short-chain cationic surfactant into anionic micelles and effective screening of electrostatic repulsions on the micellar surface. Temperature measurements at different cationic / anionic surfactant molar ratios revealed that viscoelastic properties of the system are governed both by binding strength of surfactant molecules within the micelle and electrostatic effects. The findings of this paper provide a new way of creating effective surfactant compositions for solutions with highly controllable mechanical properties, with great potential for application, e.g. as thickening agents in the petroleum industry.

Acknowledgments

This work was supported by the Russian Science Foundation (project No 15-13-00114). The authors express their gratitude to Ms. K. A. Abrashitova (Moscow State University) for help with some rheological measurements.

References

- [1] Rehage H., Hoffmann H. Rheological properties of viscoelastic surfactant systems. *J. Phys. Chem.*, 1988, **92**(16), P. 4712–4719.
- [2] Khatory A., Lequeux F., Kern F., Candau S.J. Linear and nonlinear viscoelasticity of semidilute solutions of wormlike micelles at high salt content. *Langmuir*, 1993, **9**(6), P. 1456–1464.
- [3] Koehler R.D., Raghavan S.R., Kaler E.W. Microstructure and dynamics of wormlike micellar solutions formed by mixing cationic and anionic surfactants. *J. Phys. Chem. B*, 2000, **104**(47), P. 11035–11044.
- [4] Raghavan S.R., Fritz G., Kaler E.W. Wormlike micelles formed by synergistic self-assembly in mixtures of anionic and cationic surfactants. *Langmuir*, 2002, **18**(10), P. 3797–3803.
- [5] Schubert B.A., Kaler E.W., Wagner N.J. The microstructure and rheology of mixed cationic/anionic wormlike micelles. *Langmuir*, 2003, **19**(10), P. 4079–4089.
- [6] Shibaev A.V., Abrashitova K.A., Kuklin A.I., Orekhov A.S., Vasiliev A.V., Iliopoulos I., Philippova O.E. Viscoelastic synergy and microstructure formation in aqueous mixtures of nonionic hydrophilic polymer and charged wormlike surfactant micelles. *Macromolecules*, 2017, **50**(1), P. 339–348.
- [7] Shibaev A.V., Kuklin A.I., Philippova O.E. Effect of polymer on the arrangement of mixed anionic/cationic wormlike surfactant micelles revealed by SANS. *J. Phys.: Conf. Ser.*, 2017, **848**, P. 012006.
- [8] Molchanov V.S., Shashkina Y.A., Philippova O.E., Khokhlov A.R. Viscoelastic properties of aqueous surfactant (potassium oleate) solutions. *Colloid J.*, 2005, **67**(5), P. 606–609.
- [9] Dreiss C.A. Wormlike micelles: where do we stand? Recent developments, linear rheology and scattering techniques. *Soft Matter*, 2007, **3**(8), P. 956–970.
- [10] Chu Z., Dreiss C.A., Feng Y. Smart wormlike micelles. *Chem. Soc. Rev.*, 2013, **42**(17), P. 7174–7203.
- [11] Koroleva S.V., Victorov A.I. Modeling of the effects of ion specificity on the onset and growth of ionic micelles in a solution of simple salts. *Langmuir*, 2014, **30**(12), P. 3387–3396.
- [12] Shibaev A.V., Tamm M.V., Molchanov V.S., Rogachev A.V., Kuklin A.I., Dormidontova E.E., Philippova O.E. How a viscoelastic solution of wormlike micelles transforms into a microemulsion upon absorption of hydrocarbon: new insight. *Langmuir*, 2014, **30**(13), P. 3705–3714.
- [13] Shibaev A.V., Molchanov V.S., Philippova O.E. Rheological behavior of oil-swollen wormlike surfactant micelles. *J. Phys. Chem. B*, 2015, **119**(52), P. 15938–15946.
- [14] Shibaev A.V., Makarov A.V., Aleshina A.L., Rogachev A.V., Kuklin A.I., Philippova O.E. Structure and oil responsiveness of viscoelastic fluids based on mixed anionic/cationic wormlike surfactant micelles. *J. Phys.: Conf. Ser.*, 2017, **848**, P. 012019.
- [15] Kwiatkowski A.L., Molchanov V.S., Orekhov A.S., Vasiliev A.L., Philippova O.E. Impact of salt co- and counterions on rheological properties and structure of wormlike micellar solutions. *J. Phys. Chem. B*, 2016, **120**(49), P. 12547–12556.
- [16] Yang J. Viscoelastic wormlike micelles and their applications. *Curr. Opin. Colloid Interface Sci.*, 2002, **7**(5–6), P. 276–281.
- [17] Philippova O.E., Khokhlov A.R. Smart polymers for oil production. *Petroleum Chemistry*, 2010, **50**(4), P. 266–270.
- [18] Philippova O.E., Shibaev A.V., Muravlev D.A., Mityuk D.Yu. Structure and rheology of solutions and gels of stiff polyelectrolyte at high salt concentration. *Macromolecules*, 2016, **49**(16), P. 6031–6040.
- [19] Fukuda H., Goto A., Yoshioka H., Goto R., Morigaki K., Walde P. An electron spin resonance study of the pH-induced transformation of micelles to vesicles in an aqueous oleic acid/oleate system. *Langmuir*, 2001, **17**(14), P. 4223–4231.

- [20] Flood C., Dreiss C.A., Croce V., Cosgrove T., Karlsson G. Wormlike micelles mediated by polyelectrolyte. *Langmuir*, 2005, **21**(17), P. 7646–7652.
- [21] Raghavan S.R., Kaler E.W. Highly viscoelastic wormlike micellar solutions formed by cationic surfactants with long unsaturated tails. *Langmuir*, 2001, **17**(17), P. 300–306.
- [22] Ziserman L., Abezgauz L., Ramon O., Raghavan S.R., Danino D. Origins of the viscosity peak in wormlike micellar solutions. 1. Mixed catanionic surfactants. A cryo-transmission electron microscopy study. *Langmuir*, 2009, **25**(18), P. 10483–10489.
- [23] Magid L.J. The surfactant-polyelectrolyte analogy. *J. Phys. Chem. B*, 1998, **102**(21), P. 4064–4074.
- [24] Pimenta P., Pashkovski E.E. Rheology of viscoelastic mixed surfactant solutions: effect of scission on nonlinear flow and rheochaos. *Langmuir*, 2006, **22**(9), P. 3980–3987.
- [25] Granek R., Cates M.E. Stress relaxation in living polymers: results from a Poisson renewal model. *J. Chem. Phys.*, 1992, **96**(6), P. 4758–4767.
- [26] Siriwatwechakul W., LaFleur T., Prud'homme R.K., Sullivan P. Effects of organic solvents on the scission energy of rodlike micelles. *Langmuir*, 2004, **20**(21), P. 8970–8974.
- [27] Molchanov V.S., Philippova O.E. Dominant role of wormlike micelles in temperature-responsive viscoelastic properties of their mixtures with polymeric chains. *J. Colloid Interface Sci.*, 2013, **394**, P. 353–359.
- [28] Cox W.P., Merz E.H. Correlation of dynamic and steady flow viscosities. *J. Polym. Sci.* 1958, **28**, P. 619–622.
- [29] Fisher P., Rehage H. Rheological master curves of viscoelastic surfactant solutions by varying the solvent viscosity and temperature. *Langmuir*, 1997, **13**(26), P. 7012–7020.
- [30] Soltero A., Puig J.E., Manero O. Rheology of the cetyltrimethylammonium tosilate-water system. 2. Linear viscoelastic regime. *Langmuir*, 1996, **12**(11), P. 2654–2662.
- [31] Shukla A., Fuchs R., Rehage H. Quasi-anomalous diffusion processes in entangled solutions of wormlike surfactant micelles. *Langmuir*, 2006, **22**(7), P. 3000–3006.

Kinetic coefficients of semiconductor superlattices in high-frequency electromagnetic fields

A. V. Shorokhov¹, N. S. Prudskikh¹, M. B. Semenov², V. D. Krevchik²,
M. A. Pyataev¹, S. E. Golovatyuk¹, Tian-Rong Li³, Yu-Hua Wang³

¹ National Research Mordovia State University, Bolshevistskaya, 68, Saransk, 430005, Russia

² Penza State University, Krasnaya, 40, Penza, 440026, Russia

³ Institute of Functional and Environmental Materials, Lanzhou University, Lanzhou, China
alex.shorokhov@mail.ru

PACS 73.63.-b

DOI 10.17586/2220-8054-2017-8-6-740-745

Kinetic coefficients of semiconductor superlattice are obtained from the Boltzmann transport equation with Bhatnagar–Gross–Krook (BGK) collision term and Poisson equation. Using the universal analytic procedure, we found kinetic coefficient in the quasistatic limit starting from the exact solution of the Boltzmann transport equation. It is shown that the Einstein relation for the diffusion coefficient is applicable only for weak fields and it is not valid in the general case. As a consequence, a drift-diffusion model of miniband transport in the case of strong dc and ac fields should be corrected, taking into account the kinetic coefficients obtained from the Boltzmann equation.

Keywords: superlattice, Boltzmann equation, drift-diffusion model, THz radiation, diffusion coefficient, drift velocity, Maxwell frequency, Einstein relation.

Received: 13 November 2017

Revised: 29 November 2017

1. Introduction

The problem of electric stability for a semiconductor superlattice is a crucial one for the practical realization of sub-THz- and THz-based devices. For example, it is well-known that the development of instabilities and the formation of electric domains in a superlattice placed in a dc electric field leads to the destruction of the THz gain [1]. Therefore, the main problem in the realization of superlattice-based THz devices is finding operational conditions which simultaneously allow one to achieve gain at THz frequencies and to avoid destructive space-charge instabilities. Correct description of instability effects requires taking into account spatial-dispersion effects. Such approach for the case of dc biased superlattice was formulated by Ignatov and Shashkin [1–3] and Bonilla et al. [4–6]. As a rule, a drift-diffusion model is used to describe transport and high-frequency properties of superlattices in the quasistatic case. In particular, this model allows taking into account spatial-dispersion effects. However, as it will be shown below, this model can give incorrect results because the correct dependence of kinetic coefficients on the amplitudes of dc and ac fields as well as temperature in the quasistatic case can be obtained only from the Boltzmann and Poisson equations. Note that the analysis of kinetic coefficients of superlattice can give the important information about spatial-dispersion effects and instabilities by analogy with the Gunn effect.

In this paper, we present an approach from which general expressions for the field-dependent average drift velocity, Maxwell frequency and diffusion coefficient are derived starting from the exact solution of Boltzmann equation. As a rule the diffusion coefficient is obtained from the Einstein relation in the framework of drift-diffusion model. However the Einstein relation is not always applicable for strong fields [5, 7]. In connection with it, the calculation of the diffusion coefficient is an important separate question. In this paper we obtain the diffusion coefficient from the exact solution of Boltzmann equation and show that it is sufficiently different from the diffusion coefficient obtained from the Einstein relation.

Let us consider a superlattice under the action of the dc field E_0 directed along the x -axis and the strong ac field $E_1 \cos(\omega_1 t)$. Our main goal is to find and analyze the kinetic coefficients of semiconductor superlattice in quasi-static approximation starting from the exact solution of the kinetic equation and taking into account spatial-dispersion effects connected with a small perturbation $E_2 \cos(\omega_2 t - k_2 x)$.

In the following, we will use the standard dispersion relation in the tight-binding approximation:

$$\varepsilon(p) = \frac{\Delta}{2} \left[1 - \cos\left(\frac{pd}{\hbar}\right) \right], \quad (1)$$

where d is the period of a superlattice, Δ is the miniband width, p is the quasimomentum.

2. Boltzmann equation

In this paper, we will use the traditional method for calculating a high-frequency current based on the use of kinetic equation for miniband electrons with BGK (Bhatnagar-Gross-Krook) collision integral, which permits adequate allowance for the particle-number conservation law for scattering in inhomogeneous field and, as a consequence, makes it possible to take into account the influence of the carrier drift and diffusion effects on the space-charge wave spectrum:

$$\frac{\partial f}{\partial t} + V(p) \frac{\partial f}{\partial x} + eE(x, t) \frac{\partial f}{\partial p} = -\frac{1}{\tau} \left(f - \frac{n(x)}{n_0} f_0 \right), \quad (2)$$

where $V(p) = V_0 \sin(pd/\hbar)$, $V_0 = d\Delta/2\hbar$ is the maximum electron velocity in the miniband, $E(x, t) = E_0 + E_1 \cos(\omega_1 t) + E_2 \cos(\omega_2 t - k_2 x)$ is the total electric field, $n(x)$ is the electron density, $f_0 = (n_0 d/2\pi\hbar I_0) \exp[(\Delta/2T) \cos(pd/\hbar)]$ is the equilibrium distribution function normalized to the equilibrium electron density n_0 , I_m ($m \in \mathbb{Z}$) is the modified Bessel function of argument $\Delta/2T$, τ is the relaxation time, T is the lattice temperature.

The electron distribution functions, due to the periodicity of the quasimomentum, permit representation in the form of a Fourier series:

$$f(p) = \sum_{m=-\infty}^{\infty} f_m(x) e^{im\varphi}, \quad f_0(p) = \sum_{m=-\infty}^{\infty} f_m^0 e^{im\varphi}, \quad (3)$$

where $\varphi = pd/\hbar$, $f_m^0 = n_0 d I_m / 2\pi\hbar I_0$.

In its turn, $f_m(x)$ as well as $n(x)$ permits in the segment $0 < x < L$ (L is the superlattice length) a representation in the form of the following Fourier series:

$$f_m(x) = \sum_{s=-\infty}^{\infty} f_{ms} e^{ikx}, \quad n(x) = \sum_{s=-\infty}^{\infty} n_s e^{ikx}, \quad (4)$$

where $k = 2\pi s/L$ is the wave number, $s \in \mathbb{Z}$.

Substituting (3) and (4) into (2), we get:

$$\frac{\partial f_{ms}}{\partial t} + ikV(\varphi) f_{ms} + \frac{ed}{\hbar} E(x, t) im f_{ms} + \nu f_{ms} = \nu \frac{n_s}{n_0} f_m^0. \quad (5)$$

To find $n_s(t)$ we need to use the Poisson equation:

$$\frac{\partial E(x, t)}{\partial x} = \frac{4\pi e}{\varepsilon} (n(x) - n_0), \quad (6)$$

where ε is the lattice dielectric constant.

As a result we get the exact solution of the kinetic equation (2) in the form:

$$f = \sum_{m=-\infty}^{\infty} f_m^0 \sum_{l_1, l_2=-\infty}^{\infty} \sum_{\nu_1, \nu_2=-\infty}^{\infty} J_{l_1}(m\beta_1) J_{l_2}(m\beta_2) J_{l_1+\nu_1}(m\beta_1) J_{l_2+\nu_2}(m\beta_2) \times \\ \times \left[\frac{\varepsilon k_2 E_2}{8i\pi e n_0} \left(\frac{\exp[-i(\nu_1 \omega_1 + (\nu_2 - 1)\omega_2)t] \exp(-ik_2 x)}{-ik_2 \tau V(\varphi) + 1 + im\Omega_0 \tau + i(l_1 \omega_1 + (l_2 + 1)\omega_2)\tau} - \frac{\exp[-i(\nu_1 \omega_1 + (\nu_2 + 1)\omega_2)t] \exp(ik_2 x)}{ik_2 \tau V(\varphi) + 1 + im\Omega_0 \tau + i(l_1 \omega_1 + (l_2 - 1)\omega_2)\tau} \right) + \frac{\exp[i(\nu_1 \omega_1 + \nu_2 \omega_2)t]}{1 + im\Omega_0 \tau + i(l_1 \omega_1 + l_2 \omega_2)\tau} \right] \exp[i(\nu k_2 x + m\varphi)]. \quad (7)$$

Here $\nu = 1/\tau$, $\beta_i = \Omega_i/\omega_i$ ($i = 1, 2$), $\Omega_j = edE_j/\hbar$ ($j = 0, 1, 2$), $J_l(\beta)$ is the Bessel function.

Using the distribution function (7), one can find the average electron velocity:

$$V_a(t) = \langle V(\varphi) \rangle_\varphi = \frac{\hbar}{d} \int_0^{2\pi} V(\varphi) f(\varphi) d\varphi \quad (8)$$

and the average complex current on the frequency ω_2

$$j = 2e \langle V_a(t) \exp[i(\omega_2 t - k_2 x)] \rangle_t, \quad (9)$$

In the case of a small perturbation $\beta_2 \ll 1$ and a small k_2 , we get the following expression for the complex current:

$$\begin{aligned}
j = & -\frac{\varepsilon k_2 E_2 V_0 I_1}{8\pi I_0} \sum_{l_1=-\infty}^{\infty} J_{l_1}^2(\beta_1) \left[\frac{1 - i(l_1\omega_1 - \omega_2 + \Omega_0)\tau}{1 + (l_1\omega_1 - \omega_2 + \Omega_0)^2\tau^2} - \frac{1 - i(l_1\omega_1 - \omega_2 - \Omega_0)\tau}{1 + (l_1\omega_1 - \omega_2 - \Omega_0)^2\tau^2} \right] + \\
& + \frac{\varepsilon k_2^2 E_2 V_0^2 \tau}{16\pi} \left[2 \frac{(1 + i\omega_2\tau)^2}{(1 + \omega_2^2\tau^2)^2} - \frac{I_2}{I_0} \sum_{l_1=-\infty}^{\infty} J_{l_1}^2(2\beta_1) \times \right. \\
& \times \left. \left(\frac{(1 - i(l_1\omega_1 - \omega_2 + 2\Omega_0)\tau)^2}{(1 + (l_1\omega_1 - \omega_2 + 2\Omega_0)^2\tau^2)^2} + \frac{(1 - i(l_1\omega_1 - \omega_2 - 2\Omega_0)\tau)^2}{(1 + (l_1\omega_1 - \omega_2 - 2\Omega_0)^2\tau^2)^2} \right) \right] + \\
& + \frac{ie^2 dn_0 V_0 I_1 E_2}{2I_0 \hbar} \sum_{l_1=-\infty}^{\infty} J_{l_1}^2(\beta_1) \left[-\frac{2}{1 + (l_1\omega_1 + \Omega_0)^2\tau^2} + \right. \\
& \left. + \frac{1 - i(l_1\omega_1 + \omega_2 + \Omega_0)\tau}{1 + (l_1\omega_1 + \omega_2 + \Omega_0)^2\tau^2} + \frac{1 - i(l_1\omega_1 + \omega_2 - \Omega_0)\tau}{1 + (l_1\omega_1 + \omega_2 - \Omega_0)^2\tau^2} \right]. \quad (10)
\end{aligned}$$

3. Quasistatic limit

To find the quasistatic limit of the current we have to impose the additional limitation on ω_1 and ω_2 : $\omega_1\tau \ll 1$, $\omega_2\tau \ll 1$. Using the saddle-point method [8,9] we get the formula for the current in quasistatic limit as a power series in k_2 :

$$j = \frac{\varepsilon}{4\pi} E_2 (\omega_m + ik_2 V_d + k_2^2 D). \quad (11)$$

In formula (11), the drift velocity can be written as [10]

$$V_d = \frac{V_p I_1}{\pi I_0} \int_0^{2\pi} I^{ET}(\Omega_1 \cos \theta + \Omega_0) d\theta, \quad (12)$$

where:

$$I^{ET}(\omega) = \frac{\omega\tau}{1 + \omega^2\tau^2} \quad (13)$$

is the Esaki–Tsu characteristic, and $V_p = V_0/2$ is the peak drift velocity.

The dependence of V_d on E_0 is shown on Fig. 1. The ratio of Bessel functions in (12) takes into account the effect connected with the thermal distribution of miniband electron. It follows from Eq. (12) that the effect of temperature leads to a reduction of the drift velocity. The growth of amplitude of ac field leads to a shift of the maximum of the dependence of the drift velocity on the dc bias to the region of higher static fields and reduction of the drift velocity (Fig. 1).

The differential Maxwell frequency is expressed in terms of the drift velocity as:

$$\omega_m = \frac{4\pi en_0}{\varepsilon} \frac{dV_d}{dE_0}. \quad (14)$$

The dependence of Maxwell frequency on the dc bias is shown on Fig. 2 at the different values of ac field.

The diffusion coefficient has the following form:

$$D = \frac{V_0^2 \tau}{4} \left\{ 2 - \frac{I_2}{4\pi\tau I_0} \frac{\partial}{\partial \Omega_0} \int_0^{2\pi} [I^{ET}(2\Omega_1 \cos \theta + 2\Omega_0) - I^{ET}(2\Omega_1 \cos \theta - 2\Omega_0)] d\theta \right\}. \quad (15)$$

Note that the Einstein relation $D(E) = TV_d(E)/eE$ is not valid in this case. In connection with it, the use of the Einstein relation is incorrect for systems with strong dc and ac fields, except in some particular cases.

In the limit of the pure dc field $E_1 = 0$, we obtain for the Maxwell frequency:

$$\omega_m = \omega_p^2 \tau, \quad N^{ET}(\Omega_0) = \omega_p^2 \frac{\partial I^{ET}(\Omega_0)}{\partial \Omega_0}, \quad (16)$$

for the drift velocity [11,12] (this dependence is in a good agreement with experimental data [13]):

$$V_d = 2V_p \frac{I_1}{I_0} I^{ET}(\Omega_0), \quad (17)$$

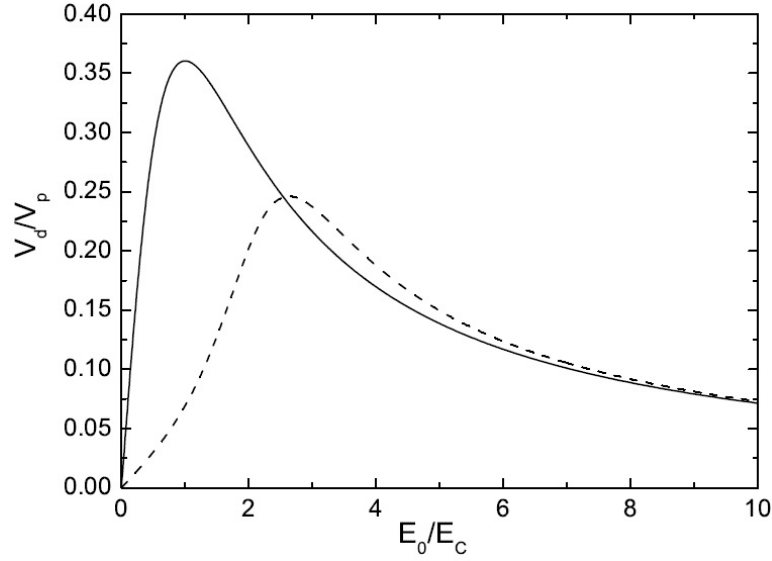


FIG. 1. The dependence of the drift velocity on the dc bias E_0 at $T = 300$ K. Solid line corresponds to $E_1 = 0$, the dash line corresponds to $E_1\tau = 2.1$. $E_c = \hbar/ed\tau$ ($\Omega_0\tau = E_0/E_c$) is the critical field corresponding to the maximum of Esaki-Tsu I-V characteristic at $E_1 = 0$

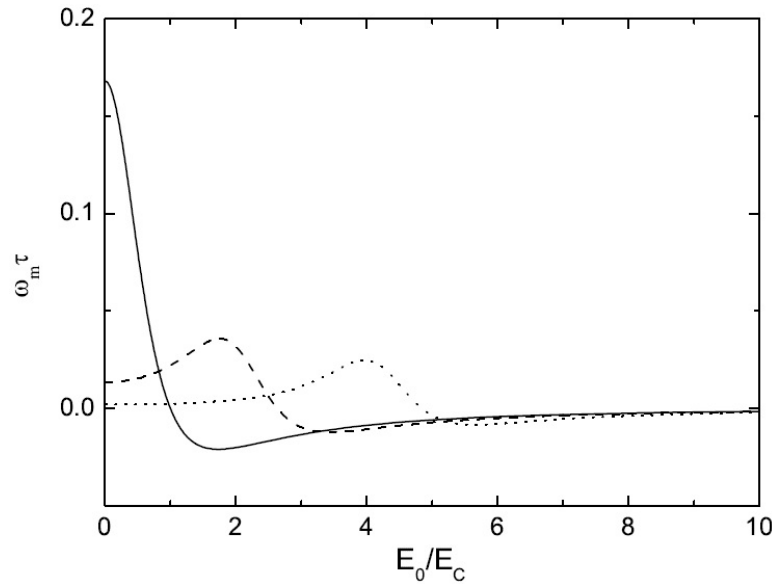


FIG. 2. The dependence of the Maxwell frequency on the dc bias E_0 at $T = 300$ K. Solid line corresponds to $E_1 = 0$, the dash line corresponds to $E_1\tau = 2.1$, the dot line corresponds to $E_1\tau = 4.3$. $\tau = 200$ fs, $\Delta = 40$ meV, $n_0 = 0.5 \times 10^{16}$ cm $^{-3}$, $d = 6$ nm

and for the diffusion coefficient:

$$D = \frac{V_0^2\tau}{4} \left[1 - \frac{I_2}{I_0} N^{ET}(2\Omega_0) \right]. \quad (18)$$

Here:

$$N^{ET}(\omega) = \frac{1 - \omega^2\tau^2}{(1 + \omega^2\tau^2)^2}. \quad (19)$$

The difference between the diffusion coefficients obtained from the Boltzmann equation and from the Einstein relation is shown on Figs. 3 and 4 for the case of the pure dc field. One can see that the Einstein relation gives the correct result only in the case of small dc fields $\Omega_0\tau < 0.1$. At the same time, the diffusion coefficient obtained

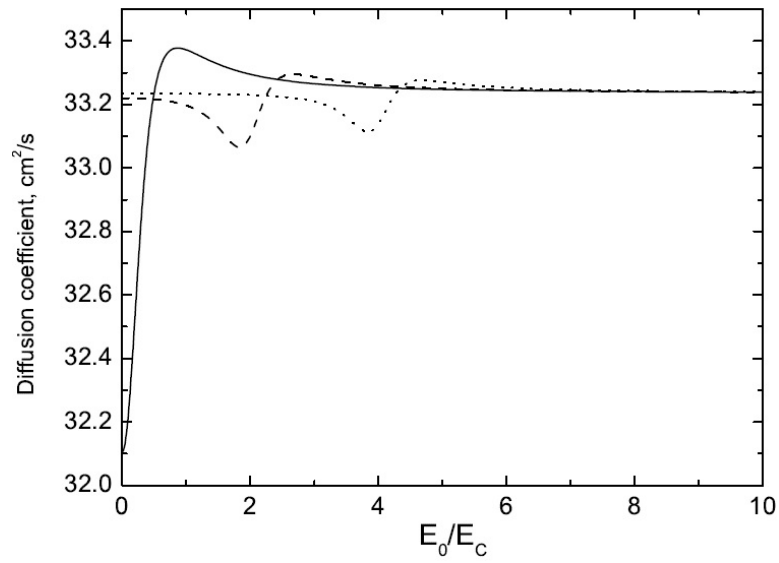


FIG. 3. The dependence of the diffusion coefficient on the dc bias E_0 at $T = 300$ K. Solid line corresponds to $E_1 = 0$, the dash line corresponds to $E_1\tau = 2.0$, the dot line corresponds to $E_1\tau = 4.0$. The other parameters are the same as in Fig. 2

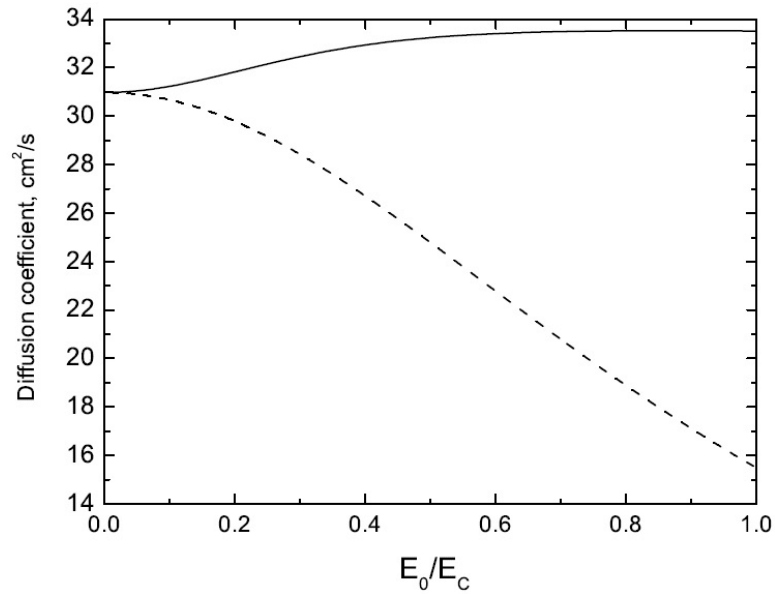


FIG. 4. The dependence of the diffusion coefficient on the dc bias E_0 at $T = 300$ K. Solid line corresponds to the diffusion coefficient calculated by formula (18), the dash line corresponds to the diffusion coefficient calculated by the Einstein relation. The other parameters are the same as in Fig. 2

from the Boltzmann equation increases with an increase in the dc field, while the diffusion coefficient obtained from the Einstein relation decreases with the increasing of dc field.

In the opposite case of the ac pump field ($E_0 = 0$), the kinetic coefficients have the form:

$$\omega_m = \frac{\omega_p^2 \tau}{(1 + \Omega_1^2 \tau^2)^{3/2}}, \quad (20)$$

$$V_d = 0, \quad (21)$$

$$D = \frac{V_0^2 \tau}{2} \left[1 - \frac{I_2}{I_0} \frac{1}{(1 + 4\Omega_1^2 \tau^2)^{3/2}} \right]. \quad (22)$$

4. Conclusion

We have modified the drift-diffusion model for the semiconductor superlattice using the exact solution of the Boltzmann equation. The obtained kinetic coefficient such as the Maxwell frequency, drift velocity and diffusion coefficient differ from the common coefficients of standard drift-diffusion model. In particular, the Maxwell frequency and drift velocity has the additional temperature factor though the relationship between these coefficients are the same as in the drift-diffusion model. At the same time, the diffusion coefficient differs drastically from that of the drift-diffusion model, and as a consequence, the Einstein relationship is not valid in this case.

Acknowledgements

The authors would like to thank Kirill Alekseev for collaboration and useful ideas. This work was supported by the Ministry of Education and Science of the Russian Federation (Project No. 3.6321.2017/8.9), and RFBR (Project No. 17-02-00969).

References

- [1] Ignatov A. A., Shashkin V. I. Bloch oscillation of electrons and instabilities of space-charge waves in semiconductor superlattices. *Sov. Phys. JETP*, 1987, **66**, P. 526–530.
- [2] Ignatov A. A., Shashkin V. I. Diffusion coefficient of heated carries, spectrum of space-charge waves, and characteristic instability frequencies of semiconductor superlattices. *Sov. Phys. Semicond*, 1984, **18**, P. 721–724.
- [3] Ignatov A. A., Shashkin V. I. Quasihydrodynamic description of the instability of space charge waves and impedance of bounded superlattice structures. *Sov. Phys. Semicond*, 1987, **21**, P. 973–976.
- [4] Bonilla L. L., Alvaro M., Carretero M. Theory of spatially inhomogeneous Bloch oscillations in semiconductor superlattices. *Physical Review B*, **84**, 2011, P. 155316 1–17.
- [5] Bonilla L. L., Escobedo R., Perales Á. Generalized drift-diffusion model for miniband superlattices. *Physical Review B*, 2003, **68**, P. 2413041-4(R).
- [6] Ivaro M., Carretero M., Bonilla L. L. Numerical method for hydrodynamic modulation equations describing Bloch oscillations in semiconductor superlattices. *Journal of Computational Physics*, 2012, **231**, P. 4499–4514.
- [7] Bryksin V. V., Kleinert P. Theory of quantum diffusion in biased semiconductors. *J. Phys.: Condens. Matter*, 2003, **15**, P. 1415–1425.
- [8] Shorokhov A. V., Aleksev K. N. High-frequency absorption and gain in superlattices: Semiquasistatic approach. *Physica E*, 2006, **33**, P. 284–295.
- [9] Shorokhov A. V., Aleksev K. N. Quantum Derivatives and Terahertz Gain in a Superlattice. *JETP*, 2006, **105**, P. 198–200.
- [10] Winnerl S., Schomburg E., Grenzer J., Regl H.-J., Ignatov A. A., Semenov A. D., Renk K. F., Pavel'ev D. G., Koschurinov Yu., Melzer B., Ustinov V., Ivanov S., Schaposchnikov S., Kop'ev P. S. Quasistatic and dynamic interaction of high-frequency fields with miniband electrons in semiconductor superlattices. *Physical Review B*, 1997, **56**, P. 10303–10307.
- [11] Suris R. A. and Shchamkhalova B. S. Heating of electrons in superlattice semiconductors. *Sov. Phys. Semicond*, 1984, **18**, P. 738–742.
- [12] Ignatov A. A., Dodin E. P., Shashkin V. I. Transient response theory of semiconductor superlattices: connection with Bloch oscillations. *Mod. Phys. Lett. B*, 1991, **5**, P. 1087–1094.
- [13] Grahn H. T., von Klitzing K., Ploog K., Dohler G. H. Electrical transport in narrow-miniband semiconductor superlattices. *Phys. Rev. B*, 1991, **43**, P. 12094–12097.

Instantons describing tunneling between magnetic states at finite temperatureS. M. Vlasov^{1,2}, P. F. Bessarab^{1,2}, V. M. Uzdin^{2,3}, H. Jónsson^{1,4}¹Science Institute and Faculty of Physical Sciences, Univ. of Iceland 107 Reykjavík, Iceland²ITMO University, Kronverkskiy, 49, St. Petersburg, 197101, Russia³St. Petersburg State University, St. Petersburg, 198504, Russia⁴Center for Nonlinear Studies, Los Alamos, NM 87545, USA

van_der_paul@yahoo.co.uk, v_uzdin@mail.ru, hj@hi.is

DOI 10.17586/2220-8054-2017-8-6-746-759

A method is presented for finding instantons in magnetic systems – optimal paths corresponding to tunneling from one magnetic state to another at a finite temperature. The method involves analytical continuation of the energy to allow for complex values of the angle variables. First, a set of discretization points are placed equally spaced on a chosen energy contour. Then, an estimate of the corresponding temperature is obtained using Landau-Lifshitz dynamics in imaginary time along the contour. Finally, the distribution of the discretization points as well as the energy are systematically refined by converging on the nearest stationary point of the Euclidean action, thereby obtaining a discrete representation of the closest instanton at the given temperature. The method is illustrated with an application to a system consisting of a single spin subject to uniaxial anisotropy and transverse external magnetic field. First-order and second-order crossovers from over-the-barrier mechanism to tunneling are found depending on the applied field, and the difference in the dependence of the instanton temperature on the energy illustrated for the two cases. By comparing the Boltzmann factors for over-the-barrier and tunneling transitions, the crossover temperature between the two mechanisms is estimated for both first- and second-order crossover.

Keywords: magnetic transitions, tunneling, instanton, path optimization.

Received: 15 November 2017

Revised: 24 November 2017

1. Introduction

Transitions between (meta)stable states of atomic systems are typically thermally activated, i.e. they occur as a result of thermal fluctuations due to coupling to a heat bath. The states are separated and can be identified because of an energy barrier, an energy ridge on the multidimensional energy surface. At high enough temperature, the transitions rely on large energy fluctuations in the right degrees of freedom that enable the system to overcome the energy barrier. This is referred to as over-the-barrier transition mechanism. For high barriers, these are rare events compared with the timescale of vibrations. The rate of such rare events can be estimated from statistical rate theories, in particular, transition state theory and Kramers/Langer theory [1–3]. These theoretical tools make it possible to predict and analyze the typically observed Arrhenius dependence of the transition rate on temperature, where the activation energy is essentially the height of the energy barrier. This methodology was initially developed in the context of atomic rearrangements such as chemical reactions, diffusion events and conformational changes of molecules. More recently, statistical rate theories have been extended to describe transitions from one magnetic state to another [4–8]. More generally, atomic coordinates and orientation of magnetic moments should be treated on an equal footing.

At low enough temperature a different transition mechanism will eventually become dominant. There, the system advances from one state to another by quantum mechanical tunneling through the energy barrier. The crossover from over-the-barrier mechanism to tunneling is evident from a rapid drop in the activation energy as the temperature is lowered. For atomic rearrangements and temperature close to room temperature, this kind of behavior is mostly observed in transitions involving light atoms, such as hydrogen. Transition state theory for atomic rearrangements has been extended by use of Feynman path integrals to take into account the possibility of tunneling [9–13]. Full free energy calculations for determining transition rates have been carried out as well as sampling based on dynamical approaches [14–17].

Most of the time, transition state theory is used within the harmonic approximation where the calculations are simplified by approximating the energy surface with a quadratic expansion in the vicinity of the initial state minimum and at a first-order saddle point on the energy ridge separating the initial state from the final state(s). For over-the-barrier transitions, this leads to the widely used harmonic transition state theory expression for the rate constant [18]. The main challenge in such calculations is finding the relevant first-order saddle point(s) and

evaluating the energy there as well as its second derivatives. If both the initial and final states of the transition are known, the minimum energy path on the energy surface connecting the two local energy minima can be found and thereby the first-order saddle point – the highest energy point on that path. The nudged elastic band (NEB) method is commonly used for this task [19–21]. A more challenging task is to find saddle points on the energy ridge given only the initial state minimum. For this, the minimum mode following method can, for example, be used [22,23].

An analogous harmonic approximation to quantum transition state theory has been developed [10–13,24]. It relies on finding special transition paths corresponding to thermally activated tunneling. Such paths are first-order saddle points on an extended quantum mechanical energy surface underlying the statistical properties of Feynman path integrals. These first-order saddle points are often referred to as ‘instantons’. Evaluation of the rate of thermally activated tunneling within instanton theory requires much fewer computations than full quantum transition state theory calculations. Efficient implementations of instanton theory calculations for atomic rearrangements have recently been presented and applied to various chemical reactions [25–27]. Instantons can be found using saddle point search methods, such as the minimum mode following method, or by using a line integral extension of the NEB method.

Much less has been done on quantum mechanical rate theory for magnetic transitions. Most of this work has relied on a mapping of the magnetic system onto a particle system with an effective Hamiltonian, however, this can only be done for certain simple spin systems [28,29]. One such system consists of a single spin with uniaxial anisotropy and a transverse magnetic field [30]. In the particle mapping method, a spin wave function using the \hat{S}_z eigenstates is constructed and then transformed to an eigenvalue equation $\hat{H}|\psi\rangle = E|\psi\rangle$, a Schrödinger equation with an effective potential and possibly coordinate dependent mass. The energy spectrum of the spin system coincides with the first $2j+1$ levels of the corresponding particle system, where j is the quantum number giving the length of the magnetic momentum vector. Thereby, one can use techniques developed for particle systems to study spin systems. This approach, however, is not universal, since a general way to construct the corresponding particle Hamiltonian is not known. In fact, there are no known strategies for systems with multiple spins, as well as for single spin systems with a Hamiltonian containing higher-order terms (cubic and higher) as is often the case in molecular magnets, for example [31,32]. As far as we know, there is only one study based on spin-particle mapping for a two-spin system [33]. Furthermore, the action of the corresponding particle system does not contain a topological term (14) that affects quantum interference in magnetic systems [34–36]. An efficient method for finding instantons for magnetic systems without relying on spin-particle mapping is, therefore, needed.

Interesting results have, nevertheless, been obtained from studies using the spin-particle mapping technique. It has, in particular, been shown that crossover from over-the-barrier to tunneling mechanism can be of two different types, a smooth second-order crossover where the activation energy changes rather gradually and a more abrupt first-order crossover, where the activation energy drops suddenly as temperature is lowered [30]. A general expression has been presented recently for the second-order crossover temperature applicable to any system for which the energy can be evaluated, including self-consistent field calculations [37,38]. The calculations can be carried out based on the second derivatives of the energy at the first-order saddle point. Such an estimate of the crossover temperature can be useful when assessing the lifetime of magnetic states since it shows whether tunneling needs to be taken into account, while classical rate theory would overestimate the lifetime. An estimate of a first-order crossover temperature is more difficult, however, since it cannot be obtained from the vicinity of the first-order saddle point. For this purpose, it is necessary to find the magnetic instantons for the temperature of interest, but we are not aware of such calculations in the literature.

In this article, we present a method for finding instantons representing tunneling in magnetic systems. The formulation is based on the Euclidean action obtained from the coherent state path integral formulation of the partition function. A numerical technique is presented for finding instantons as stationary points of the action. This approach is applied to a system consisting of a single spin with uniaxial anisotropy in the presence of a transverse magnetic field, and a comparison made with results obtained from spin-particle mapping. The approach can in principle be applied to any magnetic system, including multiple spins, as long as the energy of the system can be described by an analytical function.

2. Theoretical background

A brief review of the theoretical background for coherent spin states and the formulation of path integrals and Euclidean action for spin systems is given below for completeness. The reader is referred to the work by Fradkin for more detailed discussion [39]. An alternative derivation has been given by Kochetov [40].

2.1. Coherent spin states

Coherent states are well known in the context of the quantum harmonic oscillator, where they have been used to relate quantum mechanical dynamics as closely as possible to classical dynamics. They are in many cases a useful addition to other descriptions of a quantum mechanical system, but in the case of spins, they are the only known way to develop a path integral representation. The reason is that the Hilbert space of a spin does not have continuously parameterized eigenstates corresponding to classical variables such as coordinates and momenta. For a system with spin j , (for example, the total magnetic moment of an atom) there are $2j + 1$ eigenstates of the \hat{S}_z operator: $\hat{S}_z|\mu, j\rangle = \mu|\mu, j\rangle$, where μ runs from $-j$ to j . They can be used to construct coherent states, $|\hat{\mathbf{n}}\rangle$, that correspond to particular orientation of the spin specified by continuous spherical polar coordinates, θ and ϕ as:

$$|\hat{\mathbf{n}}\rangle = |\theta, \phi\rangle = \sum_{m=-j}^j \sqrt{\frac{(2j)!}{(j+m)!(j-m)!}} \left(\sin \frac{\theta}{2}\right)^{j+m} \left(\cos \frac{\theta}{2}\right)^{j-m} e^{-i(j+m)\phi} |m, j\rangle. \quad (1)$$

The coherent states satisfy the following closure relation:

$$1 = \frac{2j+1}{4\pi} \int d\hat{\mathbf{n}} |\hat{\mathbf{n}}\rangle \langle \hat{\mathbf{n}}|. \quad (2)$$

Matrix elements of the spin operators in terms of coherent states are:

$$\langle \hat{S}_z \rangle = -j + 2j \sin^2 \frac{\theta}{2} = -j \cos \theta, \quad (3)$$

$$\langle \hat{S}_x \rangle = -j \sin \theta \cos \phi, \quad (4)$$

$$\langle \hat{S}_y \rangle = -j \sin \theta \sin \phi.$$

2.2. Path integral representation of the partition function

The partition function for a spin system can be written as:

$$Z = \text{Tr}(e^{-\beta \hat{H}}) = \int d\hat{\mathbf{n}} \langle \hat{\mathbf{n}} | e^{-\beta \hat{H}} | \hat{\mathbf{n}} \rangle. \quad (5)$$

As for Feynman path integrals for particles, the interval β is divided up into N parts:

$$\langle \hat{\mathbf{n}} | e^{-\beta \hat{H}} | \hat{\mathbf{n}} \rangle = \lim_{N \rightarrow \infty} \langle \hat{\mathbf{n}} | \left(1 - \epsilon \hat{H}\right)^N | \hat{\mathbf{n}} \rangle, \quad (6)$$

where $\epsilon = \beta/N$. Then, the resolution of the identity (2) is inserted between the segments of the interval and the expression for the partition function takes the form:

$$Z = \lim_{N \rightarrow \infty} \int \prod_{k=1}^N d\mu(\hat{\mathbf{n}}_k) \langle \hat{\mathbf{n}}_k | \left(1 - \epsilon \hat{H}\right) | \hat{\mathbf{n}}_{k-1} \rangle, \quad (7)$$

where $d\mu(\hat{\mathbf{n}}_k) = \left(\frac{2j+1}{4\pi}\right) d\hat{\mathbf{n}} \delta(\mathbf{n}^2 - 1)$ is the invariant integration measure and $\hat{\mathbf{n}}_0 = \hat{\mathbf{n}}_N$, i.e. periodic boundary conditions are fulfilled.

2.3. Euclidean action

The matrix elements in (7) can be approximated up to quadratic terms as:

$$\begin{aligned} \langle \hat{\mathbf{n}}_k | \left(1 - \epsilon \hat{H}\right) | \hat{\mathbf{n}}_{k-1} \rangle &= \langle \hat{\mathbf{n}}_k | \hat{\mathbf{n}}_{k-1} \rangle \left(1 - \epsilon \frac{\langle \hat{\mathbf{n}}_k | \hat{H} | \hat{\mathbf{n}}_{k-1} \rangle}{\langle \hat{\mathbf{n}}_k | \hat{\mathbf{n}}_{k-1} \rangle}\right) \\ &\simeq \langle \hat{\mathbf{n}}_k | \hat{\mathbf{n}}_{k-1} \rangle \exp\left(-\epsilon \frac{\langle \hat{\mathbf{n}}_k | \hat{H} | \hat{\mathbf{n}}_{k-1} \rangle}{\langle \hat{\mathbf{n}}_k | \hat{\mathbf{n}}_{k-1} \rangle}\right). \end{aligned} \quad (8)$$

The first term in (8) does not equal zero since coherent states are not orthogonal. It leads to an important feature of the spin path integral, a topological phase equivalent to Berry phase [41]. This term can be rewritten as:

$$\langle \hat{\mathbf{n}}_k | \hat{\mathbf{n}}_{k-1} \rangle = 1 - \epsilon \frac{\langle \hat{\mathbf{n}}_k | (|\hat{\mathbf{n}}_k\rangle - |\hat{\mathbf{n}}_{k-1}\rangle) \rangle}{\epsilon} \simeq \exp\left(-\epsilon \frac{\langle \hat{\mathbf{n}}_k | (|\hat{\mathbf{n}}_k\rangle - |\hat{\mathbf{n}}_{k-1}\rangle) \rangle}{\epsilon}\right). \quad (9)$$

which in the limit $\epsilon \rightarrow 0$ gives the path integral expression for the partition function as:

$$Z = \int D[\hat{\mathbf{n}}(\tau)] e^{-S_E}, \quad (10)$$

where the Euclidean action:

$$S_E(\Omega) = \int_0^\beta d\tau \left[\langle \hat{\mathbf{n}} | \frac{\partial}{\partial \tau} | \hat{\mathbf{n}} \rangle + \langle \hat{\mathbf{n}} | \hat{H} | \hat{\mathbf{n}} \rangle \right], \quad (11)$$

is an integral over a closed path $\Omega = (\theta(\tau), \phi(\tau)) \equiv \omega(\tau)$ on the energy surface $E(\omega)$. The integration variable, τ , can be interpreted as imaginary time.

The first term in the integrand can be rewritten using the expression for the coherent states, (1), as:

$$\langle \hat{\mathbf{n}} | = \sum_{p=0}^{2j} \sqrt{\frac{(2j)!}{p!(2j-p)!}} \left(\cos \frac{\theta}{2} \right)^{2j} \left(\tan \frac{\theta}{2} \right)^p e^{ip\phi} \langle -j+p, j |, \quad (12)$$

$$\begin{aligned} \left| \frac{\partial \hat{\mathbf{n}}}{\partial \tau} \right\rangle = \sum_{p=0}^{2j} \sqrt{\frac{(2j)!}{p!(2j-p)!}} \left(\cos \frac{\theta}{2} \right)^{2j} \left(\tan \frac{\theta}{2} \right)^p e^{-ip\phi} \\ \left[\left(p \csc \theta - j \tan \frac{\theta}{2} \right) \dot{\theta} - ip\dot{\phi} \right] | -j+p, j \rangle, \end{aligned} \quad (13)$$

and

$$\langle \hat{\mathbf{n}} | \frac{\partial}{\partial \tau} | \hat{\mathbf{n}} \rangle = -j \tan \frac{\theta}{2} \dot{\theta} + j \tan \frac{\theta}{2} \dot{\theta} - ij(1 - \cos \theta) \dot{\phi} = -ij(1 - \cos \theta) \dot{\phi}. \quad (14)$$

Hence, the partition function (10) affords the phase:

$$\begin{aligned} \exp \left(\int_0^\beta d\tau \langle \hat{\mathbf{n}} | \frac{\partial}{\partial \tau} | \hat{\mathbf{n}} \rangle \right) &= \exp \left(-ij \int_0^\beta d\tau (1 - \cos \theta) \dot{\phi} \right) \\ &= \exp \left(-ij \int_\Gamma (1 - \cos \theta) d\phi \right), \end{aligned} \quad (15)$$

where Γ is a closed path described by the vector $\hat{\mathbf{n}} = \{\theta(\tau), \phi(\tau)\}$. This term has a geometric interpretation. It is proportional to the area bounded by the curve Γ .

The final expression for the Euclidean action of a system with a spin j can be written as:

$$S[\Omega] = \int_{-\beta/2}^{\beta/2} d\tau \left[-ij(1 - \cos \theta) \dot{\phi} + E(\omega) \right]. \quad (16)$$

2.4. Instantons

Instantons are stationary paths for (16), i.e. they correspond to $\delta S = 0$. Differentiation gives the equations of motion:

$$\begin{aligned} \dot{\theta} &= \frac{i}{j \sin \theta} \frac{\partial E}{\partial \phi}, \\ \dot{\phi} &= -\frac{i}{j \sin \theta} \frac{\partial E}{\partial \theta}, \end{aligned} \quad (17)$$

where θ and ϕ satisfy the boundary condition $\Omega(0) = \Omega(\beta)$. These are the Landau-Lifshitz equations for spin dynamics in imaginary time.

These equations of motion have two types of solutions. The first type corresponds simply to a stationary point on the energy surface, $\Omega = \omega_0$, with energy $E(\omega_0)$. This can, in particular, be the first-order saddle point on the energy surface $\omega^\dagger = (\theta^\dagger, \phi^\dagger)$. The corresponding action is:

$$S_{jump} = \beta E(\omega^\dagger) = \beta E^\dagger. \quad (18)$$

This solution characterizes the classical over-the-barrier transition mechanism which dominates at high enough temperature.

The second type of solutions are extended closed paths, so-called instantons. They correspond to tunneling between two potential wells. In the limit of zero temperature $T \rightarrow 0$, i.e. $\beta \rightarrow \infty$, the instanton corresponds to tunneling from the ground state, but at finite temperature, it corresponds to thermally assisted tunneling. An instanton is a trajectory in imaginary time that conserves energy (analogous to Landau–Lifshitz dynamics in real time) as can be shown by taking the time derivative of E and inserting into (17). This gives:

$$\frac{dE}{d\tau} = \frac{\partial E}{\partial \theta} \dot{\theta} + \frac{\partial E}{\partial \phi} \dot{\phi} = \frac{i}{j \sin \theta} \frac{\partial E}{\partial \phi} \frac{\partial E}{\partial \theta} - \frac{i}{j \sin \theta} \frac{\partial E}{\partial \theta} \frac{\partial E}{\partial \phi} = 0. \quad (19)$$

In contrast to particle systems, magnetic systems have no kinetic energy. As a result, in order to find paths that satisfy the boundary conditions and solve (17), it is necessary to analytically continue the function $E(\omega)$ to allow for complex values of the angles, ω .

3. Method for finding magnetic instantons

This section describes the method we have developed for finding instantons for magnetic transitions. Since the instanton corresponds to a stationary point of the action, it corresponds to a periodic orbit described by Landau–Lifshitz equations in imaginary time. As the dynamics conserve energy, the instantons lie on equienergy contours. The first step is, therefore, to identify the contour for a given value of the energy. In order to map out the dependence on temperature, the calculations need to be carried out for a grid of energy values in the interval from the initial state minimum to the first-order saddle point. Once the energy contour has been identified and represented by a set of discretization points, the corresponding temperature is estimated by evaluating the period of the Landau–Lifshitz dynamics along the closed contour. The distribution of the discretization points along the energy contour as well as a refinement of the value of the energy is then carried out using iterative zeroing of the derivatives of the action. The resulting distribution of discretization points then represents an instanton for the given temperature.

3.1. Energy contours

The method for finding and representing energy contours with an even distribution of discretization points is essentially the one previously presented by Einarsdóttir *et al.* [26]. This procedure is a modification of the NEB method [19,20]. The contour is represented with a set of discretization points, $k = \{1, N\}$. Each point corresponds to a configuration of the system, i.e. a value of all variables, ω_k . For a system with a single magnetic moment, $\omega_k = (\theta_k, \phi_k)$. More generally, for systems with more than one magnetic moment, ω_k is a vector with values of θ and ϕ for each one of the magnetic moments. For simplicity, the presentation here will be for a system with a single magnetic moment, but it can be generalized easily. In order to find non-trivial instantons, the angles need to be able to have complex values so a configuration can be written as $\omega_k = (\theta_k^R, \theta_k^I, \phi_k^R, \phi_k^I)$. The energy of the system is some known function of the orientation, $E(\omega)$, analytically continued to the complex plane.

In order to find the energy contour corresponding to some particular value of the energy, E' , an objective function, S^{iso} , is defined as the sum of quadratic deviations of the energy:

$$S^{iso}(\omega_1, \dots, \omega_N) = \frac{1}{2} \sum_{k=0}^N |E(\omega_k) - E'|^2. \quad (20)$$

Given some initial distribution of the discretization points, an iterative algorithm is used to converge on the energy contour corresponding to energy E' . The iterative algorithm is based on zeroing the derivatives of S^{iso} with respect to the variables.

The negative gradient of the objective function with respect to the variables ω_k :

$$g_k = -\nabla_k S^{iso} = -(E(\omega_k) - E') \nabla_k E(\omega_k), \quad (21)$$

gives the direction of steepest descent for discretization point k . It represents a force acting on the discretization point that can be used to move it towards the energy contour. As in the NEB method, the displacements of the discretization point parallel and perpendicular to the path are treated separately. A tangent to the path, \hat{t}_k , described by the current location of discretization points is evaluated as in the NEB method [42]. It is used to distinguish between displacements that represent changes in the shape of the path and displacements that are related to the distribution of the discretization points along the path. The component of the gradient representing a change in the shape of the path is given by the force component perpendicular to the path:

$$g_k^\perp = g_k - (g_k \cdot \hat{t}_k) \hat{t}_k. \quad (22)$$

An even distribution of the discretization points along the path is obtained by including a spring force between adjacent images in the direction parallel to the tangent:

$$g_k^{sp} = (k_{sp}(|\omega_{k+1} - \omega_k| - |\omega_k - \omega_{k-1}|)) \hat{t}_k, \quad (23)$$

where k_{sp} is a spring force chosen in such a way that g_k^{sp} is roughly of the same magnitude as g_k^\perp .

The total force acting on each discretization point is then:

$$g_k^{opt} = g_k^\perp + g_k^{sp}. \quad (24)$$

A minimization procedure based on the velocity Verlet algorithm is then used to move all the discretization points simultaneously in the direction given by the total force, analogous to what is often done in NEB calculations of minimum energy paths [20].

Figure 1 shows an example calculation where an energy contour is found using the algorithm described above. First, the discretization points are arranged arbitrarily in a circle. Then, they are moved iteratively in the direction of g_k^{opt} until an even distribution is obtained on the desired energy contour. This is an arbitrary test case where the energy surface is generated by adding up a few Gaussians for illustration purposes only.

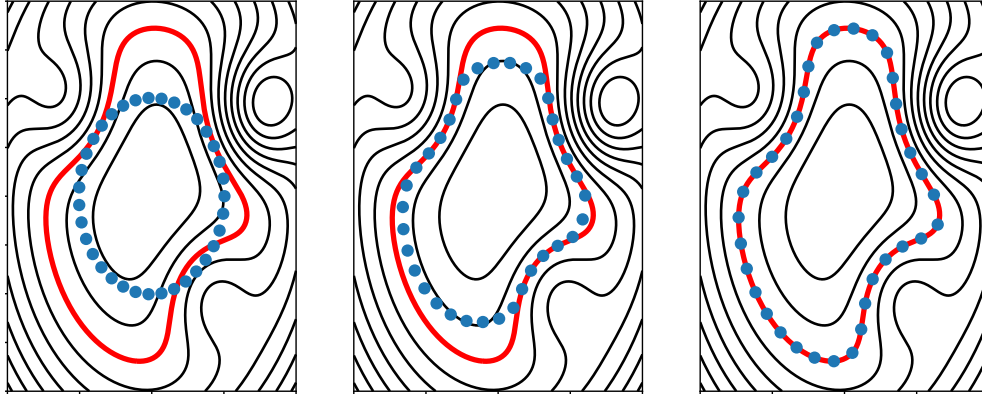


FIG. 1. Illustration of the method for finding and representing an energy contour of a model energy surface. The target contour is shown by the bold red line. Starting with a discrete representation of a circle in configuration space (left), the iterative algorithm moves the discretization points towards the specified energy contour (middle) and eventually converges on it (right).

3.2. Temperature estimate

Given an even distribution of discretization points along an energy contour, the next task is to estimate what temperature an instanton on this energy contour would correspond to. For this purpose, an approximate Landau–Lifshitz dynamics calculation is carried out to estimate the imaginary time it takes to go from one discretization point to another. From the total time it takes to go along the full path, the period, τ , can be estimated, and then the temperature as $T = 1/\tau$.

Let the closed path described by the set of N discretization points be denoted as $\Omega^{iso} = \{\omega_1^{iso}, \omega_2^{iso} \dots \omega_N^{iso}\}$. The time it takes to go from one discretization point to another can be estimated as:

$$\Delta\tau_i = \frac{|v_i|}{|d_i|}, \quad (25)$$

where the distance between the two points is $|d_i| = |\omega_{i+1}^{iso} - \omega_i^{iso}|$ and the velocity can be estimated from Landau–Lifshitz equations as:

$$v_i = \begin{pmatrix} \frac{i}{j \sin \theta_i} \frac{\partial E}{\partial \phi_i} \\ -\frac{i}{j \sin \theta_i} \frac{\partial E}{\partial \theta_i} \end{pmatrix}. \quad (26)$$

Recall that θ and ϕ are complex variables. The total time period corresponding to the closed path along the contour is:

$$\tau = \sum_{i=1}^N \Delta\tau_i. \quad (27)$$

This approximate calculation gives an estimate of the instanton temperature associated with the given energy contour. The even distribution of the discretization points along the contour and the temperature estimate are subsequently used as initial conditions for a calculation where an accurate distribution of the discretization points corresponding to an instanton is found, as well as a revised value of the energy for which the obtained temperature value corresponds more closely. This refinement is described in the following section.

3.3. Refinement of discretization points and energy

Given the even distribution of discretization points along an energy contour and the value of the temperature obtained as described above, a refinement calculation is carried out where the temperature is kept fixed but the distribution of the discretization points and the value of the energy are refined so as to converge on a stationary point of the action. This is done by zeroing the derivatives of the action with respect to all variables describing the path, $\Omega = \{\omega_1, \omega_2 \dots \omega_N\}$.

The scaled action, $\tilde{S} \equiv \beta S(\Omega)$, is approximated using the set of N discretization points:

$$\tilde{S}(\Omega) = \sum_{k=1}^N \left[k(T) \left(1 - \frac{\cos \theta_k + \cos \theta_{k+1}}{2} \right) (\phi_{k+1} - \phi_k) + \frac{E(\theta_k, \phi_k) + E(\theta_{k+1}, \phi_{k+1})}{2N} \right], \quad (28)$$

where $k(T) = -ijTk_B$. The task is to find a stationary point of the function \tilde{S} for a given value of T , that is, to solve the system of differential equations:

$$\begin{aligned} \frac{\partial \tilde{S}}{\partial \theta_k} &= \frac{1}{2} k(T) \sin \theta_k (\phi_{k+1} - \phi_{k-1}) + \frac{\partial E}{\partial \theta_k} = 0, \\ \frac{\partial \tilde{S}}{\partial \phi_k} &= \frac{1}{2} k(T) (\cos \theta_{k+1} - \cos \theta_{k-1}) + \frac{\partial E}{\partial \phi_k} = 0, \quad k \in [1, N]. \end{aligned} \quad (29)$$

Since the action is complex, it is convenient here to define a real objective function, $F(\Omega)$, by summing up the magnitude squared of the derivatives of \tilde{S} with respect to all the variables. The minimum value of F is zero and corresponds to a stationary point of the action. Standard minimization techniques can be applied to find the minimum of F since it is a real function.

We first define the vector function $f(\tilde{\Omega})$ as:

$$f(\Omega) = \begin{pmatrix} \frac{\partial S(\Omega)}{\partial \theta_1} \\ \vdots \\ \frac{\partial S(\Omega)}{\partial \phi_N} \end{pmatrix}, \quad (30)$$

the objective function can be written as the squared norm of $f(\Omega)$:

$$F(\Omega) \equiv \frac{1}{2} \bar{f}(\Omega) \cdot f(\Omega). \quad (31)$$

The task is to find the N discretization points that give $F(\Omega) = 0$ for the given temperature value (obtained as described in the previous section). Since the temperature estimate does not correspond exactly to the energy contour initially chosen, the discretization points will converge on a slightly different energy contour and their distribution will not be uniform.

The BFGS algorithm is used for the iterative minimization of F . It is important to start with the discretization points located on a contour of roughly the right energy to avoid converging on the trivial solution where the discretization points are all at the same location (the classical limit).

The BFGS algorithm requires the first derivatives of F with respect to all the variables. These, in turn, involve the second derivatives of \tilde{S} :

$$\left\{ \begin{array}{l} \frac{\partial F}{\partial \theta_j^R} = \sum_{k=1}^N \Re \frac{\partial \tilde{S}}{\partial \theta_k} \Re \frac{\partial^2 \tilde{S}}{\partial \theta_k \partial \theta_j} + \Im \frac{\partial \tilde{S}}{\partial \theta_k} \Im \frac{\partial^2 \tilde{S}}{\partial \theta_k \partial \theta_j} + \Re \frac{\partial \tilde{S}}{\partial \phi_k} \Re \frac{\partial^2 \tilde{S}}{\partial \phi_k \partial \theta_j} + \Im \frac{\partial \tilde{S}}{\partial \phi_k} \Im \frac{\partial^2 \tilde{S}}{\partial \phi_k \partial \theta_j}, \\ \frac{\partial F}{\partial \theta_j^I} = \sum_{k=1}^N \Im \frac{\partial \tilde{S}}{\partial \theta_k} \Re \frac{\partial^2 \tilde{S}}{\partial \theta_k \partial \theta_j} - \Re \frac{\partial \tilde{S}}{\partial \theta_k} \Im \frac{\partial^2 \tilde{S}}{\partial \theta_k \partial \theta_j} + \Im \frac{\partial \tilde{S}}{\partial \phi_k} \Re \frac{\partial^2 \tilde{S}}{\partial \phi_k \partial \theta_j} - \Re \frac{\partial \tilde{S}}{\partial \phi_k} \Im \frac{\partial^2 \tilde{S}}{\partial \phi_k \partial \theta_j}, \\ \frac{\partial F}{\partial \phi_j^R} = \sum_{k=1}^N \Re \frac{\partial \tilde{S}}{\partial \theta_k} \Re \frac{\partial^2 \tilde{S}}{\partial \theta_k \partial \phi_j} + \Im \frac{\partial \tilde{S}}{\partial \theta_k} \Im \frac{\partial^2 \tilde{S}}{\partial \theta_k \partial \phi_j} + \Re \frac{\partial \tilde{S}}{\partial \phi_k} \Re \frac{\partial^2 \tilde{S}}{\partial \phi_k \partial \phi_j} + \Im \frac{\partial \tilde{S}}{\partial \phi_k} \Im \frac{\partial^2 \tilde{S}}{\partial \phi_k \partial \phi_j}, \\ \frac{\partial F}{\partial \phi_j^I} = \sum_{k=1}^N \Im \frac{\partial \tilde{S}}{\partial \theta_k} \Re \frac{\partial^2 \tilde{S}}{\partial \theta_k \partial \phi_j} - \Re \frac{\partial \tilde{S}}{\partial \theta_k} \Im \frac{\partial^2 \tilde{S}}{\partial \theta_k \partial \phi_j} + \Im \frac{\partial \tilde{S}}{\partial \phi_k} \Re \frac{\partial^2 \tilde{S}}{\partial \phi_k \partial \phi_j} - \Re \frac{\partial \tilde{S}}{\partial \phi_k} \Im \frac{\partial^2 \tilde{S}}{\partial \phi_k \partial \phi_j}, \end{array} \right. \quad \forall j \in [1, N]. \quad (32)$$

4. Model

The methodology described above is applied to a uniaxial spin in transverse magnetic field. The anisotropy axis is taken to be the z -axis and the applied field is pointing along the x -axis. The Hamiltonian of the system is:

$$\hat{H} = D\hat{S}_z^2 + B\hat{S}_x, \quad (33)$$

where D is the anisotropy constant and B the strength of the field.

The corresponding energy surface is:

$$E(\theta, \phi) = Dj^2 \cos^2 \theta + Bj \sin \theta \cos \phi + Dj^2 + \frac{B^2}{4D}. \quad (34)$$

The energy is shifted here by the constant $Dj^2 + B^2/4D$ to set the minimum energy of the system to zero.

This system has been studied by Chudnovsky using the particle mapping technique [30]. For small field, $B < 0.5Dj$, the crossover from over-the-barrier mechanism to tunneling is first-order, while it is second-order for larger field. The second-order crossover temperature can be obtained from the second derivatives of the energy at the first-order saddle point on the energy surface [37,38,43]. The expression is [43]:

$$T_{(2)} = \frac{B(2Dj - B)}{2\pi k_B}. \quad (35)$$

The temperature for the first-order crossover can, however, only be found from calculations of the instantons, as illustrated below.

For convenience, the energy function is rather written in terms of dimensionless quantities:

$$\tilde{E}(\theta, \phi) = -\cos^2 \theta - 2h_x \sin \theta \cos \phi + 1 + h_x^2, \quad (36)$$

where $\tilde{E} = Dj^2 E$ is the scaled energy and $h_x = B/2Dj$ is the scaled field strength.

The energy surface is shown in Fig. 2 for two values of the scaled field, $h_x = 0.50$ and 0.05 . The two minima corresponding to the ground states of the system as well as the minimum energy path connecting them are located at $\phi = 0$. The larger the field, the further away the minima are from the anisotropy axis.

The analytical continuation to complex angles is:

$$\tilde{E}(\theta, \phi) = -\cos^2(\theta^R + i\theta^I) - 2h_x \sin(\theta^R + i\theta^I) \cos(\phi^R + i\phi^I) \quad (37)$$

where θ^R and ϕ^R are the real parts and θ^I and ϕ^I are the imaginary parts of the angular variables.

5. Results

Figure 3 shows calculated instantons for an applied field of $h_x = 0.50$ and 0.05 . It turns out that $\phi^R = \theta^I = 0$ for all these instantons and the energy is real:

$$\tilde{E} = E = -\cos^2(\theta^R) - 2h_x \sin(\theta^R) \cosh(\phi^I), \quad (38)$$

so the instantons can be visualized in the (θ^R, ϕ^I) plane. For higher temperature values, the replicas are nearly equally distributed along the equipotential contours. But, for the lowest temperature, the distribution is distinctly uneven, with larger density of discretization points near the extreme values of θ^R .

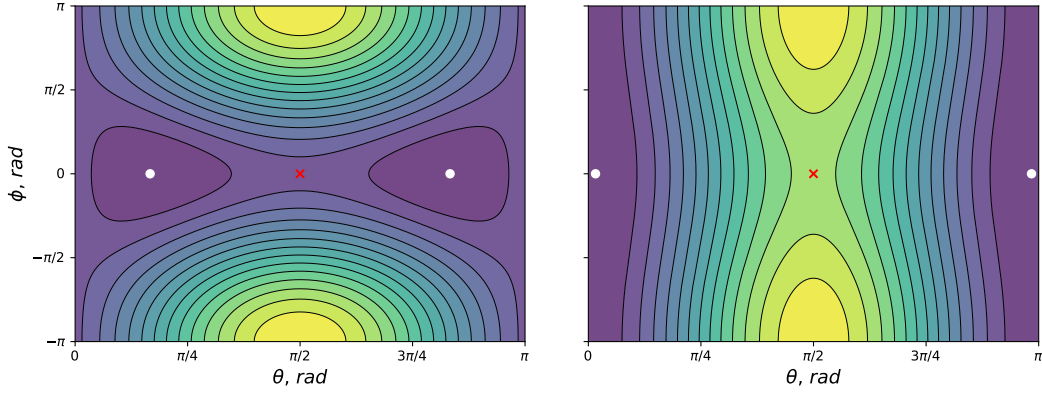


FIG. 2. The energy surface of a system with a single spin subject to anisotropy along the z -axis and an applied magnetic field in x -direction of magnitude $h_x = B/2Dj = 0.50$ (left) and $h_x = 0.05$ (right), see eqn. (34). The local minima corresponding to initial and final states are marked with a white \times . For the weaker field, they are located closer to the anisotropy axis. The minimum energy path for the transition is a straight line at $\phi = 0$ between the minima. The maximum along the minimum energy path, a first-order saddle point on the energy surface, is marked with a red \times .

The temperature corresponding to each of the instantons is given in the legend of Fig. 3. The classical first-order saddle point on the energy surface appears as a maximum in this plane. An instanton corresponding to a slightly lower energy contour has all discretization points at nearly the same location, as the path just barely opens up. The corresponding temperature is denoted as $T_{(2)}$ (1.592 K for the higher field, 0.694 K for the lower field).

Instantons on lower energy contours correspond to lower temperatures in the high field case. There is a monotonic decrease in the temperature as the energy is decreased. This behavior can be seen for the high field case in Fig. 4. The crossover from over-the-barrier mechanism to tunneling then occurs at a temperature of $T_{(2)}$ and this is referred to as second-order crossover. The relevant instantons for the onset of tunneling appear at an energy just below E^\dagger and correspond to an energy contour lying in the vicinity of the classical first-order saddle point on the real energy surface. There is a continuous transition from over-the-barrier to tunneling mechanism. The value of $T_{(2)}$ can be obtained from the second derivatives of the energy at the saddle point [37,38]. In the limit of zero energy, the temperature approaches zero and the instanton lies on the energy contour that goes through the initial and final state minima.

For the low field case, $h_x = 0.05$, the situation is different. From Fig. 3, it can be seen that the shapes of the instantons are quite different from the high field case. The change in the instanton temperature as the energy is lowered from the saddle point energy is non-monotonic. The temperature first increases as the energy is decreased, reaching a maximum at a value T_m (see Fig. 4) and then decreases, but eventually reaches zero at the energy of the initial state minimum. Two of the instantons shown in Fig. 3 for the low field case have a temperature that is higher than $T_{(2)}$. Even though the instantons are more spread out, and the corresponding periodic orbits longer, the imaginary time period is shorter. Apparently, this is related to the long vertical segments that can be seen in Fig. 3 for the instantons in low field. There, the partial derivative of the energy with respect to θ^R is large and the acceleration in ϕ^I given by the Landau-Lifshitz equations has a correspondingly large magnitude.

Figure 5 compares the exponents of the Boltzmann factors for the two mechanisms: over-the-barrier, $E^\dagger/k_B T$, and tunneling, $S_{ins}/k_B T$. The smaller this exponent is, the larger the transition rate. For the large field case, $h_x = 0.50$, a smaller exponent is obtained for tunneling as the temperature drops below $T_{(2)}$, consistent with a second-order crossover from over-the-barrier to tunneling mechanism. After a slight increase in the value of $S_{ins}/k_B T$ as the temperature is lowered below $T_{(2)}$, it remains relatively independent of temperature.

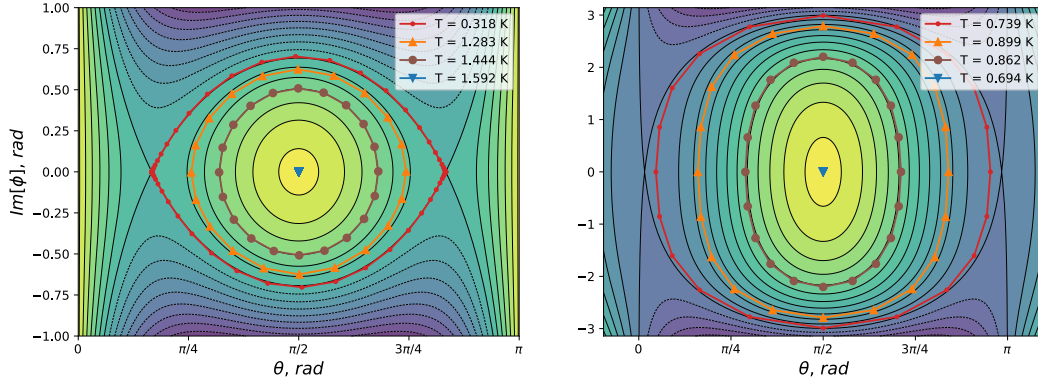


FIG. 3. Analytically continued energy surface in (θ^R, ϕ^I) plane for field strength of $h_x = B/2Dj = 0.50$ (left) and 0.05 (right). For the system studied here, the instantons are at $\Re\phi = 0$ and $\Im\theta = 0$ so it is sufficient to show them in the $(\Im\phi, \Re\theta)$ plane. Instantons for various energy contours are shown (red, orange, brown and blue lines with dots, upper triangles, and filled circles indicating the location of the discretization points) and the corresponding values of the temperature are given in the legend. The blue instantons are near the first-order saddle point on the real energy surface, corresponding to over-the-barrier mechanism and temperature close to the second-order crossover temperature, $T_{(2)}$. For the stronger field, $h_x = 0.50$, the lower energy and more extended instantons correspond to longer period for the periodic orbit and lower temperature. The crossover from over-the-barrier mechanism to tunneling is second-order. For the weaker field, $h_x = 0.05$, the period decreases and the temperature increases as the energy is lowered from the value at the first-order saddle point until a maximum is reached (notice the high temperature associated with the brown curve with circles). The crossover is first-order and occurs at a temperature $T_{(1)}$ that is higher than $T_{(2)}$.

For the small field case, $h_x = 0.05$, the instantons on energy contours just below the saddle point energy turn out to have a larger Boltzmann exponent than over-the-barrier transitions so they do not lead to crossover to tunneling. The instanton temperature continues to increase as the energy of the contour is lowered until a maximum value is obtained at T_m . Further lowering of the energy then gives a second set of instantons for each temperature value between $T_{(2)}$ and T_m . The Boltzmann exponent for these instantons is smaller and at a certain temperature, $T_{(1)}$, an instanton has the same value of the exponent as the over-the-barrier mechanism, indicating a crossover to tunneling (see Fig. 5). The stationary point of the action that gives the fastest transition rate then changes abruptly from the classical saddle point to an instanton that has significantly lower energy.

Since the first-order crossover corresponds to an instanton that is far removed from the first-order saddle point on the energy surface, it is not possible to estimate $T_{(1)}$ from the energy and its derivatives at the saddle point, as can be done for second-order crossover. Identification of first-order crossover to tunneling requires the evaluation of instantons over the relevant energy range from $E = 0$ to E^\dagger .

The difference between first and second-order crossover can be seen from calculations carried out at and slightly below the critical field, $h_x = B/2Dj = 0.25$, as shown in Fig. 6. The second-order crossover is characterized by a monotonic decrease of the instanton temperature as the energy decreases. On the other hand, the first-order crossover is characterized by non-monotonic behavior. Over a certain range in temperature, instantons on two different energy contours correspond to the same value of the temperature. The instanton lying on the lower energy contour corresponds to a smaller exponent in the Boltzmann factor and therefore higher tunneling rate.

The critical value of $h_x = 0.25$ between first- and second-order crossover had previously been determined for this system by Chudnovsky using the particle mapping technique [30]. The calculations presented here of finite temperature instantons are clearly in good agreement with this previous estimate.

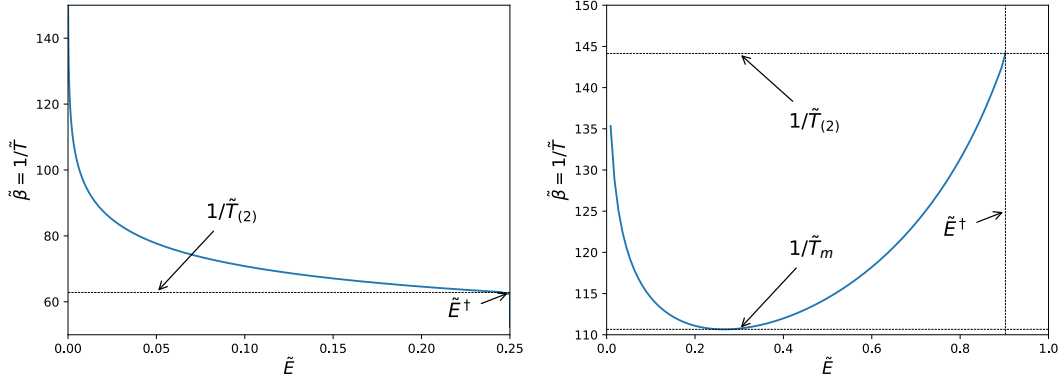


FIG. 4. Inverse scaled temperature, $1/\tilde{T} = 2Dj/Tk_B$, found from the period of Landau-Lifshitz orbits in imaginary time vs. scaled energy, $\tilde{E} = Dj^2E$, of the contour where the instanton lies for field strength of $h_x = B/2Dj = 0.50$ (left) and 0.05 (right). \tilde{E}^\dagger is the scaled energy of the first-order saddle point on the energy surface corresponding to the activation energy of the classical over-the-barrier mechanism. $\tilde{T}_{(2)}$ is the scaled temperature for an instanton at an energy contour just below \tilde{E}^\dagger . For strong field, $h_x = 0.50$, this is the highest instanton temperature and a second-order crossover to tunneling occurs there. For weak field, $h_x = 0.05$, the crossover is first-order and the instanton involved is not located near the saddle point. There, the instanton temperature increases as the energy is lowered from \tilde{E}^\dagger and reaches a maximum of \tilde{T}_m for an energy that is intermediate between that of the initial state and the first-order saddle point. The crossover temperature turns out to be higher than $\tilde{T}_{(2)}$ in this case (see Fig. 5).

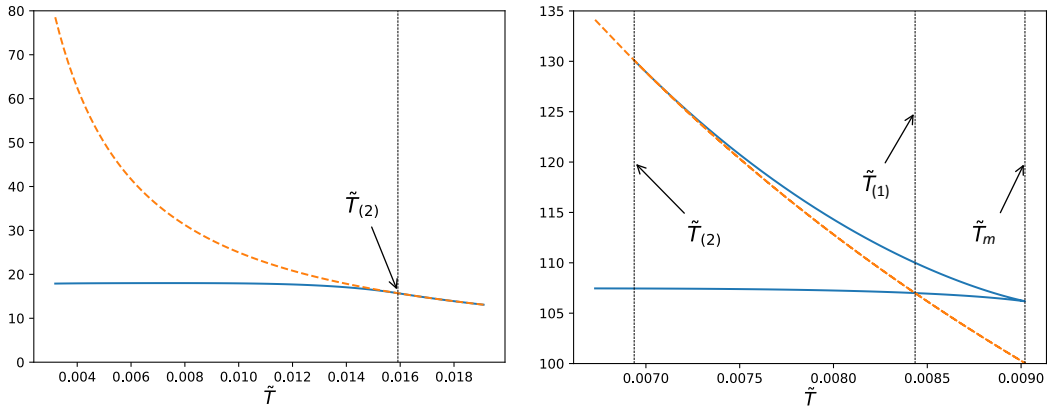


FIG. 5. Exponents of the Boltzmann factor, $S_{ins}/k_B T$ for instantons (blue curve) and $E^\dagger/k_B T$ for over-the-barrier mechanism (dashed orange curve), as a function of scaled temperature, $\tilde{T} = Tk_B/2Dj$, for field strength of $h_x = B/2Dj = 0.50$ (left) and 0.05 (right). For strong field, the highest temperature instanton is obtained for energy contour just below the saddle point energy and the crossover temperature, $T_{(2)}$, can be deduced from the second derivatives of the energy at the saddle point [37, 38]. For weak field values, the instanton temperature increases as the energy is lowered from the saddle point energy and the Boltzmann exponent for those instantons is larger than for over-the-barrier transitions. After reaching a maximum at T_m , the instanton temperature decreases as the contour energy is lowered and at a temperature of $T_{(1)}$ the exponent for the instanton equals that of the over-the-barrier mechanism indicating a first-order crossover to tunneling.

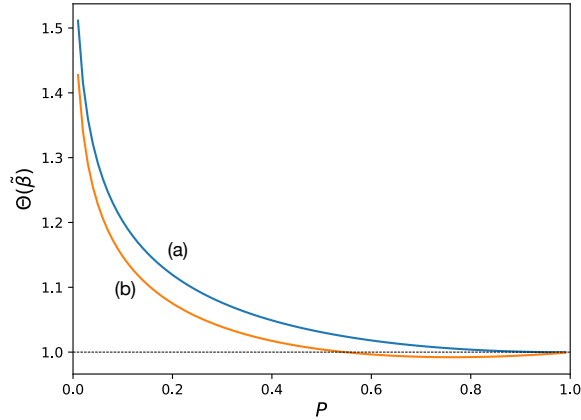


FIG. 6. Illustration of the change from first-order to second-order crossover to tunneling as the applied field is increased from $h_x = B/2Dj = 0.20$ (orange line (b)) to 0.25 (blue line (a)). Scaled inverse temperature $\Theta = T_c/T$ is shown as a function of scaled energy $P = E/E^\dagger$. The instanton temperature is a monotone function of the energy when the the crossover to tunneling is second-order. When the crossover is first-order, the temperature corresponding to the instantons first increases as the energy of the contour is lowered below E^\dagger , but then decreases for even lower energy.

6. Discussion

A method is presented for finding instantons corresponding to tunneling between magnetic states at finite temperature. The method is based on analytical continuation of the energy of the system to complex angular variables and identification of an energy contour, followed by evaluation of the corresponding temperature and finally refinement of the distribution of discretization points to converge on a stationary point of the action. This method takes advantage of the fact that the Landau–Lifshitz equations of motion for spin systems conserve energy. Since the instanton corresponds to a stationary point of the action, it also corresponds to a periodic orbit along an energy contour. The refinement is based on local minimization of the magnitude of the gradients of the action with respect to the degrees of freedom in the system. Since a good initial guess for this iterative refinement procedure can be obtained from an even distribution of discretization points along the energy contour, such a local minimization most likely will converge on the appropriate instanton, rather than some other stationary point of the action.

This method is quite different from the ones used to find instantons for atomic rearrangements [25,26] where the equations of motion conserve the total energy, i.e. kinetic plus potential energy. In some sense, it is easier to find instantons for magnetic systems since their shape can so clearly be identified on the energy surface. The additional complication, however, lies in the analytical continuation of the energy expression to allow for complex values of the angular variables. While this is relatively straightforward when the energy of the system is given by an analytical expression, it is not clear how to approach this problem when self-consistent calculations (such as the non-collinear Alexander–Andersson model [44]) are used to evaluate the energy.

By finding the instantons as a function of temperature, the crossover temperature for both first-order and second-order crossover can be estimated. Previously, a general expression for the second-order crossover temperature based on second derivatives of the energy at the first-order saddle point on the energy surface had been presented [37,38], however, calculation of the first-order crossover temperature is more challenging because it does not relate directly to the first-order saddle point. There is not a continuous transition from the over-the-barrier to tunneling mechanism in that case. By finding the instantons, however, the first-order case can be treated.

The method has been illustrated here with an application to a system with a single spin. It is, however, easily generalized to systems with an arbitrary number of spins. The method for finding the energy contour, an extension

of the NEB method which is routinely used for multidimensional systems, the Landau–Lifshitz dynamics and the BFGS minimization of the magnitude of the gradient of the action can all be carried out in a straightforward way for many degrees of freedom. We anticipate that tunneling of, for example, magnetic skyrmions and other localized non-collinear states can be studied with the technique presented here.

Acknowledgements

We thank Igor Lobanov for helpful discussions. This work was supported by the Icelandic Research Fund, the Academy of Finland (grant 278260) and the Government of the Russian Federation (grant 074U01).

Appendix

Then, as in the NEB algorithm, using some iterative procedure of minimization, like steepest descent, conjugate gradients method and etc., all the points Ω_k will be displaced simultaneously at each iteration. The example of searching an isocontour $f(x, y) = 4.5$ for the function

$$f(x, y) = \frac{1}{2}(k_x x^2 + k_y y^2) + \sum_{i=1}^3 b_i e^{-a((x-x_i)^2+(y-y_i)^2)} \quad (39)$$

using equations (20) and (24) is shown in Fig. 1. The parameters from (39) are shown in Table. 1.

TABLE 1. Parameters used for the test example.

$x_1 = 1.5$	$y_1 = 0.9$	$b_1 = 10$
$x_2 = 0.8$	$y_2 = -1$	$b_2 = 5$
$x_3 = -1.2$	$y_3 = 1$	$b_3 = 6$

References

- [1] Wigner E. The transition state method. *Trans. Faraday Soc.*, 1938, **34**, P. 29–41.
- [2] Kramers H. A. Brownian motion in a field of force and the diffusion model of chemical reactions. *Physica*, 1940, **7**(4), P. 284–304.
- [3] Langer J. S. Statistical theory of the decay of metastable states. *Ann. Phys.*, 1969, **54**, P. 258–275.
- [4] Braun H.-B. Kramers’s rate theory, broken symmetries and magnetization reversal. *J. Appl. Physics*, 1994, **76**, P. 6310–6315.
- [5] Coffey W. T., Garanin D. A. and McCarthy D. J. Crossover formulas in the Kramers theory of thermally activated escape rates-application to spin systems. *Adv. Chem. Phys.*, 2001, **117**, P. 483–765.
- [6] Fiedler G., Fidler J., Lee J., Schrefl T., Stamps R. L., Braun H. B., Suess D. Direct calculation of the attempt frequency of magnetic structures using the finite element method. *J. Appl. Phys.*, 2012, **111**(9), P. 093917(7 pp.)
- [7] Bessarab P. F., Uzdin V. M. and Jónsson H. Harmonic Transition State Theory of Thermal Spin Transitions. *Phys. Rev. B*, 2012, **85**, P. 184409(4 pp.)
- [8] Bessarab P. F., Uzdin V. M. and Jónsson H. Potential Energy Surfaces and Rates of Spin Transitions. *Z. Phys. Chem.*, 2013, **227**, P. 1543–1557.
- [9] Feynman R. P., Hibbs A. R. *Quantum Mechanics and Path Integrals*. McGraw-Hill, NY, 1965.
- [10] Miller W. H. Semiclassical limit of quantum mechanical transition state theory for nonseparable systems. *J. Chem. Phys.*, 1975, **62**, P. 1899–1906.
- [11] Coleman S. Fate of the false vacuum: Semiclassical theory *Phys. Rev. D*, 1977, **15**, P. 2929–2936.
- [12] Callan C., Coleman S. Fate of the false vacuum. II. First quantum corrections. *Phys. Rev. D*, 1977, **16**, P. 1762–1768.
- [13] Benderskii V. A., Makarov D. E., Wight C. A. *Chemical dynamics at low temperatures*, John Wiley & Sons, New York, 1994.
- [14] Mills G., Schenter G. K., Makarov D. E. and Jónsson H. Generalized path integral based quantum transition state theory. *Chem. Phys. Letters*, 1997, **278**, P. 91–96.
- [15] Mills G., Schenter G. K., Makarov D. E., and Jónsson H. RAW quantum transition state theory. in *Classical and Quantum Dynamics in Condensed Phase Simulations*, edited by Berne B. J., Ciccotti G., and Coker D. F., World Scientific, 1998, P. 405–421.
- [16] Craig I. R., Manolopoulos D. E. *J. Chem. Phys.*, 2005, **123**, P. 034102.
- [17] Habershon S., Manolopoulos D. E., Markland T. E. and Miller III T. F. *Annu. Rev. Phys. Chem.*, 2013, **64**, P. 387–413.
- [18] Vineyard G. H. Frequency factors and isotope effects in solid state rate processes. *J. Phys. Chem. Solids*, 1957, **3**(1), P. 121–127.
- [19] Mills G., Jónsson H., and Schenter G. K. Reversible work based transition state theory: application to H₂ dissociative adsorption. *Surf. Sci.*, 1995, **324**, P. 305–337.
- [20] Jónsson H., Mills G., and Jacobsen K. W., “Nudged elastic band method for finding minimum energy paths of transitions,” in *Classical and Quantum Dynamics in Condensed Phase Simulations*, edited by Berne B. J., Ciccotti G., and Coker D. F., World Scientific, 1998, P. 385–404.
- [21] Bessarab P. F., Uzdin V. M. and Jónsson H. Method for finding mechanism and activation energy of magnetic transitions, applied to skyrmion and antivortex annihilation. *Comp. Phys. Commun.*, 2015, **196**, P. 335–347.
- [22] Henkelman G., Jónsson H. A Dimer Method for Finding Saddle Points on High Dimensional Potential Surfaces Using Only First Derivatives. *J. Chem. Phys.*, 1999, **111**, P. 7010–7022.

- [23] Gutiérrez M. P., Argáez C. and Jónsson H. Improved Minimum Mode Following Method for Finding First Order Saddle Points *J. Chem. Theor. Comput.*, 2017, **13**, P. 125–134.
- [24] Richardson J. O. Derivation of instanton rate theory from first principles. *J. Chem. Phys.*, 2016, **144**, P. 114106(5 pp.).
- [25] Andersson S., Nyman G., Arnaldsson A., Manthe U. and Jónsson H. Comparison of Quantum Dynamics and Quantum Transition State Theory Estimates of the H + CH₄ Reaction Rate. *J. Phys. Chem. A*, 2009, **113**, P. 4468–4478.
- [26] Einarsdóttir D. M., Arnaldsson A., Óskarsson F. and Jónsson H. Path Optimization with Application to Tunneling. *Lecture Notes in Computer Science*, 2012, **7134**, P. 45–55.
- [27] Rommel J. B., Liu Y., Werner H.-J. and Kästner J. Role of tunneling in the enzyme glutamate mutase. *J. Phys. Chem. B*, 2012, **116**, P. 13682–13689.
- [28] Zaslavskii O. Spin tunneling and the effective potential method. *Phys. Lett. A*, 1990, **145**(8), P. 471–475.
- [29] Ulyanov V. V., Zaslavskii O. B. New methods in the theory of quantum spin systems. *Phys. Rep.*, 1992, **216**, P. 179–251.
- [30] Chudnovsky E. M., Garanin D. A. First- and Second-Order Transitions between Quantum and Classical Regimes for the Escape Rate of a Spin System. *Phys. Rev. Lett.*, 1997, **79**, P. 4469–4472.
- [31] Wernsdorfer W., Aliaga-Alcalde N., Hendrickson D. N., Christou G. Exchange-biased quantum tunnelling in a supramolecular dimer of single-molecule magnets. *Nature*, 2002, **416**, P. 406–409.
- [32] Wernsdorfer W., Murugesu M. and Christou G. Resonant Tunneling in Truly Axial Symmetry Mn₁₂ Single-Molecule Magnets: Sharp Crossover between Thermally Assisted and Pure Quantum Tunneling. *Phys. Rev. Lett.*, 2006, **96**, P. 057208(4 pp.).
- [33] Owerre S. A. and Paranjape M. B. Phase transition between quantum and classical regimes for the escape rate of dimeric molecular nanomagnets in a staggered magnetic field. *Phys. Lett. A*, 2014, **378**, P. 1407–1412.
- [34] von Delft J. and Henley C. L. Destructive quantum interference in spin tunneling problems. *Phys. Rev. Lett.*, 1992, **69**, P. 3236–3239.
- [35] Loss D., DiVincenzo D. P. and Grinstein G. Suppression of tunneling by interference in half-integer-spin particles. *Phys. Rev. Lett.*, 1992, **69**, P. 3232–3236.
- [36] Garg A. Topologically Quenched Tunnel Splitting in Spin Systems without Kramers Degeneracy. *Europhys. Lett.* 1993. **22**(3), P. 205–210.
- [37] Vlasov S., Bessarab P. F., Uzdin V. M. and Jónsson H. Classical to quantum mechanical tunneling mechanism crossover in thermal transitions between magnetic states. *Faraday Discuss.*, 2016, **195**, P. 93–109.
- [38] Vlasov S. M., Bessarab P. F., Uzdin V. M. and Jónsson H. Calculations of the onset temperature for tunneling in multispin systems. *Nanosystems: Physics, Chemistry, Mathematics*, 2017, **8**, P. 454–461.
- [39] Fradkin E. *Field Theories of Condensed Matter Physics*. Cambridge University Press, New York, 2013, 190 p.
- [40] Kochetov E. SU(2) coherent state path integral. *J. Math. Phys.*, 1995, **36**, P. 4667–4679.
- [41] Berry M. V. Quantal Phase Factors Accompanying Adiabatic Changes. *Proceedings of the Royal Society of London. Series A, Mathematical and Physical Sciences*, 1984, **392**(1802), P. 45–57.
- [42] Henkelman G., Jónsson H. Improved tangent estimate in the nudged elastic band method for finding minimum energy paths and saddle points. *J. Chem. Phys.*, 2000, **113**, P. 9978–9985.
- [43] Vlasov S. M., Bessarab P. F., Uzdin V. M. and Jónsson H. Crossover temperature for quantum tunnelling in spin systems. *J. Phys. Conf. Ser.*, 2016, **741**, P. 012183(5 pp.).
- [44] Bessarab P. F., Uzdin V. M. Jónsson H. Calculations of magnetic states and minimum energy paths of transitions using a noncollinear extension of the Alexander-Anderson model and a magnetic force theorem. *Phys. Rev. B*, 2014, **89**(21), P. 214424(12 pp.).

Cerium dioxide nanoparticles as third-generation enzymes (nanozymes)

A. L. Popov¹, A. B. Shcherbakov², N. M. Zholobak², A. Ye. Baranchikov³, V. K. Ivanov^{3,*}

¹Institute of Theoretical and Experimental Biophysics, Russian Academy of Sciences,
Pushchino, Moscow region, 142290, Russia

²Zabolotny Institute of Microbiology and Virology, National Academy of Sciences of Ukraine,
Kyiv D0368, Ukraine

³Kurnakov Institute of General and Inorganic Chemistry of Russian Academy of Sciences,
Moscow 119991, Russia

van@igic.ras.ru

PACS 87.55.ne, 87.85.Rs, 81.07.Bc

DOI 10.17586/2220-8054-2017-8-6-760-781

Ceria nanoparticles are capable of performing the function of some enzymes (such as oxidoreductases, phosphatase) and can be classified as nanozymes. In this review, the actual data on the enzymatic activity of ceria were critically analyzed and specific conditions under which the cerium dioxide nanoparticles can act as enzymes were defined. The presented analysis may be useful in the planning, design and synthesis of ceria nanoparticles having the desired enzymatic functions required for various processes, including the development of the nanodrugs, which exhibit the therapeutic effect depending on their composition and pH of media, development of molecular sensors and biosensors, *etc.*

Keywords: ceria, nanomaterials, nanozymes, peroxidase, catalase, phosphatase, superoxide dismutase.

Received: 24 November 2017

Revised: 30 November 2017

1. Introduction

It is a well-established fact that almost all biological processes involve enzymes; therefore, the development of the non-proteinaceous analogues of enzymes is among the most interesting and promising tasks in pharmacological and biomedical research. Over the last few decades there have been a series of artificial enzymes created that have replaced the natural ones in a number of practical applications [1–4]. Finally, in very recent years, it has been found that some nanomaterials also exhibit enzymatic activity. Such nanoscale artificial enzymes were called “nanozymes” and were separated into a particular class of biomimetics [5–7]. The diagram (Fig. 1) shows the chronology of the discovery and research of natural and artificial enzymes.

Natural enzymes and well-known industrial inorganic catalysts have a lot of common features. Both natural enzymes and inorganic catalysts are able to increase the rate of chemical reactions; they are also capable of recycling, which means that after the completion of the catalytic cycle the reagents are regenerated to the initial state. Obviously, the previously summarized knowledge of the catalysis and the properties of the catalysts is useful for biomedical applications, including enzyme-mimetic ones.

Generally, the main difference between natural enzymes and technical catalysts is in the rate of the corresponding chemical (biochemical) processes, where the natural enzymes are more active than the artificial ones. However, recent advances in the field of nanomaterials have allowed the creation of catalysts whose characteristics are not inferior to the native enzymes and, in some cases, even surpass them. The natural enzymes, being proteins, are sensitive to reaction conditions and could be inactivated at high temperatures and at a critical pH. The natural enzymes are: 1) highly selective towards the substrate, 2) selective towards the reaction catalysed and 3) stereoselective. The artificial non-proteinaceous analogues of enzymes are attractive due to their low cost, and also because of the wide range of the conditions in which they maintain their activity and stability. Nanozymes are able to operate under harsher conditions, but typically are less selective. The reactions catalysed by nanozymes follow Michaelis-Menten kinetics; however, nanozymes do not satisfy the above-mentioned “triple selectivity” rule. Curiously, some nanozymes can mimic different enzymes, depending on the conditions of the reaction. Thus, the nanoparticles of noble metals and carbon nanotubes are able to exhibit catalase, oxidase and superoxide dismutase activities. Cerium dioxide nanoparticles possess oxidoreductase, phosphatase and possibly NO-reductase activities.

Some metals, semiconductors and insulators are known for their catalytic properties; however, only a small part of them are suitable for *in vivo* biomedical applications. This is caused by the toxicity of nanomaterials, which is determined by several factors, such as the release of their toxic constituents into biological fluids, in molecular or ionic form. The nanoparticles of the transition metal compounds can participate in Fenton/Haber-Weiss reactions,

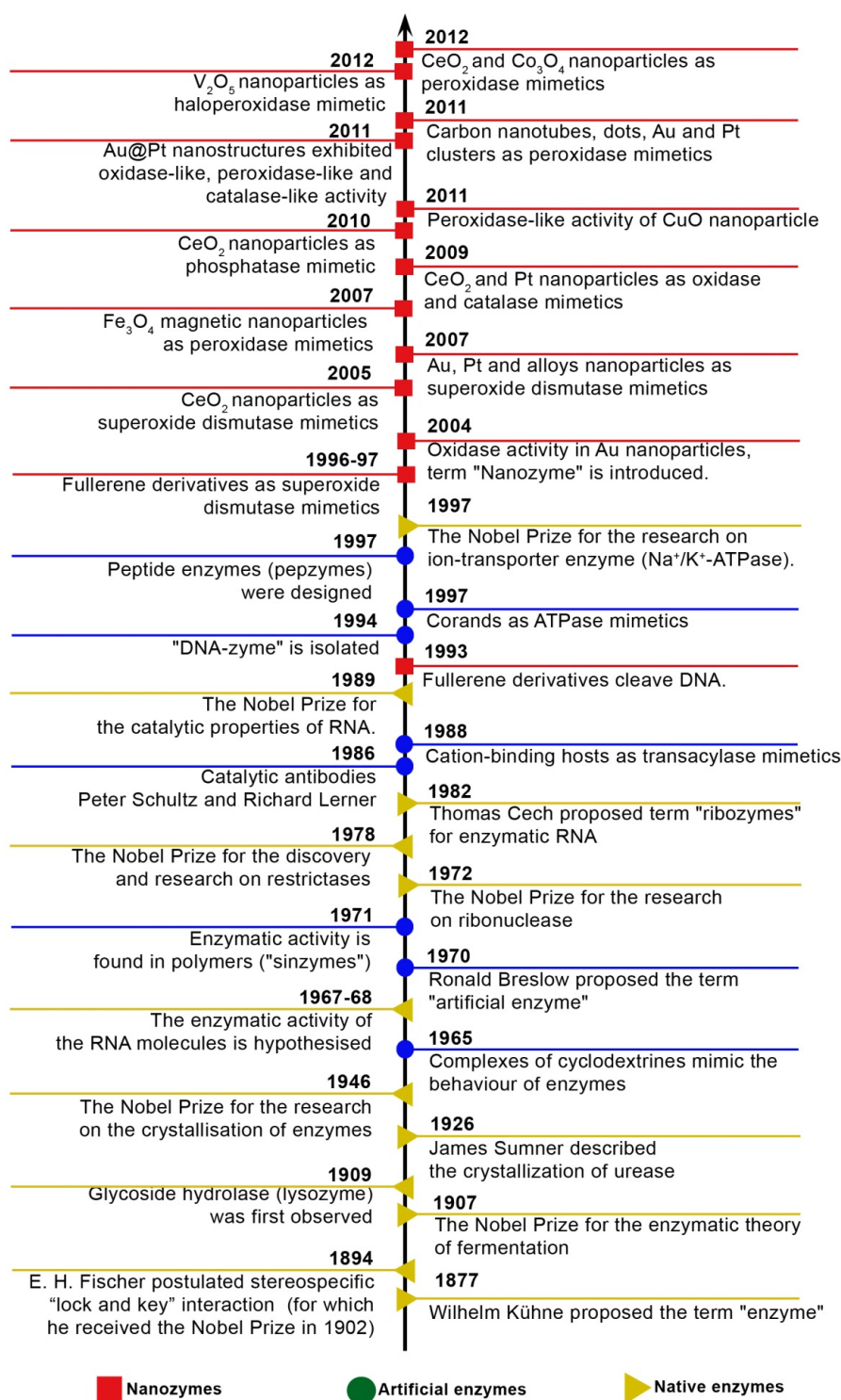


FIG. 1. The chronology of the discovery and research of the three generations of enzymes (adopted from [7])

resulting in the formation of the very toxic hydroxyl radical. Finally, due to their catalytic properties, some of the nanomaterials (oxides of zinc, titanium, cobalt, copper and some other materials, such as carbon nanotubes, etc.) can generate reactive oxygen species (ROS) and cause oxidative stress. This limits the current selection of nanozymes for potential pharmaceutical applications, narrowing it down to the noble metals' nanoparticles (gold, platinum and palladium) and cerium dioxide.

Ceria-based nanomaterials play a key role amongst the currently available nanozymes. The well-known ability of nanoceria to catalyze the redox reactions is widely used in industrial applications (for example, as catalytic converters, reducing harmful emissions in the exhaust fumes from automobiles). Biomedical applications of nanocrystalline cerium dioxide are promising because of two main reasons: its redox activity and its relatively low toxicity. The first factor measures the ability of the cerium dioxide nanoparticle (CDN) to participate in the redox processes in living cells, particularly in the destruction of ROS. The second factor provides that the *in vivo* application of cerium dioxide nanoparticles is safe. One of the key properties of CDNs is the capability of regeneration, which implies that cerium dioxide nanoparticles that have participated in the redox process can return to the initial state over a relatively short period of time.

From the chemical point of view, the dimensional effects are manifested most significantly in the particles where the ratio of surface atoms versus bulk atoms is ≥ 1 (which for the octahedral-shaped CeO_2 particles corresponds to the calculated size of about 4.7 nm (Fig. 2)). In terms of condensed matter physics, the size effects are manifested in the particles of a semiconductor, which are smaller than the Bohr radius of exciton of the corresponding material (for CeO_2 ~ 7.0 – 8.0 nm [8]). Finally, from the biological point of view, the preferred size of CeO_2 particles is less than 6 nm, when their cytotoxicity is at the lowest [9]. To date, several methods that would satisfy the denoted criteria have been developed for the synthesis of CDNs, in which the CDNs could form biocompatible sols suitable for nanopharmaceutical applications (some examples are shown in Fig. 3) [10–14]. The conditions of CeO_2 nanoparticle formation were studied, especially their impact on the characteristics of the formed particles, such as size, degree of crystallinity, oxygen stoichiometry, stability and ζ -potential, as well as other parameters that determine the behaviour of the particles in biological systems [9, 15]. The resulting nanoparticles had low toxicity and were able to participate in the reversible redox processes, to protect organic molecules from oxidative degradation. They were also able to inactivate free radicals and had the functionalities of some enzymes.

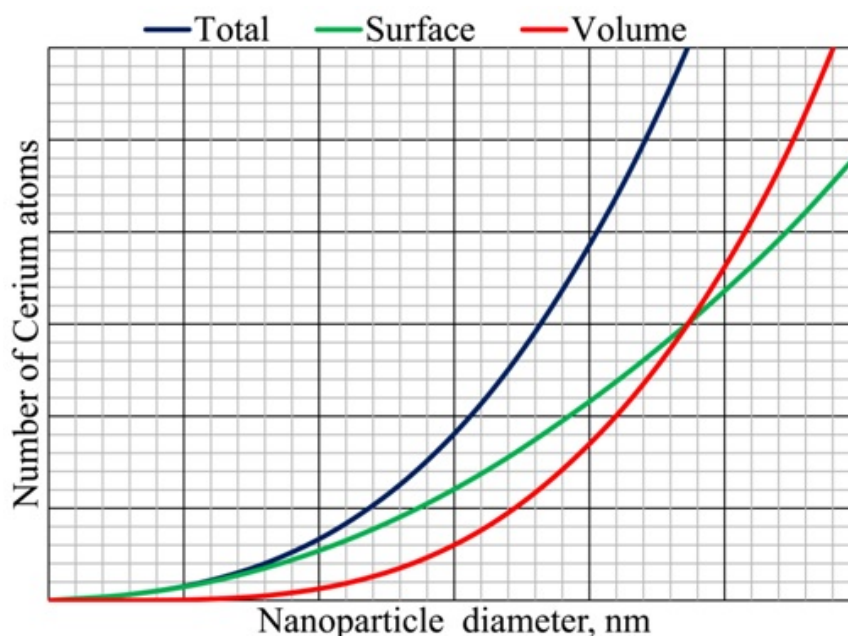


FIG. 2. The calculated number of surface and bulk cerium atoms in CeO_2 nanoparticles as a function of the particle size. Data for calculation of octahedral-shaped ceria nanocrystal taken from [16]

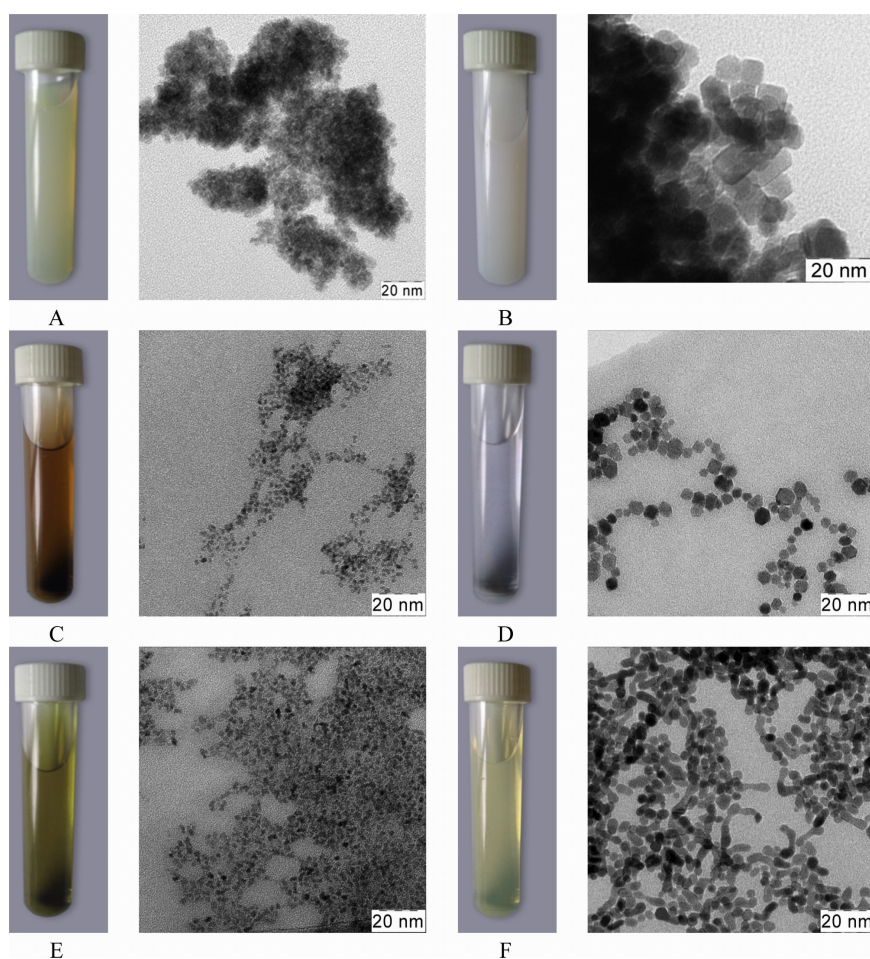
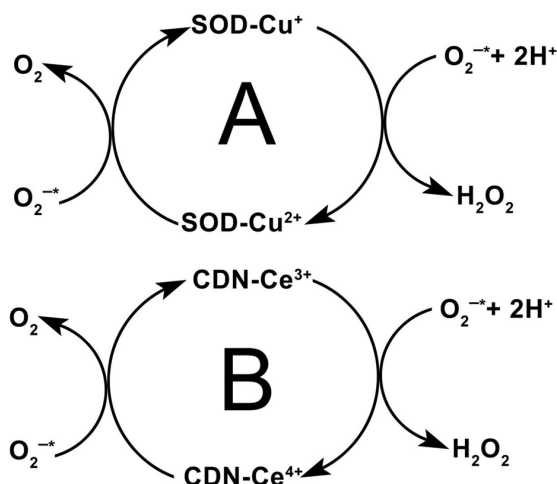


FIG. 3. The appearance and electron micrographs of cerium dioxide samples obtained under various conditions: A – cerium dioxide precipitated from cerium(III) nitrate solution in the mixture of isopropanol:water (19:1) [10], B – sample prepared by microwave hydrothermal treatment at 210 °C for 3 h [10], C – sample prepared by the combination of anionite and microwave-hydrothermal treatments at 190 °C for 3 h [11], D – sample prepared using polyacrylate as stabilizer and further treated hydrothermally at 180 °C for 15 min [12], E – sample prepared using citrate as stabilizer and further treated hydrothermally at 180 °C for 15 min [12], F – sample prepared using citrate as stabilizer and further treated hydrothermally at 180 °C for 3 h [12]

2. CDN is superoxide dismutase mimetic

Superoxide radical ($O_2^{\cdot-}$) is one of the most damaging ROS. In cells, superoxide radicals are formed primarily in the mitochondria, where these radicals damage proteins and initiate lipid peroxidation. Protonation of superoxide radicals leads to the formation of even more aggressive hydroperoxyl (HO_2^{\cdot}) radicals, reaction with nitric oxide forms peroxynitrite (ONO_2^-) radicals. Superoxide radicals destroy iron-sulphur clusters of some enzymes, releasing ferric ions, which are then involved in a Fenton reaction, leading to the formation of hydroxyl radicals (OH^{\cdot}).

Superoxide dismutase (SOD) mimetic activity was one of the first discovered enzyme-like functionalities of CDNs [17–20]. For natural SOD and nanoceria, the mechanisms of the reactions with superoxide are similar [20]. It is well known that the inactivation of superoxide anions by superoxide dismutase is a two-stage process: enzymatic radical dismutation leads to the formation of less toxic hydrogen peroxide and oxygen, and then SOD is regenerated. The reaction for copper containing SOD is shown in Scheme 1(A), where the catalyzed reaction is written as follows: $2O_2^{\cdot-} + 2H^+ \rightarrow H_2O_2 + O_2$. Nanoparticulate CeO_2 accelerates the same reaction, which includes two stages [20]. After the reaction is completed the effective oxidation state of cerium in CeO_2 remains unchanged; see Scheme 1(B).



Scheme 1. Superoxide dismutase-like activity of CDN

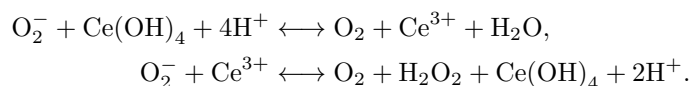
Interestingly, prior treatment of ceria nanoparticles with hydrogen peroxide led to the oxidation of the surface from Ce^{3+} to Ce^{4+} , which caused the complete loss of superoxide dismutase-like activity in CeO_2 nanoparticles [18]. However, after a while, the nanoparticles regained the activity, i.e. the particles returned to their original state. These results strongly suggest that the state of the surface of the CeO_2 particles is important for the inactivation of superoxide radicals, whereas the presence of cerium (III) in the surface layer is the most significant factor. It was also observed that the activity of CeO_2 nanoparticles, to a great extent, depends on the thickness and permeability of the organic layer of stabilizer on its surface [19].

The ability of the nanosized cerium dioxide to mimic SOD is directly determined by the size factor. Thus, the SOD mimetic activity level of the sample of CeO_2 , with the particle size of 3–5 nm, was comparable to ferricytochrome C, whereas the sample of CeO_2 with a larger particle size (5–8 nm) was significantly less active [20].

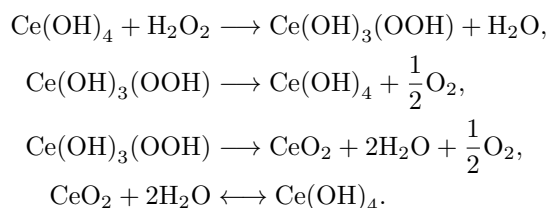
Similarly, epinephrine auto-oxidation in an alkaline medium occurs via the formation of the superoxide radical; nanosized cerium dioxide inhibits this process and the mechanism of the inhibition is similar to that of SOD, whereas the inhibition rate of the process depends on the particle size and pH of the solution [21]. SOD-mimetic activity of CDNs depends on the aggregative stability of sols; it strongly decreases when the threshold of coagulation has been achieved [22].

Batinić-Haberle *et al.* [23] studied a number of SOD-mimetics (manganese compounds, metal nitroxides and oxides, porphyrin and metalloporphyrin derivatives, fullerenes) in detail. It was shown that, among other compounds, SOD-like activity for CDNs (particle size 3–5 nm) had the maximal value, practically at the level of the natural enzyme, $\log(k_{cat}[\text{O}_2^-]) = 9.55$. Authors investigated the catalytic dismutation of the superoxide radical from the standpoint of its electrochemical behavior in solution.

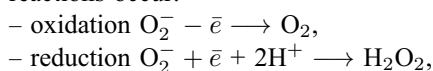
The dismutation of the superoxide radical on the hydrated CDN surface can be written as follows:



The release of hydrogen peroxide leads to the formation and decomposition of cerium hydroperoxide $\text{Ce}(\text{OH})_3(\text{OOH})$ on the CDN surface:



In practice, on the CDN surface during the dismutation of the superoxide radical, three basic electrochemical reactions occur:



– oxidation-reduction $\text{Ce}^{3+} + 4\text{H}_2\text{O} \longleftrightarrow \text{Ce}(\text{OH})_4 + 4\text{H}^+ + \text{e}^-$.

The electrode potential of the superoxide radical dismutation at pH 7.0 in the case of the oxidation reaction is $E = -0.16$ V, in the case of the reduction reaction is $E = +0.89$ V (relative to the standard hydrogen electrode) [23,24].

The standard electrode potential of the cerium species in the case of $\text{Ce}^{3+}/\text{Ce}(\text{OH})_4$ pair is $E^\circ = +1.97$ V [25]; according to the Nernst equation at pH 7.0:

$$E = 1.97 + 2.3 \frac{RT}{nF} \left(\log \left(\frac{[\text{Ce}(\text{OH})_4]}{[\text{Ce}^{(3+)}]}\right) - 4pH \right) = 0.314 - 0.05916 \cdot \log \left(\frac{[\text{Ce}^{(3+)})]}{[\text{Ce}(\text{OH})_4]} \right).$$

It is obvious that the redox potential essentially depends on the $[\text{Ce}^{3+}]/[\text{Ce}(\text{OH})_4]$ ratio on the nanoparticle surface.

Figure 4 shows the redox diagram of the reduction and oxidation of a superoxide radical with SOD, as well as the calculated values of the redox potential of stoichiometric and non-stoichiometric CDN at pH 7.0. In the range of 0.2–0.4 V, there is a redox potential of the “ideal” O_2^- dismutation catalyst. It can be seen from the figure that CDN is a good redox analogue of SOD, the optimum value of the redox potential is located in the region of a high content of cerium (III) ions when $[\text{Ce}^{3+}] \approx [\text{Ce}(\text{OH})_4]$ on the surface of the particle.

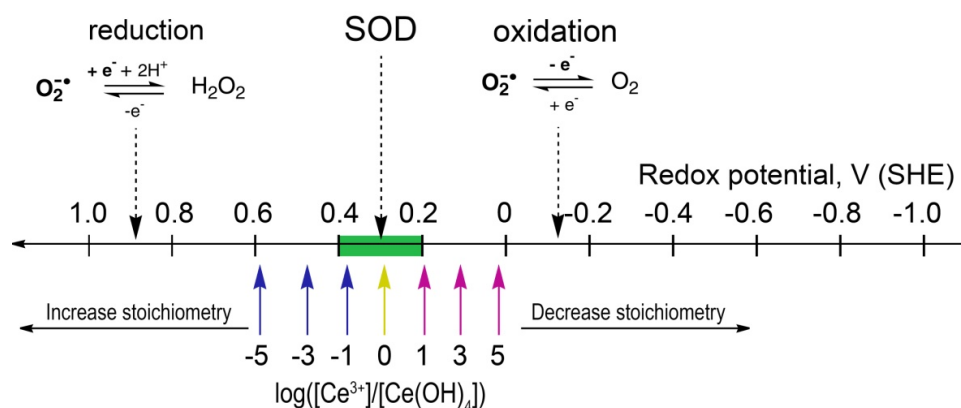


FIG. 4. The diagram of the reduction and oxidation of superoxide radical with SOD (upper part). Green zone shows data for the “ideal” O_2^- dismutation catalyst [23,24]. Calculated values of the redox potential of stoichiometric and nonstoichiometric CDN at pH 7.0 (lower part)

This result confirms the authors’ conclusions [18] that cerium dioxide nanoparticles having a high concentration of trivalent cerium possess high SOD-like activity. At the same time, it can be seen from the figure that with increasing Ce^{3+} concentration the catalytic activity of the system increases nonlinearly, and after reaching a certain value, its decrease will be observed.

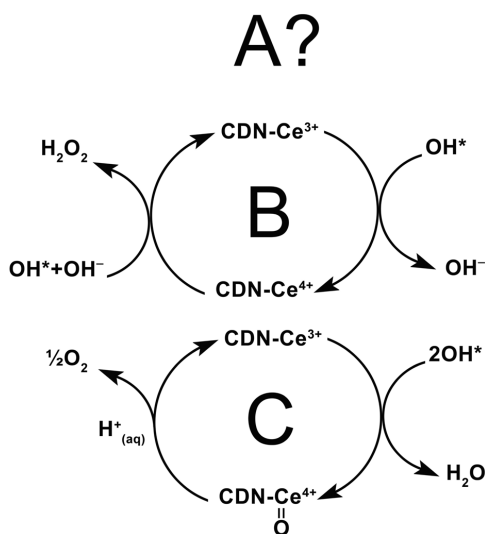
SOD is an anti-oxidant enzyme and plays a vital role in oxidative stress protection systems in most cells which have contact with oxygen. Nanocrystalline cerium dioxide, like SOD, is a powerful protector, enabling the survival of the cells under oxidative stress from exogenous or endogenous ROS.

3. CDN can destroy hydroxyl radicals

The hydroxyl radical (OH) is one of the most aggressive ROS: it oxidizes almost all organic molecules - including proteins, nucleic acids and other biopolymers.

This radical is able to tear off hydrogen from molecules of non-saturated fatty acids and to initiate peroxidation of lipids. The specific enzyme, capable of inactivating the hydroxyl radical, is absent in the nature: unlike superoxide, which can be detoxified by superoxide dismutase, the hydroxyl radical is scavenged by molecular antioxidants (vitamin E, ascorbic acid) – but not by an enzymatic reaction, since the hydroxyl radical is extremely reactive and its diffusion to the possible enzyme’s active site is slower than the radical half-life [26]. In the presence of ceria nanoparticles, the blasting activity of the hydroxyl radical decreases, which allows us to assume that CDNs can catalytically destroy OH [15]. In view of the absence of the conforming natural analogue of such a catalyst, it is not obviously possible to define the scheme of the corresponding process (Scheme 2(A)). However, in a pioneering work, the mechanism of interaction of the hydroxyl radical with cerium ions in solution

is described [27]. Possibly, the mechanism of the hydroxyl radical inactivation by cerium dioxide nanoparticles can have a similar appearance (Scheme 2(B)).

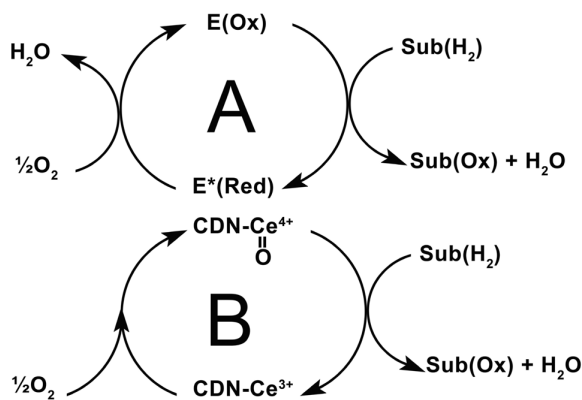


Scheme 2. CDN scavenges the hydroxyl radical

The protective action of CDNs against hydroxyl radical has been confirmed by the data reported: cerium dioxide nanoparticles provided an effective protection for methyl violet dye molecules from the oxidation by hydroxyl radicals, which were formed in Fenton's reaction [28]. The probable mechanism of hydroxyl radical scavenging activity of CeO_2 nanoparticles was proposed; see Scheme 2(C). It should be noted that the ability of CeO_2 nanoparticles to inactivate hydroxyl radicals sharply increased with decreasing particles size, which, according to the authors, is due to the increased content of Ce^{3+} on the surface of the particle. This pattern was recently confirmed for CeO_2 nanoparticles stabilized with maltodextrin [29]. The ability of ceria nanoparticles, with the particle size of 3–5 nm, to inactivate superoxide and hydroxyl radicals was also confirmed by EPR [30].

4. CDN is oxidase mimetic

In oxidase-catalyzed reactions, the substrate is oxidized by molecular oxygen, leading to the formation of water, hydrogen peroxide or free oxygen radicals. The mechanism of these reactions is shown in Scheme 3(A) in a simplified form, where $\text{E}^*(\text{Red})$ and $\text{E}(\text{Ox})$ are the reduced and oxidized forms of the enzyme. $\text{Sub}(\text{H}_2)$ and $\text{Sub}(\text{Ox})$ are the reduced and oxidized forms of the substrate respectively. CDN is shown to possess catalase-like activity; for instance, at low pH, the dextran-stabilized CeO_2 nanoparticles could oxidize the organic dyes, such as 3,3,5,5'-tetramethylbenzidine and 2,2-azinobis(3-ethylbenzothiazoline-6-sulfonic acid), as was reported [31]. The authors demonstrate that oxidase-mimetic properties of CDNs could be used in immunoassays, including those for identification of cancer cells. The most plausible mechanism of the oxidase-like activity of CDNs is shown in Scheme 3(B), which is similar to Scheme 3(A) [31].



Scheme 3. Oxidase-like activity of CDN

According to the Pourbaix diagram for cerium, upon decreasing pH, the oxidizing ability of Ce^{4+} is enhanced and the reaction rate under Scheme 3(B, right part) increases, while the possibility of particles' regeneration under Scheme 3 (B, left part) drops. Probably, CDNs exhibit maximal oxidase-like activity at certain pH in the acidic domain.

The concentrations of quadrivalent (as CeO_2) and trivalent cerium ions in aqueous media are linked by the equation [25]

$$\log(\text{Ce}_{\text{CeO}_2}^{4+}/\text{Ce}^{3+}) = 3\text{pH} - 7.288 + \frac{1}{4} \log(p_{\text{O}_2}).$$

At atmospheric pressure ($p_{\text{O}_2} = 0.2$), $\text{Ce}_{\text{CeO}_2}^{4+}$ is equal to Ce^{3+} at $\text{pH} \approx 2.5$; at pH 2 only approximately 1 % of Ce^{3+} ions in CeO_2 can be oxidized by the dissolved oxygen to Ce^{4+} [25]. Moreover, at low pH values, especially in the presence of acids capable of forming complexes with cerium ions (citric, ethylenediaminetetraacetic, etc.), after the stage of substrate oxidation (Scheme 3(B), on the right), CeO_2 nanoparticles can even dissolve [32]. However, over time (especially upon the increasing of pH) Ce^{3+} ions can be re-oxidized by the dissolved oxygen, forming CeO_2 nanoparticles again (see Figs. 5,6). For instance, at pH=5 the equilibrium ratio of $\text{Ce}_{\text{CeO}_2}^{4+}/\text{Ce}^{3+}$ concentrations is ca. $3 \cdot 10^7$, i.e. there are practically no free Ce^{3+} ions in the solution.

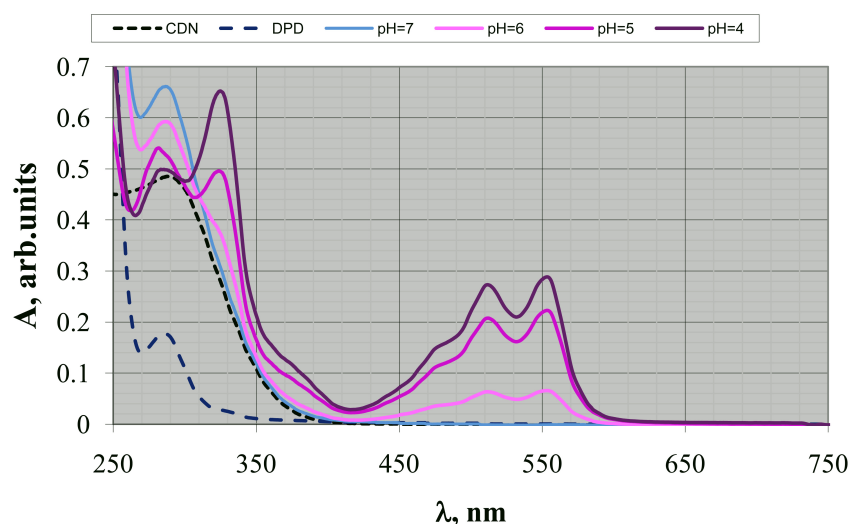


FIG. 5. Absorption spectra of 0.1 mM ceria sol (particle size 3–5 nm, stabilized by citrate, ζ -potential -20 mV), 0.1 mM solution of N,N-diethyl-p-phenylenediamine (DPD) and their mixture upon 5 min exposition at different pH

Oxidase-like activity of CDNs does not depend on the presence of small ions in solution (including acetate or citrate); however, DNA adsorption completely eliminates this enzymatic activity, restricting substrate access to the surface of nanoceria [33].

5. CDN is catalase mimetic

Hydrogen peroxide (H_2O_2) is one of the most important ROS in a cell. In catalase-catalyzed reactions, hydrogen peroxide is a substrate that is decomposed into non-toxic constituents (water and oxygen) in the presence of the enzyme. Catalase (as well as glutathione peroxidase) is the enzymatic component of the primary antioxidant system of the cell's protection. The well-known mechanism of catalase action is shown in Scheme 4(A). The commonly accepted mechanism of CDNs' catalase-like activity is shown in Scheme 4(B). However, this scheme is not fully correct, because the process of hydrogen peroxide decomposition in the presence of nanoceria is more complex and actually proceeds in several stages 4(C).

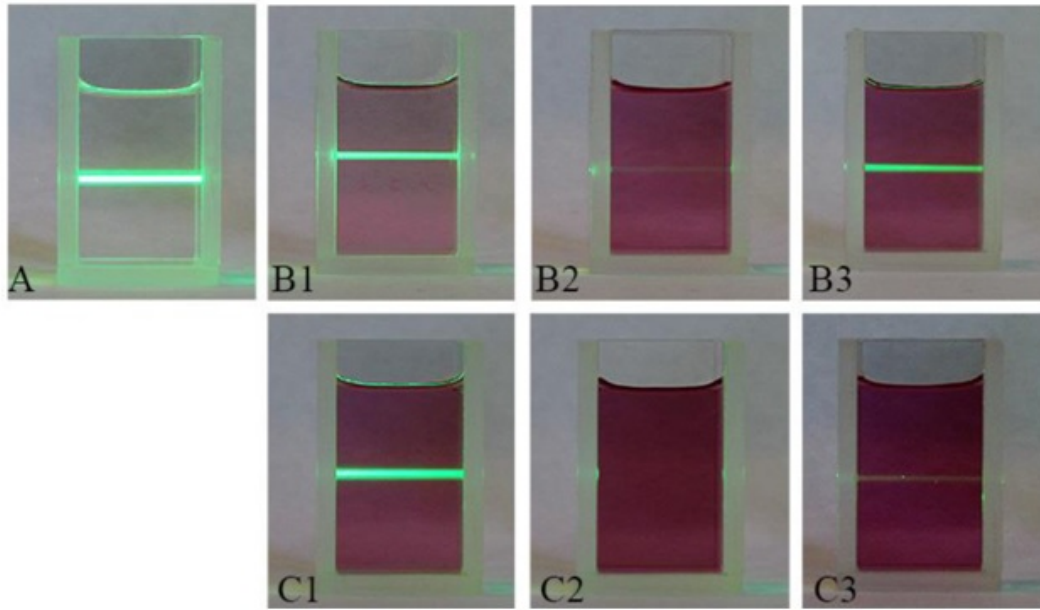
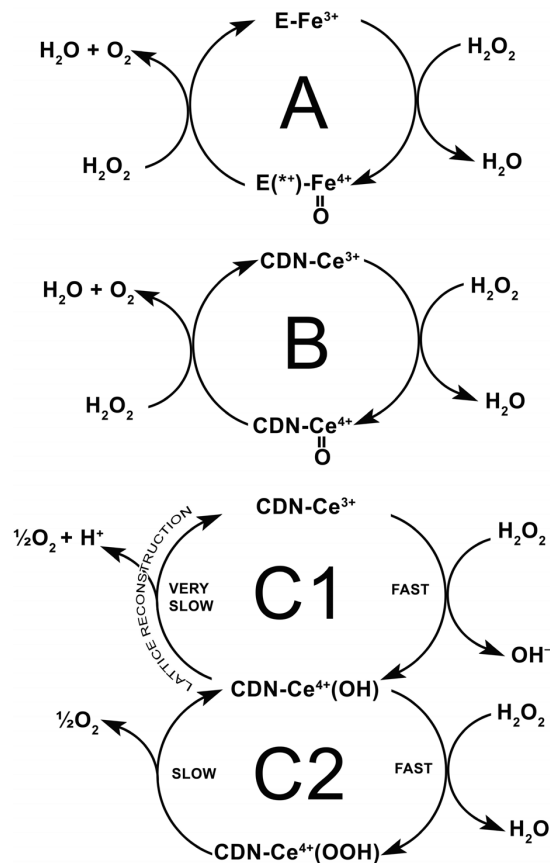


FIG. 6. A series of photographs showing the Tyndall effect (laser irradiation at $\lambda = 543$ nm) upon the oxidation of 1.0 mM DPD in the presence of 1.0 mM ceria sol (particle size 3–5 nm, stabilized by citrate, ζ -potential -20 mV): A – pH = 7.0; B – pH = 5.0; C – pH = 4.0.; B1, C1 – immediately after mixing of ceria sol and DPD solution; B2, C2 – 5 min after mixing of ceria sol and DPD solution; B3, C3 – 6 h after mixing of ceria sol and DPD solution with intermediate shakings. pH was adjusted by hydrochloric acid (if needed)



Scheme 4. Catalase-like activity of CDN

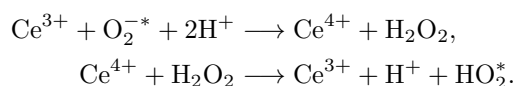
At the first stage, the trivalent cerium ions on the surface of CDNs are oxidized by hydrogen peroxide to Ce^{4+} (Scheme 4(C1, right)). Simultaneously, H_2O_2 is irreversibly bonded to Ce^{4+} ions on the surface of nanoceria, forming cerium perhydroxide (Scheme 4(C2, right)) [34]; in turn, cerium perhydroxide further decomposes with oxygen formation (Scheme 4(C2, left)). The presence of hydroxyl groups on the surface of CeO_2 particles considerably facilitates the formation of perhydroxide (see Scheme 4(C)). For this reason, ceria sols obtained using “soft chemistry” methods in mild conditions show enhanced catalase mimetic activity, while for well-annealed ceria particles this ability is suppressed or nearly absent [35].

Typically, the injection of H_2O_2 decreases the aggregative stability of ceria sols. Hydrogen peroxide is strongly adsorbed on the surface of cerium dioxide nanoparticles, displacing inorganic or organic ligands (stabilizers, dyes etc.).

The mechanism of perhydroxide decomposition on a surface of CDN is not clear yet. In the case of aqueous solutions of cerium salts, the formation of hydroxyl and superoxide (hydroperoxyl) radicals as intermediates is assumed [36, 37]; it was established that decomposition of hydrogen peroxide by cerium (III) ions occurs via Fenton/Haber-Weiss mechanisms [38]. However, in the case of cerium dioxide nanoparticles, these free radicals either cannot be formed or decay at the moment of their formation, according to Schemes 1 and 2. The ability to decompose H_2O_2 without releasing the aforementioned harmful oxygen radicals is a specific feature of cerium dioxide nanoparticles that distinguishes CDNs from both cerium salts and most other metal oxides (including nanocrystalline ones). Due to the catalase-like activity of CDNs, the free hydrogen peroxide cannot be released in SOD-mimetic (Scheme 1(B)) or hydroxyl radical scavenging (Scheme 2(B)) cycles because H_2O_2 is immediately decomposed by CeO_2 , according to Scheme 4(C). Cerium perhydroxide formation was observed during the interaction of cerium compounds and O_2 -radicals [39].

To estimate the contribution of the C1 process into the mechanism of hydrogen peroxide decomposition by cerium dioxide nanoparticles, it is useful to analyze the redox behavior of H_2O_2 and cerium species in aqueous systems (see below). On the other hand, it was demonstrated that the catalase mimetic property of CDNs (unlike the SOD mimetic one) essentially depends on the content of quadrivalent cerium in a particle [40, 41]. Therefore, it is possible to assume that the C2 cycle introduces an appreciable (or even the major) contribution to the catalytic decomposition of hydrogen peroxide by cerium dioxide nanoparticles.

Das *et al.* [41] proposed the mechanism of H_2O_2 decomposition by tetravalent cerium ion as a part of the ROS-scavenging cycle of CDNs in a biological tissue:



According to the Pourbaix diagram, hydrogen peroxide reduces ceric ions in acidic media. Probably, the proposed scheme explains pro-oxidant properties of CDNs under acidic conditions, because thus forming hydroperoxyl radicals is more aggressive than both the starting superoxide radicals and intermediate hydrogen peroxide.

The formation and decomposition of the dark-colored cerium perhydroxide led to the common misconception that visual changes of the CeO_2 sol's color occur due to the oxidation and reduction of cerium ions in ceria particles. Fig. 7 shows the changes in the absorption spectra and the color of $(\text{NH}_4)_2\text{Ce}(\text{NO}_3)_6$ aqueous solution upon peroxide injection. Surely, Ce^{4+} ions cannot be further oxidized; nevertheless, the solution becomes deeply colored. In turn, the addition of hydrogen peroxide to an aqueous cerium (III) nitrate solution doesn't lead to an immediate change of color.

The absorption spectra of ceria aqueous sols before the injection of hydrogen peroxide and during several cycles of decomposition at different pH are presented in Fig. 8.

One can see that a decrease in pH decreases the intensity of the sols' coloration caused by CeO_2 interaction with hydrogen peroxide, which indicates slowdown of C1 and C2 (right) stages. The kinetics of interaction is shown in Fig. 9. The duration of a single redox-cycle (formation and decomposition of cerium perhydroxide) only slightly depends on a ratio of concentrations of ceria nanoparticles and H_2O_2 , and strongly depends on the pH of the solution. The rate of formation of cerium perhydroxide and the decomposition of hydrogen peroxide decreases abruptly with a decrease in pH. For aqueous ionic cerium complexes, the rate of H_2O_2 disproportionation at $t = 25^\circ\text{C}$ and $\text{pH} \rightarrow 5.0$ drops practically to zero [37]. The available data shows that the catalase-like activity of nanoceria also depends on the pH of the solution (catalase activity increases with the pH of the solution and decreases with the decrease of the pH) [42].

6. CDN as peroxidase mimetic and the interplay of CDN's pro-oxidant and anti-oxidant properties

The ability of CDNs to catalyze the oxidation of organic molecules by hydrogen peroxide in an acidic medium (peroxidase activity) was observed, e.g. in the reaction of H_2O_2 with bioflavonoids (e.g. anthocyanins of

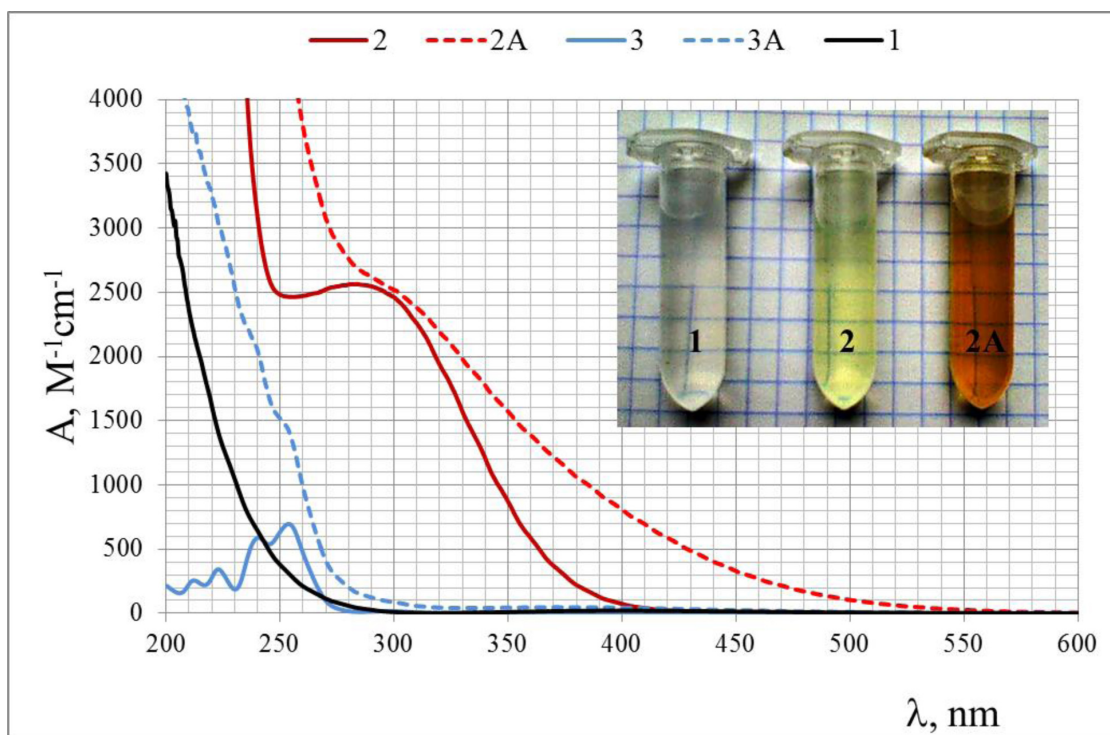
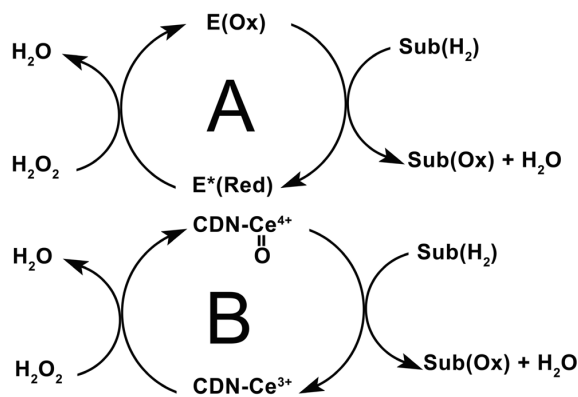


FIG. 7. Absorption spectra of hydrogen peroxide (1), $(\text{NH}_4)_2\text{Ce}(\text{NO}_3)_6$ aqueous solution before (2) and after injection of H_2O_2 (2A) and CeCl_3 aqueous solution before (3) and after (3A) injection of equimolar quantity of H_2O_2 . Inset: Appearance of corresponding solutions

grape) [43]. There, it was shown that the balance of pro-oxidant and anti-oxidant properties of CDNs is dependent on the pH. A detailed study of the peroxidase activity of CDNs (including Michaelis–Menten constants) justified the possibility for the replacement of horseradish peroxidase (HRP) by cerium dioxide sols for the oxidation of the substrate (3,3,5,5-tetramethylbiphenyl dihydrochloride) in a glucose test [44]. It was shown for H_2O_2 -substrate that the maximal reaction rate in the presence of CDNs exceeds the similar value for HRP ($5.07 \cdot 10^{-8} \text{ M} \cdot \text{s}^{-1}$ and $3.34 \cdot 10^{-8} \text{ M} \cdot \text{s}^{-1}$, accordingly).

Scheme 5(A) shows a simplified catalytic cycle of peroxidase; here, $\text{E}^*(\text{Red})$ and $\text{E}(\text{Ox})$ are reduced and oxidized forms of the enzyme, while $\text{Sub}(\text{Red})$ and $\text{Sub}(\text{Ox})$ are reduced and oxidized forms of the substrate, respectively. As well as in the case of oxidase mimetic, the decrease in pH enhances pro-oxidant properties of CeO_2 and raises the reaction rate under Scheme 5B (right part), but the possibility of the particles' regeneration under Scheme 5(B, left part) drops. It is obvious that for peroxidase-like activity of CDNs (as in the case of oxidase mimetic) there should be also an optimum pH value, located in the acidic area. For instance, Jiao *et al.* [44] also show that peroxidase-like activity of CDNs is maximal at pH 4, while at pH < 2 and pH > 6 it is lost. As mentioned above, at high pH values, nanocrystalline cerium dioxide exhibits catalase mimetic activity.



Scheme 5. Peroxidase-like activity of CDN

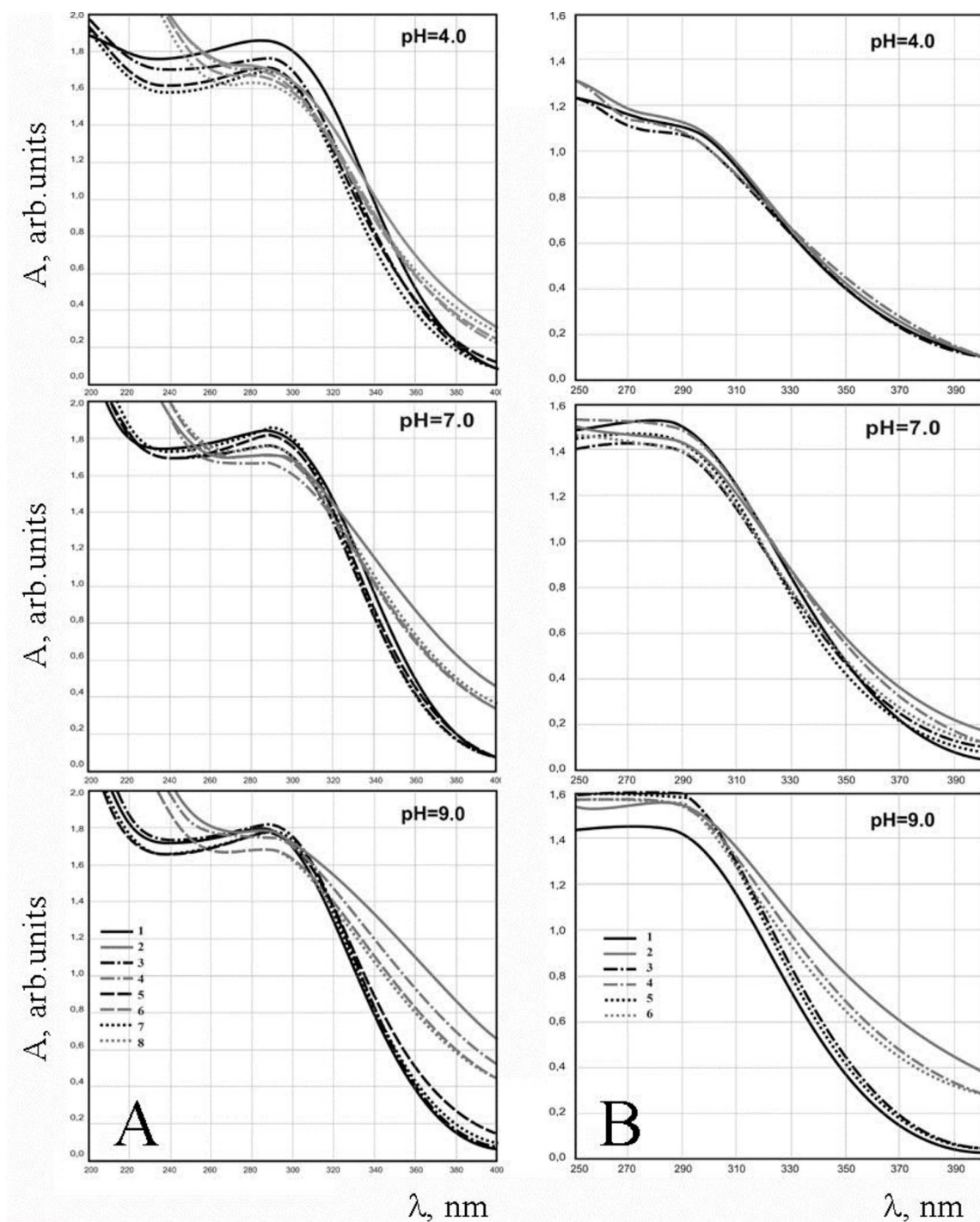


FIG. 8. Regeneration of 0.5 mM CeO₂ sol in alkaline, neutral and acidic media upon treatment by hydrogen peroxide: 1 – initial CeO₂ sol; 2 – injection of 1 mM H₂O₂; 3 – boiling for 5 minutes; 4 – injection of additional 1 mM H₂O₂; 5 – additional boiling for 5 minutes; 6 – injection of additional 1 mM H₂O₂; 7 – additional boiling for 5 minutes; 8 – injection of additional 1 mM H₂O₂. A – the data for citrate-stabilized ceria sol containing 2–3 nm particles; B – the data for polyacrylate-stabilized ceria sol containing 4–5 nm particles

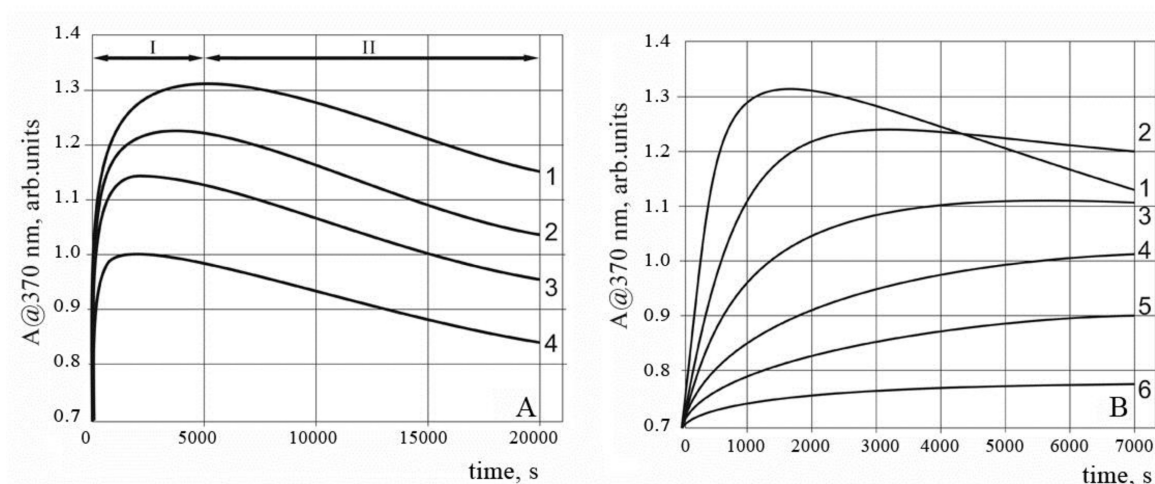


FIG. 9. (A) Dynamics of optical density change at 370 nm wavelength of 400 μM aqueous colloid solution of CeO_2 nanoparticles upon injection of hydrogen peroxide of different concentrations: 1 – 400 μM ; 2 – 200 μM ; 3 – 100 μM ; 4 – 50 μM (pH 80). (B) Dynamics of optical density change at 370 nm wavelength of 400 μM aqueous colloid solution of CeO_2 nanoparticles upon injection of hydrogen peroxide at different pH values: 1 – pH 9; 2 – pH 8; 3 – pH 7; 4 – pH 6; 5 – pH 5; 6 – pH 4 (concentration of H_2O_2 is 200 μM)

Pro- and anti-oxidant properties of CDNs are closely related and determined by several key factors. Let us consider the role of CDNs in the oxidation of indigoid dyes by hydrogen peroxide as an example. Indigo carmine is decomposed by ROS in the whole range of pH (Fig. 10). In the presence of nanoceria (particle size 3–5 nm, stabilized by citrate, ζ -potential of about -20 mV), the oxidation rate of indigo carmine by H_2O_2 is changed: at pH <6 , the rate of dye degradation by hydrogen peroxide is enhanced, i.e. CDNs exhibit peroxidase-like activity. Contrarily, at pH >7 the rate of discoloration of the solution decreased, thus revealing the catalase-like activity of CDNs (Fig. 11).

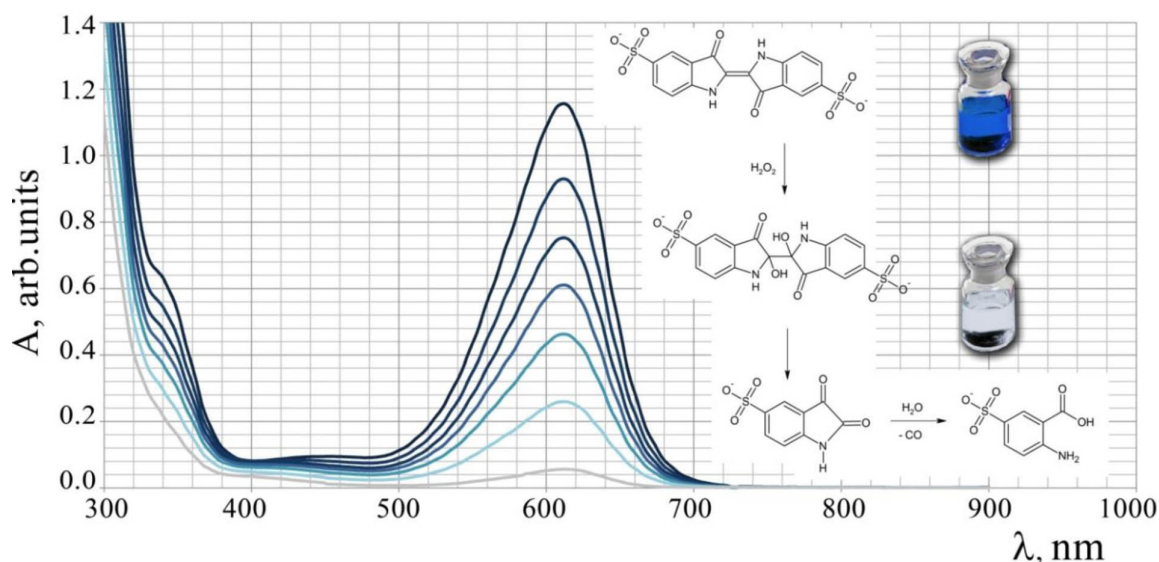


FIG. 10. The kinetics of indigo carmine dye solution (75 μM) decomposition in the presence of hydrogen peroxide (1 mM), and scheme of the corresponding process

The ability of CeO_2 to decompose hydrogen peroxide can also be described in terms of its electrochemical behavior in aqueous solutions. The standard electrode potential (E°) for $\text{CeO}_2/\text{Ce}^{3+}$ is 1.66 V; for $\text{O}_2/\text{H}_2\text{O}_2$ E° it is 0.695 V [25].

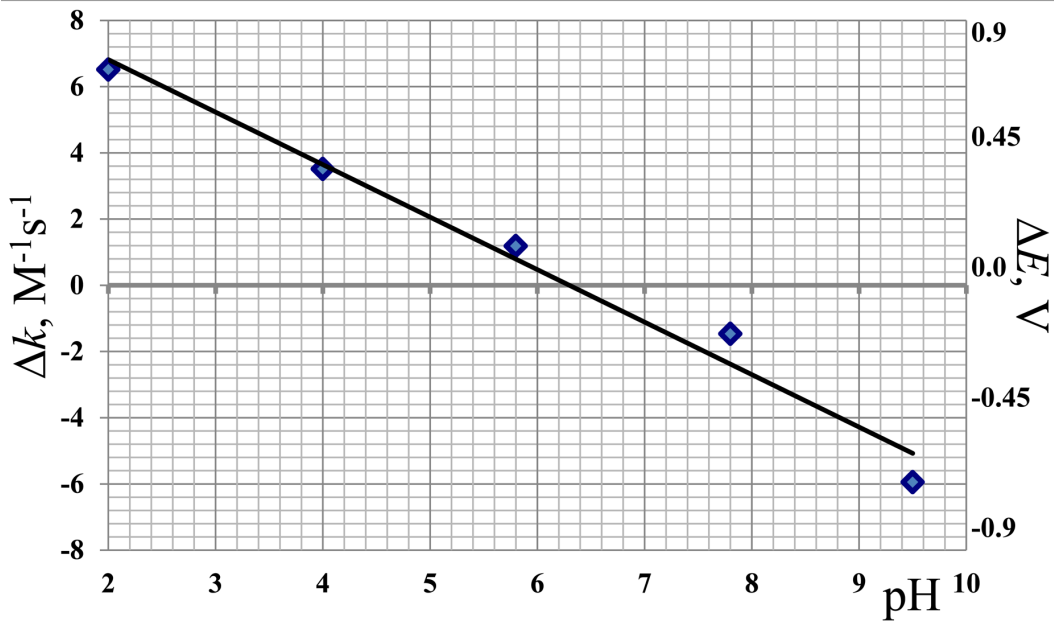


FIG. 11. Square dots denote changes of the rate constant of indigo carmine dye ($75 \mu\text{M}$) discoloration by hydrogen peroxide (1 mM) caused by the introduction of CDNs ($50 \mu\text{M}$) as a function of pH (left axis). The solid line is the calculated difference between the redox potentials of CDNs and hydrogen peroxide as a function of pH (right axis)

In accordance with the Nernst equation, for $\text{Ce}^{3+} + 2\text{H}_2\text{O} \rightarrow \text{CeO}_2 + 4\text{H}^+ + \text{e}^-$ reaction the redox potential depends on pH, as follows:

$$E1 = 1.66 + 2.3 \frac{RT}{nF} \left(\log \left(\frac{[\text{CeO}_2]}{[\text{Ce}^{(3+)})]} \right) - 4pH \right) = 1.66 + 0.05916 \left(\log \left(\frac{[\text{CeO}_2]}{[\text{Ce}^{(3+)})]} \right) - 4pH \right).$$

Redox potential of $\text{H}_2\text{O}_2 \rightarrow \text{O}_2 + 2\text{H}^+ + 2\text{e}^-$ reaction depends on the pH as:

$$E2 = 0.695 + 2.3 \frac{RT}{nF} \left(\log \left(\frac{p_{\text{O}_2}}{[\text{H}_2\text{O}_2]} \right) - 2pH \right) = 0.695 + 2.3 \frac{RT}{2F} \left(\log \left(\frac{p_{\text{O}_2}}{[\text{H}_2\text{O}_2]} \right) - 2pH \right) = 0.695 + 0.02958 \left(\log \left(\frac{p_{\text{O}_2}}{[\text{H}_2\text{O}_2]} \right) - 2pH \right).$$

Therefore, if $E1 < E2$ or

$$1.66 + 0.05916 \left(\log \left(\frac{[\text{CeO}_2]}{[\text{Ce}^{(3+)})]} \right) - 4pH \right) < 0.695 + 0.02958 \left(\log \left(\frac{p_{\text{O}_2}}{[\text{H}_2\text{O}_2]} \right) - 2pH \right),$$

then nanoceria reduces hydrogen peroxide (i.e. it acts as an anti-oxidant and protects from hydrogen peroxide). This condition is satisfied when $\text{pH} > 5.6 - \frac{1}{3} \left(\log(D) - \frac{1}{2} \log[\text{H}_2\text{O}_2] \right)$. We assume that $p_{\text{O}_2} = 0.1$ and denotes the mole fraction of Ce(III) in the particle as D (since cerium dioxide is insoluble there are no cerium ions present in the solution).

The total concentration of hydrogen peroxide above $\approx 1 \text{ mM}$ causes cell death in mammals. The decomposition of the hydrogen peroxide to a lower concentration will occur at $\text{pH} \geq 5.1 - \frac{1}{3} \log(D)$.

In stoichiometric coarse-grained CeO_2 , trivalent cerium ions are almost absent ($D \leq 10^{-8}$). For such material, the limiting value is $\text{pH} > 5.1 - \log(10^{-8}) = 7.77$. In other words, at $\text{pH} < 7.8$, stoichiometric cerium dioxide could not function as an anti-oxidant against hydrogen peroxide (because in this pH range the redox potential of ceria is higher than that of H_2O_2). In non-stoichiometric cerium dioxide (especially in the presence of organic stabilizer), the D value reaches 0.01–0.001 and above [45]. For CeO_2 with $D = 0.001$, the threshold pH value is $\text{pH} > 5.1 - \log(10^{-3}) = 6.1$. In other words, at $\text{pH} > ca. 6$, non-stoichiometric ceria is able to protect biological systems and their components from hydrogen peroxide.

Figure 11 shows the dependence of the difference between the redox potentials of CDNs ($D = 0.001$) and 1 mM of hydrogen peroxide ($\Delta E = E1 - E2$) from the pH of media (solid line). The difference between the rate

constants of indigo carmine dye decomposition by hydrogen peroxide in the absence and the presence of nanoceria is also shown as square dots ($\Delta k = k_1 - k_2$). This straight line coincides with the trend of the kinetic constant change of indigoid dye oxidation by hydrogen peroxide that is caused by ceria introduction.

The proposed calculation allows one to evaluate the protective ability of various cerium dioxide particles against ROS (e.g. hydrogen peroxide), taking into account the pH value of the medium in cells or cell organelles [46]. The respective data obtained for stoichiometric and non-stoichiometric cerium dioxide specimens are shown in Fig. 12. Alteration of the stoichiometry can be used to control pro- or anti-oxidant properties of CDNs across a wide range of biologically relevant pH values. As can be seen from the figure, the minimum protection against oxidation is observed for the content of some vesicles (lysosomes and endosomes). It is well known that in eukaryotes, most of the substances are transported into cells via vesicular uptake mechanisms. Endocytosis provides a path for the useful nutrients (such as proteins, nucleic acids, polysaccharides and lipoprotein complexes) as well as the undesirable species (such as toxins, antibodies and virions, etc.). The oxidizing properties of CDNs may be useful for the destruction of dangerous exogenous components in the course of the vesicular transportation of nutrients into the cells. On the other hand, the analysis of pH-dependent redox behavior of CDNs suggests that the maximum protection from oxidative stress is manifested in the mitochondria. As is known, the endogenous oxidative processes in cells take place in mitochondria; they are actively involved in the generation of ROS and participate in the cascade of the programmed cell death. There is a proven correlation between excessive mitochondrial generation of ROS and aging [47]. Mitochondria-targeted anti-oxidants are effective protectors of cells and their organelles, under the conditions of oxidative stress or aging [48].

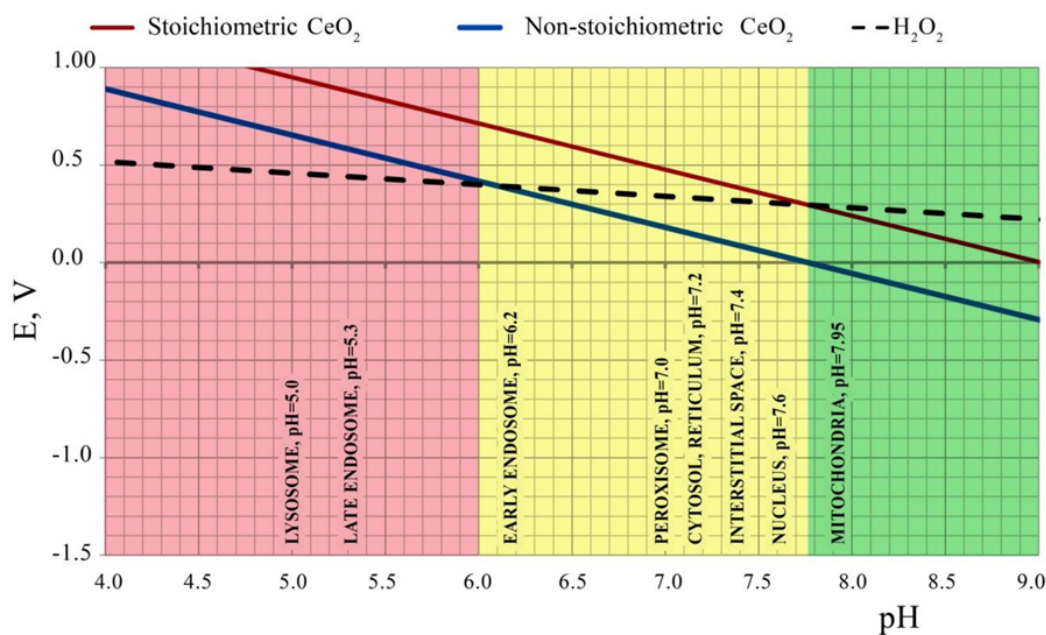


FIG. 12. E-pH diagram for hydrogen peroxide and stoichiometric and non-stoichiometric CeO_2 . The cellular organelles with the corresponding pH values are shown along the absciss

Figure 12 demonstrates that the CDN's behavior strictly depends on its stoichiometry, even in similar biological experiments. For example, recently we have demonstrated that ceria nanoparticles (2–5 nm) protect against oxidative stress in murine oocytes and boost their activity [49], while authors [50] have found that cerium dioxide nanoparticles of the same size (~ 3 nm) are pro-oxidants for murine oocytes and invoke oxidative damage of DNA. In the first case, nanoparticles have been obtained from salts of cerium (III) under “mild conditions” and contained more than 15 % Ce^{3+} [45]; in the second case nanoparticles (Rhodia) have been synthesized from cerium (IV) salts and practically did not contain Ce^{3+} (less than 0.04 %) [51].

From the point of view of nanopharmaceutics, a pH-dependent equilibrium of pro- and anti-oxidant properties of the CDNs is of great interest; it could be applied for the development of antiviral drugs, for instance. Most viruses penetrate cells via endocytosis. The agglutination and release of genetic material require a low pH in vesicles. Thus, influenza hemagglutinin is inactive at pH 7. Fusion peptides change their conformation in acidic media only (at $\text{pH} \leq 5$). At this pH, nanocrystalline cerium dioxide exhibits pro-oxidant properties, and thus can damage the nucleic acids of the virion. In vitro experiments revealed that CDNs (particles size 3–5 nm,

stabilized with citrate, ζ -potential of about -20 mV, concentration of 0.01 – 0.1 mM) provide virus-resistance both in prophylactic and therapeutic (1 h after infecting) schemes, and also demonstrate a significant virucidal effect, reducing the titer of RNA virus (vesicular stomatitis) and DNA virus (herpes simplex type 1) in L929 and RF cells by 2.6 – 4.8 lg [52]. The selectivity index (the ratio of the effective antiviral and cytotoxic doses) is more than 16.0 , which is typical for active antiviral drugs.

The prospect of the application of nanoceria for the redox treatment of tumours is even more exciting. Due to anaerobic respiration that occurs in the cytosol (lactic acid fermentation), rather than oxidative phosphorylation in the mitochondria (the Warburg effect), cancer cells express increased glycolysis. It is known that the pH value of the medium in a tumor is decreased (Fig. 13 [53]). Further, the tumor exists in a state of hypoxia permanently, and the partial oxygen pressure in the carcinogenesis area is also decreased [54]. For the calculation of pH-dependent redox activity (see above) of CDNs in normal tissue $p_{O_2} \approx 0.1$ was used. The partial pressure of oxygen in tumors may be in the range of $p_{O_2} \approx 0.01 - 0.001$, therefore the redox activity of CDNs towards ROS (hydrogen peroxide) would be observed at 0.2 – 0.4 pH points higher than in normal tissue. Thus, CeO_2 nanoparticles can selectively protect the normal cells (unlike malignant cells) from oxidative stress.

The pioneering experiments with oxidative destruction of normal tissue cells (cardiomyocytes and fibroblasts) and tumor cells (lung carcinoma and breast cancer) substantiated this assumption [42]. Our latest experiments confirm it also: according to the data presented in paper [55], panthenol-stabilized non-stoichiometric cerium dioxide nanoparticles provide strong protection for both normal (diploid epithelial swine testicular, ST) and malignant (human epidermoid cancer, HEP-2) cells under oxidative stress conditions induced by UV irradiation. However, the degree of protection against H_2O_2 -induced oxidative stress dramatically differs: the application of $63 \mu M$ CeO_2 sols increases the viability of malignant cells not more than 10 – 15 % over negative control (H_2O_2), while the same concentration of the CeO_2 protects normal cells almost completely (Fig. 14).

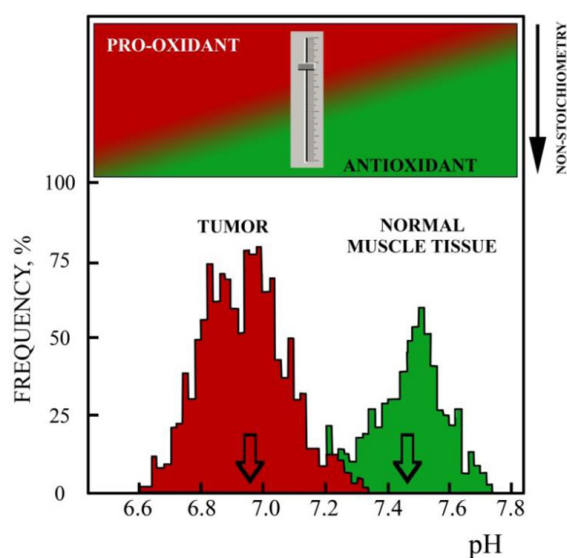


FIG. 13. Bottom: average frequency of measured pH values in the area of SCK-cells in carcinoma and normal muscle tissue in mice [53]. Top: pro-oxidant and anti-oxidant properties of the CeO_2 nanoparticles of various stoichiometry and the possibility of fine-tuning of such properties in the given pH range (see Fig. 12)

Usually, seriously damaged cells undergo programmed cell death (apoptosis), a mechanism of self-destruction that involves mitochondria, but this mechanism fails in cancer cells. It was shown that 20 nm ceria nanoparticles in the concentrations of 3.5 , 10.5 and $23.3 \mu g/ml$ after 24 , 48 and 72 h exposure had an oxidative effect on A549 human lung cancer cells [56]. Cell viability was reduced proportionally to the administered dose of nanoparticles and the duration of the exposure. In the whole range of studied concentrations, the nanoparticles induced oxidative stress. The concentrations of glutathione and α -tocopherol were reduced, whilst the concentrations of malondialdehyde and lactate dehydrogenase, evidencing lipid peroxidation and cell membrane damage, were increased. The authors [57] showed that CDNs reduce viability of SMMC-7721 human hepatoma cells by inducing the apoptosis via the oxidative stress mechanism. CeO_2 nanoparticles significantly increase the production of ROS and simultaneously reduce the activity of superoxide dismutase, glutathione peroxidase and catalase.

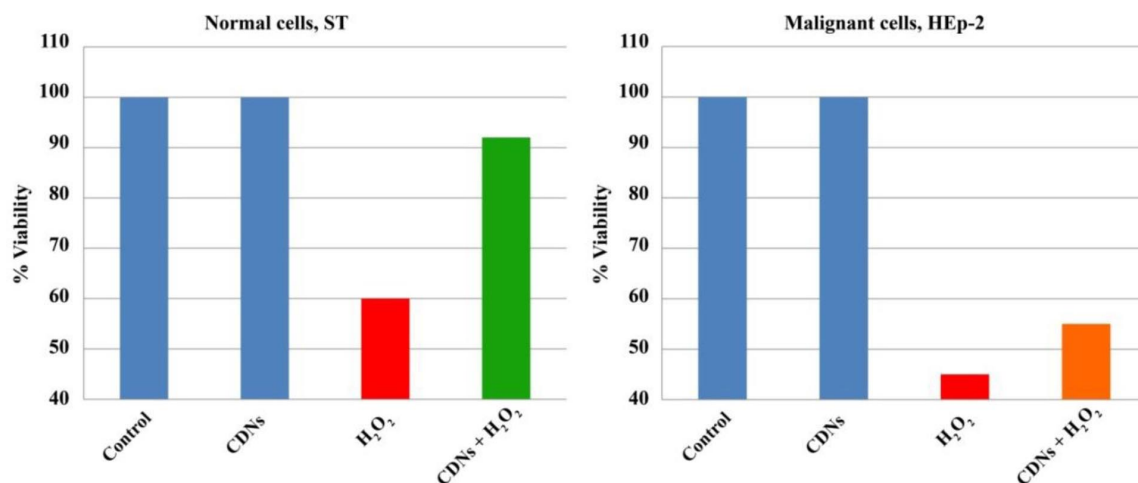


FIG. 14. The number of surviving diploid epithelial swine testicular (ST) and human epidermoid cancer (HEp-2) cells under the following conditions (left to right): control, in the presence of 63 μM cerium dioxide nanoparticles, in the presence of 0.5 mM hydrogen peroxide, in the presence of 0.5 mM hydrogen peroxide and 63 μM cerium dioxide nanoparticles [55]

Melanoma is the most aggressive type of skin cancer that is caused by the uncontrolled proliferation of melanocytes. Melanoma cells are highly metastatic and treatment of melanoma is ineffective, due to its high resistance to conventional chemotherapy. The authors investigated the inhibition of human melanoma cells (A375) by CDNs *in vitro* and *in vivo* in immunodeficient mice [58]. Unstabilized CeO₂ nanoparticles and nanoparticles coated with dextran were used in the experiments. According to the authors, Ce³⁺/Ce⁴⁺ ratio in the particles was 67/33 and 21/79 respectively. It was found that nanoparticles were not toxic to stromal cells (fibroblasts and endothelial cells) in all the studied concentrations. However, in the presence of nanoparticles, the viability of tumor cells was significantly decreased. Inhibition of melanoma cells' activity was proportional to the applied concentration of ceria nanoparticles and the duration of exposure. Analysis of the oxidative stress and apoptosis indicators showed that the presence of CDNs caused oxidative stress in cancer cells, resulting in their lower viability and reduced proliferation. The authors showed that CDNs (particle size 3–5 nm, dextran-stabilized) had a cytotoxic effect on SCL-1 carcinoma tumor cells and also reduced their proliferation [59]. Simultaneously, CDNs were non-toxic to the stromal cells and were capable of protecting normal (non-malignant) human dermal fibroblasts from oxidative stress. CeO₂ nanoparticles (with a size of about 100 nm) were synthesized by two different techniques [60]. In the first case, the particles were annealed at 800 °C at the final step of the synthesis, whilst in the second case, the particles in the solution were heated up to a temperature of 60 °C. The first type of particles was presumably free of trivalent cerium, whereas the particles of the second type contained Ce³⁺ on the surface. The particles without trivalent cerium were slightly more toxic to the normal cells of the L929 line and significantly more toxic to PC-3 prostate cancer cells.

The study of parameters affecting the redox-properties of cerium dioxide will allow the designing of the ceria-based nanozymes for required biochemical processes. CDNs with a high level of non-stoichiometry protect both normal and malignant cells against ROS, whilst the stoichiometric CDNs could serve as pro-oxidants for both types of cells, as can be seen from Fig. 12 and Fig. 13. There is also a transient area between these two extremities: CeO₂ nanoparticles of a certain size and stoichiometry are capable of providing a selective protection in normal cells, and serve as an oxidative stress promoter in malignant cells. We have developed several techniques for the synthesis of ceria preparations with the desired physical and chemical parameters ("fine tuning", see Fig. 13). Examples of such preparations are the sols of cerium dioxide, stabilized by low molecular weight glucans [29,61]. The protective effects of thus prepared cerium dioxide particles, such as inactivation of the hydroxyl radicals or protection of cells against hydrogen peroxide, depend on the size of the particles, which in turn depends on the cerium/glucose ratio in the precursor's mixture [29]. It should be noted that hypoxia and the decrease of pH in tumors is caused by the enhanced aerobic glycolysis, where tumors "trap" glucose [54]. It is expected that a CDN-glucan composite is to have an enhanced affinity towards cancer cells. Furthermore, due to the glucose presence, such a composite would accelerate hypoxia and decrease the pH, whilst simultaneously enhancing the oxidative stress in tumor cells.

Absence of specificity of chemical drugs to cancer cells is the basic problem of oncology. Ceria-based selective protection from oxidative stress opens new frontiers in the redox treatment of malignant tumors [62–64].

7. CDN can destroy nitrogen radicals

Cerium dioxide nanoparticles are able to inactivate nitrogen-containing free radicals, including reactive nitrogen species (RNS). RNS act together with ROS to damage cells, causing nitrosative stress. Dowding *et al.* [65] have demonstrated the activity of CeO₂ particles against the nitrosyl (short-lived nitroxyl) radical (*NO). We have reported that nanocrystalline cerium dioxide also inactivates the stable nitroxyl radical (2,2,6,6-tetramethyl-4-piperidone-N-oxyl) [66]. Two types of CeO₂ nanoparticles were studied: 1–2 nm (stabilized by sodium citrate) and 3–5 nm (stabilized by sodium adenosine triphosphate). Interestingly, the inactivation rate was dependent on the particle size of CeO₂, where it increased proportionally as the particle size decreased. As the particle size decreases, Ce³⁺/Ce⁴⁺ ratio increases, so obviously trivalent cerium is crucial for the inactivation of radicals. Oxidation of Ce³⁺ during nitroxyl inactivation suggests that cerium oxide nanoparticles adopt the NO-reductase function and possibly serve as an electron donor. Dowding *et al.* [67] have shown the ability of CDNs to scavenge a highly reactive molecule of peroxyxynitrite (ONO₂⁻). The rate of inactivation was independent of the Ce³⁺/Ce⁴⁺ ratio on the surface of the particles, but was significantly reduced in the inert atmosphere.

8. CDN as phosphatase mimetic

It was recently shown that nanosized cerium oxide, which is capable of acting as oxidoreductases, could also exhibit phosphatase activity [68]. For example, cerium oxide catalyses the cleavage of the ester bond in the organic phosphoric acid esters, such as p-nitrophenyl phosphate, adenosine triphosphate, o-phospho-L-tyrosine, etc. The initial reaction rate increases with the decrease in the pH. The pre-oxidation of nanoceria by hydrogen peroxide leads to the decrease in the concentration of Ce³⁺ and also to the drastic decrease of the dephosphorylation reaction rates. A plausible mechanism of the phosphatase activity of CDNs can be studied by using the hydrolysis of p-nitrophenyl phosphate (NPP), which is a standard substrate for testing serum alkaline phosphatase. In the presence of the enzyme or CDNs the colourless NPP releases the phosphate group forming p-nitrophenol, which has a bright yellow colour in the alkaline medium (see Fig. 15). The figure also shows the plausible mechanism of CDNs' catalysis of the dephosphorylation of the organic compounds. The comparison of the simplified mechanism of phosphatase (Scheme 6(A)) and CDN (B) action shows that nanocrystalline cerium dioxide could hardly be called a phosphatase analog, since phosphate groups bind to cerium ions irreversibly. However, cerium phosphate is shown to be eliminated from the CeO₂ particle, resulting in the regeneration of its surface. The renewed particle could repeatedly take part in the reaction (similar to the enzyme) until the complete disappearance of the particle.

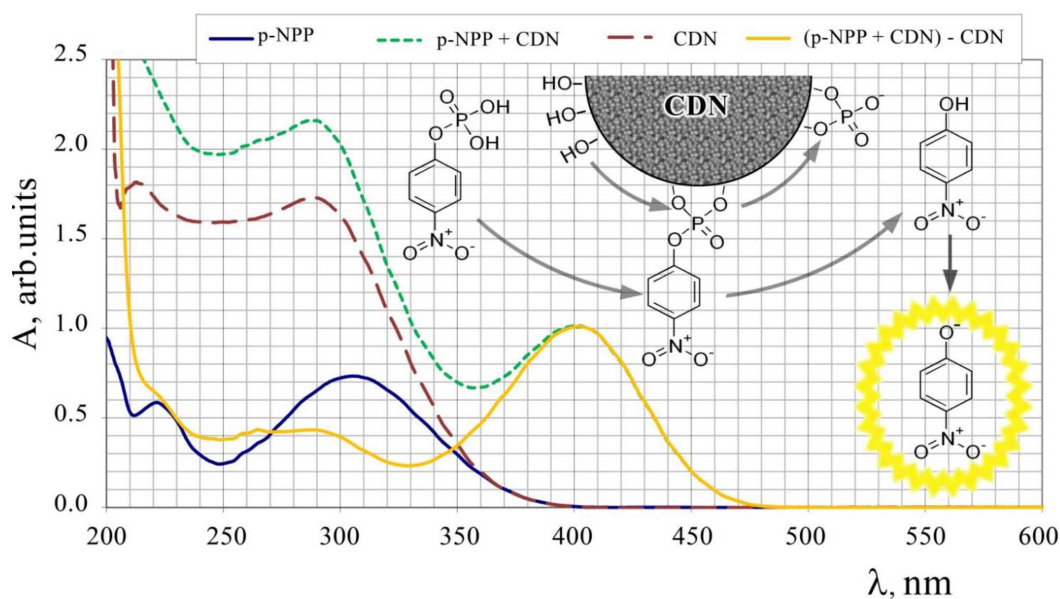
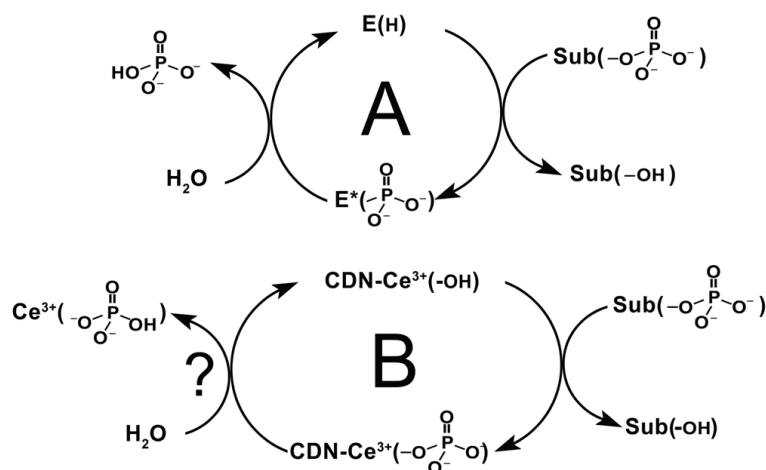


FIG. 15. The absorption spectra of p-nitrophenylphosphate (50 mM) before and after adding of CDNs (500 μM) at pH 7.8. Inset: Proposed mechanism of dephosphorylation of organic compounds in the presence of CDN



Scheme 6. CDN showing phosphatase-like activity

Jia *et al.* [69] used nanosized cerium dioxide for concentrating and quantitative dephosphorylation of phosphopeptides. Park *et al.* [70] reported that nanosized cerium oxide can initiate the phosphorylation of the mitogen-activated protein kinase in human bronchial epithelial cells (Beas2B).

The activation of the transcription factor NF- κ B depends on the phosphorylation of the protein-inhibitor by I κ B α kinases (IKK). NF- κ B is involved in inflammatory processes and is activated by the external physical or chemical factors (radiation, ultraviolet light or toxins), infectious agents (bacteria, viruses, parasites and their metabolic products), or by the signal molecules etc. Hyperactivation of the NF- κ B leads to the synthesis of a number of pro-inflammatory cytokines, such as the family of interleukins, the tumour necrosis factor (TNF- α), the γ -interferon and macrophages activator, etc. Stress-kinase p38 activates the cascade of arachidonic acid, which is released from the phospholipids in the course of cell membrane lipid peroxidation, thus activating the cyclooxygenase, which is followed by the synthesis of inflammatory prostaglandins and lipoxygenase; it is then followed by the synthesis of leukotrienes – the mediators of the immediate-type allergic reaction. All these cascades have a pro-oxidant function and enhance the inflammatory response. The possibility of the targeted regulation of activity of the nuclear transcription factor is promising for a large number of pathological processes in the cell. For instance, the toxins in cigarette smoke extracts cause an inflammatory response in H9c2 cardiomyocytes. Pre-treatment of cells with CeO₂ nanoparticles (10 nM for 24 hours incubation prior to administration of 10% cigarette smoke extract) improves the survival of the cells' culture [71]. Biochemical studies have shown that nanoparticles inhibit phosphorylation of I κ B α , thus reducing translocation of the p65 subunit, which is caused by the activation of NF- κ B. Furthermore, the cells treated with cerium dioxide nanoparticles have reduced levels of some interleukins, e.g. tumor necrosis factor and inducible nitric oxide synthase (iNOS).

For their own replication, viruses use the signalling pathways and transcription factors of living cells. They activate IKK kinase; phosphorylation of the protein-inhibitor I κ B causes the activation of the nuclear factor NF- κ B; this activation increases the expression of viral genetic material. Conventional antiviral drugs do not affect IKK cascades. Simultaneously, the use of prostaglandin A₁, which reduces the activity of IKK, results in a more than 3000-fold reduction of viral replication [72]. The development of effective drugs, inhibiting the phosphorylation of I κ B, and their introduction into clinical practice, would open a new avenue in the treatment of viral infections [13]. Reversible phosphorylation and dephosphorylation reactions constitute the basis of the energy, metabolism and signalling pathways in cells. Phosphatase-like properties of ceria nanoparticles open a new way in assessing and predicting the biological activities of cerium oxide nanoparticles [73]. Probably, in the near future, there will be investigations into other biochemical processes that involve CDNs as a phosphatase (phosphate anion or organic phosphates acceptor). For example, the study of acetylcholinesterase reactivation by CDNs would be advantageous for the development of novel antidotes against the intoxication by organophosphorus compounds, etc.

9. Conclusions

CDN-based nanozymes are being widely used in nanopharmaceutical applications (such as development of the nanoscale techniques of chemical analysis, and development of the biomaterials for implants, which exhibit the desired therapeutic effect depending on the composition of blood development of molecular sensors and biosensors, etc. [74]). It should be noted that ceria's behavior in living systems and its unique biological activity and ability to perform the function of certain enzymes are determined by a number of factors, many of which are yet to be

established. The scope of application of nano-ceria is far from being restricted to the examples presented here. While the potential of CDNs as an active component of pharmaceuticals of the new generation is already evident, the development and clinical trials of ceria-based preparations will require further joint interdisciplinary efforts.

Acknowledgments

This research has been supported by the Russian Science Foundation (project 17-73-10417).

References

- [1] Kirby A.J. Enzyme Mechanisms, Models, and Mimics. *Angew. Chem.*, Int. Ed. 1996, **35**, P. 706–724.
- [2] Breslow R. *Artificial Enzymes and Enzyme Models*, in *Advances in Enzymology and Related Areas of Molecular Biology*, ed. A. Meister, John Wiley & Sons, Inc., Hoboken, NJ, USA, 1986, V. 58, pp. 1–60.
- [3] Schmuck C., Merschky M., Rether C., Geibel B. *Artificial Enzyme Mimics*, in *Supramolecular Chemistry: from Molecules to Nanomaterials*, ed. J.W. Steed and P.A. Gale, 2012.
- [4] Breslow R., Overman L.E., “Artificial enzyme” combining a metal catalytic group and a hydrophobic binding cavity. *J. Am. Chem. Soc.* 1970, **92**, P. 1075–1077.
- [5] Manea F., Houillon F.B., Pasquato L., Scrimin P. Nanozymes: Gold-Nanoparticle-Based Transphosphorylation Catalysts. *Angew. Chem.*, Int. Ed. 2004, **43**, P. 6165–6169.
- [6] Hu X.N., Liu J.B., Hou S., Wen T., Liu W.Q., Zhang K., He W.W., Ji Y.L., Ren H.X., Wang Q., Wu X.C. Research progress of nanoparticles as enzyme mimetics. *Sci. China Phys. Mech. Astron.*, 2011, **54**, P. 1749–1756.
- [7] Wei H., Wang E. Nanomaterials with enzyme-like characteristics (nanozymes): next-generation artificial enzymes. *Chem. Soc. Rev.*, 2013, **42**, P. 6060–6093.
- [8] Wang Z., Quan Z., Lin J. *Inorg. Chem.*, 2007, **46**, P. 5237.
- [9] Shcherbakov A.B., Ivanov V.K., Zholobak N.M., Ivanova O.S., Krysanov E.Y., Baranchikov A.E., Spivak N.Ya., Tretyakov Y.D. Nanocrystalline ceria based materials-Perspectives for biomedical application. *Biophysics*, 2011, **56**, P. 987–1004.
- [10] Ivanov V.K. Habil. Thesis, IGIC RAS of Moscow, 2011.
- [11] Ivanov V.K., Polezhaeva O.S., Shcherbakov A.B., Gil' D.O., Tret'yakov Y.D. Microwave-hydrothermal synthesis of stable nanocrystalline ceria sols for biomedical uses. *Russ. J. Inorg. Chem.*, 2010, **55**, P. 1–5.
- [12] Ivanov V.K., Polezhaeva O.S., Shaporev A.S., Baranchikov A.E., Shcherbakov A.B., Usatenko A.V. Synthesis and thermal stability of nanocrystalline ceria sols stabilized by citric and polyacrylic acids. *Russ. J. Inorg. Chem.* 2010, **55**, P. 328–332.
- [13] Ivanov V.K., Shcherbakov A.B., Baranchikov A.E., Kozik V.V. *Synthesis, structure, physicochemical properties and biological activity of nanodispersed cerium dioxide*. Tomsk, Tomsk State University, 2013.
- [14] Ivanova O.S., Shekunova T.O., Ivanov V.K., Shcherbakov A.B., Popov A.L., Davydova G.A., Tret'yakov Y.D. One-stage synthesis of ceria colloid solutions for biomedical use. *Doklady Chem.*, 2011, **437**, P. 103–106.
- [15] Ivanov V.K., Shcherbakov A.B., Usatenko A.V. Structure-sensitive properties and biomedical applications of nanodispersed cerium dioxide. *Russ. Chem. Rev.*, 2009, **78**, P. 855–871.
- [16] Sun C., Xue D. Size-dependent oxygen storage ability of nano-sized ceria. *Phys. Chem.*, 2013, **15**(34), P. 14414–14419.
- [17] Tarnuzzer R.W., Colon J., Patil S., Seal S. Vacancy engineered ceria nanostructures for protection from radiation-induced cellular damage. *Nano Lett.*, 2005, **5**, P. 2573–2577.
- [18] Heckert E.G., Karakoti A.S., Seal S., Self W.T. The role of cerium redox state in the SOD mimetic activity of nanoceria. *Biomater.*, 2008, **29**, P. 2705–2709.
- [19] Karakoti A.S., Singh S., Kumar A., Malinska M., Kuchibhatla S.V.N.T., Wozniak K., Self W.T., Seal S. PEGylated nanoceria as radical scavenger with tunable redox chemistry. *J. Am. Chem. Soc.*, 2009, **131**, P. 14144–14145.
- [20] Korsvik C., Patil S., Seal S., Self W.T. Superoxide dismutase mimetic properties exhibited by vacancy engineered ceria nanoparticles. *Chem. Commun.*, 2007, P. 1056–1058.
- [21] Shcherbakov A.B., Ivanov V.K., Sirota T.V., Tret'yakov Y.D. Inhibition of adrenaline autooxidation by nanocrystalline ceria. *Doklady Chem.*, 2011, **437**, P. 60–62.
- [22] Klochkov V.K., Grigorova A.V., Sedyh O.O., Malyukin Yu.V. The influence of agglomeration of nanoparticles on their superoxide dismutase-mimetic activity. *Colloids Surf. A.*, 2012, **409**, P. 176–182.
- [23] Batinić-Haberle I., Rebouças J.S., Spasojević I. Superoxide dismutase mimics: chemistry, pharmacology, and therapeutic potential. *Antioxid. Redox Signal.*, 2010, **13**, P. 877–918.
- [24] Iranzo O. Manganese complexes displaying superoxide dismutase activity: A balance between different factors. *Bioorg. Chem.*, 2011, **39**, P. 73–87.
- [25] Yu P., Hayes S.A., O'Keefe T.J., O'Keefe M., Stoffer J.O. The phase stability of cerium species in aqueous systems II. The Ce(III/IV)-H₂O-H₂O₂/O₂ systems. Equilibrium considerations and Pourbaix diagram calculations. *J. Electrochem. Soc.*, 2006, **153**, P. C74–C79.
- [26] Manda G., Nechifor M.T., Neagu T.-M. Reactive oxygen species, cancer and anti-cancer therapies. *Curr. Chem. Biol.*, 2009, **3**, P. 22–46.
- [27] Evans M.G., Uri N. Photo-oxidation of water by ceric ions. *Nature*, 1950, **166**(4223), P. 602–603.
- [28] Xue Y., Luan Q., Yang D., Yao X., Zhou K. Direct evidence for hydroxyl radical scavenging activity of cerium oxide nanoparticles. *J. Phys. Chem. C*, 2011, **115**, P. 4433–4438.
- [29] Shcherbakov A.B., Zholobak N.M., Ivanov V.K., Ivanova O.S., Marchevsky A.V., Baranchikov A.E., Tretyakov Y.D. Synthesis and antioxidant activity of biocompatible maltodextrin-stabilized aqueous sols of nanocrystalline ceria. *Russ. J. Inorg. Chem.*, 2012, **57**, P. 1411–1418.
- [30] Babu S., Velez A., Wozniak K., Szydłowska J., Seal S. Electron paramagnetic study on radical scavenging properties of ceria nanoparticles. *Chem. Phys. Lett.*, 2007, **442**, P. 405–408.
- [31] Asati A., Santra S., Kaitanis C., Nath S., Perez J.M. Oxidase-like activity of polymer-coated cerium oxide nanoparticles. *Angew. Chem. Int. Ed.*, 2009, **48**, P. 2308–2312.

- [32] Peng Y., Chen X., Yi G., Gao Z. Mechanism of the oxidation of organic dyes in the presence of nanocerium. *Chem. Commun.*, 2011, **47**, P. 2916–2918.
- [33] Pautler R., Kelly E.Y., Huang P.J.J., Cao J., Liu B., Liu J. Attaching DNA to nanocerium: Regulating oxidase activity and fluorescence quenching. *ACS Appl. Mater. Interfaces*, 2013, **5**, P. 6820–6825.
- [34] Makarov S.Z., Ladeinova L.V. Peroxy compounds of cerium. *Russ. Chem. Bull.*, 1961, **10**, P. 1091–1096.
- [35] Karakoti A.S., Munusamy P., Hostetler K., Kodali V., Kuchibhatla S., Orr G., Pounds J.G., Teeguarden J.G., Thrall B.D., Baer D.R. Preparation and characterization challenges to understanding environmental and biological impacts of nanoparticles. *Surf. Interface Anal.*, 2011, **44**, P. 882–889.
- [36] Floor M., Kieboom A.P.G., Van Bekkum H. *Recueil des Travaux Chimiques des Pays-Bas*. 1989, **108**, P. 128.
- [37] Rizkalla E.N., Lajunen L.H.J., Choppin G.R. Kinetics of the decomposition of hydrogen peroxide in the presence of ethylenediaminetetraacetatoceria(IV) complex. *Inorg. Chim. Acta.*, 1986, **119**, P. 93–98.
- [38] Heckert E.G., Seal S., Self W.T. Fenton-like reaction catalyzed by the rare earth inner transition metal cerium. *Environ. Sci. Technol.*, 2008, **42**, P. 5014–5019.
- [39] Halbhuer K.J., Hulstaert C.E., Feuerstein H., Zimmermann N. Cerium as capturing agent in phosphatase and oxidase histochemistry. Theoretical background and applications. *Prog. Histochem. Cytochem.*, 1994, **28**, P. 1–120.
- [40] Pirmohamed T., Dowding J.M., Singh S., Wasserman B., Heckert E., Karakoti A.S., King J.E., Seal S., Self W.T. Nanocerium exhibit redox state-dependent catalase mimetic activity. *Chem. Commun.* 2010, **46**, P. 2736–2738.
- [41] Das S., Dowding J.M., Klump K.E., McGinnis J.F., Self W., Seal S. Cerium oxide nanoparticles: applications and prospects in nanomedicine. *Nanomedicine*, 2013, **8**, P. 1483–1508.
- [42] Perez J.M., Asati A., Nath S., Kaitanis A. Synthesis of biocompatible dextran-coated nanocerium with pH-dependent antioxidant properties. *Small*, 2008, **4**, P. 552–556.
- [43] Ivanov V.K., Usatenko A.V., Shcherbakov A.B. Antioxidant Activity of Nanocrystalline Ceria to Anthocyanins. *Russ. J. Inorg. Chem.*, 2009, **54**, P. 1522–1527.
- [44] Jiao X., Song H., Zhao H., Bai W., Zhang L., Lv Y. Well-redispersed ceria nanoparticles: Promising peroxidase mimetics for H₂O₂ and glucose detection. *Anal. Methods.*, 2012, **4**, P. 3261–3267.
- [45] Stoianov O.O., Ivanov V.K., Shcherbakov A.B., Stoyanova I.V., Chivireva N.A., Antonovich V.P. Determination of cerium(III) and cerium(IV) in nanodisperse ceria by chemical methods. *Russ. J. Inorg. Chem.*, 2014, **59**, P. 15–23.
- [46] Linnane A.W., Kios M., Vitetta L. Healthy aging: regulation of the metabolome by cellular redox modulation and prooxidant signaling systems: the essential roles of superoxide anion and hydrogen peroxide. *Biogerontology*, 2007, **8**, P. 445–467.
- [47] Finkel T., Holbrook N.J. Oxidants, oxidative stress and the biology of ageing. *Nature*, 2000, **408**(6809), P. 239–247.
- [48] Smith R.A., Murphy M.P. Mitochondria-targeted antioxidants as therapies. *Discov. Med.*, 2011, **11**, P. 106–114.
- [49] Shepel E.A., Zholobak N.M., Shcherbakov A.B., Antonovitch G.V., Yanchiy R.I., Ivanov V.K., Tretyakov Y.D. Ceria Nanoparticles Boost Activity of Aged Murine Oocytes. *Nano Biomed. Eng.*, 2012, **4**, P. 188–194.
- [50] Courbiere B., Auffan M., Rollais R., Tassistro V., Bonnefoy A., Botta A., Perrin J. Ultrastructural interactions and genotoxicity assay of cerium dioxide nanoparticles on mouse oocytes. *Int. J. Mol. Sci.*, 2013, **14**, P. 21613–21628.
- [51] Chane-Ching J.-Y. Cerium IV compound and method for its preparation. *Europ. Pat.* EP0208580 B1, 1990.
- [52] Zholobak N., Shcherbakov A., Ivanov V., Olevinskaya Z., Spivak N. Antiviral effectivity of ceria colloid solutions. *Antiviral Res.*, 2011, **90**, P. A67.
- [53] Song C.W., Griffin R., Park H.J. *Influence of tumor pH on therapeutic response*. In: *Cancer Drug Resistance*. ed. Teicher B.A. Humana Press, New Jersey, 2006, P. 21–42.
- [54] Osinsky S., Vaupel P. *Microphysiology of tumors*. Naukova dumka, Kiev, 2009.
- [55] Zholobak N.M., Shcherbakov A.B., Bogorad-Kobelska A.S., Ivanova O.S., Baranchikov A.Ye., Spivak N.Ya., Ivanov V.K. Panthenol-stabilized cerium dioxide nanoparticles for cosmetic formulations against ROS-induced and UV-induced damage. *J. Photochem. Photobiol. B*, 2014, **130**, P. 102–108.
- [56] Lin W., Huang Y.W., Zhou X.D., Ma Y. Toxicity of cerium oxide nanoparticles in human lung cancer cells. *Int. J. Toxicol.*, 2006, **25**, P. 451–457.
- [57] Cheng G., Guo W., Han L., Chen E., Kong L., Wang L., Ai W., Song N., Li H., Chen H. Cerium oxide nanoparticles induce cytotoxicity in human hepatoma SMMC-7721 cells via oxidative stress and the activation of MAPK signaling pathways. *Toxicol. Vitro*, 2013, **27**, P. 1082–1088.
- [58] Alili L., Sack M., von Montfort C., Giri S., Das S., Carroll K.S., Zanger K., Seal S., Brenneisen P. Downregulation of tumor growth and invasion by redox-active nanoparticles. *Antioxid. Redox Signal*, 2013, **19**, P. 765–778.
- [59] Alili L., Sack M., Karakoti A.S., Teuber S., Puschmann K., Hirst S.M., Reilly C.M., Zanger K., Stahl W., Das S., Seal S., Brenneisen P. Combined cytotoxic and anti-invasive properties of redox-active nanoparticles in tumor-stroma interactions. *Biomaterials*, 2011, **32**, P. 2918–2929.
- [60] Renu G., Divya V.V. Rani, Nair S.V., Subramanian K.R.V., Lakshmanan V.K. Development of cerium oxide nanoparticles and its cytotoxicity in prostate cancer cells. *Adv. Sci. Lett.*, 2012, **6**, P. 17–25.
- [61] Scherbakov A.B., Ivanov V.K., Zholobak N.M., Baranchikov A.E., Spivak N.Y., Ivanova O.S., Tretyakov Y.D. *Rus. Pat.* RU2012112921 C1, 2012.
- [62] Wondrak G.T. Redox-directed cancer therapeutics: Molecular mechanisms and opportunities. *Antioxid. Redox Signal*, 2009, **11**, P. 3013–3069.
- [63] McGinnis J.F., Wong L.L., Zhou X. Inhibition of neovascularization by cerium oxide nanoparticles, *US Pat.* US20090269410 A1, 2009.
- [64] Wason M.S., Zhao J. Cerium oxide nanoparticles: potential applications for cancer and other diseases. *Am. J. Transl. Res.*, 2013, **5**, P. 126–131.
- [65] Dowding J.M., Dosani T., Kumar A., Seal S., Self W.T. Cerium oxide nanoparticles scavenge nitric oxide radical (NO). *Chem. Commun.*, 2012, **48**, P. 4896–4898.
- [66] Ivanov V.K., Shcherbakov A.B., Ryabokon' I.G., Usatenko A.V., Zholobak N.M., Tretyakov Y.D. Inactivation of the nitroxyl radical by ceria nanoparticles. *Doklady Chem.*, 2010, **430**, P. 43–46.

- [67] Dowding J.M., Seal S., Self W.T. Cerium oxide nanoparticles accelerate the decay of peroxynitrite (ONOO⁻). *Drug Deliv. Transl. Res.*, 2013, **3**, P. 375–379.
- [68] Kuchma M.H., Komanski C.B., Colon J., Teblum A., Masunov A., Alvarado B., Babu S., Seal S., Summy J., Baker C.H. Phosphate ester hydrolysis of biologically relevant molecules by cerium oxide nanoparticles. *Nanomed. Nanotech. Biol. Med.*, 2010, **6**, P. 738–744.
- [69] Jia W., Andaya A., Leary J.A. Novel mass spectrometric method for phosphorylation quantification using cerium oxide nanoparticles and tandem mass tags. *Anal. Chem.*, 2012, **84**, P. 2466–2473.
- [70] Park E.J., Choi J., Park Y.K., Park K. Oxidative stress induced by cerium oxide nanoparticles in cultured BEAS-2B cells. *Toxicology*, 2008, **245**, P. 90–100.
- [71] Niu J.L., Wang K.K., Kolattukudy P.E. Cerium oxide nanoparticles inhibit oxidative stress and nuclear factor- κ B activation in H9c2 cardiomyocytes exposed to cigarette smoke extract. *J. Pharmacol. Exp. Ther.*, 2011, **338**, P. 53–61.
- [72] Amici C., Belardo G., Rossi A., Santoro M.G. Activation of I κ B kinase by herpes simplex virus Type 1. A novel target for anti-herpetic therapy. *J. Biol. Chem.*, 2001, **276**, P. 28759–28766.
- [73] Celardo I., Pedersen J.Z., Traversa E., Ghibelli L. Pharmacological potential of cerium oxide nanoparticles. *Nanoscale*, 2011, **3**, P. 1411–1420.
- [74] Rytting H. Pharmaceutical nanotechnology: A new section in IJP. *Int. J. Pharm.*, 2004, **281**, P. 1.

CdS quantum dot sensitized zinc oxide based solar cell with aluminum counter electrodeA. Ganguly¹, S. S. Nath², G. Gope², M. Choudhury¹¹National Institute of Technology, Silchar, Assam-788010, India²CIL, Assam University, Silchar, Assam- 788011, India

avigyan_ganguly@hotmail.com, nathss08@gmail.com, gopemail@gmail.com, m_chhanda@rediffmail.com

DOI 10.17586/2220-8054-2017-8-6-782-786

High cost conducting metals such as Au or Pt are generally used as counter electrodes in quantum dot sensitized solar cells. In this article, we report working of a CdS quantum dot sensitized ZnO thin film solar cell, having FTO as working electrode and aluminium as counter electrode. The CdS quantum dots are prepared by simple low cost chemical technique and characterized by absorption spectroscopy, X-ray diffraction, atomic force microscopy and high resolution trans electron microscopy. These quantum dots are used as an active layer in a solar cell and current density–voltage characteristic of the solar cell is obtained under white light illumination and dark conditions.

Keywords: CdS quantum dots, solar cell, Al counter electrode.

Received: 20 September 2017

Revised: 12 October 2017

Final revision: 1 November 2017

1. Introduction

The Shockley-Queisser limit predicts that due to thermodynamic limitations, the conversion efficiency in solar cells cannot exceed $\sim 32\%$ for single junction devices [1]. There are few methods for overcoming this upper limit, such as generating multiple electrons per photon, hot carrier extraction and the use of multiple layers, such as tandem devices [2]. Among various wide band gap semiconductors, TiO₂ and ZnO are widely used in photovoltaic cells because of their high carrier mobilities and energy levels [3]. In this context, ZnO is better suited as an active layer because the nanostructures can be easily formed and it has a large diffusion coefficient [4]. Quantum dots are used as sensitizing materials in solar cells because of their unique properties such as large absorption coefficient, size tunable band gap, quantum confinement, large extinction coefficient which are beneficial for photosensitization purposes [5]. Size-tuned QDs can be incorporated in the fabrication of tandem and multijunction cells for improved utilization of the full solar spectrum [6]. In particular, CdS QDs have been used in the fabrication of devices because of their direct band gap electronic structure and broad light harvesting capability, spanning the UV, visible, and NIR regions of the spectrum [7].

The counter electrode plays a crucial role in the efficient working of solar cells. But commonly used counter electrode materials in QDSSCs suffers from major disadvantages. For example, platinum suffers from oxidation, migration, loss of active surface area which can ‘poison’ the oxide, reducing its activity and efficiency [8]. On contrary, though gold plated electrodes improve efficiency to certain extent in comparison to platinum, but it also suffers from the surface poisoning problem [9, 10]. Also, the high cost and purity requirement of platinum or gold makes them a less practical material for photovoltaic applications. Furthermore, carbon electrodes are a popular choice as counter electrode in Perovskite solar cells only, and are not compatible with QDSSCs. The polysulfide electrolyte that is employed as a redox electrolyte in quantum dot sensitized solar cells provides stability to the photoanode but introduces significant redox limitations in carbon based counter electrode through undesirable surface reactions [11]. In the present work aluminum (Al) metal plates has been explored as counter electrode instead of the commonly used electrode materials for QDSSC. Al does not suffer from surface poisoning problems and is compatible with polysulfide electrolytes. Also as an added advantage, Al is a cheap and readily available metal and thus can be considered a more practical and economic alternative counter electrode material for low cost photovoltaics.

In this work, we fabricated a Quantum Dot Solar cell with ZnO oxide layer and CdS as the sensitizing QD layer and aluminum plates as the counter electrode. The general structure and working of a QDSSC is shown in Fig 1. The colloidal quantum dots were synthesized using polyvinyl alcohol (PVA) as capping layer as it restrains the QD size growth during synthesis. Quantum dots were studied using UV-VIS, XRD, AFM and TEM. The current density v/s voltage characteristics of the QDSC were obtained and solar cell parameters such as open circuit voltage (V_{oc}), short circuit current (I_{sc}), fill factor (FF) and power conversion efficiency (PCE) values were calculated from it.

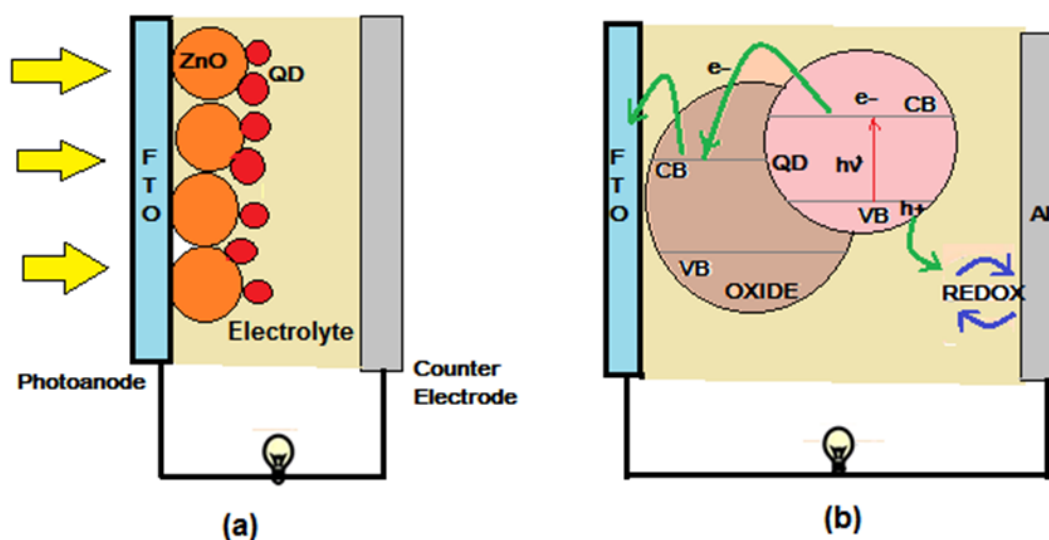


FIG. 1. (a) General structure and (b) working of a typical QDSSC

2. Experimental

2.1. CdS quantum dot synthesis

To synthesize CdS quantum dots by chemical route via one pot synthesis, 8 g of PVA were dissolved into 120 ml double distilled water. This mixture is taken in a three necked flask fitted with thermometer pocket and N_2 inlet. The solution was stirred in a magnetic stirrer at a rate of 200 rpm at a constant temperature of $70^\circ C$ for 5 hours. Thus, a transparent water solution of PVA was prepared. Similarly, a $CdCl_2$ solution was prepared by dissolving 7 g of $CdCl_2$ in 100 ml double distilled water. The solutions were degassed by N_2 bubbling for 3 – 4 h. Next, the PVA and $CdCl_2$ solutions were mixed and few drops of HNO_3 is added to the mixture followed by moderate stirring while an aqueous solution of Na_2S was added slowly by means of a dropper until the whole solution turned yellow. The precipitate was filtered out and washed with de-ionized water multiple times to remove the traces of PVA. This solution is kept in darkness at room temperature for 14 hours for its stabilization.

2.2. QDSSC fabrication

Zinc Acetate and Sodium Sulfide (Na_2S) were mixed in ethanol to obtain ZnO, which was then deposited on conductive FTO coated glass (resistivity $< 10 \text{ Ohm/sq.}$) by using tape template method and doctor's blade technique. Then it was heated at $80^\circ C$ and annealed at $450^\circ C$. Next, the ZnO coated glass plates were coated by immersion in the previously prepared CdS quantum dot solution to form CdS QD layer on the oxide by chemical bath deposition (CBD).

A polysulfide electrolyte solution was prepared by mixing 2M Na_2S and 3M S solutions [12]. A few drops of polysulfide solution were then added to the ZnO–CdS deposited FTO plate and then it was sandwiched with a thin aluminum plate, with thin glass cover slip spacers in between. The aluminum plate acted as a counter electrode and it was held together with the glass plate with adhesive tape and clips. Two metal crocodile clips were connected, with one to the FTO plate and the other to the aluminum plate.

3. Characterization

X-ray diffraction (XRD) patterns were obtained with a Philip X'pert X-ray diffractometer equipped with $Cu K\alpha$ irradiation ($\lambda = 1.5406 \text{ \AA}$). The high resolution microstructure images were obtained by a JEM-2100 electron microscope. UV-vis light absorption spectra were obtained using Perkin Elmer Lambda 35 ultraviolet visible (UV-vis) spectrophotometer. Current voltage values were obtained using a multimeter (Keithley 2001) and photocurrent values were obtained using 500 W xenon lamp illumination.

4. Results and discussion

Figure 2 shows the optical absorption spectra of CdS quantum dots. A strong absorbance edge is observed at 350 nm and from the absorbance edge, particle size has been estimated using hyperbolic band model [13]:

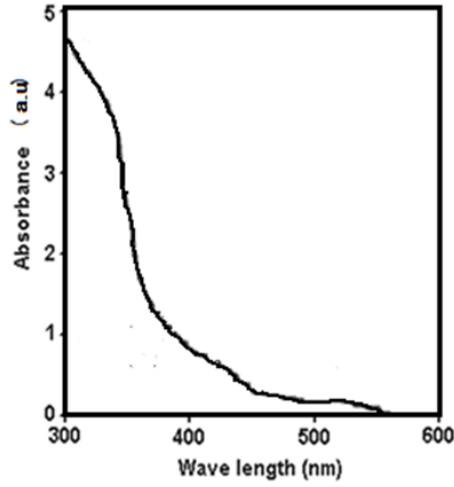


FIG. 2. UV-Visible absorption spectra of CdS quantum dots

$$R = \sqrt{\frac{2\pi^2 h^2 E_{gb}}{m^* (E_{gn}^2 - E_{gb}^2)}}, \quad (1)$$

where R is the quantum dot radius, E_{gb} is the bulk band gap, E_{gn} is the quantum dot band gap, h is Planck's constant, m^* is the effective mass of electron of the specimen. Here, the bulk band gap (E_{gb}) for CdS is 2.84 eV and electron effective mass at room temperature is $0.211m_0$ [10]; where m_0 is the electron rest mass. The quantum dot band gap (E_{gn}) of the prepared sample, as determined from the absorption edge wavelength is 3.54 eV for CdS. Thus, the radius (R) of the pure CdS quantum dots is determined to be around 4 nm i.e size is around 8 nm.

The XRD pattern for CdS quantum dots is shown in Fig. 3, the different peaks correspond to different crystalline planes of CdS. The average particle size (crystallite size) was obtained from X-ray diffraction data using the Scherrer formula [14, 15]:

$$D = \frac{0.9\lambda}{W \cos \theta}, \quad (2)$$

where, λ is the wavelength of the X-ray (0.1541 nm), W is FWHM (full width at half maxima), θ (theta) is the glancing angle and D is particle diameter (crystallite size). XRD investigation shows that pure CdS shows peaks at 24.8 (100), 29 (111) and 30 (200). Considering all the peaks (2θ in degree) in the X-ray diffractogram, the average crystallite (quantum dot) size was obtained using JCPDS to be 8.1 nm for CdS quantum dots.

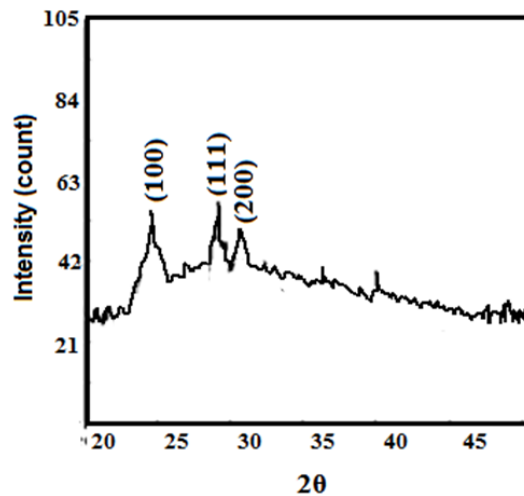


FIG. 3. XRD spectroscopy of CdS quantum dots

The surface topography and roughness of CdS quantum dots have been studied by atomic force microscope (AFM) as shown in Fig. 4(a) and the HRTEM image shows the formation of quantum dots in Fig. 4(b).

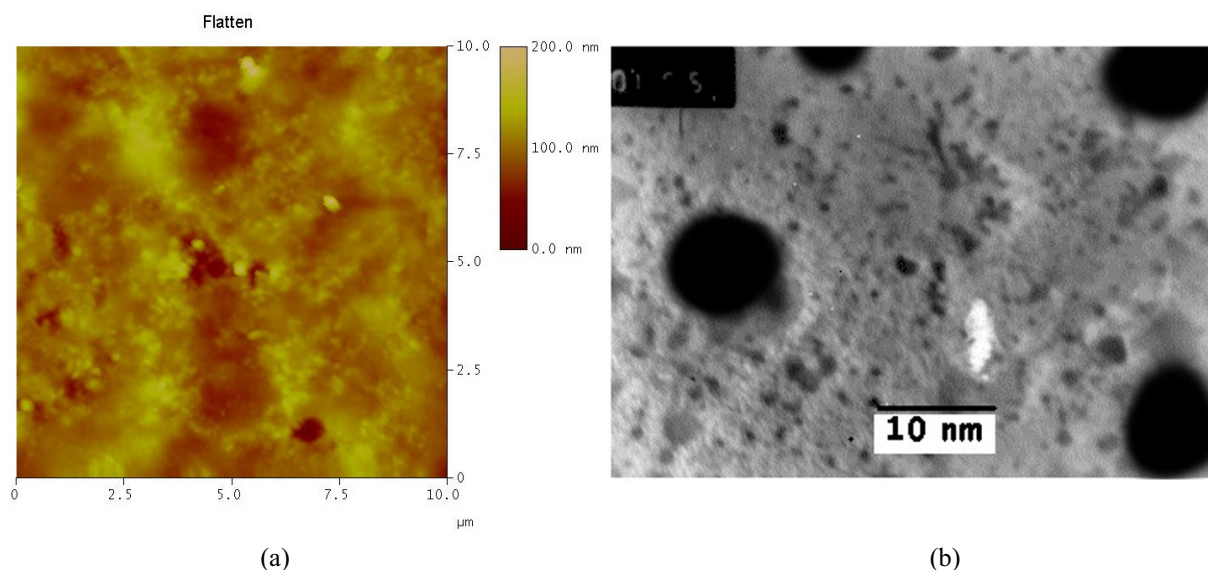


FIG. 4. (a) AFM topography of CdS quantum dots on PVA host; (b) HRTEM image of CdS quantum dots on PVA

The current density and voltage characteristics of the device were obtained under both dark and illuminated conditions. In order to study the photo-current characteristics, the fabricated device was illuminated by a white light 500 W xenon lamp with an illumination area of about 0.3 cm^{-2} and the current density (J) *v/s* voltage (V) was measured. In practice, the measurements were taken in 5 cycles, each at an interval of three days. As similar J - V characteristics were obtained each time, the single characteristics for the fabricated device are presented in Fig. 5. The short circuit current density (J_{sc}) and open circuit voltage (V_{oc}) were obtained from J - V curve. The fill factor (FF) and efficiency (η) were calculated using equations (3) and (4). The efficiency was found to be around 0.99 % and other solar cell parameters for the CdS QDSSCs are shown in Table 1. Previously, an efficiency of 0.69 % was obtained for a single layer CdS-QD/ZnO-based solar cell as reported by Chen et al. [14]. Thus, the fabricated QDSSC displayed higher efficiency.

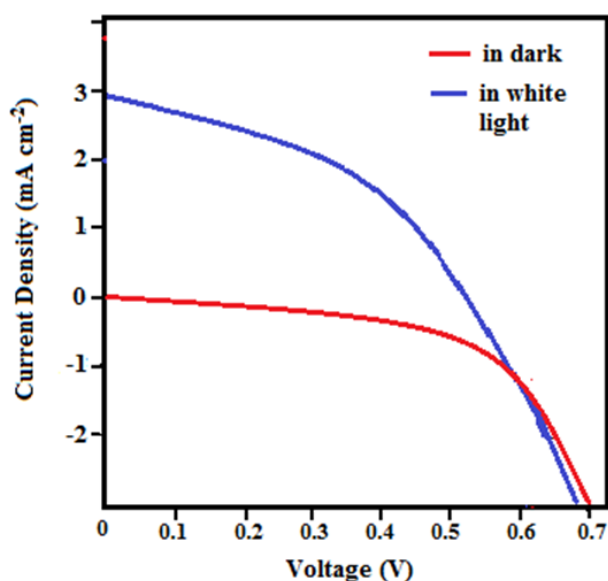


FIG. 5. Current density-voltage (J - V) characteristic in dark and white light illumination

TABLE 1. Solar cell parameters of the fabricated device

Solar cell parameters	Values obtained from J - V characteristics
J_{sc}	3 mA·cm ⁻²
V_{oc}	0.6 V
FF	0.55
η	0.99

$$FF = \frac{J_{\max} V_{\max}}{J_{sc} V_{oc}}, \quad (3)$$

$$\eta = \frac{V_{oc} \times I_{sc} \times FF}{P_{in}}. \quad (4)$$

5. Conclusion

CdS quantum dots were synthesized using a chemical method and were then characterized by using various techniques to determine their size, structural and optical properties. These quantum dots were introduced into a ZnO oxide based solar cell as sensitizing layer via simple dip coating technique. FTO glass was used as operating electrode and a low cost aluminum plate was used as counter electrode instead of commonly used platinum, gold or carbon based materials. The dark current and photocurrent response of the device clearly indicated that aluminum can be used as an alternate counter electrode material in low cost photovoltaic cells. An efficiency of as high as 0.99 % was obtained for the reported QDSSC device.

References

- [1] Shockley W., Queisser H.J. Detailed balance limit of efficiency of p-n junction solar cells. *Journal of Applied Physics*, 1961, **32**, P. 510–519.
- [2] Semonin O.E., Luther J.M., Beard M.C. Quantum dots for next-generation photovoltaics. *Materials Today*, 2012, **15**, P. 508–515.
- [3] Beard M.C., Luther J.M., Semonin O.E., Nozik A.J. Third generation photovoltaics based on multiple exciton generation in quantum confined semiconductors. *Accounts of Chemical Research*, 2013, **46** (6), P. 1252–1260.
- [4] Nozik A.J., et al. Semiconductor Quantum Dots and Quantum Dot Arrays and Applications of Multiple Exciton Generation to Third-Generation Photovoltaic Solar Cells. *Chem. Rev.*, 2010, **110**, P. 6873–6890.
- [5] Shabaev A., Hellberg C.S., Efros A.L. Efficiency of Multiexciton Generation in Colloidal Nanostructures. *Acc. Chem. Res.*, 2013, **46**, P. 1242–1251.
- [6] Martinson A.B.F., Goes M.S., et al. Electron Transport in Dye-Sensitized Solar Cells Based on ZnO Nanotubes: Evidence for Highly Efficient Charge Collection and Exceptionally Rapid Dynamics. *J. Phys. Chem. A*, 2009, **113**, P. 4015–4021.
- [7] Raja M., Muthukumarasamy N., et al. Enhanced photovoltaic performance of quantum dot-sensitized solar cell fabricated using Al-doped ZnO nanorod electrode. *Superlattices and Microstructures*, 2015, **80**, P. 53–62.
- [8] Sealy C. Problems with platinum. *Materials Today*, 2008, **11** (12), P. 65–68.
- [9] Seo M.H., Hwang W.P., Kim Y.K., Kim M.R. Improvement of Quantum Dot-Sensitized Solar Cells based on CdS and CdSe Quantum Dots. *37th IEEE Photovoltaic Specialists Conference (PVSC)*, 2011, DOI: 10.1109/PVSC.2011.6186493.
- [10] Jun H.K., Careem M.A., Arof A.K. Performances of some low-cost counter electrode materials in CdS and CdSe quantum dot-sensitized solar cells. *Nanoscale Res. Lett.*, 2014, **9** (1), P. 69.
- [11] Radich J.R., Dwyer R., Kamat P.V. Cu₂S Reduced Graphene Oxide Composite for High-Efficiency Quantum Dot Solar Cells. Overcoming the Redox Limitations of S²/S_n²⁻ at the Counter Electrode. *J. Phys. Chem. Lett.*, 2011, **2** (19), P. 2453–2460.
- [12] Badawi A., Al-Hosiny N., et al. CdTe quantum dots sensitized TiO₂ Electrodes for photovoltaic cells. *J. Mater. Sci. Eng. A*, 2011, **1**, P. 942–947.
- [13] Nath S.S., Chakdar D., et al. Green luminescence of ZnS and ZnS:Cu quantum dots embedded in zeolite matrix. *Journal of Applied Physics*, 2009, **105** (9), P. 4305.
- [14] Walton A.K., Moss T.S., Ellis B. Determination of Effective mass in the Lead Salts by Infra-red Farady Effect. *Proceedings of the Physical Society*, 1962, **79** (5), P. 1065.
- [15] Das R., Gope G., Nath S.S., Chakdar D. Improving the tuning phenomenon of CdS quantum dot by Fe³⁺ Doping. *J. Nanotech. Prog. Int.*, 2011, **4**, P. 6.
- [16] Chen H., Li W., Liu H., Zhu L. CdS quantum dots sensitized single- and multi-layer porous ZnO nanosheets for quantum dots-sensitized solar cells. *Electrochemistry Communications*, 2011, **13**, P. 331–334.

Synthetic pathway of a $\text{Cu}_2\text{ZnSnS}_4$ powder using low temperature annealing of nanostructured binary sulfides

N. S. Kozhevnikova¹, A. S. Vorokh¹, O. I. Gyrdasova¹, I. V. Baklanova¹, A. N. Titov^{2,3}, M. V. Kuznetsov¹

¹Institute of Solid State Chemistry of Ural Branch of Russian Academy of Sciences, 620990, Pervomayskaya str. 91, Ekaterinburg, Russian Federation

²Ural Federal University, 620002, Mira str. 19, Ekaterinburg, Russian Federation

³Mikheev Institute of Metal Physics of Ural Branch of Russian Academy of Sciences, 620108, S. Kovalevskaya str.18, Ekaterinburg, Russian Federation

kozhevnikova@ihim.uran.ru, vorokh@ihim.uran.ru, gyrdasova@ihim.uran.ru, baklanova@ihim.uran.ru, anti-tov@mail.ru, kuznetsov@ihim.uran.ru

PACS 81.05.Hd, 81.07.Bc, 81.16.Be, 81.10.Jt

DOI 10.17586/2220-8054-2017-8-6-787-792

Cost-effective route to quaternary $\text{Cu}_2\text{ZnSnS}_4$ nanostructured powder fabrication was developed by utilizing a two-step approach. In the first stage, nanostructured binary sulfides Cu_2S , ZnS , and SnS were synthesized by chemical bath deposition. In the second stage, ternary sulfide $\text{Cu}_2\text{ZnSnS}_4$ was obtained by low-temperature annealing of binary sulfides' mixtures at 70 and 300 °C. The compounds obtained on both stages were investigated by X-ray diffraction, scanning electron microscopy, optical absorbance and Raman spectroscopy. On the basis of our findings, we established that $\text{Cu}_2\text{ZnSnS}_4$ phase has already formed at 300 °C. The synthetic pathway revealed in this work allows reducing the temperature of $\text{Cu}_2\text{ZnSnS}_4$ synthesis and as a result, offers the possibility of reducing the manufacturing costs. This work was supported by the Russian Foundation for Basic Research (grant No. 16-03-00566), UrB RAS (grant No.15-20-3-11).

Keywords: nanopowder, CZTS, metal sulfides, low temperature annealing.

Received: 23 November 2017

Revised: 27 November 2017

1. Introduction

Earth abundant kesterite copper-zinc-tin-sulfide $\text{Cu}_2\text{ZnSnS}_4$ (CZTS) is considered as cost-effective material for next generation solar cells. CZTS, a quaternary chalcogenide p-type semiconductor, is actively studied as a photovoltaic material due to its high absorption coefficient ($\sim 10^4 \text{ cm}^{-1}$), optimal direct band energy of ~ 1.0 – 1.5 eV, as well as being composed of naturally abundant and nontoxic elements [1] In other words, CZTS contains non-toxic and cheap Zn and Sn, the production volume of which exceeds 20,000 and 500 times the volume of In production [2]. The similarity of the CZTS crystal structure and physical properties with $\text{CuIn}_x\text{Ga}_{(1-x)}\text{Se}_2$ (CIGS) allows production of solar cells by simply replacing the CIGS layer with a CZTS layer without developing a new technology [3–5]. The efficiency increase of solar cells prototypes based on CZTS was increased from 6.7 % [6] in 2009 to 10.1 % in 2011 [4].

The CZTS structure is described both stannite and kesterite [7]. Solid solution range of CZTS is significantly narrower than for CIGS [8]. One-phase powder can be synthesized from a precursor mixture with the elemental ratio: $\text{Cu}/(\text{Zn}+\text{Sn}) = 0.92$ – 0.95 and $\text{Zn}/\text{Sn} = 1.0$ – 1.03 [8]. However, in [9] it was assumed that the CZTS solid solution range with the kesterite structure is wider: $\text{Cu}/(\text{Zn}+\text{Sn}) = 0.97$, and $\text{Zn}/\text{Sn} = 1.42$. Higher energy conversion efficiency is demonstrated by CZTS powders, which are “enriched” in zinc and “depleted” in copper [10].

All methods of synthesizing CZTS, as well as CIGS, are traditionally divided into vacuum and non-vacuum procedures. Vacuum methods are based on the deposition of pure elements of atoms, comprising CZTS on a substrate by sputtering [11] or evaporation [12, 13] at certain pressures These methods require complex equipment and high power consumption, which leads to higher costs for the synthesized compounds. In order to reduce a production technology cost, non-vacuum deposition methods such as spraying with pyrolysis, electrochemical deposition, chemical bath deposition, are used. These techniques have been developed in the production of semiconductor CIGS and CdTe thin films [14] and now can be used for the synthesis of CZTS [15–18]. Chemical bath deposition method allows easy regulation of the reagent concentrations and the deposition time.

CZTS structure can be obtained by annealing at 55 °C [19]. According to this, the main limitation of chemical bath deposition method is that the temperature of the bath water cannot exceed 90–95 °C. In this study we propose decreasing the synthetic temperature by a two-step approach. In the first stage, nanostructured binary sulfides Cu_2S , ZnS , and SnS are synthesized by chemical bath deposition. In the second stage, ternary sulfide $\text{Cu}_2\text{ZnSnS}_4$

was obtained by low-temperature annealing of binary sulfides' mixtures at different temperatures. The compounds obtained at both stages were investigated by X-ray diffraction, scanning electron microscopy, optical absorbance and Raman spectroscopy.

2. Methods

Synthesis of the initial copper sulfide Cu_xS was carried out by the interaction of a soluble CuSO_4 salt using thiourea $\text{N}_2\text{H}_4\text{CS}$ as the sulfur source. The initial concentration of CuSO_4 and $\text{N}_2\text{H}_4\text{CS}$ were 0.01 and 0.03 M, respectively. Based on the concept of reversibility of the $\text{N}_2\text{H}_4\text{CS}$ hydrolytic decomposition in aqueous alkaline solutions, the reaction was carried out at $\text{pH} = 11.35$ and temperature 70°C for 2.5 hours. The pH was adjusted by adding aq. NH_4OH to the initial solution of CuSO_4 . After synthesis, the Cu_xS powder was filtered, washed with 0.1 M aq. NH_4OH and distilled water, and air-dried at room temperature.

The initial zinc sulfide powder ZnS was obtained by reaction of 0.02 M aq. ZnSO_4 with 0.1 M aq. sodium thiosulfate $\text{Na}_2\text{S}_2\text{O}_3$. The reaction was carried out at $\text{pH} = 6$ and temperature 90°C for 27 hours. The prolonged reaction time was due to the kinetic factor of decomposition of the sulfur source, $\text{Na}_2\text{S}_2\text{O}_3$. The obtained ZnS powder was also filtered, washed by distilled water and air-dried at room temperature.

To synthesize the initial SnS_x tin sulfide, 0.01 M aq. SnCl_2 and 0.05 M aq. sodium sulfide Na_2S were used. In aqueous solutions Sn^{2+} ions usually undergo hydrolysis; to suppress this process, the synthesis of SnS_x was carried out at $\text{pH} 0.46$ in a solution of ethylenediaminetetraacetic acid (EDTA, 0.01 M). The reaction mixture temperature in the SnS_x synthesis was 70°C , the deposition time was 3 hours. After synthesis, the resulting SnS_x powder was filtered and air-dried at room temperature.

Besides, the used pH values allowed obtaining not only the basic phases of the sulfides, but also a phase containing crystalline elemental sulfur.

The second stage is synthesis of the ternary sulfide $\text{Cu}_2\text{ZnSnS}_4$ by annealing the corresponding amounts of individual sulfides obtained at the first stage. Based on the X-ray phase analysis data, weights of 2 moles of CuS , 1 mole of ZnS and 1 mole of SnS_x were calculated. The sulfides CuS , ZnS and SnS_x were mixed, ground and pressed into tablets. The obtained tablets were annealed *in vacuo* at 70°C for two weeks and 300°C for two days. Elemental sulfur S_8 in the initial powders allowed us to conduct annealing experiments without the need for adding extra crystalline sulfur to the initial mixture.

X-ray diffraction (XRD) patterns of all composites were obtained using a Stadi automatic diffractometer with CuK_α ($\lambda = 1.5406 \text{ \AA}$) with 2θ angle step 0.03° and exposure time of 40 sec. Scanning electron microscopy (SEM) was carried out in order to analyze the microstructure and morphology of all synthesized samples using JEOL-JSM LA 6390. To confirm the change in bandgap, the UVVis spectra in the wavelength range of 300–700 nm (BaSO_4 was used as the standard) of composites were recorded using Shimadzu UV-2401 PC spectrophotometer. The chemical composition of the samples was determined by two methods: (i) by the energy-dispersive X-ray analysis (EDX) using a JEOL-JSM LA 6390 electron microscope with a JED 2300 analyzer; (ii) by X-ray photoelectron spectrometry (XPS) using ESCALAB MKII electron spectrometer with MgK_α ($E = 1253.6 \text{ eV}$) irradiation beam. The Raman spectra of the samples were obtained at room temperature on a RENISHAW-1000 spectrometer ($\lambda = 532 \text{ nm}$, $P = 25 \text{ mW}$).

3. Results and discussion

The phase composition, crystal structure and particle size (coherent scattering regions) of the individual sulfides synthesized at the first stage were studied by X-ray diffraction analysis. According to the diffraction data, Cu_xS powder contains 81 % CuS , 3 % Cu_2S , 16 % CuSO_4 (wt %). The content of initial salt CuSO_4 in the Cu_xS powder is explained by insufficient washing of the obtained Cu_xS after the reaction. The particle size of CuS was 10.6 nm. Zinc sulfide powder consists of the main ZnS phase 78 % and 22 % sulfur S_8 . The ZnS particle size was 4.6 nm. The synthesized powder SnS_x was a mixture of phases: 10 % SnS , 23 % SnS_2 , 14 % SnO , 53 % S_8 . The presence of tin oxide SnO was due to the impossibility to suppress the Sn^{2+} ions hydrolysis process.

The powder annealed at 70°C differs from initial mixture by presence of $\text{Cu}_5\text{Sn}_2\text{S}_7$ phase (Fig. 1). This indicates that formation of CZTS began from the intercalation of tin into the Cu_xS matrix.

Currently, different methods are required to characterize the crystal structure and compositional purity of CZTS nanoparticles obtained by the annealing at 300°C . Fig. 2 demonstrates the SEM images and XRD pattern. The EDX measurements revealed the compositional non-stoichiometry within the quaternary sulfide nanopowder. Therefore, CZTS particles have different structures. The XRD pattern (Fig. 2b) proved two binary sulfides CuS and SnS_2 to present in the CZTS powder as impurities. The CZTS phase cannot be identified by X-ray diffraction unambiguously, because three main peaks of ZnS and CuS coincide with three peaks of CZTS phase. Presence

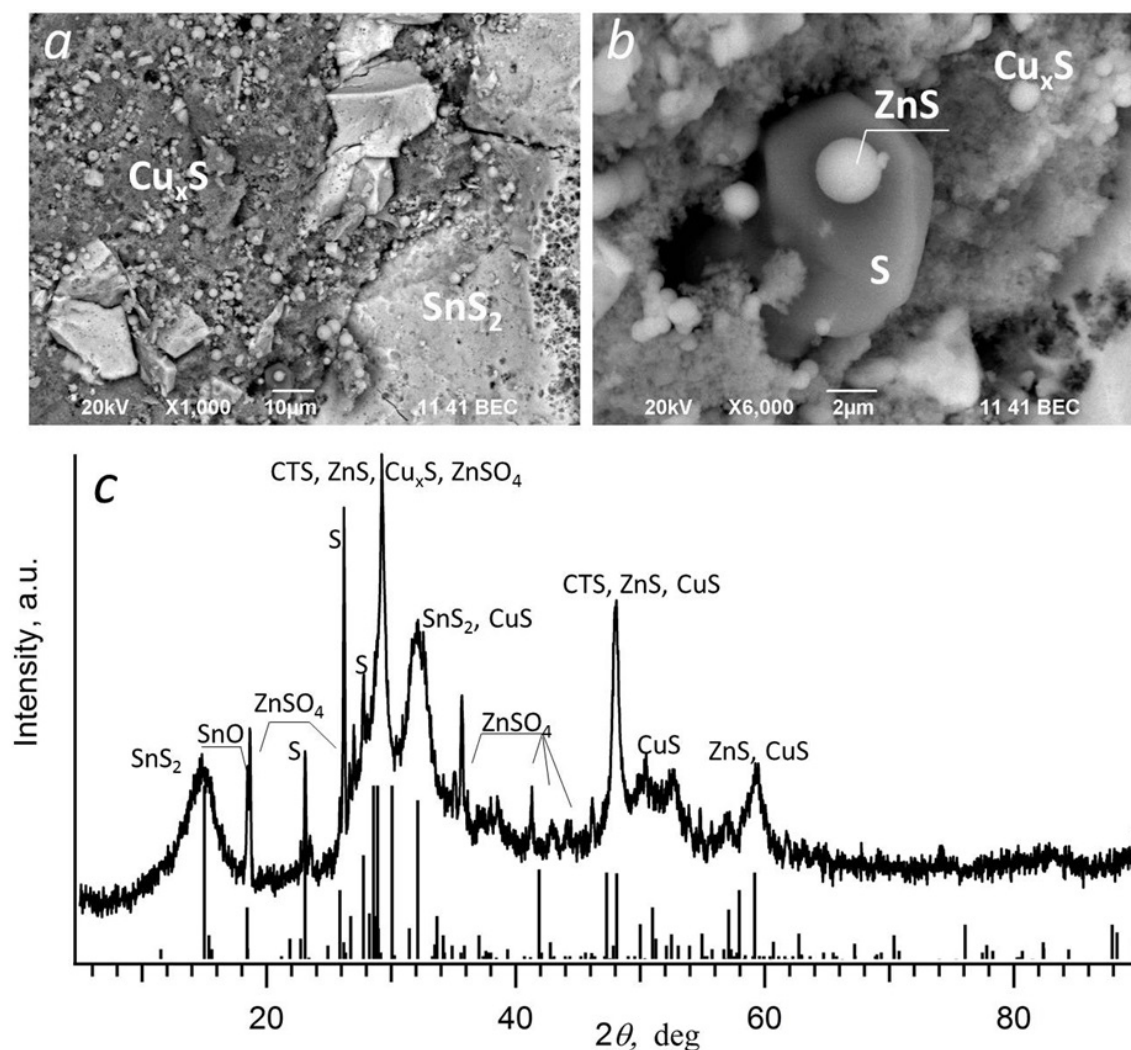


FIG. 1. a, b – SEM images of CZTS sample annealed at 70 °C. The composition of marked regions was determined by EDX analysis; c – XRD pattern of CZTS sample annealed at 70 °C. The main peaks are marked as belonging to phases CuS, CuS_2 , ZnS, ZnSO_4 , SnS_2 , SnO, $\text{Cu}_5\text{Sn}_2\text{S}_7$ (CTS)

of CZTS phase was determined by Raman shift spectroscopy (Fig. 3a). The most intense peak at 329 cm^{-1} corresponds to kesterite structure [20,21]. The small peaks at 248 , 289 and 370 cm^{-1} could be referred to as ‘shoulders’ of the main peak. It is important that the ZnS and CTS phases were not present in the Raman spectrum. This fact allowed the interpretation that the most intensive XRD peaks belong to the CZTS phase. According to X-ray diffraction analysis, the resulting powder was a mixture of $\text{Cu}_2\text{ZnSnS}_4$: SnS_2 :CuS phases, predominantly CZTS in a ratio of 96:2:2. The particle size of $\text{Cu}_2\text{ZnSnS}_4$ was $\sim 100\text{ nm}$.

The optical measurements are consistent with the XRD analysis and Raman spectroscopy data. Three inflections are visible in the optical absorption curve (Fig. 3). This indicates that the powder consists of three phases. In order to determine the effective band gap E_g of each phase, the experimental absorption spectra were reduced to the form $(\alpha h\nu)^2 = f(h\nu)$. Bandgap of 1.7 eV could be attributed to either $\text{Cu}_2\text{ZnSnS}_4$ or SnS_2 [22], 1.3 eV – to CuS, and 1.2 eV – to SnS. Increasing of the band gap to 1.7 eV in comparison to $E_g \approx 1.5\text{ eV}$ for bulk $\text{Cu}_2\text{ZnSnS}_4$ [23] may be due to either small particle size (100 nm), or to the ratio of $[\text{Sn}]/[\text{Cu}]$ in CZTS. According to experimental data [24], an increase in the fraction of [Sn] can lead to an increase in E_g for $\text{Cu}_2\text{ZnSnS}_4$ films up to 1.63 eV, but the mechanism of this phenomenon has not been studied yet.

Analysis of the stoichiometric ratios for the elements was carried out using XPS spectrometry. The XPS spectrum from the surface of the powder annealed at 300 °C is shown in Fig. 4. Apart from, the XPS measurements

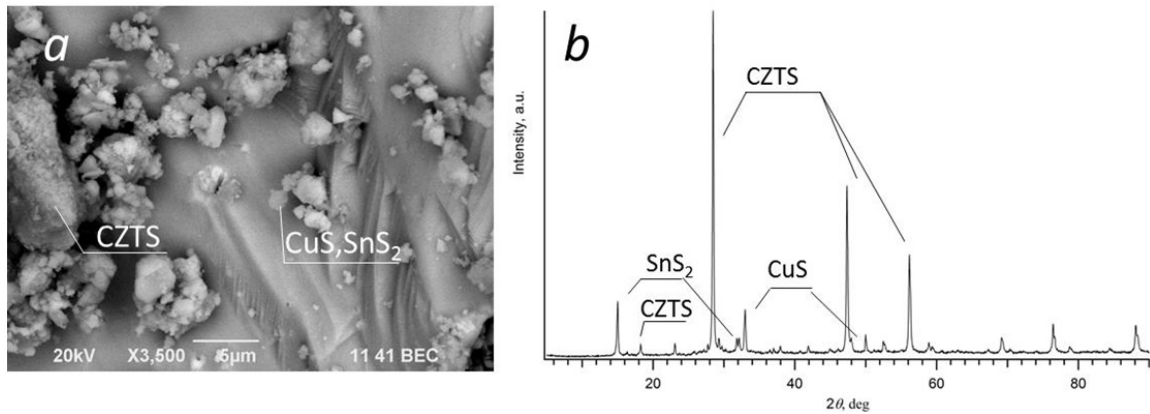


FIG. 2. a – SEM images of CZTS sample annealed at 300 °C. The composition of marked regions was determined by EDX analysis; b – XRD pattern of CZTS sample annealed at 300 °C

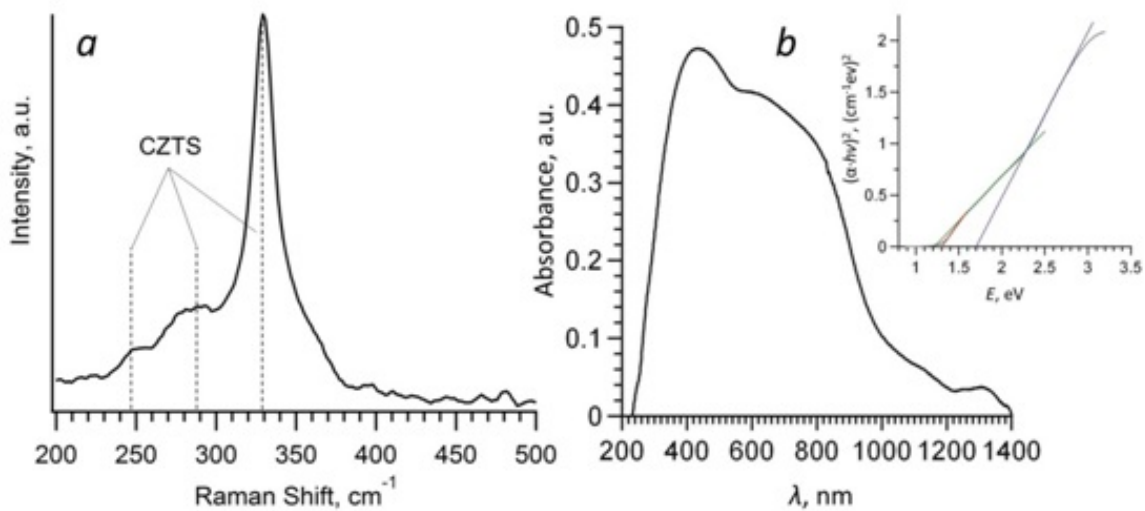


FIG. 3. Raman spectra (a) and optical absorbance (b) of CZTS sample annealed at 300 °C. In the inset: the Tauc plot was used for E_g determination. E_g ($\text{Cu}_2\text{ZnSnS}_4$) = 1.7 eV, E_g (CuS) = 1.3 eV, E_g (SnS) = 1.2 eV

were made after etching the sample by an argon beam. The etching led to removal of surface impurities. The elemental composition was quantified by measuring the partial area under the peaks: (i) in the case of metals (Cu, Zn, Sn) - according to the detailed XPS spectrum (right-hand insert in Fig. 4); (ii) in the case of sulfur according to the review spectrum. The results are shown by histogram (left-hand insert in Fig. 4).

The penetration sample depth of the XPS analysis is several nanometers. In contrast, the EDX chemical analysis allows a depth of about one micron within a local area. In order to compare these methods, elemental composition of the CZTS particle, shown in Fig. 2a, was investigated by using both XPS and EDX analyses. In its turn, the XRD data refer to the entire volume of the sample. Thus, the elemental composition analysis fulfilled by using all methods mentioned above made it possible to determine the distribution of metals and sulfur within synthesized nanopowder of quaternary sulfide.

The chemical composition data obtained by different methods are given in the Table 1. It can be seen from the Table that the Cu content on the surface is smaller than in the bulk. On the other hand, the Sn content is larger on the surface than in the bulk. This experimental fact could be explained by the suggestion that the tin-containing impurity phases are located mainly on the surface of the sample.

Obviously, the stoichiometry of the sample changes strongly both while moving from the surface into the bulk, and from the local area to the entire volume of the sample. According to EDX, there is a lack of tin and sulfur in a separate CZTS particle. The XRD data reveals that the powder composition has an exact stoichiometric ratio

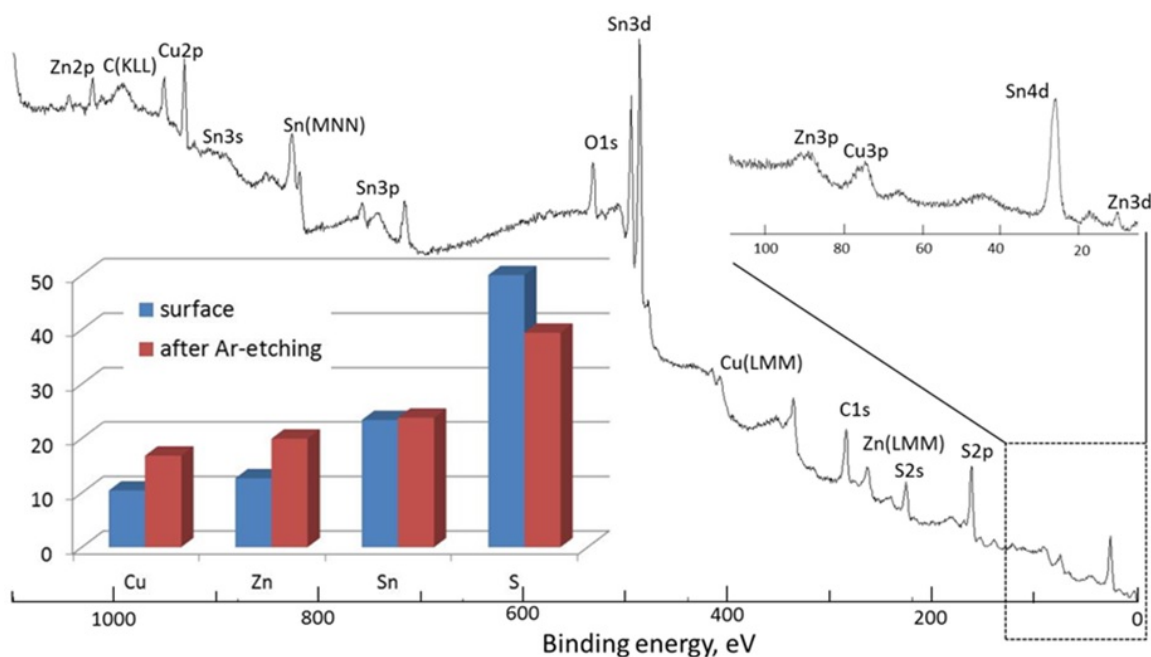


FIG. 4. Survey XPS spectrum for CZTS powder annealed at 300 °C. In the right-hand inset: detailed XPS spectrum of 0–110 eV range. In the left-hand inset bar chart of element content calculated from XPS data

TABLE 1. Chemical composition within nanopowder of quaternary sulfide CZTS synthesized at 300 °C obtained by XPS, EDX and XRD methods

Content	XPS-surface	XPS-Ar_20min etching	EDX, CZTS particle	XRD
Cu, at%	10.4	16.8	31.6	22.2
Zn, at%	12.7	19.9	15.5	15.8
Sn, at%	23.4	23.8	12.7	11.7
S, at%	53.5	39.4	40.2	50.3
Stoichiometry				
Cu/(Sn+Zn)	0.29	0.38	1.12	0.81
Zn/Sn	0.54	0.84	1.22	1.35
S/(Cu+Zn+Sn)	1.15	0.65	0.67	1.01

between metals and sulfur, but an excess of Zn is observed among metals. In its turn, the Raman spectroscopy data proved the absence separate Zn-containing phase, so Zn may be assumed to enter the CZTS lattice. In this case, the stoichiometric composition of the powder can be written approximately as follows: $\text{Cu}_{2-x}\text{Zn}_{1+x}\text{SnS}_4$, $x \approx 0.3$.

4. Conclusion

Thus, the use of nanocrystalline sulfides CuS, ZnS and SnS_x as intermediate compounds may lead to a decrease in the solid-phase synthesis temperature from the traditional 550 °C to 300 °C and the formation of $\text{Cu}_2\text{ZnSnS}_4$ in the nanocrystalline state. On the basis of our findings, we established that $\text{Cu}_2\text{ZnSnS}_4$ phase had already formed at 300 °C. The synthetic pathway revealed in this work allows reduction of the temperature at which $\text{Cu}_2\text{ZnSnS}_4$ synthesis occurs, and as a result, offers the possibility of reducing the manufacturing costs. Finally, it is apparent that the creation of compositionally uniform and stoichiometric multinary CZTS semiconductor nanoparticles requires further study.

Acknowledgments

This work was supported by the Russian Foundation for Basic Research (grant No. 16-03-00566), Ural Branch of Russian Academy of Sciences (grant No. 15-20-3-11), and was carried out in accordance with the scientific and research plans and state assignment of the ISSC UrB RAS (AAAA-A16-116122810214-9, AAAA-A16-116122810209-5).

References

- [1] Tan J.M.R., Lee Y.H., Pedireddy S., Baikie T., Ling X.Y., Wong L.H. Understanding the Synthetic Pathway of a Single-Phase Quarternary Semiconductor Using Surface-Enhanced Raman Scattering: A Case of Wurtzite $\text{Cu}_2\text{ZnSnS}_4$ Nanoparticles. *J. Am. Chem. Soc.*, 2014, **136**(18), P. 6684–6692.
- [2] USGS, Commodity Statistics and Information, USGS Minerals Information, 2010. URL: <http://minerals.usgs.gov/minerals/pubs/commodity/>.
- [3] Choubrac L., Lafond A., Guillot-Deudon C., Moëlo Y., Jobic S. Structure flexibility of the $\text{Cu}_2\text{ZnSnS}_4$ absorber in low-cost photovoltaic cells: from the stoichiometric to the copper-poor compounds. *Inorg. Chem.*, 2012, **51**(6), P. 3346–3348.
- [4] Barkhouse D.A.R., Gunawan O., Gokmen T., Todorov T.K., Mitzi D.B. Device characteristics of a 10.1% hydrazine-processed $\text{Cu}_2\text{ZnSn}(\text{Se,S})_4$ solar cell. *Prog. Photovolt: Res. Appl.*, 2012, **20**, P. 6–11.
- [5] Bag S., Gunawan O., Gokmen T., Zhu Y., Todorov T.K., Mitzi D.B. Low band gap liquid-processed CZTSe solar cell with 10.1% efficiency. *Energy Environ. Sci.*, 2012, **5**, P. 7060–7065.
- [6] Katagiri H., Jimbo K., Maw W.S., Oishi K., Yamazaki M., Araki H., Takeuchi A. Development of CZTS-based thin film solar cells. *Thin Solid Films*, 2009, **517**(7), P. 2455–2460.
- [7] Hall S.R., Szymanski J.T., Stewart J.M. Kesterite $\text{Cu}_2(\text{Zn Fe})\text{SnS}_4$ and stannite $\text{Cu}_2(\text{FeZn})\text{SnS}_4$ structurally similar but distinct minerals. *Can. Mineral.*, 1978, **16**, P. 131–137.
- [8] Muska K., Kauk M., Altosaar M., Pilvet M., Grossberg M., Volobujeva O. Synthesis of $\text{Cu}_2\text{ZnSnS}_4$ monograin powders with different compositions. *Energy Procedia*, 2011, **10**, P. 203–207.
- [9] Nozaki H., Fukano T., Ohta S., Seno Y., Katagiri H., Jimbo K. Crystal structure determination of solar cell materials: $\text{Cu}_2\text{ZnSnS}_4$ thin films using X-ray anomalous dispersion. *J. Alloys Comp.*, 2012, **524**, P. 22–25.
- [10] Katagiri H., Jimbo K., Tahara M., Araki H., Oishi K. The influence of the composition ratio on CZTS-based thin film solar cells. *MRS Proceedings*, 2009, P. 1165.
- [11] Ito K., Nakazawa T. Electrical and optical properties of stannite-type quaternary semiconductor thin films. *Japan. J. Appl. Phys.*, 1988, **27**(11R), P. 2094.
- [12] Katagiri H., Ishigaki N., Ishida T., Saito K. Characterization of $\text{Cu}_2\text{ZnSnS}_4$ thin films prepared by vapor phase sulfurization. *Japan. J. Appl. Phys.*, 2001, **40**(2R), P. 500.
- [13] Tanaka T., Kawasaki D., Nishio M., Guo Q., Ogawa H. Fabrication of $\text{Cu}_2\text{ZnSnS}_4$ thin films by co-evaporation. *Phys. Stat. Sol. C*, 2006, **3**(8), P. 2844–2847.
- [14] Hibberd C.J., Chassaing E., Liu W., Mitzi D.B., Lincot D., Tiwari A.N., Hibberd C.J., Chassaing E., Liu W., Mitzi D.B., Lincot D., Tiwari A.N. Non-vacuum methods for formation of $\text{Cu}(\text{In,Ga})(\text{Se,S})_2$ thin film photovoltaic absorbers. *Prog. Photovolt: Res. Appl.*, 2010, **18**, P. 434–452.
- [15] Nakayama N., Ito K. Sprayed films of stannite $\text{Cu}_2\text{ZnSnS}_4$. *Appl. Surf. Sci.*, 1996, **92**, P. 171–175.
- [16] Kamoun N., Bouzouita H., Rezig B. Fabrication and characterization of $\text{Cu}_2\text{ZnSnS}_4$ thin films deposited by spray pyrolysis technique. *Thin Solid Films*, 2007, **515**(15), P. 5949–5952.
- [17] Kumar Y.B.K., Babu G.S., Bhaskar P.U., Raja V.S. Preparation and characterization of spray-deposited $\text{Cu}_2\text{ZnSnS}_4$ thin films. *Sol. Energy Mater. Solar Cells*, 2009, **93**(8), P. 1230–1237.
- [18] Kumar Y.B.K., Babu G.S., Bhaskar P.U., Raja V.S. Effect of starting-solution pH on the growth of $\text{Cu}_2\text{ZnSnS}_4$ thin films deposited by spray pyrolysis. *Phys. Stat. Sol. A*, 2009, **206**(7), P. 1525–1530.
- [19] Scragg J.J., Dale P.J., Peter L.M. Towards sustainable materials for solar energy conversion: preparation and photoelectrochemical characterization of $\text{Cu}_2\text{ZnSnS}_4$. *Electrochem. Comm.*, 2008, **10**(4), P. 639–642.
- [20] Sun L., He J., Kong H., Yue F., Yang P., Chu J. Structure, composition and optical properties of $\text{Cu}_2\text{ZnSnS}_4$ thin films deposited by Pulsed Laser Deposition method. *Solar Energy Materials & Solar Cells*, 2011, **95**, P. 2907–2913.
- [21] Guc M., Levchenko S., Bodnar I.V., Izquierdo-Roca V., Fontane X., Volkova L.V., Arushanov E. Pérez-Rodríguez A. Polarized Raman scattering study of kesterite type $\text{Cu}_2\text{ZnSnS}_4$ single crystals. *Sci Rep.*, 2016, **6**, P. 19414.
- [22] Cifuentes C., Botero M., Romero E., Calderón C., Gordillo G. Optical and structural studies on SnS films grown by co-evaporation. *Braz. J. Phys.*, 2006, **36**(3b), P. 1046–1049.
- [23] Sarswat P.K., Free M.L. A study of energy band gap versus temperature for $\text{Cu}_2\text{ZnSnS}_4$ thin films. *Physica B: Cond. Mat.*, 2012, **407**(1), P. 108–111.
- [24] Malerba C., Biccari F., Ricardo C.L.A., Valentini M., Chierchia R., Müller M., Santoni A., Esposito E., Mangiapane P., Scardi P., Mittiga A. CZTS stoichiometry effects on the band gap energy. *J. Alloys and Compounds*, 2014, **582**, P. 528–534.

Generation of laser radiation by nanostructured solid active elements with selective optical nanoresonators formed in nanoporous aluminum oxide films

G. A. Lyubas

Vorozhtsov Institute of Organic Chemistry, Siberian Branch, Russian Academy of Sciences,
Novosibirsk, 630090 Russia
sciencenano@yandex.ru

PACS 82.45.Cc; 82.45.Aa; 82.45.Yz; 81.15.Pq; 81.07.-b; 33.50.-j; 78.45.+h; 42.55.Mv; 77.55.+f

DOI 10.17586/2220-8054-2017-8-6-793-797

The generation of laser radiation by a nanostructured solid active element with natural selective optical nanoresonator formed in a nanoporous aluminum oxide film activated with rhodamine 6G has been obtained for the first time. The lasing is characterized by high-quality radiation with the absence of a spontaneous component. Chemical deposition of noble metals leads to the formation of internal nanoresonator into the porous structure. This reduces generation threshold more than two fold.

Keywords: nanoporous aluminum oxide films, electrochemical and chemical metallization, nanoparticles, nanostructured solid active elements, generation of laser radiation.

Received: 30 November 2017

Revised: 8 December 2017

1. Introduction

The development of solid lasers based on organic compounds and, in particular, the use of nanoporous aluminum oxide (NAO) as the active medium activated with rhodamine 6G is a topical problem of modern material engineering [1]. There is the possibility of creating compact microlasers based on them, which will find wide application in various spheres of science and engineering [2, 3]. At present, research concerning the creation of laser generation using nanostructured materials activated with organic laser dyes is being actively carried out [4–6], in particular, with the use of aluminum oxide porous ceramics [7]. The studies of fluorescent properties of rhodamine dyes incorporated into aluminum oxide pores were carried out in [8–10], where it was shown that the fluorescence intensity of rhodamine 6G dye in aluminum oxide matrix increased compared to that in porous glass. The induced emission in the geometry to transmission in a porous matrix of anodic aluminum oxide doped with rhodamine 6G was obtained in [11]. The induced emission was observed against the background of a dye spontaneous radiation. The possibilities of generation in other modes and the ways to improve the quality were not considered. The generation of laser radiation by nanostructured solid active elements based on NAO films activated with rhodamine 6G in the geometry to reflection was obtained in [12].

This work was aimed at obtaining the generation of laser radiation by solid active elements with selective nanoresonators formed in the nanoporous structures.

2. Experimental

Aluminum plates with a thickness of 0.1 mm, highpurity grade of 99.95 % AL, and size of 50×50 mm² were taken for anodization. Before anodizing, the plates were purified by de-oiling in 10 % solution of NaOH and blooming in 10 % solution of nitric acid. Then the material was electrochemically polished in a solution of the following composition: orthophosphoric acid (relative density of 1.7) 34 g, sulfuric acid (relative density of 1.84) 34 g, chromic anhydride 4 g, and water to 100 g. The electropolishing mode was $U_{post} = 12$ V, current density was 2.5 A/dm², temperature was 80–90 °C, and duration was 2–3 min. The anodization of the samples was carried out in 2 and 20 % solutions of sulfuric acid at 20 °C, $U_{post} = 12$ V, and current density of 2 A/dm² in potentiostatic mode. The anodization parameters are described more detail in [13–21]. The anodizing duration amounted from 10 to 300 min. For the chosen mode and duration of aluminum anodization, layers from ≈200 nm to ≈85 μm, respectively, were formed on its surface.

Deposition of copper particles was performed electrochemically by the current of alternating polarity $U_{alter} = 12–14$ V and a current density of 0.2–0.5 A/dm² (potentiostatic regime) from an electrolyte with the following composition: copper sulfate 50 g/L, magnesium sulfate 20 g/L, and sulfuric acid (up to pH = 1). Treatment time was 3–4 min. Further treatment of layers containing copper nanoparticles in solutions of silver nitrate

and gold tetrachloride to form silver and gold nanoparticles by exchange reactions was done from solutions of the following composition: for Ag, silver nitrate 1 g/L, sulfuric acid (to pH = 2); for Au, chloroauric acid (HAuCl₄) 1 g/L, sulfuric acid (up to pH = 1–2). Treatment time was 3–4 min.

The adsorption of rhodamine 6G molecules on NAO films in most cases was carried out from a solution with a concentration $C = 10^{-3}$ mol/L, which is the optimal value.

In order to obtain the images of pores with a superhigh resolution, we used a Zeiss MERLIN VP Compact scanning electron microscope with a resolution of 5 nm, which works at 20 kV.

In order to measure the laser-generation spectra, we used an Avantas (AvaSpec-1024) spectrometer with a resolution of 0.4 nm in a wavelength range of 235–735 nm. In the pulsed mode, we used an Nd:YAG laser LOTIS TII (model LS2147) as a source of the laser generation excitation in the samples. The measurements were carried out by single pulses on the second harmonic (wavelength $\lambda_{ex} = 532$ nm), pulse energy E from 0 to 90 mJ, and pulse duration $t = 20$ ns.

3. Results and discussion

3.1. Formation of selective optical nanoresonators in the NAO films

Formation of nanoresonators in the NAO films is explained by the specificity of chemical deposition; as a result, an additional effective layer of noble metal is formed on the surface of NAO, which leads to the formation of the film nanostructure of NAO, like the structure of a Fabry-Perot nanointerferometer (Fig. 1).

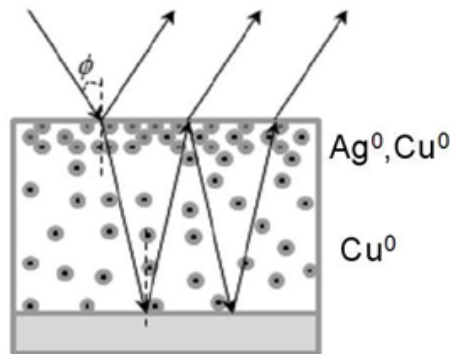
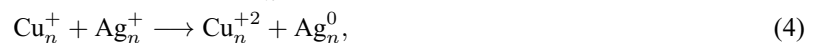
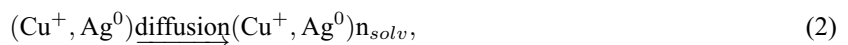


FIG. 1. Scheme of selective nanoresonator in the NAO film, similar to the structure of Fabry-Perot nanointerferometer

According to electron microscopy studies (see Fig. 2), alumina films have a high pore density. The pores are close to each other, have a wall thickness from 7 to 10 nm and a diameter of about 9–14 nm. As can be seen from the Fig. 2, the NAO films have the hexagonal (honeycomb) structure of arrangement of pores. The formed silver nanoparticles have a diameter from ≈ 5 to ≈ 85 nm and are located predominantly on the surface or near the upper boundary of the porous layer (see Fig. 2). Silver nanoparticles being reduced on copper inside the pores are released from the pores and localized on the surface. According to the general opinion, metal electrodeposition in NAO occurs within the alumina pores and starts at the bottom part of pores [22]. However, according to the electron-microscopic image (Fig. 2), during the chemical deposition, silver nanoparticles cover open ends of pores on the surface of the film. The process of directed diffusion migration of silver nanoparticles during chemical deposition of the latter can explain this fact. Silver cations are reduced within the pores on copper particles, copper being oxidized to the monovalent state. At the same state, intermediate solvated contact pairs of cations Cu^+ bonded to an Ag^0 atom are formed in a NAO narrow pore with a diameter of about 9–14 nm. Since these pairs have the same positive charge, the Coulomb repulsion facilitates their directional diffusion from the bottom of the pore to its surface. This leads to the formation of nanoparticles of noble metals predominantly on the surface of the NAO film or near it. Possible chemical reactions are shown on the scheme below:



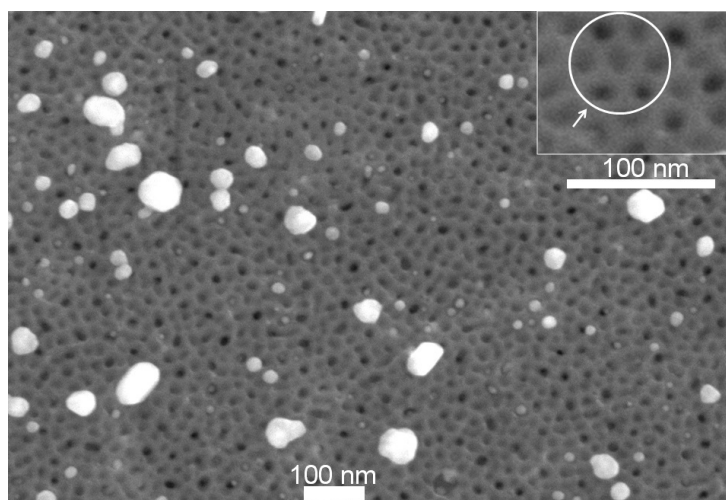
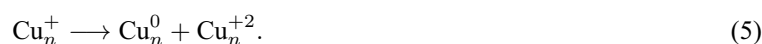


FIG. 2. Electron microscopic photograph of superhigh resolution of the film of NAO (top view; hexagonal structure of arrangement of pores)



Reactions (3)–(5) occur on the film surface. Disproportionation of intermediate Cu^+ cations again yields Cu^0 atoms (step 5), which actively reduce silver cations not inside but on the surface of the pores and reactions (1)–(5) repeated with subsequent aggregation of silver nanoparticles on the surface of the NAO film. Similar reactions occur in the case of chemical deposition of gold. Thus, the process of chemical deposition of noble metals on NAO with electrochemically predeposited copper nanoparticles leads to a redistribution of nanoparticles of noble metal from the bottom and walls to the top part of pores. A thin surface layer enriched with Ag or Au nanoparticles makes a high contribution to the imaginary part of the complex refractive index due to the nature of the Plasmon absorption of light by nanoparticles; therefore, the reflection coefficient of the surface layer increases as compared with a pure NAO film. A nanoresonator in which practically ideal conditions are created for multiple beam passing is formed automatically. Formation of the nanostructure of such a Fabry-Perot nanointerferometer increases the number of rereflections within the layer of NAO film, which increases the gain of active medium (active medium is NAO film activated with rhodamine 6G). As can be seen from the Fig. 2, large silver nanoparticles are distributed on the surface of NAO at the distance of about 30–250 nm; i.e., the film is not continuous and pores are available for penetration of dye (rhodamine 6G) molecules.

In our case, the phenomenon of the formation of the surface film of noble metal is unusual because it occurs spontaneously by redistributing the metal nanoparticles from the bottom of pore to its surface during the chemical reduction of a salt of noble metal on the electrochemically metallized NAO. Technically, the process of applying of the surface metal film by immersing of the metallized NAO film in a solution of noble metal salt is considerably simpler to perform than to carry out the vacuum deposition of a metal film.

The reflection spectra of the alumina films with deposited silver (solid line) and gold (dotted line) nanoparticles in reference to aluminum mirror are shown in Fig. 3. It can be seen the effective reflection region for silver and gold is observed at $\lambda_{em} = 572$ nm (a wavelength of the generated laser radiation). From Fig. 3 it is evident that gold and silver have a relatively effective selectivity. In the case of gold the wavelength of 572 nm is reflected in ~ 2.4 times better than a wavelength of 532 nm; i.e., $R(\text{Au})_{572\text{nm}}/R(\text{Au})_{532\text{nm}} \approx 2.4$, where R is the reflection intensity. With silver the situation is similar; $R(\text{Ag})_{572\text{nm}}/R(\text{Ag})_{532\text{nm}} \approx 2.5$. This allows the use of nanoparticles of gold and silver as the mirrors of the nanoresonator for amplifying of the generated laser radiation ($\lambda_{em} = 572$ nm).

3.2. Generation of laser radiation by NAO film with selective optical nanoresonator formed in the porous structure

In the absence of an external resonator, the generation of laser radiation by NAO film with natural selective nanoresonator formed into the porous structure was obtained. Fig. 4 shows the spectrum of laser radiation generation by the film of NAO activated with rhodamine 6G with internal nanoresonator. The generation occurs at a wavelength of 572 nm. The line half-width is narrow and amounts to $\Delta\lambda_{FWHM} = 9$ nm. It is important to note that a component of spontaneous radiation is completely absent in the induced radiation spectrum. The

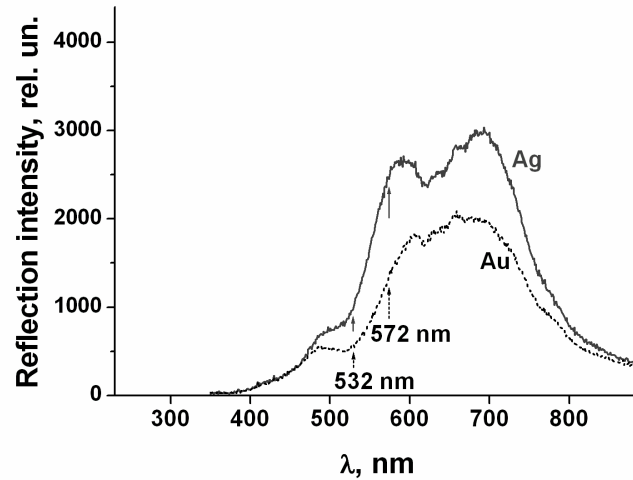


FIG. 3. Reflection spectra of the alumina films with deposited silver (solid curve) and gold (dotted curve) nanoparticles

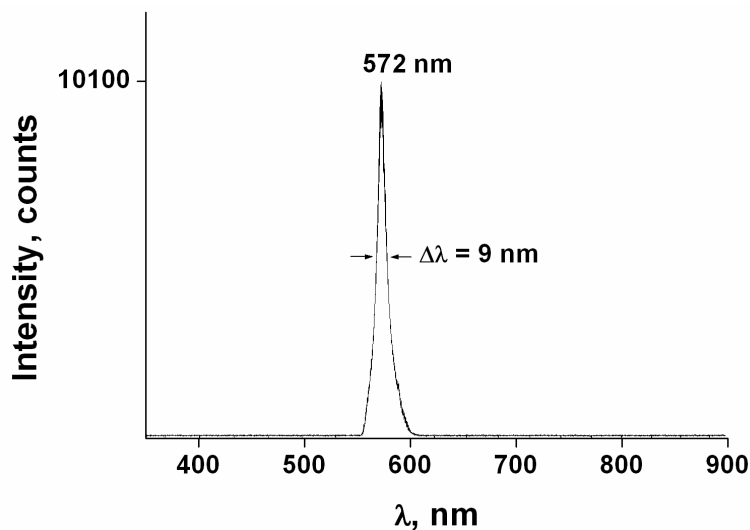


FIG. 4. Spectrum of laser radiation generation by the film of NAO activated with rhodamine 6G with internal natural nanoresonator

absence of a spontaneous radiation component indicates the efficient pumping of the energy from the contour of the luminescence spectrum into a line of generation, which, for example, was not achieved in [11]. The transition from the photoluminescence to laser generation by the full absence of a spontaneous component occurs at a value of impinging radiation power density of about $P_w \sim 1 \text{ MW/cm}^2$. By taking into account small sample thickness and low quality of the internal nanoresonator, this value can be considered small.

4. Conclusion

Thus, in this work we have obtained and studied the generation of laser radiation by nanostructured solid active elements based on the films of nanoporous aluminum oxide with natural selective optical nanoresonators. Chemical deposition of noble metals leads to a redistribution of nanoparticles from the bottom to the top part of the nanoporous layer. This method achieves a sharper Fabry–Perot interference in a layered structure and reduces generation threshold more than two fold. The experiments have shown that the value of the generation threshold decreases to $\sim 1 \text{ MW/cm}^2$, when nanoresonator is formed into the porous structure. In the absence of an external resonator, the generation of laser radiation with natural selective optical internal nanoresonator is obtained for the

first time. In this case, the background of spontaneous luminescence is completely absent in the laser generation. The absence of a spontaneous radiation component indicates the efficient pumping of the energy from the contour of the luminescence spectrum into a line of generation. As a rule, this is inherent in solid lasers, like Nd:YAG, but in our case this phenomenon is observed in the solid element activated with an organic dye, which indicates the high quality of the obtained nanostructured solid elements approaching solid lasers in their properties.

Possible applications include micro/nanoscale lasers with indirect electrical pumping by laser diodes.

References

- [1] Zemskii V.I., Kolesnikov Yu.L., and Meshkovskii I.K. *Physics and Technology of Pulsed Dye Lasers*. SPbGU ITMO, St. Petersburg, 2005, 176 p. [in Russian].
- [2] Zhang W., Yao J., Zhao Y.S. Organic Micro/Nanoscale Lasers. *Acc. Chem. Res.*, 2016, **49**(9), P. 1691–1700.
- [3] Li Y.J., Yan Y., Zhao Y.S., Yao J. Construction of Nanowire Heterojunctions: Photonic Function-Oriented Nanoarchitectonics. *Adv. Mater.*, 2016, **28**, P. 1319–1326.
- [4] Bol'shchikov F.A., Garibin E.A., Gusev P.E., Demidenko A.A., Kruglova M.V., Krutov M.A., Lyapin A.A., Mironov I.A., Osiko V.V., Reitirov V.M. Ryabochkina P.A., Sakharov N.V., Smirnov A.N., Ushakov S.N., and Fedorov P.P. Nanostructured Tm:CaF₂ ceramics: potential gain media for two micron lasers. *Quantum Electron.*, 2011, **41**, P. 193.
- [5] Shin H.W., Cho S.Y., Choi K.H., and Kim Y.R. Directional random lasing in dye-TiO₂ doped polymer nanowire array embedded in porous alumina membrane. *Appl. Phys. Lett.*, 2006, **88**, P. 263112.
- [6] Costel A., Garcia-Moreno I., del Agua D., García O., and Sastre R. Highly photostable solid-state dye lasers based on silicon-modified organic matrices. *J. Appl. Phys.*, 2007, **101**(7), P. 731–742.
- [7] Marinho S.J., Jesus L.M., Barbosa L.B., Ardila D.R., Alencar M., Rodrigues J.J. Bi-chromatic random laser from alumina porous ceramic infiltrated with rhodamine B. *Jr. Laser Phys. Lett.*, 2015, **12**, P. 055801–055805.
- [8] Moadhen A., Elhouichet H., Nosova L., Oueslati M. Rhodamine B absorbed by anodic porous alumina: Stokes and anti-Stokes luminescence study. *J. Lumin.*, 2007, **126**(2), P. 789–794.
- [9] Li Z., Huang K. Optical properties of alumina membranes prepared by anodic oxidation process. *J. Lumin.*, 2007, **127**(2), P. 435–440.
- [10] Zhang Z.L., Zhang H.R., Dong J., Yan X.Q., Sun Y., Xu H.X. Surface enhanced fluorescence by porous alumina with nanohole arrays. *Sci. China, Ser. G.*, 2012, **55**(5), P. 767–771.
- [11] Ibrayev N.Kh., Zeinidenov A.K., Aimukhanov A.K. and Napolskii K.S. Stimulated emission from aluminium anode oxide films doped with rhodamine 6G. *Quantum Electron.*, 2015, **45**, P. 663.
- [12] Lyubas G.A. Generation of laser radiation by nanostructured solid active elements based on nanoporous aluminum oxide films activated with rhodamine 6G. *Nanotechnologies in Russia*, 2017, **12**(5-6), P. 276–284.
- [13] Lyubas G.A., Shelkovnikov V.V., and Korotaev S.V. Optical interferometric sensor based on thin layers of nanoporous anodized aluminum containing nanoparticles of noble metals. *Nanotechnologies in Russia*, 2016, **11**(1-2), P. 29–40.
- [14] Shelkovnikov V.V., Lyubas G.A., and Korotaev S.V. Enhanced reflective interference spectra of nanoporous anodic alumina films by double electrochemical deposition of chemical metal nanoparticles. *Prot. Met. Phys. Chem. Surf.*, 2016, **52**(2), P. 227–231.
- [15] Shelkovnikov V.V., Lyubas G.A., Korotaev S.V. Controlled interference color of the metal surface by combination of the chemical and electrochemical aluminum surface treatment. *Nanosystems: Physics, Chemistry, Mathematics*, 2014, **5**(5), P. 718–727.
- [16] Kumeria T., Rahman M.M., Santos A., Ferré-Borrull J., Marsal L.F., Losic D. Structural and optical nanoengineering of nanoporous anodic alumina rugate filters for real-time and label-free biosensing applications. *Anal. Chem.*, 2014, **86**, P. 1837–1844.
- [17] Santos A., Kumeria T., Losic D. Nanoporous Anodic Alumina: A Versatile Platform for Optical Biosensors. *Materials*, 2014, **7**, P. 4297–4320.
- [18] Santos A., Kumeria T., Losic D. Optically optimized photoluminescent and interferometric biosensors base on nanoporous anodic alumina: A comparison. *Anal. Chem.*, 2013, **85**, P. 7904–7911.
- [19] Ferré-Borrull J., Rahman M.M., Pallares J., Marsal L.F. Tuning nanoporous anodic alumina distributed-Bragg reflectors with the number of anodization cycles and the anodization temperature. *Nanoscale Research Letters*, 2014, **9**, P. 416–422.
- [20] Ferré-Borrull J., Pallares J., Macias G., Marsal L.F. Nanostructural Engineering of Nanoporous Anodic Alumina for Biosensing Applications. *Materials*, 2014, **7**, P. 5225–5253.
- [21] Macias G., Hernández-Eguía L.P., Ferré-Borrull J., Pallares J., Marsal L.F. Gold-coated ordered nanoporous anodic alumina bilayers for future label-free interferometric biosensors. *ACS Appl. Mater. Interfaces*, 2013, **5**, P. 8093–8098.
- [22] Hwang S.K., Jeong S.H., Lee O.J., Lee K.H. Fabrication of vacuum tube arrays with a submicron dimension using anodic aluminum oxide nanotemplates. *Microelectronic Engineering*, 2005, **77**, P. 2–7.

Porous polypropylene membrane contactors for dehumidification of gases

D. I. Petukhov, Ar. A. Eliseev, A. A. Poyarkov, A. V. Lukashin, An. A. Eliseev

Department of Materials Science, Lomonosov Moscow State University,
1-73 Leninskiye gory, Moscow, 119991, Russia
di.petukhov@gmail.com, eliseev@inorg.chem.msu.ru

PACS 81.05.Rm, 47.56.+r

DOI 10.17586/2220-8054-2017-8-6-798-803

We report the application of porous polypropylene hollow fiber membranes with 100×500 nm slit pores in membrane contactor for air dehumidification using triethylene glycol (TEG) as an absorbent. Experiment geometry with gas flow through the lumen of fiber and absorbent circulated on the shell side was utilized to enhance water vapor stage cut. The influence of gas flow rate, liquid circulation rate and water content in triethylene glycol solution on the performance of membrane contactor was studied. The obtained results reveal that the limiting step of water vapor absorption for lumen gas flow configuration is the diffusion of water into TEG volume. Using dry TEG solution and high circulation rate the dew point of feed gas can be decreased down to ~ -30 °C for the membrane contactor performance of 30 – 60 l/(m²h), while with reducing dew point requirements to -10 °C the performance of the contactor over 1 m³/(m²h) is achievable.

Keywords: dehumidification, membrane contactor, polypropylene membrane, gas-liquid contactor.

Received: 10 October 2017

Revised: 26 October 2017

1. Introduction

Gas dehumidification is known as one of the most common technical tasks required in various industrial applications, such as natural gas treatment, air drying, pneumatic fluids conditioning, etc. Dehumidification can be accomplished using cooling cycles [1], including those based on vapor capillary condensation effect [2, 3], vapor absorption [4] or adsorption [5] with desiccants and exploiting membrane separation equipment [6]. Among the methods mentioned, gas, dehumidification by vapor absorption with hygroscopic liquids gained most widespread use due to low energy consumption, the absence of water droplets and its high efficiency.

Two types of hygroscopic liquid absorbents are applied commonly for water vapor capture: aqueous solutions of hygroscopic salts (such as, LiCl, LiBr or CaCl₂) which are typically utilized for humidity control in residential or commercial buildings and di- or triethylene glycols (DEG or TEG) used primarily for industrial facilities. The main disadvantages of salt solutions are related to corrosion and salt crystallization [7]. The utilization of salt solutions for apartment air dehumidification is governed by the absence of desiccant pick-up due to the much lower salt vapor pressure in comparison with glycols [8]. Moreover, the comfort humidity values for working and living spaces is ranges from 30 % to 60 %. These humidity values can be achieved by using salt solutions and there is no need to utilize strong absorbents like TEG. At the same time, technological applications, such as gas pipeline transport, air compression for pneumatic systems required very low dew point values from -60 °C to -40 °C, which can be achieved only by using 99.99 % TEG as a desiccant [9].

Typically gas dehumidification is realized by direct gas-liquid contact in packed columns or bubble towers [4]. However, the interfacial contact area of those contactors depends strongly on the operation conditions, such as flow rate or operating pressure. Tight control of the operation parameters is required to avoid foaming, channeling, flooding or unloading of the dehumidification columns. Gas-liquid membrane contactors where the liquid and gas phases are separated by a semipermeable membrane (especially hollow fiber membranes) were suggested as an alternative technology for overcoming drawbacks of direct gas-liquid contactors [10–12]. Moreover, utilization of membrane contactors allows to increase interfacial contact area over 2000 m²/m³ compared to 50 – 600 m²/m³ typical for classic contact devices [13].

Membrane contactors are generally divided into two groups: non-porous contactors (usually having an asymmetric structure with selective layer) and porous contactors. Despite providing much better isolation of contacting phases, non-porous contactors generally have much lower permeability for the target components, resulting in proportional growth of capital and operational costs in industrial uses. In the case of porous contactors, the gas-liquid interface is formed at the pore necks. Depending on the membrane's hydrophobicity and the type of absorbent, the diffusion of gas molecules or diffusion of absorbed molecules in the liquid occurs within the pores. In the second case, the resistance of membrane is significantly higher due to lower diffusivity in liquid phase in comparison with the gas phase. This necessitates the use of hydrophobic membrane material for dehumidification issues.

The first demonstration of air drying by membrane contactors was reported by Isetti and Nannei using LiCl and CaCl₂ saturated solutions as absorbents [14]. Further studies of heat and mass transfer in membrane contactors during dehumidification with aqueous LiCl have been performed by Zhang *et al.* [15–17]. In contrast, until now, only a little attention has been paid to membrane contactor dryers with DEG or TEG absorbents [18,19]. Moreover, all reports found in the literature consider contactors with absorbent flowing to the lumen side of fibers and gas flowing from the shell side. Despite the fact that using lumen liquid in hollow fiber seems logical from a practical viewpoint, as the feed stream flux generally exceeds that of absorbent many times, this configuration significantly decreases the probability that gas molecules will be drawn into the pores of membrane. This potentially leads to incomplete removal of absorbate and failure to achieve equilibrium vapor pressure. Moreover, the usage of lumen liquid requires the use of powerful pumps to push viscous absorbent through small-diameter fibers.

Thus, in the present study, we report the use membrane contactors with opposite configuration: gas flowing in the lumen side of fibers and absorbent flowing over the shell side. Hydrophobic polypropylene (PP) hollow fiber was used in contactor to avoid filling the pores with a liquid. TEG was applied as an ultimate absorbent allowing the attainment of minimal humidity levels. A schematic representation of the dehumidification process is provided in Fig. 1a. The effects of gas and liquid flow rates as well as TEG water content on the performance of polypropylene hollow-fiber membrane contactor were elucidated.

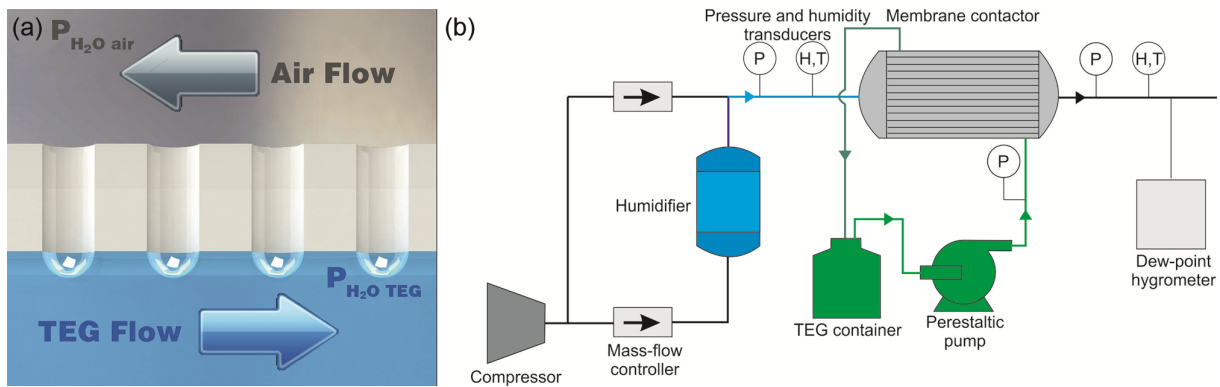


FIG. 1. Scheme of membrane contactor dehumidification process (a) and experimental setup for air dehumidification (b)

2. Experimental

Nanoporous polypropylene hollow fiber membranes were supplied by Zena S.R.O. (Czech Republic). A schematic diagram of air dehumidification setup is represented in Fig. 1b. The flux of compressed air was controlled with two mass-flow controllers SLA5850 (Brooks, USA). Air was saturated with water vapor in the humidifier by direct air-water contact. Air temperature and humidity on the inlet and outlet of membrane contactor was monitored by HIH-4000 (Honeywell, USA) sensors. The dew point temperature of treated air was also determined by dew-point hygrometer TOROS-3VY (Ukraine). Lumen side (gas) and shell side (liquid) pressures were controlled by Carel SPKT00E3R pressure transducers and kept at required values to avoid bubble formation in liquid and penetration of liquid droplets into the air stream. A peristaltic pump (BT300-2J, Longer Pump Co, China) was used for TEG circulation. At each run fresh TEG with purity higher than > 99.5 % was used. All dehumidification experiments were carried using feed air with relative humidity 95 – 97 % at the temperature of 23 °C. To ensure the steady state conditions of absorption were achieved, every measurement was performed 3 times in 30 minute intervals.

To characterize contactor performance, two major parameters of contactor devices (water absorption flux and water vapor stage cut) were extracted for each experimental conditions:

$$J = \frac{Q_{in} \cdot \frac{P_{sat}(H_2O)}{P_{in}} \cdot RH_{in} - Q_{out} \cdot \frac{P_{sat}(H_2O)}{P_{out}} \cdot RH_{out}}{S},$$

where J – water absorption flux [mol/m²], Q_{in} and Q_{out} – inlet and outlet gas flux, respectively, RH_{in} and RH_{out} – inlet and outlet relative humidity, P_{sat} – saturated water vapor pressure at given temperature (calculation was performed via Antoine Equation with coefficients determined by Stull [20] for temperature below 0 °C and

TABLE 1. Characteristics of PP membrane contactor

Parameter	
Fiber outer diameter, mm	0.31
Fiber inner diameter, mm	0.24
Average pore size, nm	200
Porosity, %	45
Module length, cm	50
Number of fibers in module	1200
Module contact area, m ²	0.584

coefficients determined by Bridgeman and Aldrich [21] for temperature above 0 °C), P_{in} and P_{out} – inlet and outlet air pressure and S – membrane area:

$$\eta = \frac{Q_{in} \cdot \frac{P_{sat}(H_2O)}{P_{in}} \cdot RH_{in} - Q_{out} \cdot \frac{P_{sat}(H_2O)}{P_{out}} \cdot RH_{out}}{Q_{in} \cdot \frac{P_{sat}(H_2O)}{P_{in}} \cdot RH_{in}},$$

where η – water vapor stage cut.

Membrane surface and porous structure were characterized by scanning electron microscopy (SEM) using Supra 50VP instrument.

3. Results and discussion

Micrographs of polypropylene hollow-fiber are represented on Fig. 2. Membrane porosity is represented by slit-like pores with sizes of 100×500 nm (average pore size ~ 200 nm), typical for hot-stretched polymers. Such geometry of the pores can be considered optimal for providing maximal contact area while maintaining small pore sizes in the membrane. The last parameter is crucial to maximize critical pressure difference needed to overcome capillary forces for polymer wetting or bubbling at the gas-membrane-liquid interface. General characteristics of hollow fiber membrane and membrane contactor module are listed in the Table 1.

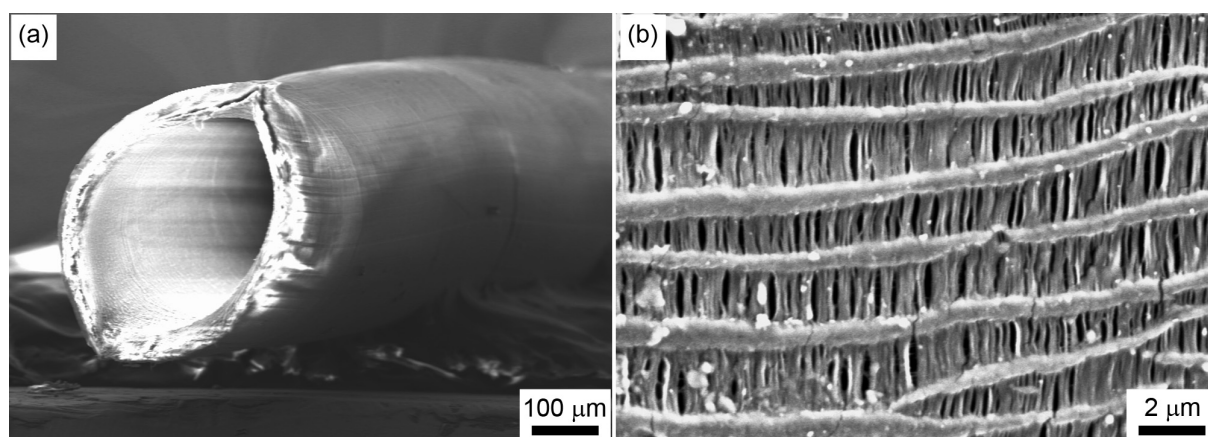


FIG. 2. Micrographs of individual hollow fiber cross-section (a) and enlarged view of membrane external surface (b)

The experiments in air dehumidification were started with revealing the role of humid air flow rate on the membrane contactor performance. Water vapor stage cut and vapor flux through the membrane show a strong dependence of residual water content on the air flow rate in the 300 – 3500 ml/min range (Fig. 3). Notably, the attained water dew point temperature in the retentate goes below -28 °C, illustrating efficiency of the lumen gas configuration as compared to earlier reports [19]. Increasing the gas flux leads to an increase in the water dew point and water vapor stage cut. To determine the limiting stage of absorption process, we have extracted the flux

of water absorbed in the contactor (Fig. 3b) and compared the values with theoretical diffusion flux through the membrane. The diffusion flux of vapor was estimated using Knudsen diffusion mechanism [22] and the assumption that the membrane pores were filled with gas and absorption occurred at the external surface of fibers:

$$J = -D_{Knudsen} \frac{P_{H_2O,air} - P_{H_2O,TEG}}{L \cdot RT},$$

where $P_{H_2O,air}$ – partial pressure of water vapor in the inlet air, $P_{H_2O,TEG}$ – equilibrium pressure of water vapor at the triethylene glycol-air interface at a given water content in a liquid (for TEG concentration 99.8 % the equilibrium partial pressure equals 0.0177 mol/m^3), L – membrane thickness, R – gas constant, T – temperature, $D_{Knudsen}$ – Knudsen diffusion coefficient, determined as:

$$D_{Knudsen} = \frac{\varepsilon d}{3\tau} \sqrt{\frac{8RT}{\pi M}},$$

where ε is the membrane porosity, d – average pore diameter, τ – pore tortuosity, M – water molecular weight. The estimated value of tortuosity in hot-stretched PP membranes was suggested to equal 2 [23]. The resulting Knudsen diffusion coefficient for average pore diameter of 200 nm and porosity of 0.45 is valued as $8.88 \cdot 10^{-6} \text{ m}^2/\text{s}$. Using the value with experimental partial pressure of water in humid air of 1.17 mol/m^3 , equilibrium partial pressure over 99.8 % TEG solution of 0.0177 mol/m^3 , and membrane layer thickness of 35 mm, one can estimate the water flux through the membrane in Knudsen regime as $0.293 \text{ mol}/(\text{m}^2\text{s})$. The derived flux exceeds experimental value by three orders of magnitude, suggesting absorption reaction or absorbent feed to be the limiting step of the process.

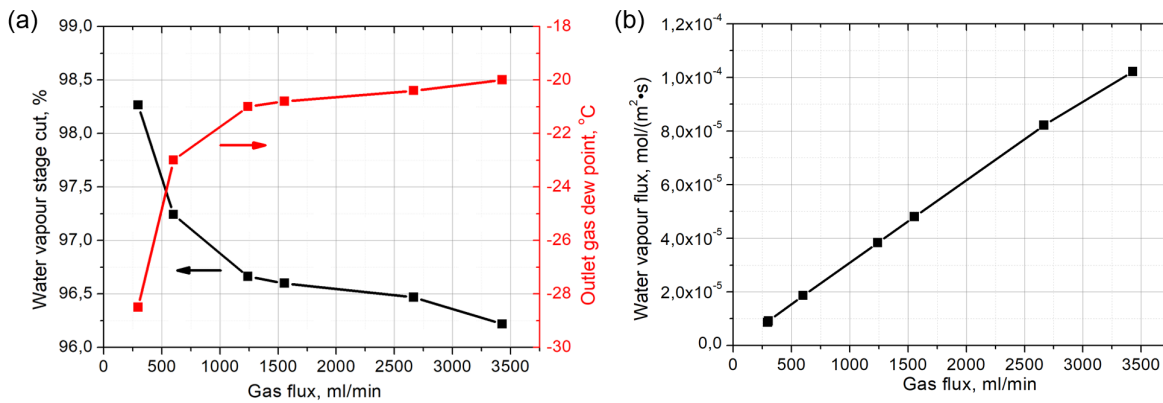


FIG. 3. Effect of gas flow rate on the water vapor stage cut, outlet gas dew point (a) and water vapor absorption flux (b). Inlet relative humidity – 96 % at 23 °C, TEG circulation rate 1000 ml/min and concentration 99.8 %

To check the effect of absorbent flux on the performance of membrane contactor, experiments with TEG circulation rate ranging from 166 ml/min to 1000 ml/min were carried out (Fig. 4). Moderate influence of TEG circulation rate on water vapor stage cut and dew point temperature of retentate flow was revealed. Increasing the circulation rate ~ 7 times leads to increase the absorption flux of only 5 %. This can be explained by a laminar flow of absorbent in the membrane contactor – for the given size of absorber (the inner diameter of 40 mm and the length of 400 mm) liquid velocity is ranged from 0.002 to 0.012 m/s. These results suggest water diffusion into TEG volume to be a limiting stage of absorption process.

As the partial pressure of water vapor is strongly affected by H₂O content in TEG, we have analyzed the role of this parameter on the contactor efficiency. Increasing water content in TEG solution leads to drastic decrease of water vapor stage cut and increase of dew point temperature of retentate due to growth of equilibrium water vapor pressure over the absorbent (Fig. 5). Nevertheless even at 3 % water content in TEG, the dew point of the retentate is reduced to relatively low value of 4 °C with vapor stage cut over 50 %. Thus water pressure over contacting liquid is seemed to be key parameter for the contactor performance. Notably, the outlet gas dew points were found relatively close to equilibrium values, especially in case of high vapor humidity [9]. This illustrates an efficiency of the proposed method for gas dehumidification. Using a lean TEG solution and a high circulation, the rate dew point of feed gas can be decreased down to –30 °C for the contactor performance of 30 – 60 l/(m²h). This result demonstrates that membrane contactors with shell side flow of TEG can be utilized for air and natural gas dehumidification.

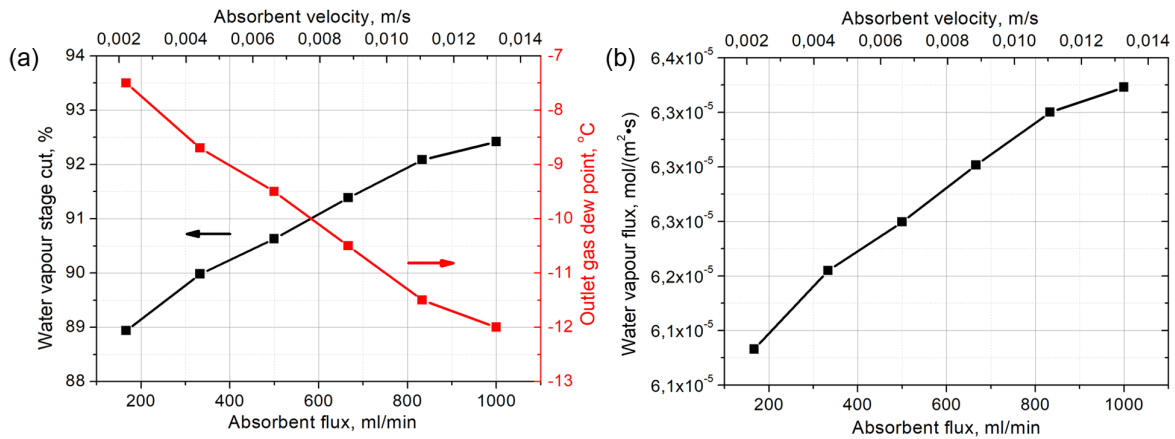


FIG. 4. Effect of absorbent flow rate on the water vapor stage cut, outlet gas dew point (a) and water vapor absorption flux (b). Inlet relative humidity – 96 % at 23 °C, gas flux – 2200 ml/min, TEG concentration 99.5 %

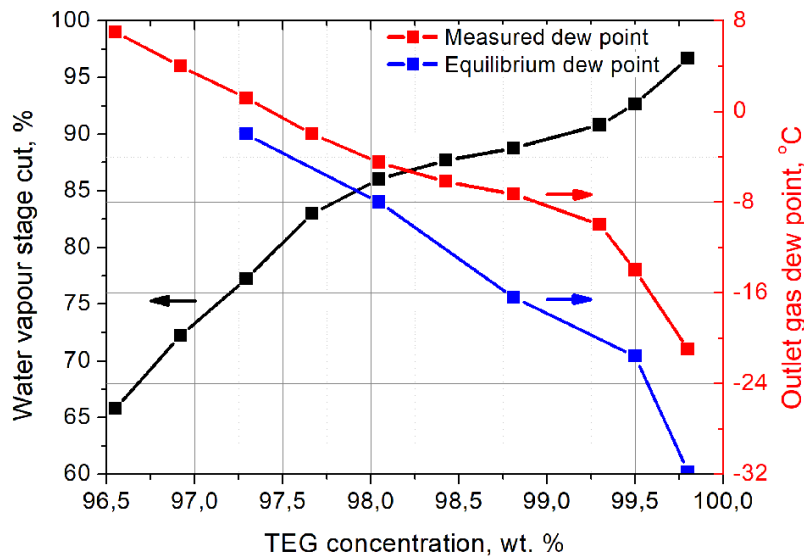


FIG. 5. Effect of TEG concentration on the water vapor stage cut, outlet gas dew point and equilibrium dew point for TEG with given concentration. Inlet relative humidity – 96 % at 23 °C, gas flux – 2200 ml/min, TEG circulation rate – 1000 ml/min

4. Conclusions

Thus, porous hollow-fiber membrane used in gas-liquid membrane contactors with lumen gas flow configuration can be successfully utilized for air dehumidification using the triethylene glycol as a desiccant. Examination of feed gas flow, absorbent circulation rate and TEG water content effects on water vapor transport through membrane reveal partial water pressure over absorbent at gas-liquid interface to be the key parameter for the contactor performance, while diffusion of dissolved water into glycol volume appears as a limiting stage of absorption process. Utilization of dry TEG solution at high absorbent circulation rates allows one to decrease the dew point of the feed gas down to ~ -30 °C from 96 % humidity level at standard conditions. These results reveal the potential of using porous membrane contactors with lumen gas flow configuration for air dehumidification and natural gas conditioning for pipeline transport.

Acknowledgements

The work is supported by the Ministry of education and science of the Russian Federation within a Federal Targeted Programme for “Research and Development in Priority Areas of Development of the Russian Scientific and Technological Complex for 2014 – 2020” (Agreement No. 14.604.21.0177, unique Project Identification RFMEFI60417X0177).

References

- [1] Owen M.S. *Handbook: Fundamentals, American Society of Heating, Refrigerating, and Air-Conditioning Engineers*. ASHRAE, Atlanta, 2005, 544 p.
- [2] Pyatkov E.S., Surtaev V.N., et al. Conditioning of associated petroleum gas using capillary condensation technique with asymmetric microporous anodic alumina membranes. *Oil Industry*, 2016, **5**, P. 82–85.
- [3] Petukhov D.I., Berekchiian M.V., et al. Experimental and Theoretical Study of Enhanced Vapor Transport through Nanochannels of Anodic Alumina Membranes in a Capillary Condensation Regime. *Journal of Physical Chemistry C*, 2016, **120** (20), P. 10982–10990.
- [4] Öberg V., Goswami D.Y. Experimental Study of the Heat and Mass Transfer in a Packed Bed Liquid Desiccant Air Dehumidifier. *Journal of Solar Energy Engineering*, 1998, **120**, P. 289–297.
- [5] Wang W., Wu L., et al. An Overview of Adsorbents in the Rotary Desiccant Dehumidifier for Air Dehumidification. *Drying Technology*, 2013, **31**, P. 1334–1345.
- [6] Lin H., Thompson S.M., et al. Dehydration of natural gas using membranes. Part I: Composite membranes. *Journal of Membrane Science*, 2012, **413–414**, P. 70–81.
- [7] Rafique M.M., Gandhidasan P., Bahaidarah H.M.S. Liquid desiccant materials and dehumidifiers – A review. *Renewable & Sustainable Energy Reviews*, 2016, **56**, P. 179–195.
- [8] Liu X.-H., Yi X.-Q., Jiang Y. Mass transfer performance comparison of two commonly used liquid desiccants: LiBr and LiCl aqueous solutions. *Energy Conversion and Management*, 2011, **52**, P. 180–190.
- [9] Kohl A.L., Nielsen R. Richard B. *Gas purification*, Gulf Pub, Oxford, 1997, 900 p.
- [10] Petukhov D.I., Poyarkov A.A., et al. Removal of acidic components of associated petroleum gas by pertraction on microporous membranes. *Oil Industry*, 2016, **11**, P. 55–58.
- [11] Ovcharova A.A., Vasilevsky V.P., et al. Porous hollow fiber membranes with varying hydrophobic–hydrophilic surface properties for gas–liquid membrane contactors. *Petroleum Chemistry*, 2016, **56** (11), P. 1066–1073.
- [12] Ovcharova A., Vasilevsky V., et al. Polysulfone porous hollow fiber membranes for ethylene-ethane separation in gas-liquid membrane contactor. *Separation and Purification Technology*, 2017, **183**, P. 162–172.
- [13] Nieves-Remacha M.J., Kulkarni A.A., Jensen K.F. Gas–Liquid Flow and Mass Transfer in an Advanced-Flow Reactor. *Industrial & Engineering Chemistry Research*, 2013, **52**, P. 8996–9010.
- [14] Isetti C., Nannei Enrico M.A. On the application of a membrane air – liquid contactor for air dehumidification. *Energy and Buildings*, 1997, **25**, P. 185–193.
- [15] Huang S.-M., Zhang L.-Z. Researches and trends in membrane-based liquid desiccant air dehumidification. *Renewable & Sustainable Energy Reviews*, 2013, **28**, P. 425–440.
- [16] Huang S.-M., Zhang L.-Z., Tang K., Pei L.-X. Fluid flow and heat mass transfer in membrane parallel-plates channels used for liquid desiccant air dehumidification. *International Journal of Heat and Mass Transfer*, 2012, **55**, P. 2571–2580.
- [17] Huang S.-M., Zhang L.-Z., Pei L.-X. Transport Phenomena in a Cross-Flow Hollow Fibre Membrane Bundle Used for Liquid Desiccant Air Dehumidification. *Indoor and Built Environment*, 2013, **22**, P. 559–574.
- [18] Usachov V.V., Teplyakov V.V., Okunev A.Y., Laguntsov N.I. Membrane contactor air conditioning system: Experience and prospects. *Separation and Purification Technology*, 2007, **57**, P. 502–506.
- [19] Fakharneshad A., Keshavarz P. Experimental investigation of gas dehumidification by tri-ethylene glycol in hollow fiber membrane contactors. *Journal of Industrial and Engineering Chemistry*, 2016, **34**, P. 390–396.
- [20] Stull D.R. Vapor Pressure of Pure Substances. Organic and Inorganic Compounds. *Industrial & Engineering Chemistry*, 1947, **39**, P. 517–540.
- [21] Bridgeman O.C., Aldrich E.W. Vapor Pressure Tables for Water. *Journal of Heat Transfer*, 1964, **86**, P. 279–286.
- [22] Petukhov D.I., Eliseev A.A. Gas permeation through nanoporous membranes in the transitional flow region. *Nanotechnology*, 2016, **27**, 085707.
- [23] Yan S.-P., Fang M.-X., et al. Experimental study on the separation of CO₂ from flue gas using hollow fiber membrane contactors without wetting. *Fuel Processing Technology*, 2007, **88**, P. 501–511.

Role of carbon in the formation of the structure and magnetic properties of Ni@CN_x nanoclusters under reactive magnetron deposition

R. V. Shalayev, V. N. Varyukhin, A. M. Prudnikov, A. I. Linnik, V. V. Syrotkin

Donetsk Institute for Physics and Engineering named after A. A. Galkin,
R. Luxembourg str. 72, 83114, Donetsk, Ukraine

sharos@donfti.ru

DOI 10.17586/2220-8054-2017-8-6-804-808

Nanostructured hybrid Ni–CN_x films were grown by magnetron sputtering of a composite graphite-nickel target. Atomic force microscopy showed the clustered nature of the films deposition on the substrate surface: a relatively high pressure in the low-temperature magnetron plasma made it possible to form the Ni@CN_x nanoclusters type “core-shell”, where metallic nickel is the core and carbon nitride is the shell. When studying the role of carbon in the formation of the structure and properties of Ni@CN_x nanoclusters, it was established that the saturation magnetization $4\pi M_s$ of nanoclusters drops sharply with a carbon content above 30 at.%. The reason is the formation of an increasingly saturated solid solution of carbon in nickel. At a carbon concentrations above 38 at.%, amorphous Ni–CN_x nanoclusters are formed in the magnetron plasma, which are deposited on the substrate. An increase in the substrate temperature leads to the crystallization of Ni atoms, and the C and N atoms are forced out onto the surface of the nickel core, forming an array of Ni@CN_x elements.

Keywords: carbon nitride, nanoclusters, magnetron sputtering.

Received: 3 November 2017

Revised: 16 November 2017

1. Introduction

Carbon nanomaterials have unique physical and chemical properties [1,2]. In recent years, attention has been drawn to the so-called hybrid nanomaterials with metal encapsulated in a carbon shell (Me@C) [3]. The carbon coating covering the ferromagnetic metal not only provides protection against mechanical damage, but also protects it from oxidation. Due to this, the limits of the potential application of such materials are expanding [4]. Areas of use of material such as Me@C: as magnetic recording devices, medical diagnostics and “transportation” of drugs in the human body [5], nanocontainers for the storage of metallic materials [6], etc. There are many methods for obtaining metallic materials coated with a carbon shell: laser ablation, arc method, chemical vapor deposition, evaporation by condensation from the gas phase, plasma-chemical deposition [7,8]. The above methods of obtaining Me@C hybrid structures are mainly high-temperature. In this paper, we propose a magnetron sputtering method (compatible with semiconductor technologies) that does not require high temperatures. Its positive factor is the relatively high pressure of the buffer gas, which leads to the formation of nanoclusters [9]. The use of a composite target makes it possible to obtain nanocluster type “core-shell”. In this case, the metal is the core, and the carbon is the shell. The physical and chemical properties of such nanoclusters are strongly dependent upon the structure of the core and the shell.

The purpose of this work was to study the role of carbon in the formation of the structure and magnetic properties of Ni@CN_x nanoclusters at reactive magnetron deposition on a cold substrate, and also its modification upon heating during growth.

2. Experiment

Nanostructured film structures of the Ni–C system doped with N were obtained by magnetron sputtering of a composite nickel-carbon target in an argon atmosphere with nitrogen admixture on quartz and cover glass substrates. The plasma power did not exceed 20 W, the buffer gas pressure was 26 Pa. The surface morphology of the films was investigated by atomic force microscopy (AFM) using the Ntegra probe nanometer laboratory of the energy dispersive spectrometer INCA Penta FETx3. X-ray analysis of the obtained samples was carried out on a DRON-3 installation in CoK α -radiation. The saturation magnetization of the material of the films was measured by means of an induction-frequency installation by the change in the resonant frequency $\Delta F \propto \Delta M = f(H)$ of the oscillatory circuit into the coil of which the sample was placed [10]. The use of an inductive-frequency method makes it possible to directly measure the saturation magnetization of $4\pi M_S$ of a ferromagnetic sample [11]. The saturation magnetization of all samples was determined at room temperature.

3. Results and discussion

Atomic force microscopy was used to investigate nucleation processes on the growth surface and the morphology of the surface of growing films. For this purpose, we used polished quartz glass substrates with a roughness of the order of 1 nm. This made it possible to control the complex morphology of the surface of the obtained samples with an accuracy also comparable to 1 nm.

As can be seen from Fig. 1a, at the initial stage of growth the substrate surface is covered by cluster elements of ~ 10 nm in size in a chaotic order. With increasing growth time, the entire surface of the substrate is covered by such cluster elements.

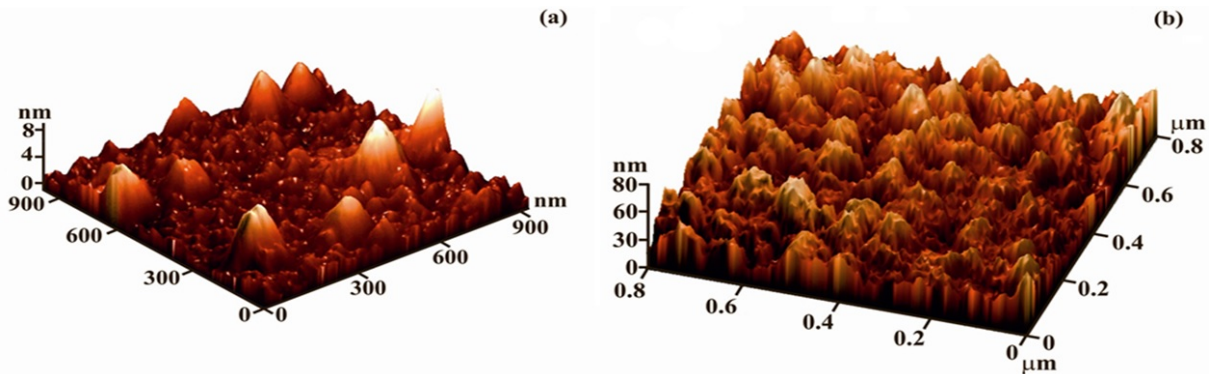


FIG. 1. AFM image of the Ni-C film surface after 10 seconds of growth (a) and after 300 seconds of growth (b)

Thus, the study of nucleation processes on the substrate surface shows that in the case of magnetron sputtering, there is a cluster character of the deposition of Ni-C films: nanosized clusters of sputtering material already formed in the plasma are deposited on the substrate surface.

The occurrence of clusters is due to the rather high pressure of the buffer gas [9], in our case about 150 mTorr. This pressure is almost an order of magnitude higher than that usually used in magnetron sputtering experiments at low powers (~ 20 W) for the magnetron plasma. As a result, a small region of plasma is characterized by a sufficiently high concentration of atomized atoms. Due to this, at a relatively low temperature, self-organization processes begin to occur – the clusters formation in the plasma from the target material and the buffer gas.

When the flow of charged clusters hits a relatively cold substrate, relative to the plasma and the clusters temperature, there is its “congealing” with the transfer of thermal energy to the substrate. In this case, nucleation centers of the film are formed, which is observed in AFM studies.

This result requires a rethinking of the growth processes of nanostructured films by the method of magnetron sputtering and the construction of new models, in particular, growth models of nanocolumns from charged nanoclusters. Figure 1b shows 3D images of the surface of the film obtained after 300 sec of growth. A “sharp” acicular nanocolumnar structure formed by individual nanoclusters is clearly visible.

To determine the role of carbon in the formation of the structure and properties of Ni@CN_x nanoclusters, a series of films differing in carbon content (from 10 to 40 at.%) with an admixture of nitrogen of 5 at.%, was grown at a constant growth time of 10 min (thickness ~ 100 nm) without heating substrate.

Analysis of the diffractograms of the obtained films showed that only reflections corresponding to (111), (200) and (220) planes of the FCC nickel lattice are present. The lattice constant is 3.529 Å, which is close to the value for the bulk nickel (3.56 Å). The only difference is in some broadening of the X-ray reflexes. This indicates a relatively small amount of Ni-crystallites, of which films are built. At the same time, the presence of carbon in the film composition and the absence of nickel oxide indicate, as shown in [3], the presence of a carbon shell around nickel nanocrystallites. Thus, we obtain in the magnetron plasma nanoclusters of the “core-shell” type Ni@CN_x – a ferromagnetic metal (Ni) coated carbon with an admixture of nitrogen. Nitrogen is necessary for curving graphene planes, because the presence of nitrogen leads to the formation of pentagons.

Figure 2 shows the dependence of the crystallite size D (determined from the broadening of X-ray reflections) and the saturation magnetization $4\pi M_S$ (measured at room temperature) on the carbon concentration in Ni@CN_x nanoclusters ($N_x = 5$ at.%). We note that the magnetization dependence has a sharply nonlinear character – with an increase in the carbon concentration (≥ 30 at.%) the magnetization $4\pi M_S$ falls very rapidly. The crystallite size also decreases with increasing carbon concentration, but is practically linear. Extrapolation of the $4\pi M_S = f(C)$

curve to the zero magnetization value yields $C = 37.5$ at.%, at which the film is not magnetically ordered at all. The crystallite size is about 8 nm. With an increase in carbon concentration (~ 38 at.%) the films become X-ray amorphous.

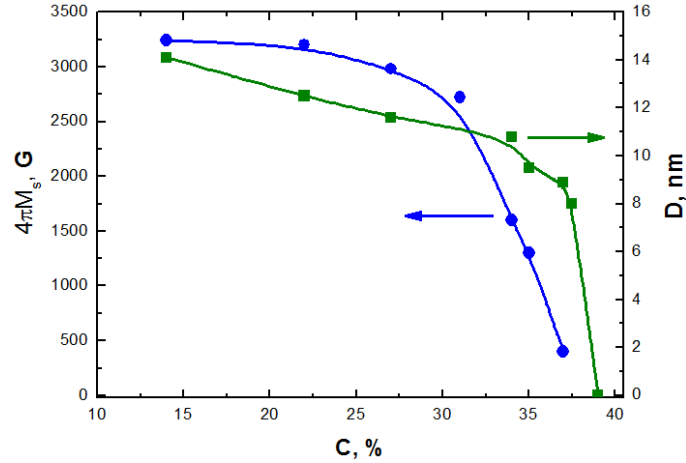


FIG. 2. Dependence of the crystallite size D and the saturation magnetization $4\pi M_S$ on the carbon concentration C in nanoclusters $\text{Ni}@\text{CN}_x$

To determine the effect of substrate temperature on the structure and magnetic properties of $\text{Ni}@\text{CN}_x$ nanoclusters, three series of films were grown, differing in the ratio of C/Ni atoms (A series – 30/70, B series – 40/60 and C series – 60/40) up to 100 nm thick.

Figure 3a shows the dependences of the Ni nanocrystallites size D (estimated from the broadening of X-ray reflections by the Debye-Scherrer formula) of nickel-carbon films of series A from the substrate temperature T_S . With increasing T_S , the crystallite size D increases smoothly and has different values for reflexes (111) and (200). It should be noted that there is practically no such difference at low temperatures. This indicates that at low temperatures the clusters deposited on the substrate have a predominantly spherical shape. And also, an increase in the size D of nanocrystallites in comparison with their size at a lower temperature makes it possible to state that the growth is due to diffusion processes during the temperature effect of the substrate.

Figure 3b shows the dependence of the Ni nanocrystallites size D of nickel-carbon films of series B on the substrate temperature. It can be seen that with increasing temperature, the size of nanocrystallites also increases. There is some specific substrate temperature T_{cr} of about 80 °C, below which the size of the nickel particles approaches zero. It should be noted that in the temperature range of the substrate T_S 125...220 °C, the size of the crystallites practically does not change, and then sharply goes up, presumably due to the fusion of individual clusters due to diffusion processes.

Figure 3c demonstrates the effect of substrate temperature T_S during film growth on the saturation magnetization $4\pi M_S$ for the films of A, B and C series. As we can see, films of group A exhibit ferromagnetism even when deposited on a cold substrate. A slight increase in $4\pi M_S$ with an increase in the substrate temperature T_S can also be easily explained by the size effect [11] associated with the growth of the crystallite size D (Fig. 3a). These results are in good agreement with the notion that, at low carbon concentrations, clusters deposited on the substrate have a structure of the “Ni-nanocrystallite/C-shell” type [3]. Moreover, they are formed in a magnetron plasma by crystallization of nickel atoms inside an amorphous nickel-carbon cluster. With increasing substrate temperature, the size of the nickel core of the cluster grows, due to diffusion processes on the substrate surface (see Fig. 3a) and the saturation magnetization of crystallites $4\pi M_S$ also increases (see Fig. 3c). It is clear that when the size of Ni crystallites at a temperature $T_S \approx 300$ °C reaches macroscopic values, the value $4\pi M_S$ approaches the magnetization of bulk nickel.

At the same time, the films of group B and C with higher carbon contents were non-magnetic when deposited on a cold substrate. They began to exhibit ferromagnetism only when deposited on heated substrates. Moreover, with an increase in the C/Ni ratio, the specific temperature T_{cr} of the onset of ferromagnetism increases: at $C/\text{Ni} = 40/60$ $T_{cr} \approx 80$ °C, at $C/\text{Ni} = 60/40$ $T_{cr} \approx 160$ °C.

We see that as the carbon concentration in the series B and C films increases, the magnetization decreases, in full accordance with the model [12–14], suggesting the formation of an increasingly saturated solid solution of carbon in nickel. Subsequently, as the substrate temperature rises, the nickel phase in the nanoclusters crystallizes

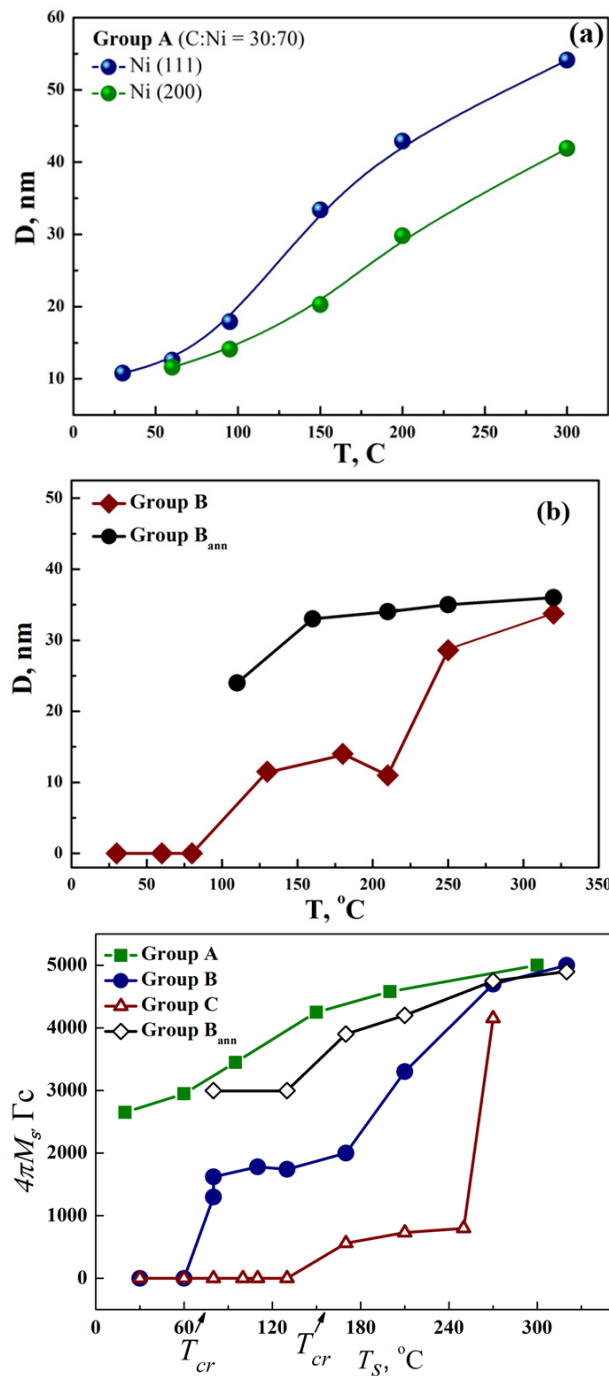


FIG. 3. Influence of substrate temperature on the nickel nanocrystallites size in films of various groups (a, b). Dependence of the saturation magnetization $4\pi M_S$ on the substrate temperature (c). B_{ann} – films of group B after annealing

first, and the more carbon in the cluster, the smaller the magnetization of the nickel crystallite and its smaller size (see Fig. 2, Fig. 3b and Fig. 3c). This process takes place in the temperature range of the substrate T_S 80 – 180 °C for B-group films and T_S 160...250 °C for C-group films. At higher T_S , due to the diffusion processes on the substrate and the release of carbon from the saturated solid solution of carbon in nickel, a fusion of separate clusters occurs into a common nickel core covered with a carbon shell and, correspondingly, an increase in the magnetization. To confirm such a model, we performed an experiment on annealing samples of group B. The experiment was carried out in air at a temperature of 350 °C for 10 min. The experimental results are shown in Fig. 3c (curve B_{ann}). As we see, the curve B_{ann} fixes the increase in magnetization after annealing for samples

obtained at low substrate temperatures. Thermal annealing of the samples to accelerate the decomposition of the supersaturated solid solution of Ni(C) confirms the diffusion mechanism of growth of nickel crystallites at high substrate temperatures. An increase in the size of the Ni crystallites is also evidenced by calculations based on X-ray data of the characteristic size D for samples of group B subjected to the above annealing. These data are presented in Fig. 3b, the curve B_{ann} .

Thus, at a low carbon concentrations, a metastable supersaturated solid solution of Ni(C) is formed first in the magnetron plasma. The supersaturated solid solution decomposes into nickel and pure carbon with the displacement of C atoms to the surface of the nickel crystallite, forming a nickel nanocluster with a carbon shell Ni@C [12–14].

4. Conclusions

The obtained results make it possible to draw the following conclusions. At high C/Ni ratios, the nickel-carbon clusters formed in the plasma are amorphous formations in the form of a mixture of Ni and C atoms. When deposited on a cold substrate, such clusters form nonmagnetic films. At substrate temperatures above T_{cr} , a weakly magnetic supersaturated solid solution of Ni(C) begins to form. Then, the supersaturated solid solution decomposes into nickel and carbon doped with nitrogen, forming a nickel nanocluster with a carbon shell. In this case, the solid solution can partially or completely decay, reducing the concentration of carbon in the metallic core [12, 14]. Further annealing, as shown by our experiments, leads to a significant additional decay of the system.

At low C/Ni ratios, ferromagnetic nickel-carbon nanoclusters of the “core-shell” type are already formed in the plasma. The mechanism of formation for such nanoclusters is caused by the formation of supersaturated solid solutions based on Ni(C) and its subsequent disintegration into pure nickel in the core and the formation of a carbon coating on the surface of the nanoparticles.

References

- [1] Gómez-Gualdrón D.A., Beetge J.M., Balbuena P.B. Characterization of Metal Nanocatalyst State and Morphology during Simulated Single-Walled Carbon Nanotube Growth. *J. Phys. Chem. C*, 2013, **117**, P. 12061–12070.
- [2] Cheng D., Wang W., Huang S. Coreshell-structured bimetallic clusters and nanowires. *J. Phys.: Condens. Matter.*, 2007, **19**, P. 356217.
- [3] Sunny V., Kumar D.S., et al. Synthesis and properties of highly stable nickel/carbon core/shell nanostructures. *Carbon*, 2010, **48**, P. 1643–1651.
- [4] Mel El A.A., Gautron E., Angleraud B., Granier A. Synthesis of nickel-filled carbon nanotubes at 350 °C. *Carbon*, 2011, **49**, P. 4595–4598.
- [5] Sacanna S., Rossi L., Pine D.J. Magnetic Click Colloidal Assembly. *Journal of the American Chemical Society*, 2012, **134**, P. 6112–6115.
- [6] Kovács Gy.J., Koós A., et al. Structure and spectroscopic properties of C–Ni and CN_x–Ni nanocomposite films. *J. Appl. Phys.*, 2005, **98**, P. 034313-5.
- [7] Navas D., Hernandez-Velez M., et al. Magnetic properties of densely packed arrays of Ni nanowires as a function of their diameter and lattice parameter. *Appl. Phys. Lett.*, 2007, **90**, P. 192501-5.
- [8] Rossi G., Rapallo A., et al. Magic Polyicosahedral Core-Shell Clusters. *Phys. Rev. Lett.*, 2004, **93**, P. 105503-7.
- [9] Kashtanov P.V., Smirnov B.M., Hippler R. Magnetron plasma and nanotechnology. *Physics–Uspekhi*, 2007, **50**, P. 455–488.
- [10] Dovgii V.T., Linnik A.I., et al. Anomalous magnetic hysteresis in La_{0.6}Sr_{0.2}Mn_{1.2}O_{3δ} manganites with a perovskite structure. *Technical Physics Letters*, 2003, **29**, P. 610–612.
- [11] Linnik A.I., Prudnikov A.M., et al. Synthesis and magnetic properties of nanocolumnar nickel films deposited in argon-nitrogen atmosphere. *Technical Physics Letters*, 2012, **38**, P. 499–502.
- [12] Tsurin V.A., Yermakov A.Ye., et al. Synthesis, Structure, and Magnetic Properties of Iron and Nickel Nanoparticles Encapsulated into Carbon. *Physics of Solid State*, 2014, **56**, P. 287–301.
- [13] Galakhov V.R., Buling A., et al. Carbon States in Carbon-Encapsulated Nickel Nanoparticles Studied by Means of X-ray Absorption, Emission, and Photoelectron Spectroscopies. *J. Phys. Chem. C*, 2011, **115**, P. 24615–24620.
- [14] Ponosov Yu.S., Uimin M.A., et al. Raman Light Scattering and Electron Microscopy of Nanocomposites with the Metal CoreCarbon Shell Structure. *Physics of Solid State*, 2013, **55**, P. 1528–1535.

Fractal analysis – a surrogate technique for material characterization

M. S. Swapna, S. Sankararaman

Department of Optoelectronics and Department of Nanoscience and Nanotechnology, University of Kerala,
Trivandrum, Kerala, 695581, India.

swapnams.opto@gmail.com, drssraman@gmail.com

PACS 81.05 U, 05.45.Df, 61.48.De, 81.20.Ka

DOI 10.17586/2220-8054-2017-8-6-809-815

Fractal analysis has emerged as a potential analytical tool in almost all branches of science and technology. The paper is the first report of using fractal dimension as a surrogate technique for estimating particle size. A regression equation is set connecting the soot particle size and fractal dimension, after investigating the Field Emission Scanning Electron Microscopic (FESEM) images of carbonaceous soot from five different sources. Since the fractal dimension is an invariant property under the scale transformation, an ordinary photograph of the soot should also yield the same fractal dimension. This enables one to determine the average size of the soot particles, using the regression equation, by calculating the fractal dimension from the photograph. Hence, instead of frequent measurement of average particle size from FESEM, this technique of estimating the particle size from the fractal dimension of the soot photograph, is found to be a potentially cost-effective and non-contact method.

Keywords: fractals, FESEM, carbon nanoparticles, particle size, box-counting.

Received: 16 October 2017

Revised: 26 October 2017

1. Introduction

The science of fractal geometry has emerged as a potential analytical tool in almost all branches of science and technology. Fractal analysis is the mathematical method put forward by the polymath Benoit Mandelbrot for quantifying the complex structures and figures [1]. The beauty of this analytical method lies in the fact that it assists in finding the hidden connections and relations existing between different areas of science, mathematics, and art. Fractals are found everywhere in nature [2, 3]. The scale in which we zoom the image determines the quality of results. The self-replication of objects while zooming differentiates a fractal and a non-fractal object. This technique is used in the chaos theory, to solve the unpredicted problems in an entirely different way, as well as in many dynamic systems [3]. Even though fractals seem complex in nature, they are self-similar structures formed by repetition of simple processes again and again [4, 5]. This nature of fractals is greatly exploited in the determination of the benign and malignant breast cancer with higher levels of accuracy and in studying the morphology of galaxies [6–8].

A fractal dimension is the non-integral numerical value which gives the statistical complexity of a fractal image. It is usually expressed as Hausdorff–Besicovitch (HB) dimension (D) which is a mathematical dimension that measures how much space is occupied by the object between Euclidean dimensions [9]. Various methods have been developed for calculating the fractal dimension. Some of the methods are the box-counting method, the successive squares method, the pair-correlation method etc. [10]. In all the methods, the variation of fractal dimensions with the measurement of fractals at different degrees is of concern [1].

Fractal geometry is recently used in the determination of morphological, optical, and thermoelectric characteristics [11] of various nanostructured materials. Such nanostructured materials had been of great interest recently due to their remarkable applications in every field of science and technology. The physical, chemical, electrical, mechanical etc., properties of nanostructured materials are dramatically different when compared with the bulk materials of the same compositions [12–14]. The clusters, molecules, crystallites are various forms of these materials. Carbon nanoparticles are one class among the widely explored nanostructures that have gained significant attention in the twenty-first century as a promising material due to its high thermal and electrical stability, biocompatibility, high tensile strength, etc. The quality and quantity of the CNPs synthesized depends on the raw materials or resources used for the synthesis along with the synthesis procedure adopted. So far, many methods have been developed for the synthesis of CNPs, including laser ablation, chemical and physical vapor deposition, pyrolysis, combustion, electrolysis, ball milling, etc. [15]. The present work describes the synthesis of CNPs by the cost-effective combustion method and a new technique of particle size estimation from the fractal dimension

of the photograph of the carbon soot. An attempt has also been made to correlate nature of combustion, particle size, structural forms of CNPs, and fractal dimension.

2. Experimental methods

To understand whether there is any structural and morphological change in the CNPs in the soot, fractal analysis is conducted. CNPs are synthesized from various sources such as ghee, coconut oil, sesame oil, diesel, and camphor. All these sources are various combinations of saturated, monosaturated and polyunsaturated fatty acids. The high temperatures present during synthesis enables controlled incomplete combustion, resulting in the formation of carbonaceous soot particles.

The samples are purified by liquid phase oxidation method. The sample is mixed with an acidic solution containing nitric acid and sulfuric acid (99.9 %, Sigma–Aldrich) in the ratio 3:1 and ultrasonicated using Scientech SE-366 for 20 minutes. Then the mixture is filtered through a Whatman 41 filter paper, washed four times with distilled water, quenched with ice-cooled water followed by addition of sodium hydroxide for basic neutralization [16]. The resulting mixture is then filtered again using a Whatman 42 filter paper after washing four times with distilled water. These samples are dried and ground in a ball milling unit. The particles are characterized by Nova Nano FESEM. The geometrically and chemically complex structure of soot particles can be analyzed by calculating the fractal dimensions from the scanning electron microscopic images of these nanoparticles.

2.1. Box counting method

The most widely used method for obtaining the dimension of self-similar mass fractals [17] in the real world is the box-counting method. In this method, grids of varying sizes (r) are superimposed on the image to be analyzed and the number of boxes containing portions of the image are counted ($N(r)$). $N(r)$ is directly proportional to r^{-D} . The box-counting dimension is mathematically represented by the logarithmic equation [1, 9]:

$$N(r) \propto r^{-D}, \quad (1)$$

where D is the fractal dimension.

Taking logarithm we get:

$$\ln N(r) = D \ln \left(\frac{1}{r} \right) + \text{constant}, \quad (2)$$

such that $\lim_{r \rightarrow 0} \frac{\ln N(r)}{\ln(1/r)} = D$.

From the slope of the $\ln(1/r)$ vs $\ln N(r)$ graph, the fractal dimension (D) can be calculated.

3. Results and discussions

The morphological analysis of the CNPs synthesized from various sources, carried out by the FESEM analysis, reveals the formation of agglomerated nanosized carbon clusters. The FESEM images of the CNPs formed from the combustion of ghee, coconut oil, sesame oil, diesel soot, and camphor are shown in Figs. 1 (a)–(e). The carbon particles obtained ranged from 20 – 150 nm. The nanospheres in the clusters are bound together by the weak Van der Waal force of attraction. The interaction between the constituent particles was enhanced by any small spatial fluctuations occurring in the samples. This interactive property of soot particles contributes to the formation of aggregates and also results in the restructuring of the CNPs which enables the nanoparticles to show various optical properties. This type of behavior is exhibited by fractals [18]. Depending on the basic source used for the synthesis the size, agglomerating tendency, etc. will also vary. The variation in the fractal dimension with respect to these factors can be studied from the FESEM images.

The SEM images shown in Fig. 1 were subjected to fractal analysis by box counting method and the plots of $\ln N(r)$ vs $\ln(1/r)$ are shown in Fig. 2. All graphs show high R^2 value, indicating a high degree of correlation between $N(r)$ and r . The fractal dimensions, R^2 values, and the particle sizes for CNPs obtained from different sources are shown in Table 1.

Varying the fractal dimensions of the CNP agglomerates formed in the soot of various hydrocarbon sources and the size of the agglomerate are shown in Fig. 3. From Fig. 4 it can be seen that the fractal dimension decreased with increasing agglomerate particle size. The fractal dimension depended on the complexity of the system; the greater the complexity, the greater the fractal dimension was. The particle size and fractal dimension (D) showed a strong correlation with R^2 value equal to one. Hence, a regression equation connecting the two variables – average particle size and fractal dimension – can be set up by fitting a curve to the data by the least squares method. The equation thus set can be used for calculating the particle size from fractal dimension. The closer the value of the

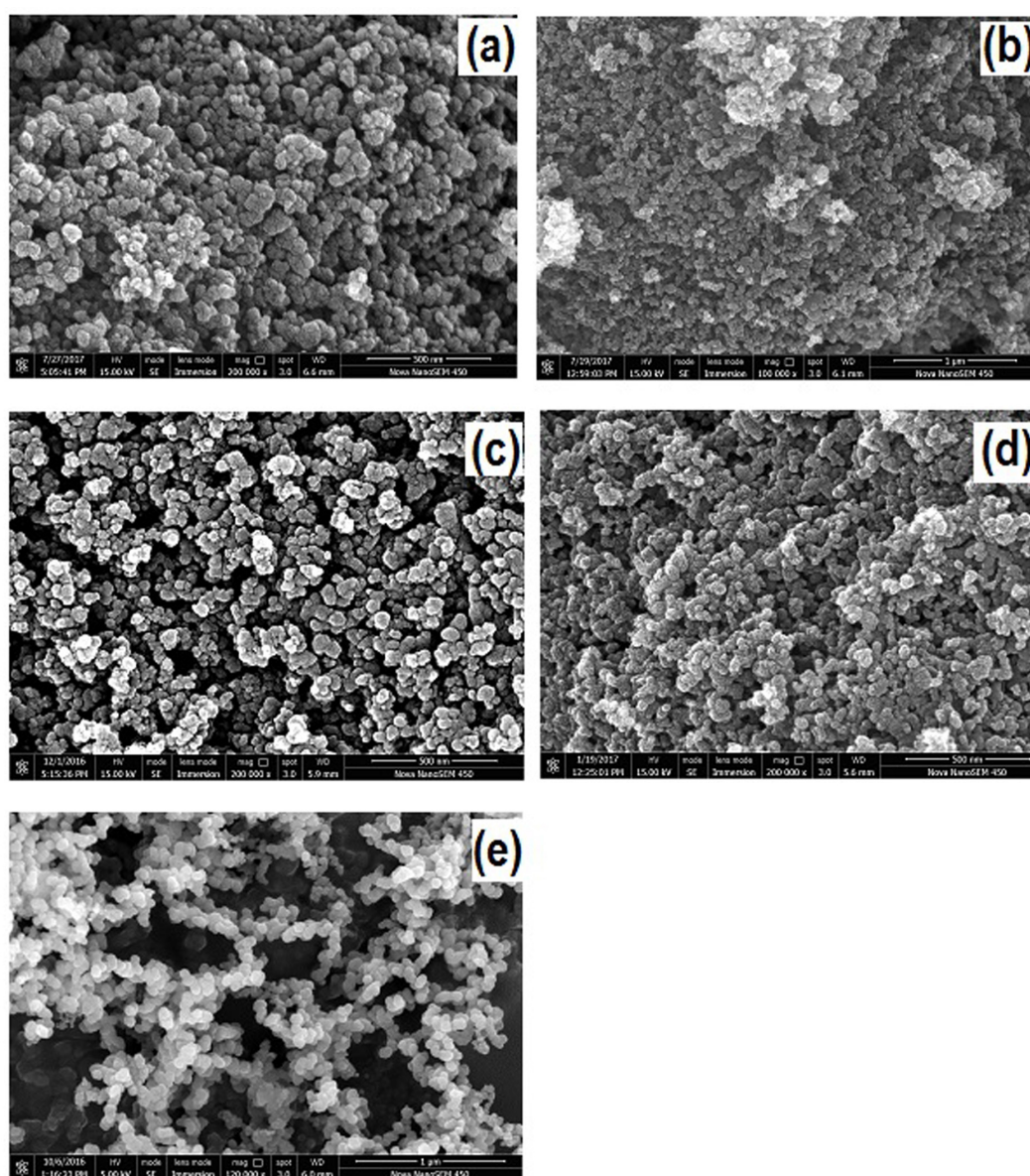


FIG. 1. FESEM images of CNPs obtained from combustion of (a) ghee; (b) coconut oil; (c) sesame oil; (d) diesel; (e) camphor

TABLE 1. Fractal dimensions, R^2 values, and the particle sizes of the CNPs

Samples	Fractal dimension (D)	R^2 value	Particle size (nm)	Average particle size (nm)
Ghee	1.5205	0.9703	40 – 90	80
Coconut oil	1.5541	0.9987	40 – 90	65
Sesame oil	1.6426	0.9949	25 – 60	58
Diesel	1.7805	0.9994	25 – 110	43
Camphor	1.8236	0.9932	20 – 60	40

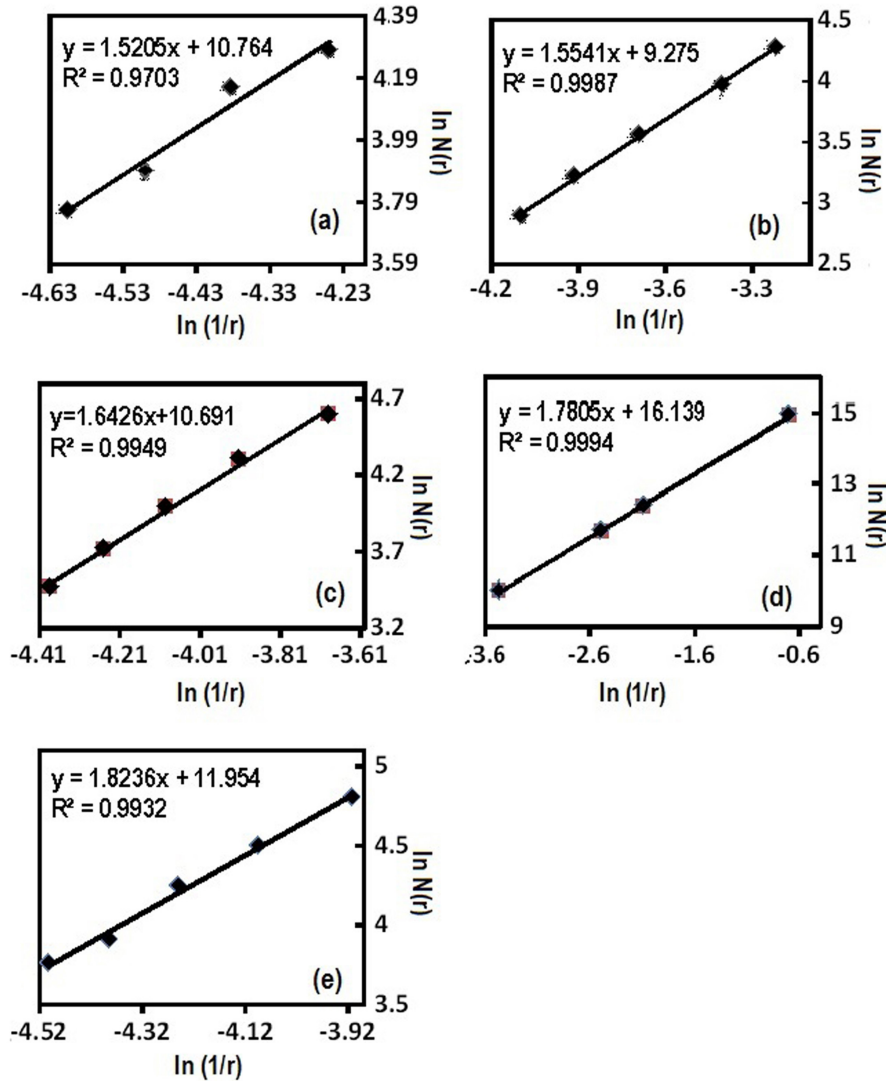


FIG. 2. The plot of $\ln N(r)$ vs $\ln(1/r)$ for the samples (a) ghee; (b) coconut oil; (c) sesame oil; (d) diesel; (e) camphor

correlation coefficient to one, the greater the accuracy is for estimating the particle size. The equation for the best fit is found to be nonlinear and is given by equation (3):

$$\text{Particle size} = 43298D^4 - 293413D^3 + 744612D^2 - 838785D + 353969. \quad (3)$$

From Fig. 4 and Table 1, it can be seen that the average particle size formed during combustion is high in ghee and low in camphor, whereas the fractal dimension is low in ghee and high in camphor. If we analyze the burning process and soot formation, it can be seen that the probability of incomplete combustion is high in ghee, as it does not burn easily as compared to oils. This is why the soot particles from ghee carry larger agglomerates. In the case of camphor, almost complete combustion occurs. Nearly complete combustion leads to the formation of carbon nanotubes, carbon dots and graphene sheets as reported in the literature [19,20]. Hence, it can be understood that when the fractal dimension is low, the particle size in the soot is high and there is a lower probability of forming carbon nanotubes and graphene.

In order to understand the possibility of estimating the particle size contained in the soot without recording the FESEM image, the soot particle of all the samples are sprinkled over a white surface, photographed, and fractal dimension is calculated as it should be invariant under scale transformation. The photographic images of the soot samples and their $\ln N(r)$ vs $\ln(1/r)$ plot are shown in Fig. 5. The fractal dimension obtained from the photographs of soot samples and the particle sizes estimated using equation (3) are given in Table 2. The values thus obtained were compared with the particle sizes estimated from FESEM analysis.

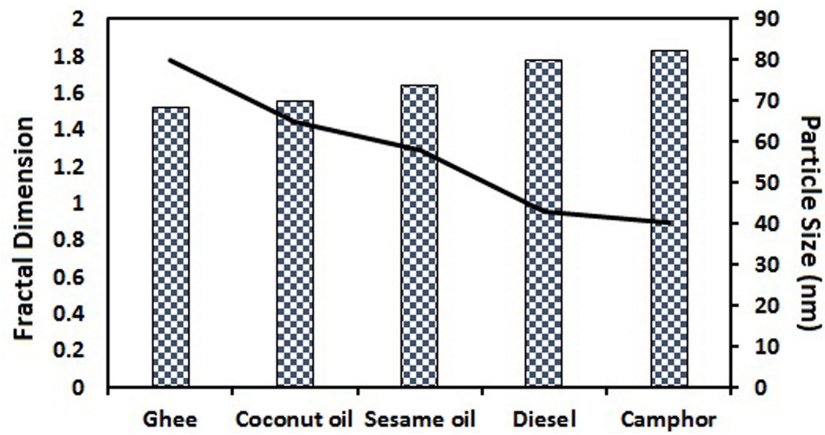


FIG. 3. Fractal dimension and average particle size for various samples

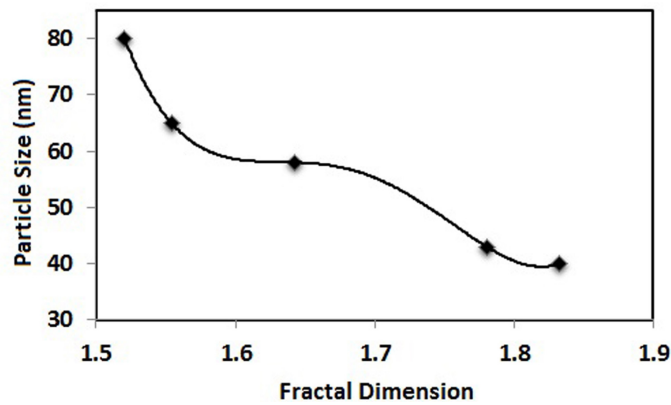


FIG. 4. Variation of particle size with Fractal dimension

TABLE 2. Particle size calculated from fractal dimension of the photograph

Sample	Fractal dimension	Estimated particle size using Eq. (3) (nm)	Measured average size from FESEM (nm)
Ghee	1.7804	41	40–90
Coconut oil	1.6508	57	40–90
Sesame oil	1.7674	44	25–60
Diesel	1.7763	43	25–110
Camphor	1.7982	40	20–60

From Table 2, it can be seen that the particle size calculated from the fractal dimension using equation (3) falls within the range measured from FESEM analysis. This reveals the potential application of estimating the size of CNPs from a photograph without recording the FESEM image, once the regression equation is set. In addition, the fractal dimension gives information regarding the presence of carbon nanotubes, dots, and graphene in the soot. Thus the fractal analysis of the soot can be used for the structural and morphological characterization of soot samples. Though the exact structure cannot be identified, information on the presence of carbon nanotubes, dots, and graphene can be obtained.

4. Conclusion

The present work is the first attempt to estimate the particle size from fractals and thus reveals the potential of fractal analysis as a surrogate technique for FESEM analysis. The CNPs present in the soot of five different

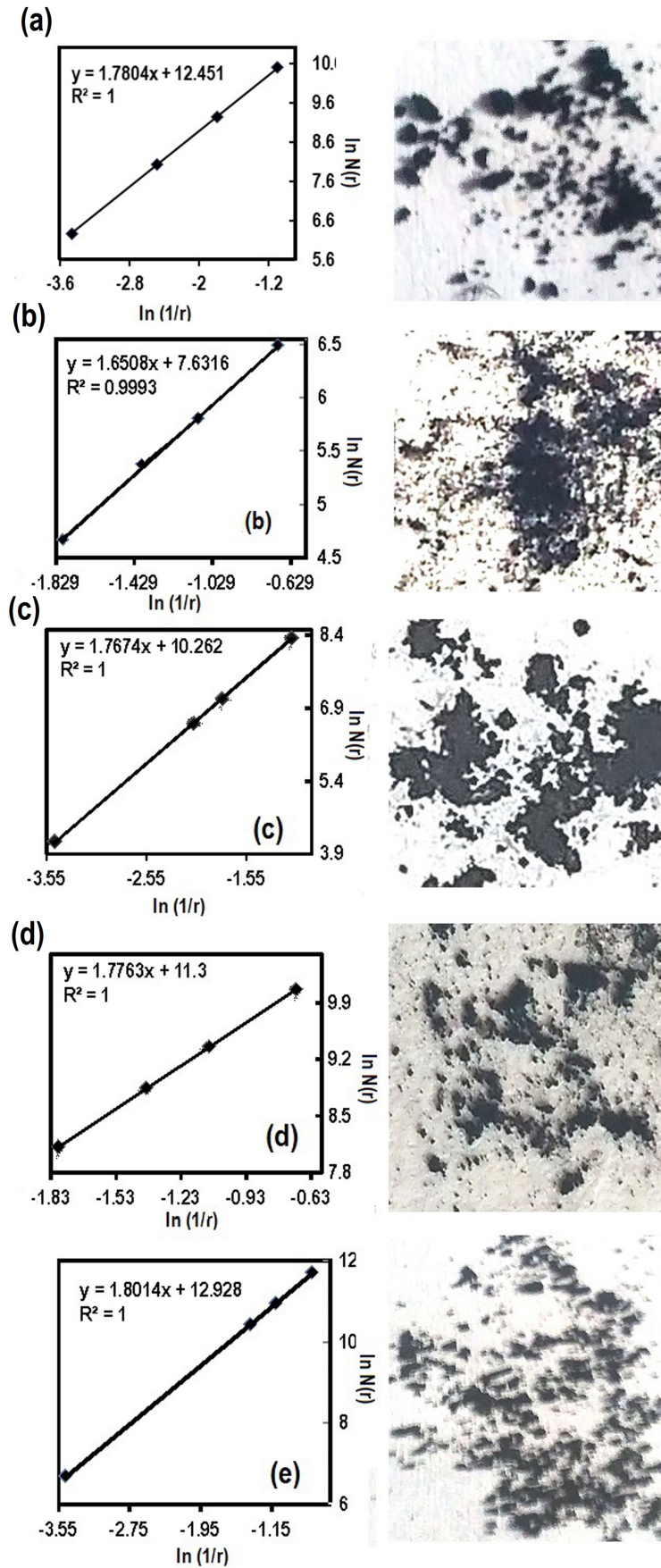


FIG. 5. The photographic image and $\ln N(r)$ vs $\ln(1/r)$ plot of the soot (a) ghee; (b) coconut oil; (c) sesame oil; (d) diesel; (e) camphor

sources such as ghee, coconut oil, sesame oil, diesel, and camphor are analyzed to set up the relation connecting particle sizes and fractal dimension. A fourth order polynomial regression equation is set, relating the particle size and fractal dimension with the FESEM images of the soot particles of known particle size. To assess the possibility of estimating the particle size using the regression equation, photographs of soot particles sprinkled over the white surface are recorded and the fractal dimensions are calculated. Results showed that it is possible to estimate the size of the CNP using the regression equation. Thus, the technique is found to be a potentially cost-effective and non-contact method for the estimation of the size of the nanoparticles from ordinary photographs without recording the FESEM image. The fractal dimension is found to be high for soot that has undergone nearly complete combustion, where carbon nanotubes, dots, and graphene are formed. In the case of incomplete combustion, as in ghee, the particle size is high and the fractal dimension is low. Thus, the present method also opens the possibility of exploring the presence of carbon nanotubes, dots and graphene in the sample. However, the method has the limitation of finding the size of isolated particles when there is agglomeration. In such cases, we will obtain the size of the agglomerate. The fractal analysis technique may also be extended to nanoparticles of other materials.

References

- [1] Falconer K. *Fractals: A Very Short Introduction*. Oxford University press, United Kingdom, 2013.
- [2] Kaandorp J.A. *Fractal modeling: growth and form in biology*. Springer-Verlag, Berlin, Germany, 1994.
- [3] Gleick J. *Chaos: making a new science*. Penguin Books, New York, 1987.
- [4] Liebovitch L.S. *Fractals and Chaos and Simplified for the Life Sciences*, Oxford University Press, 1998.
- [5] Liebovitch L.S., Shehadeh L. The Mathematics and Science of Fractals. URL: www.ccs.fau.edu/liebovitch/larry.html.
- [6] Dobrescu R., Ichim L., Mocanu S., Popescu D. Benign and Malignant Breast Tumors: Diagnosis Using Fractal Measures. *Proceedings of the 18th International Conference on System Theory, IEEE, Control and Computing*, Sinaia, Romania, October 17–19, 2014, P. 82–86.
- [7] Harrar K., Hamami L. The box counting method for evaluate the fractal Dimension in radiographic images. *6th WSEAS International Conference on Circuits, Systems, Electronics, Control & Signal Processing*, Cairo, Egypt, December 29–31, 2007, P. 385–389.
- [8] Seshadri T.R. Fractal analysis of galaxy surveys. *Bull. Astr. Soc. India*, 2005, **33**, P. 1–9.
- [9] Addison P.S. *Fractals and Chaos: An Illustrated Course*. Institute of Physics Publishing, Dirac House, UK, 1997.
- [10] Annadhason A. Methods of Fractal Dimension Computation. *International Journal of Computer Science and Information Technology & Security*, 2012, **2** (1), P. 166–169.
- [11] Tripolskii A.I., Serebrii T.G., et al. Fractal analysis of carbon nanotube agglomerates obtained by chemical vapor decomposition of Ethylene over nickel nanoparticles. *Theoretical and Experimental Chemistry*, 2009, **45** (2), P. 93–97.
- [12] Kumar D., Verma V., Dharamvir K. Elastic Moduli of Carbon Nanotubes Using Second Generation Improved Brenner Potential. *J. Nano Res.*, 2011, **15**, P. 1–10.
- [13] Anu Mohan, Manoj B. Synthesis and Characterization of Carbon Nanospheres from Hydrocarbon Soot. *Int. J. Electrochem. Sci.*, 2012, **7**, P. 9537–9549.
- [14] Ungár T., Gubicza J., Gabor R., Cristian Pantea N. Microstructure of carbon blacks determined by X-ray diffraction profile analysis. *Carbon*, 2002, **4**, P. 929–937.
- [15] Flahaut E., Peigney A., Laurent C., Rousset A. Synthesis of single-walled carbon nanotubeCoMgO composite powders and extraction of the nanotubes. *J. Mater. Chem.*, 2000, **10**, P. 249.
- [16] Hussain S., Jha P., et al. Spectroscopic Investigation of Modified Single Wall Carbon Nanotube. *J. Mod. Phys.*, 2011, **2**, P. 538–543.
- [17] Feder J. *Fractals*. Plenum Press, New York, 1988.
- [18] Markel V.A., George T.F. *Optics of Nanostructured Materials*. John Wiley & Sons, 2001.
- [19] Swapna M.S., Sankararaman S. Investigation of Graphene Oxide in Diesel Soot. *J. Mater. Sci. Nanotechnol.*, 2017, **5** (1), P. 104.
- [20] Swapna M.S., Pooja V.M., et al. Synthesis and characterization of carbon nano kaja. *JOJ Material Sci.*, 2017, **1** (4), 555566.

Stable Ti_9O_{10} nanophase grown from nonstoichiometric titanium monoxide TiO_y nanopowder

A. A. Valeeva^{1,2}, M. G. Kostenko¹

¹Institute of Solid State Chemistry, Ural Branch of the Russian Academy of Sciences,
620990 Pervomayskaya 91, Ekaterinburg, Russia

²Ural Federal University named after the first President of Russia B. N. Yeltsin,
620002 Mira 19, Ekaterinburg, Russia

anibla.v@mail.ru, makskostenko@yandex.ru

PACS 61.72.Dd, 61.72.Bb, 64.70.Nd, 71.20.Ps

DOI 10.17586/2220-8054-2017-8-6-816-822

A new stable Ti_9O_{10} nanophase (sp. gr. *Immm*) has been detected by X-ray diffraction (XRD) after high energy ball milling and long-term vacuum annealing of nanocrystalline powder of nonstoichiometric disordered and ordered titanium monoxide TiO_y with *B1* structure (sp. gr. *Fm $\bar{3}m$*). With the help of XRD data, the unit cell of the Ti_9O_{10} nanophase as well as the distribution of atoms and structural vacancies in the titanium and oxygen sublattices of this phase have been established. The crystal structure of Ti_9O_{10} is derived from that of TiO_y by (a) a migration of the vacancies to the specific crystallographic planes of *B1* structure and (b) by orthorhombic distortions. The DFT calculations of the full energy of the coarse-crystalline phases TiO_y and Ti_9O_{10} revealed that the bulk ordered phase Ti_9O_{10} is not preferable in comparison with the bulk disordered cubic phase TiO_y with the same content of vacancies in the sublattices, so, it is the nanostate that causes the formation of Ti_9O_{10} .

Keywords: Titanium monoxide, ball milling, nanophase Ti_9O_{10} , phase transition, electronic structure.

Received: 22 October 2017

Revised: 27 October 2017

1. Introduction

In the titanium–oxygen system there are many nonstoichiometric phases [1], which are interesting from both fundamental and practical standpoints. For the examination and application of nonstoichiometry, special attention is given to nonstoichiometric titanium monoxide TiO_y having a wide homogeneity range from $\text{TiO}_{0.70}$ to $\text{TiO}_{1.25}$ and a high content of structural vacancies in the titanium and oxygen sublattices of the basic *B1* structure [2–4]. Structural vacancies are an inherent part of the structure of titanium monoxide. They determine the concentration and temperature order-disorder phase transitions [5]. There is substantial documentation in the literature regarding the formation of different ordered phases with cubic, tetragonal, orthorhombic, hexagonal and monoclinic lattices [4–10]. The literature data are only available for coarse-crystalline state and often contradict each other. It is known that in titanium monoxide of stoichiometric composition $\text{TiO}_{1.0}$, at temperatures below 1263 K, a monoclinic superstructure is formed [4, 6], while at temperatures from 1253 to 1523 K, a cubic ordered phase exists [6]. In work [7], a model of cubic Ti_5O_5 superstructure is proposed. The unit cell has a triple spacing as compared with the unit cell of the basic *B1* structure. Recently [8] a new polymorph of titanium monoxide, ε - TiO , was synthesized. The single crystals of ε - TiO [8] have a hexagonal structure (sp. gr. *P $\bar{6}2m$*), which is not *B1* derived but, according to the calculations, is more stable than the ordered monoclinic phase [4, 6]. For compositions ranging from $\text{TiO}_{0.7}$ – $\text{TiO}_{0.9}$ at the temperatures higher than 873 K, an orthorhombic superstructure (*I222*) was reported [2]. However, according to [9], titanium monoxide of substoichiometric composition contains only one ordered phase with monoclinic structure (sp. gr. *C2/m* or *A2/m*). In the range $\text{TiO}_{1.00}$ – $\text{TiO}_{1.50}$, the following ordered phases were found: the orthorhombic phase $\text{TiO}_{1.20}$ (sp. gr. *Immm*, *Imm2* or *I222*) stable below (or at) 1093 K and the tetragonal phase $\text{TiO}_{1.25}$ (sp. gr. *I4/m*, *I4* or *I $\bar{4}$*) stable below 993 K [6].

The powder standard database (card ICSD #77698) contains a calculated powder XRD pattern for Ti_9O_{10} phase (sp. gr. *Immm*) with crystal structure parameters from work [6]. However, in [6], the Ti_9O_{10} is not mentioned. On the latest Ti–O phase diagram, the Ti_9O_{10} phase (sp. gr. *Immm*) is also lacking [1]. Thus, at present, we have only to deal with the calculated Ti_9O_{10} structure and there is no information about the experimentally grown Ti_9O_{10} phase.

Recently, increasing attention is being given to study the effect of small particle size on the stability, properties, nonstoichiometry and structural characteristics of the compounds during the transition from a microcrystalline state to a nanocrystalline one (see [11–13] for example). The nanocrystalline state is far from equilibrium because

of the particles' large specific surface area and excessive free energy, which is a prerequisite for varying the thermodynamic characteristics of the system and its properties as a whole. The nanostate offers vast opportunities for creating a large variety of properties of materials without changing their chemical composition but changing the size of particles and the manner of atomic ordering [12].

In this regard, the aim of this work was the determination of the changes in titanium monoxide's crystal structure during its transition from a coarse crystalline state to a nanocrystalline one.

2. Material and methods

The coarse crystalline samples of titanium monoxide $\text{TiO}_y \equiv \text{Ti}_x\text{O}_z$, where $y = z/x$, with an average size of about $25 \mu\text{m}$ were synthesized by solid-phase sintering from a mixture of titanium Ti and titanium dioxide TiO_2 powders in vacuum of 10^{-3} Pa at 1773 K. The synthesized samples of titanium monoxide contained two phases – disordered cubic phase (sp. gr. $Fm\bar{3}m$) and ordered monoclinic phase (sp. gr. $C2/m$). In order to attain the disordered state, the samples were annealed in vacuum for 3 h at 1373 K, which exceeds the temperature of the equilibrium order-disorder transition. Whereupon the ampoules with the samples were dropped into water, the quenching rate was about 200 K/s. Analysis of the XRD pattern showed that complete disordering in the samples was not reached, partial ordering retained, and the long-range order degree η of the quenched samples was 0.21 [14]. To achieve the ordered state, low-temperature annealing was carried out at 673 K for 4 h in evacuated (10^{-3} Pa) quartz ampoules. After such annealing, the ampoules were slowly cooled to ambient temperature. Analysis of the XRD patterns revealed that annealing at 673 K allowed production of samples with the long-range order degree of $\eta = 0.62$. Multiparameter characterization of the samples was performed by chemical, spectral, picnometer, X-ray phase and X-ray structural analyses [10, 15].

Nanocrystalline titanium oxide powders were produced by high-energy ball milling of coarse crystalline titanium monoxide powders in a Retsch PM 200 planetary-type ball mill. The material of the mill balls and cups was zirconium dioxide ZrO_2 stabilized by yttrium oxide Y_2O_3 . The mass ratio between the mill balls and the powder was 10:1. Isopropyl alcohol was used as a milling liquid, the rotation velocity of the backing plate of the mill cups was 500 rpm, the duration of milling was 480 min. Along with particle size reduction owing to grinding crystal lattice, microstrains appeared in the nanoparticles. The small size and microstrain contributions to the reflection broadening in XRD patterns were determined by the Williamson–Hall method [16, 17]. Owing to the fragmentation of ordered titanium monoxides with near stoichiometric composition, nanoparticles of 20 ± 10 nm in size with the least microstrains of about 0.3 % were prepared. During the fragmentation of the disordered titanium monoxides both with sub- and superstoichiometric compositions, the particle sizes were approximately the same, but the microstrains increased by 3 fold. The method for the preparation of nanoparticles by high-energy milling, analysis of XRD patterns and determination of the coherent scattering regions were reported in detail in [18].

XRD studies of the powders were performed in $\text{CuK}\alpha_1$ -radiation on a STADI-P automatic diffractometer (STOE, Germany) in the Bragg–Brentano geometry by stepwise scanning with $(2\theta) = 0.02$ in the 2θ angle interval from 10 to 120 with a high degree of statistics. Polycrystalline silicon ($a = 543.07$ pm) was used as external standard. Phase analysis of the XRD pattern was performed using Powder Cell 2.4 program. For phase identification the powder standards database ICDD PDF2 (ICDD, USA, Release 2009) was used.

The long-range order parameters of the ordered monoclinic phase were calculated on the basis of the full-profile analysis results by analyzing of the variation in the intensity of structural and superstructural reflections before and after heat treatment.

Experiments on annealing of the titanium monoxide nanopowders were performed from 300 to 1200 K in vacuum of about 10^{-3} Pa with long-term exposure for complete termination of the processes in the system and for structure stabilization. The heating and cooling rate was about 1 K/min. After each exposure, we carried out the X-ray phase analysis to estimate the structural changes occurring after the annealing.

The electronic structure and stability of the bulk Ti_9O_{10} phase were studied using first-principles calculations. The results were compared with the disordered phase of the same composition $\text{TiO}_{10/9}$. The calculations were carried out in the framework of the density functional theory [19, 20] with allowance for the exchange-correlation potential in the generalized gradient approximation (GGA) of the PBE version [21]. The PWSCF code of the Quantum ESPRESSO software suite [22] based on the plane wave and pseudopotential method was used. The energy of the plane waves did not exceed 45 Ry. Besides the valence $3d4s$ states, the semi-core $3s3p$ states were included into the titanium pseudopotential.

3. Results

3.1. The results of the experiment and discussion

Analysis of the XRD pattern of the initially quenched coarse crystalline titanium monoxide sample of stoichiometric composition ($\text{TiO}_{1.00}$) revealed that the sample contains two phases with $B1$ derived structures: cubic TiO_y (sp. gr. $Fm\bar{3}m$) with disordered distribution of the structural vacancies and the ordered monoclinic Ti_5O_5 (sp. gr. $C2/m$), the long-range order parameter η being equal to 0.21 [14]. After long-term heating from ambient temperature to 1200 K, the reflection intensity of the ordered phase Ti_5O_5 on the XRD pattern has increased. Analysis of the variation in intensity of the structural and superstructural reflection showed that the long-range order parameter reached a value of $\eta = 0.54$. Thus, slow heating to high temperatures and slow cooling to ambient temperature made it possible to increase the long-range order degree in the sample with initial strong vacancy disordering.

According to analysis of the experimental XRD patterns, the annealed crystalline titanium monoxide in the initial state also contained two phases: cubic TiO_y (sp. gr. $Fm\bar{3}m$) and monoclinic Ti_5O_5 (sp. gr. $C2/m$) (Fig. 1a). After the series of long-term heating the structure of the sample remained monoclinic. Slow annealing to high temperatures and slow cooling to ambient temperature allowed an increase in the long-range order degree in titanium monoxide from 0.62 to 1.00, which corresponds to the maximal long-range order degree.

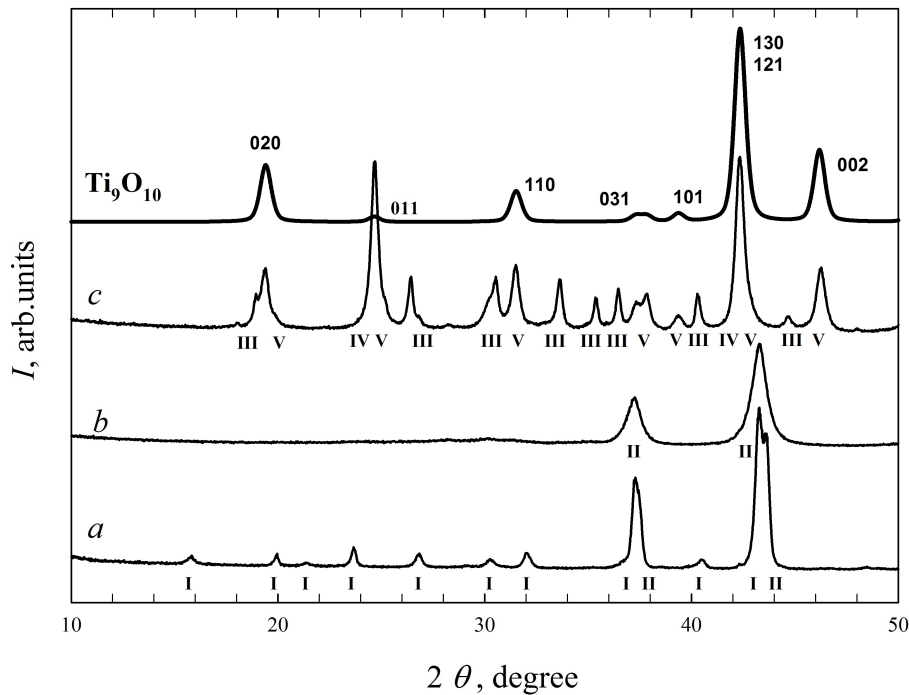


FIG. 1. The XRD patterns of the titanium oxide powders at ambient temperature: a) initial microcrystalline annealed powder (phases: I – Ti_5O_5 , II – TiO_y); b) milled nanocrystalline annealed powder (II – TiO_y phase); c) powder annealed at 1200 K and quenched from 1200 K to ambient temperature (phases: III – Ti_3O_5 , IV – Ti_9O_{10} , V – TiO_2). Calculated XRD pattern of Ti_9O_{10} (upper pattern). Additionally the reflection Miller indices for the Ti_9O_{10} phase are shown

For annealed and quenched nanocrystalline titanium monoxide TiO_y , we have observed different effects. The initial annealed nanocrystalline sample prepared by high-energy milling contained exclusively the cubic phase TiO_y (Fig. 1b). Analysis of the XRD pattern showed that milling leads to disordering and to the lowering of the long-range order degree. Long term vacuum annealing of nanopowder of the ordered titanium monoxide to 1200 K (Fig. 1c) gives rise to the following phases: Ti_9O_{10} (sp. gr. $Immm$) – 50 mass %, Ti_3O_5 (sp. gr. $I2c$) – 20 mass % and TiO_2 (anatase) – 30 mass %. Quenching of the samples from 1200 K to ambient temperature no longer transforms the sample into the initial cubic state.

Long term vacuum annealing of quenched titanium monoxide nanopowder leads, already at 673 K, to partial oxidation of titanium monoxide and, according to the X-ray structural analysis, 3 phases co-exist in the system

TABLE 1. Bond lengths (pm) and bond angles (deg.) in Ti_9O_{10} nanophase

Ti2a–O2c	196.3	O2c–Ti2a –O2c	180
		O2c–Ti2a –O4h	90
Ti2a–O4h	196.3	O4h–Ti2a –O2c	44.32
		O4h–Ti2a –O2c	45.68
Ti4g–O2c	213.7	O2c–Ti4g –O2c	44.32
		O4h–Ti4g –O2c	90
		O4h–Ti4g –O2c	180
Ti4g–O4h	196.3	O4h–Ti4g –O4h	90
		O4h–Ti4g –O4h	180
Ti4g–O4h	213.7	O4h–Ti4g –O4h	44.32

simultaneously: 60 mass % TiO_y (sp. gr. $Fm\bar{3}m$), 25 mass % Ti_9O_{10} (sp. gr. $Immm$) and 15 mass % TiO_2 (anatase). As the temperature is raised to 873 K, the amount of the Ti_9O_{10} phase increases to 60 mass %, while at 1200 K the cubic phase disappears completely and the following phases are formed: Ti_9O_{10} (sp. gr. $Immm$) – 70 mass %, Ti_2O_3 (sp. gr. $R\bar{3}2/c$) – 2 mass % and TiO_2 (anatase) – 28 mass %.

The crystal structure of the experimentally observed Ti_9O_{10} nanophase is shown in Fig. 2. The observed crystal structure can be built up from initial $B1$ structure of the disordered phase TiO_y by (a) an ordering of the structural vacancies by their diffusional shifts to the selected specific crystallographic planes and (b) by orthorhombic distortions. The last effect causes the additional reflections on the XRD pattern of milled and annealed powder (Fig. 1). As a result of the ordering, vacancy planes composed of titanium 2(a) and oxygen 2(c) positions alternate with two vacancy free planes composed of titanium 4(g) and oxygen 4(h) positions. In the initial disordered phase, TiO_y vacancy planes cannot be defined as the probability of finding a vacancy for all the sites are similar. In contrast to monoclinic and cubic Ti_5O_5 structures [4, 5, 7], the vacancy sites in Ti_9O_{10} are not 100 % completed with vacancies. The titanium 2(a) and oxygen 2(c) positions are filled with vacancies by 75 % and 50 %, respectively. The titanium 4(g) and oxygen 4(h) positions are completed with atoms.

There are six titanium and six oxygen sites in a unit cell. The lattice parameters are $a = 298.60$ pm, $b = 915.42$ pm, $c = 392.60$ pm, $\alpha = \beta = \gamma = 90^\circ$. The bond lengths and bond angles are presented in Table 1. The bond angles between nearest atoms of different types are equal to 44.32° , 45.68° and 90° . If the distortion of the basic $B1$ structure is not taken into account, the form of the Ti_9O_{10} unit cell and its position in the $B1$ matrix are similar to that of orthorhombic superstructures M_3X_2 and M_2X_3 (pr. gr. $Immm$) proposed in [23]. However, M_3X_2 and M_2X_3 contain vacancies in only one of the sublattices of the $B1$ structure (metal or nonmetal). In the structure of Ti_9O_{10} , the vacancies are available in both sublattices. Essentially, the structure of Ti_9O_{10} can be obtained with an overlapping of M_3X_2 and M_2X_3 superstructures and a partial occupation of their vacancy sites with atoms.

3.2. The results of the first-principle calculations and discussion

The disorder in the arrangement of vacancies in the disordered phase $TiO_{10/9}$, as well as the disorder in vacancy planes of the Ti_9O_{10} structure (Ti 2(a) and O 2(c) positions) was simulated by a supercell method [24]. The supercells for both $TiO_{10/9}$ and Ti_9O_{10} were constructed by twofold translations of the orthorhombic unit cell of Ti_9O_{10} along the crystallographic directions a , b and c and contained 96 sites of $B1$ structure. The crystallographic positions a of the titanium sublattice in Ti_9O_{10} were randomly occupied by 12 vacancies, whereas positions c of the oxygen sublattice were randomly occupied by 8 vacancies. The number of vacancies in the titanium and oxygen sublattices in $TiO_{10/9}$ was the same as in Ti_9O_{10} . For each phase, 10 supercells with different random arrangements of vacancies were constructed. The results of calculation for 10 superstructures were averaged. Relaxation of the atomic positions was considered.

Figure 3 displays the partial densities of electronic states calculated for the disordered cubic phase of the composition $TiO_{10/9}$ (a) and for the Ti_9O_{10} phase (b). The changes in the electronic structure during the formation of Ti_9O_{10} manifest themselves mainly in the narrowing of the Ti 3s, Ti 3p and O 2s bands, as well as in the variation of the shape of the O 2s and O 2p bands. Additionally, the width of the $p-d$ gap region between the O 2p

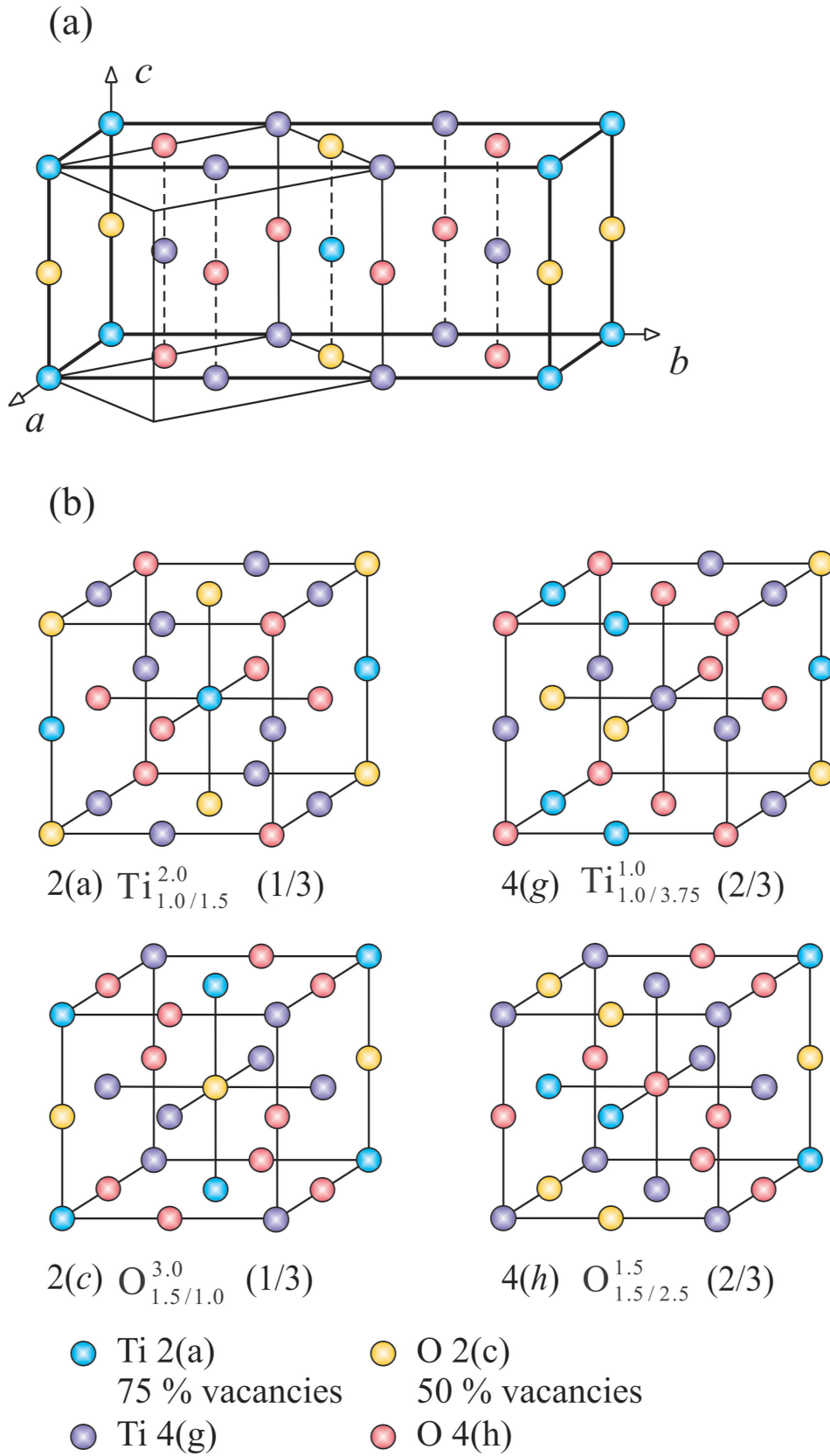


FIG. 2. The unit cell (bold line), the types of crystallographic positions and their multiplicity for the Ti_9O_{10} structure. The distorted unit cell of the B1 structure is indicated by tiny lines

and Ti $3d$ states in the Ti_9O_{10} structure is larger than that in the disordered cubic phase. Note that the dip in the density of Ti $3d$ states distribution for Ti_9O_{10} does not become more profound as compared with the disordered phase, which, according to [25–28], is typical of energetically favorable structures of titanium monoxide. On the other hand, complete disappearance of the dip occurring during the formation of energetically unfavorable local atomic vacancy correlations in the structure [29] is not observed either. The presence of the electronic states at the Fermi level is indicative of the metallic character of the considered phases.

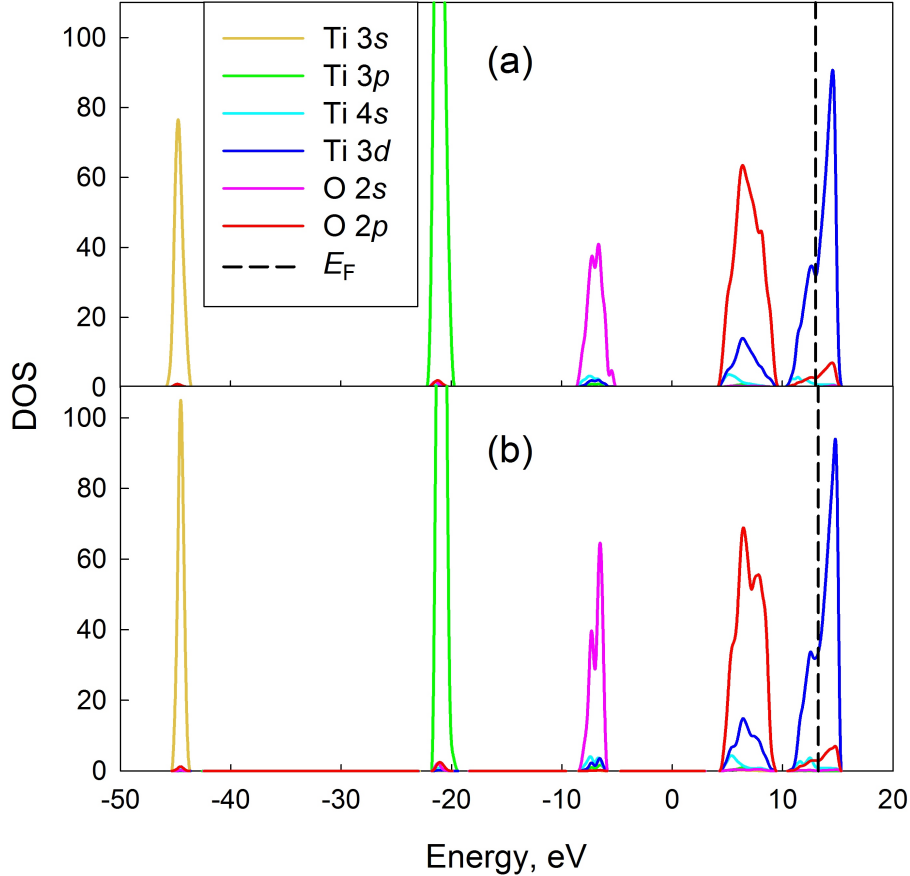


FIG. 3. The partial densities of electronic states calculated for the disordered cubic phase of the composition $TiO_{10/9}$ (a) and for the Ti_9O_{10} phase (b). The Fermi energy (E_F) is indicated by a dotted line

As the energy characteristic of the phases the cohesive energy is calculated by the formula:

$$E_{coh} = (E - N_{Ti} \cdot E_{Ti} - N_O \cdot E_O) / N_{Ti_9O_{10}}, \quad (1)$$

where E is the total energy of the phase examined per one supercell, N_{Ti} , N_O are the quantities of titanium and oxygen atoms in the supercell, respectively, E_{Ti} , E_O refers the total energy of a single Ti or O atom, and $N_{Ti_9O_{10}} = 36$ is the number of $TiO_{10/9}$ structural units in the supercell. In the calculation of energies E_{Ti} and E_O the spin polarization effect was taken account. The cohesive energy of the disordered $TiO_{10/9}$ phase is equal to -14.35 ± 0.04 , while the cohesive energy of Ti_9O_{10} phase turned out to be -14.34 ± 0.04 per formula unit. Thus, the formation of Ti_9O_{10} structure by distortion of the basic $B1$ structure and by variation of the concentration of disordered vacancies in certain crystallographic planes does not give any energy benefit in comparison to the disordered phase. As a matter of fact, the Ti_9O_{10} is the only experimentally confirmed ordered structure of titanium monoxide which ground state energy does not decrease in comparison with that of the disordered phase. We suppose it is the nanostate of the sample that causes the formation of the less energetically favorable ordered structure.

4. Conclusion

In this work, Ti_9O_{10} phase (sp. gr. *Immm*) has been synthesized by a long-term vacuum annealing of nanocrystalline titanium monoxide TiO_y at temperatures ranging from 300 to 1200 K. The unit cell for the Ti_9O_{10} phase has been found, established and constructed. The electronic structure and stability of the new Ti_9O_{10} phase have been studied using first-principle quantum-chemical calculations in comparison with the disordered phase of the same composition. The calculations showed that the Ti_9O_{10} phase is energetically unfavorable in a bulk state as compared with the cubic *B1* structure. It is supposed that the Ti_9O_{10} phase is formed by transition from a crystalline state to a nanostate.

Acknowledgements

The work was carried out at the Institute of Solid State Chemistry UB RAS with financial support from the Russian Science Foundation (project 14-23-00025).

References

- [1] Okamoto H. O–Ti (Oxygen-Titanium). *J. Phase Equil. Diffus.*, 2011, **32**, P. 473–474.
- [2] Anderson S., Collen B., Kuylenstierna U., Magneli A. Phase Analysis Studies on the Titanium–Oxygen System. *Acta Chem. Scand.*, 1957, **11**, P. 641–1652.
- [3] Banus M.D., Reed T.B. Structural, electrical and magnetic properties of vacancy stabilized cubic TiO and VO. In: *The Chemistry of Extended Defects in Non-Metallic Solids*, Amsterdam-London: North-Holland Publ., 1970, P. 488–521.
- [4] Watanabe D., Castles J.R., Jostson A., Malin A.S. Ordered Structure of Titanium Oxide. *Nature*, 1966, **210**, P. 934–936.
- [5] Rempel A.A., Valeeva A.A. Thermodynamics of atomic ordering in nonstoichiometric transition metal monoxides. *Mend. Communication*, 2010, **20**, P. 101–103.
- [6] Hilti E. Neue Phasen im System Titan–Sauerstoff. *Naturwissenschaften*, 1968, **55**, P. 130–131.
- [7] Gusev A.I., Valeeva A.A. Diffraction of electrons in the Cubic Ti_5O_5 superstructure of titanium monoxide. *JETP Letters*, 2012, **96**, P. 364–369.
- [8] Amano S., Bogdanovskii D., et al. ϵ -TiO, a Novel Stable Polymorph of Titanium Monoxide. *Angew. Chem. Int. Ed.*, 2016, **55**, P. 1652–1657.
- [9] Khaenko B.V., Kachkovskaya E. Ordering and phase ratios in Ti–O system in the range of titanium monoxide existing. *Poroshkovaya metallurgiya (Powder metallurgy)*, 1986, **6**, P. 52–59.
- [10] Valeeva A.A., Rempel A.A., Gusev A.I. Ordering of cubic titanium monoxide into monoclinic Ti_5O_5 . *Inorganic materials*, 2001, **37**, P. 603–612.
- [11] Valeeva A.A., Nazarova S.Z., Rempel A.A. Influence of Particle Size, Stoichiometry, and Degree of Long-Range Order on Magnetic Susceptibility of Titanium Monoxide. *Physics of the Solid State*, 2016, **58**, P. 771–778.
- [12] Rempel A.A. Hybrid nanoparticles based on sulfides, oxides, and carbides. *Russ. Chem. Bull.*, 2013, **4**, P. 857–868.
- [13] Schaefer H.-E. *Nanoscience*. Springer Verlag, Berlin, 2010, 772 p.
- [14] Valeeva A.A., Nazarova S.Z., Rempel A.A. In situ study of atomic-vacancy ordering in stoichiometric titanium monoxide by the magnetic susceptibility. *JETP Letters*, 2015, **101**, P. 258–263.
- [15] Valeeva A.A., Rempel A.A., Gusev A.I. Two-sublattice ordering in titanium monoxide. *JETP Letters*, 2000, **71**, P. 460–464.
- [16] Hall W.H. X-Ray Line Broadening in Metals. *Proc. Phys. Soc. London. Sect. A*, 1949, **62**, P. 741–743.
- [17] Hall W.H., Williamson G.K. The Diffraction Pattern of Cold Worked Metals: I The Nature of Extinction. *Proc. Phys. Soc. London. Sect. B*, 1951, **64**, P. 937–946.
- [18] Valeeva A.A., Petrovykh K.A., Schroettner H., Rempel A.A. Effect of stoichiometry on the size of titanium monoxide nanoparticles produced by fragmentation. *Inorganic Materials*, 2015, **51**, P. 1132–1137.
- [19] Kohn W., Sham L.J. Self-Consistent Equations Including Exchange and Correlation Effects. *Phys. Rev. A*, 1965, **140**, P. 1133–1138.
- [20] Jones R.O., Gunnarsson O. The density functional formalism, its applications and prospects. *Rev. Mod. Phys.*, 1989, **61**, P. 689–746.
- [21] Perdew J.P., Burke K., Ernzerhof M. Generalized Gradient Approximation Made Simple. *Phys. Rev. Lett.*, 1996, **77**, P. 3865–3868.
- [22] Giannozzi P., Baroni S., Bonini N. et al. Quantum espresso: a modular and open-source software project for quantum simulations of materials. *J. Phys. Condens. Matter*, 2009, **21**, 395502 (19 p.).
- [23] Gusev A.I. Ordered Orthorhombic Phases of Titanium Monoxide. *JETP Letters*, 2001, **74**, P. 91–95.
- [24] Payne M.C., Teter M.P., et al. Iterative minimization techniques for ab initio total-energy calculations: molecular dynamics and conjugate gradients. *Rev. Mod. Phys.*, 1992, **64**, P. 1045–1097.
- [25] Andersson D.A., Korzhavyi P.A., Johansson B. Thermodynamics of structural vacancies in titanium monoxide from first-principles calculations. *Phys. Rev. B*, 2005, **71**, 144101 (12 p.).
- [26] Graciani J., Mrquez A., Sanz J.F. Role of vacancies in the structural stability of α -TiO: A first-principles study based on density-functional calculations. *Phys. Rev. B*, 2005, **72**, 054117 (6 p.).
- [27] Kostenko M.G., Lukoyanov A.V., Zhukov V.P., Rempel A.A. Vacancies in ordered and disordered titanium monoxide: Mechanism of *B1* structure stabilization. *J. Sol. St. Chem.*, 2013, **204**, P. 146–152.
- [28] Kostenko M.G., Lukoyanov A.V., Zhukov V.P., Rempel A.A. Effect of the long-range order in the vacancy distribution on the electronic structure of titanium monoxide $\text{TiO}_{1.0}$. *JETP Lett.*, 2012, **96**, P. 507–510.
- [29] Kostenko M.G., Rempel A.A., Sharf S.V., Lukoyanov A.V. Simulation of the short-range order in disordered cubic titanium monoxide $\text{TiO}_{1.0}$. *JETP Lett.*, 2013, **97**, P. 616–620.

Preparation of Au/TiO₂/Ti memristive elements via anodic oxidation

P. A. Morozova^{1,2}, D. I. Petukhov²

¹Skolkovo Institute of Science and Technology, Skolkovo, Nobel Street, 3, Moscow Region, 143026, Russia

²Lomonosov Moscow State University, Department of Materials Science,
Leninskie gory, 1, building 73, Moscow, 119991, Russia

polina.morozova@skoltech.ru, di.petukhov@gmail.com

PACS 85.30.Hi, 85.30.Kk, 85.30.Mn

DOI 10.17586/2220-8054-2017-8-6-823-829

In the present paper we report utilization of porous and barrier type of titania films formed by anodic oxidation as an active layer of the memristive element in the Au–TiO₂–Ti structure. The comparison of semiconductor properties of porous and barrier type of anodic titania was performed via the Mott–Schottky technique. The obtained memristive elements show the bipolar type of switching governed by Schottky barrier screening. For barrier type film the switching potential is equal to -1.5 V and the ratio of resistance in OFF and ON stage (R_{off}/R_{on}) is equal to 34. For porous type films, the switching potential is equal to -0.6 V and $R_{off}/R_{on} = 131$. Moreover, we observed the dependence of R_{off}/R_{on} on the voltage sweeping rate, which can be explained by the limitation in diffusion of oxygen vacancies through the oxide layer.

Keywords: memristor, anodic titania, anodic oxidation, memristive element, Schottky barrier, oxygen vacancies diffusion.

Received: 8 November 2017

Revised: 13 November 2017

1. Introduction

Memristive phenomena is one of the most promising way to form non-volatile and magneto-independent information storage devices. A memristor is a circuit element which can be switched between a high resistance state (HRS) and a low resistance state (LRS) by applying a switching potential. A memristor possesses the layered structure in which a semiconductor layer is sandwiched between two metal contacts. Different types of non-stoichiometric oxide semiconductors are often used as an active layer of a memristor. In thin semiconductor films, unipolar mechanism of switching is realized by the formation of ionic, vacancy and metal filaments [1–3]. In thick films, a bipolar resistive switching mechanism is realized due to increasing of defect concentration (for example, oxygen vacancies) near one of the electrode under an applied electric field, which leads to the screening of the Schottky barrier at the metal-oxide interface. The formation of the Schottky barrier occurs in the case of the formation of the space charge region – semiconductor’s ionized donors or acceptors. Typically, memristive elements are assembled as the prototypes of memory storage devices using cross-bar architecture [4,5]. This means that the active layer of a memristor should be formed via techniques which are compatible with the techniques typically used for the manufacturing of semiconductors and electronic devices, such as photolithography, magnetron sputtering, reactive-ion etching, and so on. Anodic oxidation of valve metals appears to be one of promising method for the formation of the memristor active layer due to its compatibility with the photolithography [6] and magnetron sputtering [7] and possibility to control the thickness and the stoichiometry of a formed film [8–10].

Anodic titania is an *n*-type semiconductor with a chemical composition of TiO_{2–x}, where high mobility oxygen vacancies exist [11, 12]. By anodization of titanium in non-dissolving electrolytes (such as aqueous solution of Na₂B₄O₇, ammonium tartrate, etc.) nonporous dense film with thickness of up to one micron can be formed [13, 14]. Anodization in fluorine-containing electrolyte leads to the formation of a self-organized porous film, which consists of vertically oriented nanotubes. Nanotube geometry depends on an applied voltage, current mode and electrolyte composition [15–17]. Because of its unique porous structure, anodic titania is widely used in photocatalysis and photochromic systems [18, 19], biomedical applications [20], gas sensors [21, 22] and pigment preparation [23]. At the same time, the study of memristive properties was performed only in the few articles [24–26]. However, anodic oxidation technique allows to form amorphous highly non-stoichiometric titania, which can be considered as a promising active layer for memristive elements. That’s why in the present work we compare two types of anodic titania: a porous film formed in fluorine-containing electrolyte and a non-porous film formed in boron-containing electrolyte. The microstructure and semiconductor properties of titania films are characterized. Finally, the resistive switching behavior of Au/TiO₂/Ti memristive device is studied.

2. Experimental

2.1. Sample preparation

Titanium foil (0.25 mm thick, 99.9 % purity) was used as a starting material for the preparation of memristive structures. Before anodization, initial titanium foil was chemically polished in the mixture of 80 vol. % of H₂O₂ and 20 vol. % of saturated HF. After chemical polishing, the sample was repeatedly washed with deionized water and dried at ambient temperature in air.

For preparation of the porous anodic titania film, the synthetic approach early described in [27,28] has been used. The anodization of the titanium foil was carried out in a two-electrode cell in solution containing 10 g/L NH₄F and 10 vol. % of H₂O in ethylene glycol at a constant voltage of 60 V. The thickness of the obtained film was controlled by passing the required charge through the cell. Preparation of the barrier type anodic titania films was carried out in a galvanostatic regime with a current density of 0.2 A/cm² with a voltage limit of 60 V in 0.16 M solution of Na₂B₄O₇. After anodization, all samples were repeatedly washed with ethanol and water and dried under an air stream.

The top metal contact was sputtered on the anodic titania surface by magnetron sputtering on a Quorum Technologies Q150T ES setup.

2.2. Sample characterization

Microstructure of the obtained samples was characterized by scanning electron microscopy (Leo Supra 50VP). Mott-Schottky analysis was performed for the determination of a conductivity type and a charge current density using electrochemical impedance spectroscopy [29–32] with a Solartron SI 1287 potentiostat. Experiments were conducted in 0.5 M H₂SO₄ and a DC potential range from –0.5 to 0.8 VSCE with a potential step of 50 mV at the constant frequencies of 10 Hz, 50 Hz, and 100 Hz for an amplitude of 5 mV. The dependence of a semiconductor layer capacitance vs. DC potential was used for the determination of a conductivity type and for the calculation of charge carrier concentration. The capacitance of the semiconductor layer was calculated according to following equation:

$$C = \frac{-1}{2\pi S f Z_{im}}$$

where S – sample area, f – frequency, Z_{im} – the imaginary component of the impedance.

Solid-state current-voltage (I - V) and current-time (I - t) (memristive behavior) dependencies were obtained on an Autolab PGSTAT302N potentiostat.

3. Results and discussions

3.1. Microstructure

The microstructure of the obtained films was characterized via scanning electron microscopy (Fig. 1). According to SEM data, the surface of the sample obtained in Na₂B₄O₇ electrolyte was dense and nonporous (Fig. 1a). We were unable to determine the thickness of the formed film by microscopy, that's why we used Fabry–Perot interferometric analysis for the film thickness determination. The barrier film thickness determined from optical spectra is equal to 250 nm. At the same time, anodization in fluorine-containing electrolyte led to the formation of a highly-organized porous layer with a pore diameter of 80 ± 10 nm. The thickness of the porous film was equal to 500 nm and the required thickness was obtained by passing the charge density of 0.88 Q/cm². The correlation coefficient between the thickness of the obtained film and the passed charge density determined in the set of experiments was equal to 0.4 μm/(Qcm²).

Both oxidation conditions led to the preparation of uniform amorphous films without cracks on the surface of titanium. Moreover, the preparation technique provided the presence of bottom contact between metallic titanium and titanium dioxide film.

3.2. Mott–Schottky analysis

The Mott–Schottky behavior both for the barrier and porous type of anodic titania is in accordance with expected behavior of n -type semiconductor: increasing of the anodic bias above the flat band potential leads to decreasing of the semiconductor layer capacitance. This can be explained due to the repulsion of electrons from generated electron-hole pairs to the bulk of semiconductors, which leads to the formation of the positively charged space charge region at the surface of the semiconductor. It should be noted that for the barrier type of anodic titania, the Mott–Schottky curve contains only one linear region (Fig. 2a), at the same time, the curve for porous anodic titania contains two linear regions with different slope (Fig. 2b). The presence of two regions can be explained by the presence of multiple donor stages in the band gap formed by absorbed F⁻ or [TiF₆]²⁻ ions [33–35].

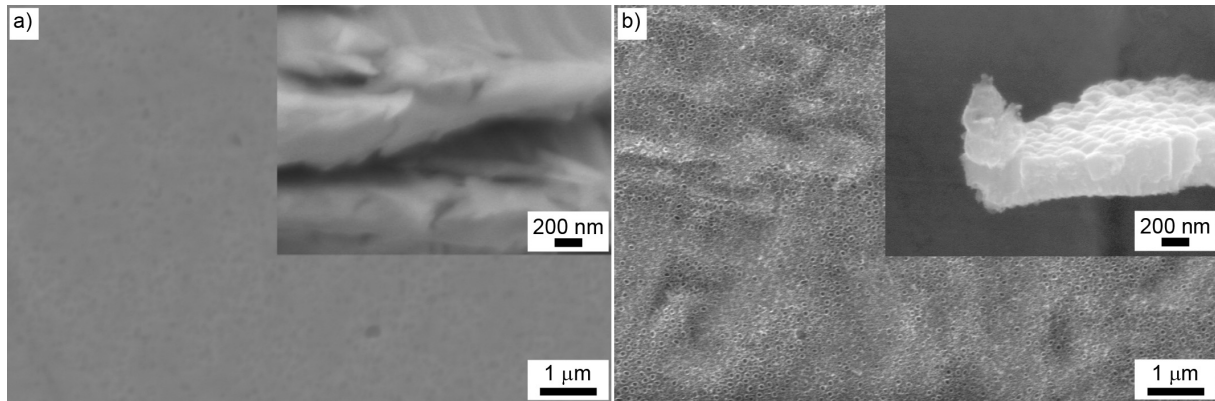


FIG. 1. The microstructure of anodic titania films formed in boron-containing (a) and fluorine-containing (b) electrolyte. The cross-section of the titania films are shown on the insets

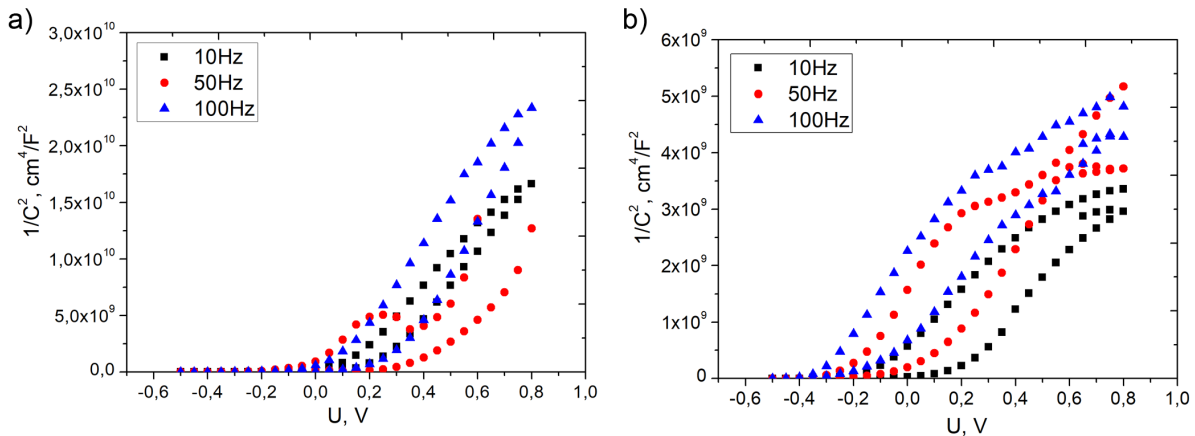


FIG. 2. Mott-Schottky analysis of the barrier (a) and porous (b) type anodic titania films at the DC potential in the range of -0.5 to $0.8V_{SCE}$ and frequencies of 10, 50 and 100 Hz

From the slope of Mott-Schottky curve, the charge carrier density was calculated according to the following equation:

$$\frac{1}{C^2} = \frac{2}{N_d q \epsilon \epsilon_0} \cdot \left(U - E_{fb} - \frac{kT}{q} \right),$$

where C – the capacitance of semiconductor layer, N_d – charge carrier density, ϵ – semiconductor dielectric constant, E_{fb} – flat band potential.

The calculated value of the charge carrier density for the barrier layer type anodic titania is $6.7 \cdot 10^{19} \text{ cm}^{-3}$. For the porous type anodic titania, the calculation of the charge current density was performed from the first linear region (from -0.1 to 0.4 V). The calculated value $3.0 \cdot 10^{20} \text{ cm}^{-3}$ is 3 – 4 times higher in comparison with the value obtained for barrier type. This can be explained by the presence of additional donor stages formed by the absorbed anions.

3.3. Memristive behavior of formed structures

For the preparation of Schottky barrier-type memristor we should choose the top electrode with the work function higher than the work function of titania. It can be gold or platinum electrodes. At the same time, the bottom contact formed on the TiO₂/Ti interface during anodization is non-rectifying contact because the work function of Ti (4.3 eV) is lower than that of TiO₂ (4.9 eV) [36, 37]. We measured the I-V curves for two different systems Cr/TiO₂/Ti where both contacts were non-rectifying (Cr work function is 4.5 eV) and Au/TiO₂/Ti where the top contact was rectifying. The Cr/TiO₂/Ti system exhibits ohmic behavior, whereas the I-V curve for Au/TiO₂/Ti has a typically rectifying characteristic (Fig. 3).

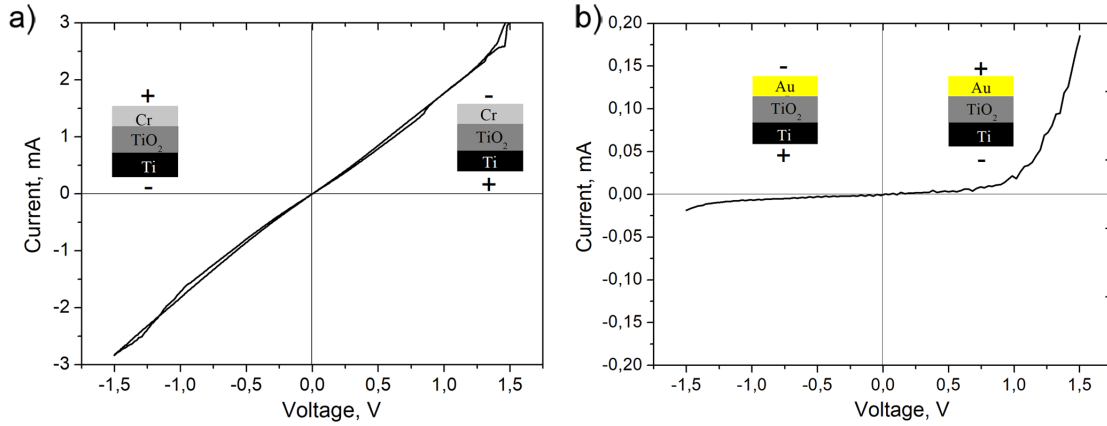
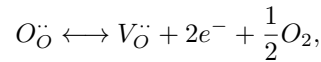


FIG. 3. I - V Curves for Cr/TiO₂/Ti structure where both contacts are non-rectifying (a), and Au/TiO₂/Ti where the top contact is rectifying (b)

The resistive switching behavior of Au/TiO₂/Ti structures both with the porous (Fig. 3a) and barrier (Fig. 3b) type of anodic titania was studied using cyclic voltammetry. The I - V curve characteristic for both type of memristors shows bipolar resistive switching behavior. Bipolar resistive switching behavior and the formation of a symmetric ohmic contact in the case of Cr/TiO₂/Ti structure and a Schottky junction in the case of Au/TiO₂/Ti allow us to conclude that the Schottky barrier screening is the main mechanism of switching between resistance stages. The Schottky barrier screening occurs due to diffusion of oxygen vacancies to the Au/TiO₂ interface under negative applied bias. The formation of oxygen vacancies in the titania structure can be described by the following quasi-chemical equation:



where $O_{\text{O}}^{\cdot\cdot}$ is the oxygen on the TiO₂ lattice, and $V_{\text{O}}^{\cdot\cdot}$ is a positively charged oxygen vacancy. This reaction also explains the n -type conductivity of TiO₂. Moreover, the mobility of oxygen vacancies in TiO₂ is quite high [38], so we expect that the diffusion of oxygen vacancies to the Au/TiO₂ interface leads to the screening of Schottky barrier.

The memristor with barrier type of oxide film switches to LRS at the negative polarity $U < -1.3$ V and reverse switching to HRS at the positive polarity $U > 1.4$ V (in following discussion the polarity is equal to polarity of the top gold electrode). For the porous type of anodic alumina, switching to LRS occurs at a negative polarity at the voltages in range from -0.6 to -0.8 V (depending on the voltage sweeping range) and reverse switching to HRS occurs at the positive polarity $0.6 \div 0.8$ V.

Average slope values of the I - V curves were used for the calculation of the specific resistivities (ρ) for high and low resistance stages (Fig. 4). For the barrier type of anodic titania the calculated specific resistivities are $285 \pm 5 \Omega\cdot\text{m}$ (LRS) and $6700 \pm 100 \Omega\cdot\text{m}$ (HRS), which corresponds to $R_{\text{off}}/R_{\text{on}} = 23.5$. For the porous anodic titania the corresponding values of the specific resistance are equal to $20 \pm 5 \Omega\cdot\text{m}$ (LRS) and $250 \pm 5 \Omega\cdot\text{m}$ (HRS), and $R_{\text{off}}/R_{\text{on}} = 12.5$. It should be noted that for the porous type of anodic alumina the resistivity ratio between on and off stages depends on the voltage sweeping rate. Measured off/on resistance ratios were equal to 131, 12.5 and 10.8 for sweeping rates 1, 10 and 50 mV/s, respectively. This dependence can be explained by the limitation in the diffusion of oxygen vacancies throughout the oxide layer: decreasing the voltage-sweeping rate leads to an increase in the duration of a potential influence. This leads to an increase in the quantity of the oxygen vacancies diffused to the Au/TiO₂ interface and to an increase in the degree of the Schottky barrier screening.

The difference between the resistivities in high resistance stage for the porous and barrier type of anodic titania films can possibly be explained by the different stoichiometry of the formed oxide film. It is well known that the conductivity of titania strongly depends on oxygen stoichiometry [39]. Oxidation in the ethylene-glycol electrolyte, containing F^{-} ions leads to the formation of a non-stoichiometric oxide with intermediate oxidation states [12], whereas oxidation in non-dissolving electrolytes leads to the formation of titania films with chemical composition closer to a stoichiometric TiO₂ [40]. Moreover, the concentration of charge carriers for the barrier and porous types of anodic titania measured using the Mott-Schottky technique also proves that the porous film should have higher conductivity.

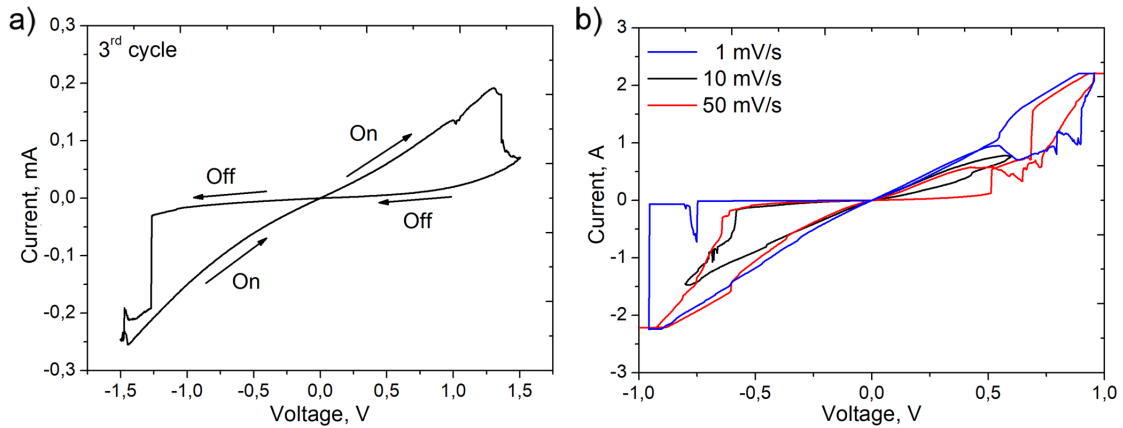


FIG. 4. I - V Curves for Au/TiO₂/Ti structure with barrier (a) and porous (b) active layer

To determine the stability of low resistance stage of the formed memristors, we measured the chronoamperometric curves of binary on-off operations (Fig. 5). The measurement was performed by applying SET potential -0.8 V for 30 s, then $-$ READ potential -0.2 V for 30 s followed by applying RESET potential of 0.6 V for 30 s and READ potential. Applying a SET potential led to switching the memristor to LRS, and applying a RESET potential leads to switching the memristor to HRS. The values of resistance in HRS and LRS were quite stable during the 110 cycles. At the same time, applying a potential lower than SET potential (-0.4 V) didn't lead to resistance switching – the sample stay in high resistance stage (Fig. 5b).

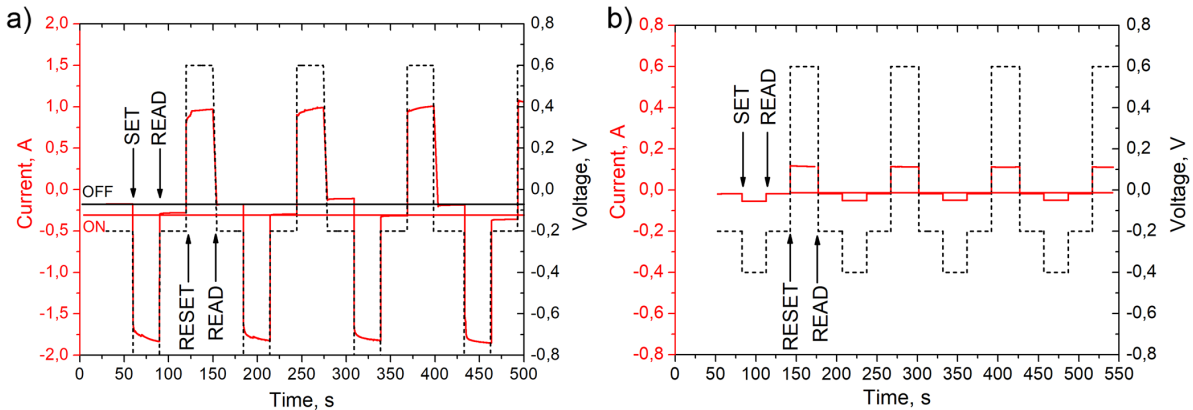


FIG. 5. I - t curves obtained by applying -0.8 V (a) and -0.4 V (b) SET potential, -0.2 V read potential and 0.6 V RESET potential with duration of 30 s

4. Conclusions

In the present work, anodic titania films of porous and barrier type were formed by anodic oxidation in fluorine-containing and boron-containing electrolytes respectively. Comparison of the semiconductor properties of the formed films was performed via the Mott-Schottky technique. It was shown that both type of films exhibit the n -type conductivity, whereas the charge carrier density in the case of the porous titania film was higher than that of the barrier type film. This can be explained by the presence of local donor impurity levels, which were formed by fluorine-ion impurities absorbed during anodization.

The obtained memristive elements show the bipolar type of switching governed by Schottky barrier screening. For the barrier type film, the switching potential is equal to -1.5 V and the ratio of resistivity in high and low resistance stage is 34. For the porous type film, the resistance strongly depends on the voltage sweeping rate, and the highest value of R_{off}/R_{on} is equal to 131, switching potential is equal to -0.6 V. This dependence can be explained by the limitation in diffusion of oxygen vacancies throughout the oxide layer. At the same time, memristive element based on barrier type film of anodic titania exhibits higher switching stability (more than

1000 cycles), has the structure with lower defect concentration and is more suitable for the application as a cell in memory storage devices.

Acknowledgements

The work is supported by Russian Foundation of Basic Research Grant No. 16-08-00574 and Lomonosov Moscow State University Development Programme. Dmitrii Petukhov is also thankful to RF President Grant MK-799.2017.3 for the financial support.

References

- [1] Kyung M.K., Tae H.P. Dual Conical Conducting Filament Model in Resistance Switching TiO₂ Thin Films. *Scientific Reports*, 2015, **5**, P. 7844.
- [2] Zhang F., Li X.M., Gao X.D. The unification of filament and interfacial resistive switching mechanisms for titanium dioxide based memory devices. *Journal of applied physics*, 2011, **109**, 104504.
- [3] Ssenyange S., Yan H. Redox-driven conductance switching via filament formation and dissolution in carbon/molecule/TiO₂/Ag molecular electronic junctions. *Langmuir*, 2006, **22** (25), P. 10689–10696.
- [4] Pickett M.D. The Materials Science of Titanium Dioxide Memristors. Electronic Thesis and Dissertations UC Berkeley, 2010, URL: http://digitalassets.lib.berkeley.edu/etd/ucb/text/Pickett_berkeley_0028E.11006.pdf
- [5] Yang J.J., Pickett M.D., Li X. Memristive switching mechanism for metal/oxide/metal nanodevices. *Nature Nanotechnology*, 2008, **3**, P. 429–433.
- [6] Albu S.P. et al. TiO₂ nanotube layers: Flexible and electrically active flow-through membranes. *Electrochemistry Communications*, 2010, **12**, P. 1352–1355.
- [7] Prusakova V., Collini C., Nardi M. The development of solgel derived TiO₂ thin films and corresponding memristor architectures. *RSC Adv.*, 2017, **7**, P. 1654–1663.
- [8] Diamanti M.V., Pisoni R., Cologni A. Anodic oxidation as a means to produce memristive films. *J. Appl. Biomater. Funct. Mater.*, 2016, **14** (3), P. 290–295.
- [9] Abunahla H., Mohammad B. *Memristor Technology: Synthesis and Modeling for Sensing and Security Applications*. Springer International Publishing, 2018, 106 p.
- [10] Diamanti M.V., Spreafico F.C., Pedferri M.P. Production of anodic TiO₂ nanofilms and their characterization. *Physics Procedia*, 2013, **40**, P. 30–37.
- [11] Pham Hieu H., Wang Lin-Wang. Oxygen vacancy and hole conduction in amorphous TiO₂. *Phys. Chem. Chem. Phys.*, 2015, **17**, P. 541–550.
- [12] Petukhov D.I., et al. Formation mechanism and packing options in tubular anodic titania films. *Microporous and Mesoporous Materials*, 2008, **114**, P. 440–447.
- [13] Zixue S., Wuzong Z. *Porous Anodic Metal Oxides*, University of St. Andrews, 2010.
- [14] Wei W. Advanced Electrochemical Approaches for the Self-organized Formation of One-Dimensional Oxide Nanoarchitectures: From Transition Metals to Superlattices. University of Erlangen–Nürnberg, 2012, URL: https://opus4.kobv.de/opus4-fau/files/2334/wei_thesis.pdf.
- [15] Chen X., Mao S.S. Titanium Dioxide Nanomaterials: Synthesis, Properties, Modifications, and Applications. *Chem. Rev.*, 2007, **107**, P. 2891–2959.
- [16] Keller F., Hunter M.S., Robinson D.L. Structural Features of Oxide Coatings on Aluminum. *J. Electrochem. Soc.*, 1953, **100** (9), P. 411–419.
- [17] OSullivan J.P., Wood G.C. The morphology and mechanism of formation of porous anodic films on aluminium. *Proc. R. Soc. Lond. A*, 1970, **317** (1531), P. 511–543.
- [18] Nakata K., Fujishima A. TiO₂ photocatalysis: Design and applications. *Journal of Photochemistry and Photobiology C: Photochemistry Reviews*, 2012, **13**, P. 169–189.
- [19] Diop D.K., Simonot L. Magnetron Sputtering Deposition of Ag/TiO₂ Nanocomposite Thin Films for Repeatable and Multicolor Photochromic Applications on Flexible Substrate. *Adv. Mater. Interfaces*, 2015, **2**, 1500134.
- [20] Roy P., Berger S., Schmuki P. TiO₂ Nanotubes: Synthesis and Applications. *Angew. Chem. Int. Ed.*, 2011, **50**, P. 2904–2939.
- [21] Kim I.D., Rothschild A., Lee B.H., Kim D.Y. Ultrasensitive chemiresistors based on electrospun TiO₂ nanofibers. *Nano Lett.*, 2006, **6** (9), P. 2009–2013.
- [22] Seo M.-H., Yuasa M., et al. Detection of organic gases using TiO₂ nanotube-based gas sensors. *Procedia Chem.*, 2009, **1**, P. 192–195.
- [23] Middlemas S., et al. A new method for production titanium dioxide pigment. *Hydrometallurgy*, 2013, **131–132**, P. 107–113.
- [24] Yoo J.E., Lee K. Highly ordered TiO₂ nanotube-stumps with memristive response. *Electrochemistry Communications*, 2013, **34**, P. 177–180.
- [25] Vokhmintsev A.S., Weinstein I.A. Memristive Effect in a Nanotubular Layer of Anodized Titanium Dioxide. *Bulletin of the Russian Academy of Sciences. Physics*, 2014, **78** (9), P. 932–935
- [26] Miller K., Nalwa K.S. Memristive Behavior in Thin Anodic Titania. *IEEE Electron device letters*, 2010, **31** (7), P. 737–739.
- [27] Smith Y.R., Ray R.S. Self-Ordered Titanium Dioxide Nanotube Arrays: Anodic Synthesis and Their Photo/Electro- Catalytic Applications. *Materials*, 2013, **6** (7), P. 2892–2957.
- [28] Ghafar A., Chong C. Fabrication of complete titania nanoporous structures via electrochemical anodization of Ti. *Nanoscale Research Letters*, 2011, **6**, P. 332–338.
- [29] Baram N., Yair E.-E. Electrochemical Impedance Spectroscopy of Porous TiO₂ for Photocatalytic Applications. *J. Phys. Chem. C*, 2010, **114**, P. 9781–9790.
- [30] Jeong D.S., Schroeder H., Waser R. Impedance spectroscopy of TiO₂ thin films showing resistive switching. *Applied Physics Letters*, 2006, **89**, 082909.

- [31] Harrington S.P., Devine T.M. Analysis of Electrodes Displaying Frequency Dispersion in Mott-Schottky Tests. *Journal of The Electrochemical Society*, 2008, **155** (8), P. 381–386.
- [32] Ling Y., Ren F., Feng J. Reverse bias voltage dependent hydrogen sensing properties on Au–TiO₂ nanotubes Schottky barrier diodes. *International journal of hydrogen energy*, 2016, **41**, P. 7691–7698.
- [33] Regonini D., Bowen C.R., Jaroenworarluck A., Stevens R. A Review of Growth Mechanism, Structure and Crystallinity of Anodized TiO₂ Nanotubes. *Materials Science and Engineering R*, 2013, **74**, P. 377–406.
- [34] Macak J.M., Tsuchiya H., Schmuki P. High-Aspect-Ratio TiO₂ Nanotubes by Anodization of Titanium. *Angew. Chem. Int. Ed.*, 2005, **44**, P. 2100–2102.
- [35] Czoska A.M., Livraghi S. The Nature of Defects in Fluorine-Doped TiO₂. *J. Phys. Chem. C*, 2008, **112** (24), P. 8951–8956.
- [36] Lide D.R. *CRC Handbook of Chemistry and Physics*, 89 edition, CRC Press, Boston, 2008, P. 12–114.
- [37] Smith G.X R., Crook R., Wadhawan J.D. Measuring the work function of TiO₂ nanotubes using illuminated electrostatic force microscopy. *Journal of Physics: Conference Series*, 2013, **471**, 012045.
- [38] Miller K.J. Fabrication and modeling of thin-film anodic titania memristors, 2010, URL: <http://lib.dr.iastate.edu/cgi/viewcontent.cgi?article=2430&context=etd>.
- [39] Yang L. *Resistive switching in TiO₂ thin films*. Forschungszentrum Jülich, Jülich, 2011.
- [40] Gils S.V., Mast P., Stijns E., Terryn H. Colour properties of barrier anodic oxide films on aluminium and titanium studied with total reflectance and spectroscopic ellipsometry. *Surf Coat Technol.*, 2004, **185** (2-3), P. 303–310.

The solubility of sodium and potassium fluorides in strontium fluoride

P. P. Fedorov^{1,3}, M. N. Mayakova¹, V. A. Maslov¹, A. E. Baranchikov², V. K. Ivanov²,
A. A. Pynenkov³, M. A. Uslamina³, K. N. Nishchev³

¹Prokhorov General Physics Institute, Russian Academy of Sciences, Moscow, 119991, Russia

²Kurnakov Institute of General and Inorganic Chemistry, Russian Academy of Sciences, Moscow, 119991, Russia

³Ogarev Mordovia State University, Saransk, 430005, Russia

ppfedorov@yandex.ru

DOI 10.17586/2220-8054-2017-8-6-830-834

The phase diagram of the NaF–SrF₂ system was studied by thermal analysis and X-ray powder diffraction analysis with the determination of the chemical composition. The system was found to be of the eutectic type. The eutectic co-ordinates are 853 °C, 32 mol % SrF₂. A narrow range of the existence of solid solution Sr_{1-x}Na_xF_{2-x} was established. The NaF solubility reaches a maximal value of $x = 0.035$ at eutectic temperature. The solubility of KF in SrF₂ is very low.

Keywords: strontium fluoride, sodium fluoride, potassium fluoride, nanofluorides, NaF–SrF₂ phase diagram, solid solution.

Received: 10 November 2017

Revised: 15 November 2017

1. Introduction

The phase diagram of the NaF–CaF₂ system was studied in [1] by thermal and X-ray phase analysis with control of the chemical composition. A narrow region of existence of Ca_{1-x}Na_xF_{2-x} solid solution was revealed. The temperature dependence of NaF solubility in the strontium fluoride has a quirky character: it reaches a maximum value $x = 0.035$ at 1200 ± 50 °C (the temperature that corresponds to the diffuse phase transition in fluoride); it reaches a local minimum (< 0.4 mol %) at 920 ± 25 °C, and again increases up to 2.2 ± 0.2 mol % at the eutectic temperature (818 °C).

Investigating the solubilities of sodium and potassium fluorides in strontium fluoride is of interest. Strontium fluoride is an important matrix for solid-state photonics, it is used in the form of melt grown single crystals [2–5], optical ceramics [6, 7], and in nanotechnology processes [6–15]. In many synthetic processes, the ions of sodium and/or potassium are in the protocols [16]. Multicomponent ionic melts, including fluorides of strontium and alkali metals, are promising for use in metallurgy and nuclear power engineering [17].

Bukhalova and Berezhnaya studied the low-temperature parts of phase diagrams of the NaF–SrF₂ [18] and KF–SrF₂ [19] systems by method of visual polythermal analysis under the air. Systems belong to the eutectic type, the coordinates of the eutectics are 33 mol % SrF₂, 856 °C for the NaF–SrF₂ system and 22 mol % of SrF₂, 744 °C for the KF–SrF₂ system. Regions near that of strontium fluoride have not been investigated. Precision measurement of NaF liquidus temperatures in the NaF–SrF₂ system was performed by Cantor [20]. Cryoscopic data [21] give no clear evidence for the formation of solid solution of sodium fluoride in strontium fluoride (as opposed to, for example, systems CaF₂:Na and BaF₂:K). According to Bollman et al. [22] single crystals of melt grown strontium fluoride can contain up to 1.8 mol % NaF, which leads to a drastic increase of ionic conductivity.

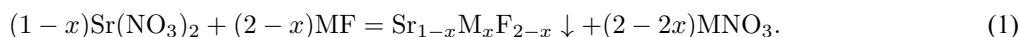
The aim of this work was to study the solubility of sodium and potassium fluorides in strontium fluoride, as well as clarifying the phase diagram of the NaF–SrF₂ system. In order to identify the region of solid solutions based on SrF₂, in addition to the classic techniques of research, we used the technique of nanotechnology: previous investigations have shown that under low temperature syntheses, as a rule, non-equilibrium phases of variable composition are formed, with the width of the homogeneity region of solid solutions based on components often correspond to the limiting width of the high-temperature solid solutions, or even exceed it [1, 6, 10, 23–25].

2. Experimental

Sodium fluoride NaF (OS. h. 9–3); potassium fluoride bihydrate KF₂·2H₂O (analytical grade 9–3); strontium chloride SrCl₂ (Alfa Aesar); strontium nitrate Sr(NO₃)₂ purity 99.99% (LANHIT company) were used as initial reagents for the synthesis as well as double distilled water.

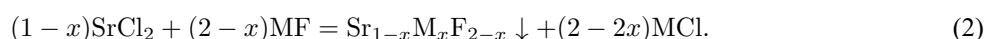
Synthesis of samples was performed by coprecipitation from aqueous solutions at room temperature on the installation of periodic action. The main units of the set up for the synthesis are: the polypropylene reactor with a magnetic stirrer, and chemical feeder. The solutions of strontium nitrate (0.15 mol/l) and a fluorinating agent

(0.25 mol/l) in doubly distilled water was prepared initially. To obtain precipitate, the aqueous solution of strontium nitrate was added dropwise to a solution of a fluorinating agent (NaF or KF). The equation of synthesis reactions is the following:



Mixing of solutions was carried out under permanent stirring with a magnetic stirrer. A suspension formed as a result of chemical reactions in the mother solution. The resulting precipitate was defended, decanted, washed with doubly distilled water until negative reaction of diphenylamine on the nitrate ions and dried under air at a temperature of 40 – 50 °C.

To determine the limit of solubility for sodium and potassium fluorides in the SrF_2 at elevated temperatures, we used the synthesis from chloride flux by the reaction



The reagents were pre-dried, thoroughly mixed in agate mortar. Samples weight was 5.3 g. The mixture was loaded into platinum crucibles (10 – 20 cm³), and then were dipped in shaft furnace, heated to 900 – 1100 °C, kept for 10 minutes. The reaction product was washed with distilled water.

The morphology of the powders, prepared in accordance with reaction (2), is shown on Fig. 1. Habitus of powder particles suggests that the formation of microcrystals occurs by a non-classical crystal growth mechanism by oriented attachment of nanoparticles [26].

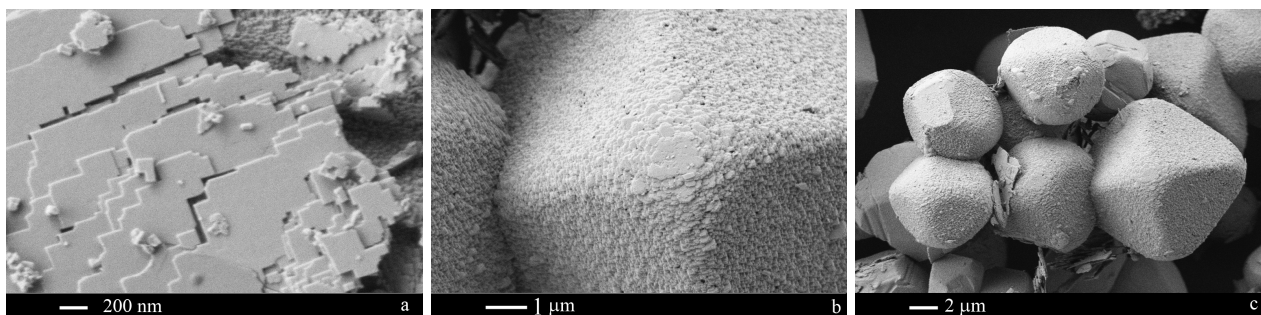


FIG. 1. Scanning electron microscopy image of a SrF_2 -based samples, obtained by chloride flux method: a – SrF_2 :Na, 950 °C; b – SrF_2 :K, 950 °C; c – SrF_2 :K, 950 °C

Differential scanning calorimetry (DSC) was performed on thermoanalyzer NETZSCH DSC 404 F1 Pegasus. The measurements were carried out in platinum crucibles under constant argon flow (20 ml/min); the heating rate was 10 K/min, and the cooling rate was 30 K/min. We analyzed carefully ground mixture of components, with weight of ~ 30 mg. X-ray phase analysis was performed with the Bruker D8 Advanced diffractometer, $\text{CuK}\alpha$ radiation. Data processing was performed by software TOPAS. Electron microscope Carl Zeiss NVision 40 was used for carrying out scanning electron microscopy (SEM) and X-ray microanalysis (RSMA).

3. Results and discussion

Nanosized powders $\text{Sr}_{1-x}\text{Na}_x\text{F}_{2-x}$ and $\text{Sr}_{1-x}\text{K}_x\text{F}_{2-x}$ were precipitated by the reactions (1). X-ray powder diffraction showed that the samples were single phase and had a cubic (fluorite-type) structure. The lattice parameters were slightly different from the lattice parameter of pure SrF_2 (5.800 Å, JCPDS card # 06-0262). According to XRD, the size of coherent scattering regions $D = 15 \pm 1$ nm (see Table 1). RSMA showed the presence in the samples of 3.1 mol % NaF and 1.2 mol % KF, respectively. Thus, wide areas of solid solutions on the basis of strontium fluoride in the systems NaF– SrF_2 and KF– SrF_2 are small.

After synthesis from a flux according to reaction (2), we obtained powders of fluorite structure with lattice parameters similar to those of SrF_2 (Table 1). A small amount of sodium fluoride found only in the sample synthesized at 950 °C. At 1000 °C sodium fluoride is not included in appreciable quantities in the lattice of SrF_2 . Admixture of potassium fluoride was not detected at all.

The constructed phase diagram of the NaF– SrF_2 system is shown in Fig. 2. Our data on this system matches well with previous studies of [18–20] in terms of the temperature of the eutectic equilibrium (our DSC measurements gave 853 °C), the curve of primary solidification (liquidus) of the NaF, and the composition of the eutectic

TABLE 1. Characterization of the synthesized samples

Composition	Preparation method	Lattice parameter, Å	MF content, mol %	<i>D</i> , nm
SrF ₂ :NaF	Coprecipitation	5.7991(3)	3.1	15±1
SrF ₂ :NaF	Flux synthesis, 950 °C	5.8001(5)	1.4	> 150
SrF ₂ :NaF	Flux synthesis, 1000 °C	5.7995(9)	Not found	> 150
SrF ₂ :NaF	Flux synthesis, 1050 °C	5.7988(4)	Not found	> 150
SrF ₂ :KF	Coprecipitation	5.8031(2)	1.2	15±1
SrF ₂ :KF	Flux synthesis, 950 °C	5.8009(4)	Not found	> 150
SrF ₂ :KF	Flux synthesis, 1000 °C	5.8001(5)	Not found	> 150
SrF ₂ :KF	Flux synthesis, 1050 °C	5.8008(4)	Not found	> 150

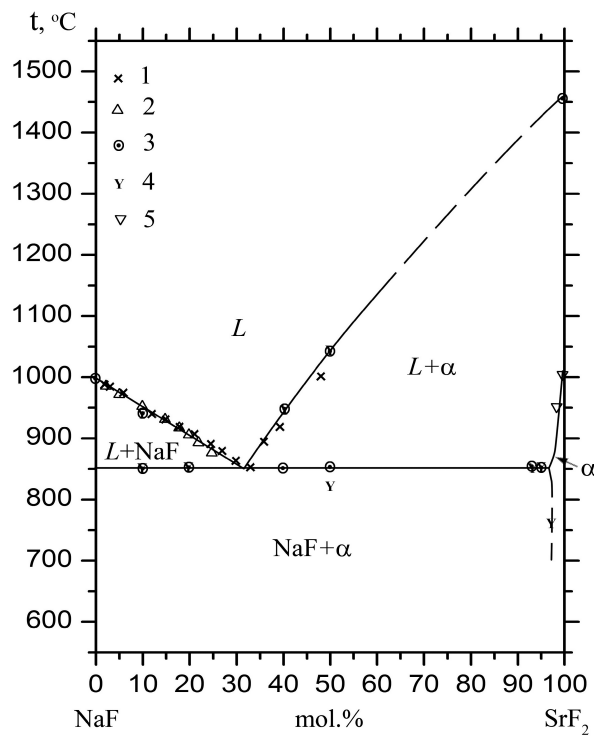


FIG. 2. Phase diagram of the NaF–SrF₂ system. 1 – data [18, 19]; 2 – data [20]; 3 – our data, DSC heating curves; 4 – our data, DSC cooling curves; 5 – our data, chemical analysis. *L* – melt, *α* – solid solution on the basis of SrF₂

point (32 mol % SrF₂). As for the SrF₂ liquidus curve, there is a difference. This is due to the fact that the study of Bukhalova and Berezhnaya were carried out under air, and the process of partial pyrohydrolysis resulted in a lowering the apparent of SrF₂ melting temperature.

The thermal effect of a eutectic is observed on the thermograms of samples containing 7 and 5 mol NaF, but it is not fixed for the composition with 3 % NaF. For the last sample, the cooling curve after the second heating is fixed effect beginning with 760 °C, which can be interpreted as the decomposition of the solid solution, see Fig. 2. Solid solution decomposition during cooling of the system is a consequence of the third law of thermodynamics [27].

Thus, we can conclude that the solubility limit of NaF in the SrF₂ is 3.5 ± 0.5 mol % at the eutectic temperature. The general formula of the solid solution can be written as Sr_{1-x}Na_xF_{2-x}. Then, the maximum solubility of sodium fluoride corresponds to $x = 0.035$.

In general, there was a negligible amount of sodium fluoride entry into the SrF₂ lattice. The solid solution revealed was heterovalent, with a variable number of ions in the unit cell [28].

It is noteworthy that the chemical analysis showed the complete absence of KF in flux prepared samples of SrF₂ phase (see Table 1).

The fluorite structure is loose; in it, cations occupy sites of an *fcc* cubic close-packed lattice, anions are located at the centers of tetrahedral voids, and octahedral voids remain vacant. In all the known cases of isomorphism in the fluorite structure, the cation sublattice remains fully occupied. Substitution of a trivalent cation for a divalent cation by the reaction:



is accompanied by the introduction of additional fluorine ions to the existing octahedral voids in the lattice, which leads to the formation of clusters of defects and to stabilization of the lattice. Conversely, the formation of anion vacancies during substitution of sodium for strontium by the reaction:



causes loosening of the lattice and is undesirable from the crystal chemical standpoint. Note that simultaneous introduction of both trivalent and monovalent ions to the fluorite lattice by the reaction:



which results in abrupt widening of the homogeneity ranges of fluorite solid solutions. This fact was revealed for the NaF–CaF₂–RF₃, NaF–PbF₂–BiF₃, NaF–BaF₂–GdF₃ systems [1]. For strontium fluoride, there are only data for solid solutions of the type NH₄F–SrF₂–RF₃ [11, 29].

The formation of solid solution must be considered in thermodynamic modeling of phase equilibria in the system NaF–SrF₂ [17].

Acknowledgements

The authors express their appreciation V. V. Voronov for his kind assistance in the X-ray diffraction experiments. The authors also wish to thank E. V. Chernova for her help in the preparation of the present manuscript.

This work was partially supported by RFBR 15-08-02481-a grant.

References

- [1] Fedorov P.P., Maykova M.N., et al. Phase diagram of the NaF–CaF₂ system and the electrical conductivity of a CaF₂-based solid solution. *Russian J. Inorg. Chem.*, 2016, **61** (11), P. 1472–1478.
- [2] Sobolev B.P. *The Rare Earth Trifluorides. P.1. The High-Temperature Chemistry of the Rare Earth Trifluorides*. Barcelona 2000, 520 pp.
- [3] Fedorov P.P., Osiko V.V. Crystal Growth of Fluorides. In *Bulk Crystal Growth of Electronic, Optical and Optoelectronic Materials*. John Wiley & Son, Ltd. 2005, P. 339–356.
- [4] Basiev T.T., Orlovskii Yu.V., et al. Continuous tunable cw lasing near 2.75 μm in diode-pumped Er³⁺:SrF₂ and Er³⁺:CaF₂ crystals. *Quantum Electronics*, 2006, **36** (7), P. 591–594.
- [5] Alimov O.K., Basiev T.T., et al. Investigation of Nd³⁺ ions spectroscopic and laser properties in SrF₂ fluoride single crystal. *Optical Materials*, 2012, **34** (5), P. 799–802.
- [6] Doroshenko M.E., Demidenko A.A., et al. Progress in fluoride laser ceramics. *Phys. Stat. Solidi C*, 2013, **10** (6), P. 952–957.
- [7] Rozhnova Yu.A., Luginina A.A., et al. White light luminophores based on Yb³⁺/Er³⁺/Tm³⁺ – coactivated strontium fluoride powders. *Mat. Chem. Phys.*, 2014, **148**, P. 201–207.
- [8] Fedorov P.P., Luginina A.A., Kuznetsov S.V., Osiko V.V. Nanofluorides. *J. Fluorine Chem.*, 2011, **132** (12), P. 1012–1039.
- [9] Luginina A.A., Fedorov P.P., et al. Synthesis of ultrafine fluorite Sr_{1-x}Nd_xF_{2+x} powders. *Inorg. Mater.*, 2012, **48** (5), P. 531–538.
- [10] Mayakova M.N., Luginina A.A., et al. Synthesis of SrF₂–YF₃ nanopowders by co-precipitation from aqueous solutions. *Mendeleev Communications*, 2014, **24** (6), P. 360–362.
- [11] Rozhnova Yu.A., Kuznetsov S.V., et al. New Sr_{1-x-y}R_x(NH₄)_yF_{2+x-y} (R = Yb, Er) solid solution as precursor for high efficiency up-conversion luminophor and optical ceramics on the base of strontium fluoride. *Math. Chem. Phys.*, 2016, **172**, P. 150–157.
- [12] Yagoub M.Y.A., Swart H.C., et al. Surface characterization and photoluminescence properties of Ce³⁺, Eu Co-doped SrF₂ nanophosphor. *Materials*, 2015, **8**, P. 2361–2375.
- [13] Sun J., Xian J., Zhang X., Du H. Hydrothermal synthesis of SrF₂:Yb³⁺/Er³⁺ micro-/nanocrystals with multiform morphologies and upconversion properties. *J. Rare Earth*, 2011, **29**, P. 32–38.
- [14] Sun J., Xian J., Du H. Facile synthesis of well-dispersed SrF₂:Yb³⁺/Er³⁺ upconversion nanocrystals in oleate complex systems. *Appl. Surf. Sci.*, 2011, **257**, P. 3592–3595.
- [15] Ritter B., Krahl T., Scholz G., Kemnitz E. Local structures of solid solutions Sr_{1-x}Y_xF_{2+x} (x = 0..0.5) with fluorite structure prepared by SolGel and mechanochemical syntheses. *J. Phys. Chem. C*, 2016, **120**, P. 8992–8999.
- [16] Fedorov P.P., Luginina A.A., Popov A.I. Transparent oxyfluoride glass ceramics. *J. Fluorine Chem.*, 2015, **172**, P. 22–50.
- [17] Renaud E., Robelin Ch., Gheribi A.E., Chartrand P. Thermodynamic evaluation and optimization of the (LiF + NaF + KF + MgF₂ + CaF₂ + SrF₂) system. *J. Chem. Thermodynamics*, 2011, **43**, P. 1286–1298.

- [18] Bukhalova G.A. The system Na, Sr, F, Cl. *Izv. AN SSSR, Sektor fiz.-khim. analiza*, 1955, **26**, P. 138–146 (in Russian).
- [19] Berezhnaya V.T., Bukhalova G.A. Ternary systems of strontium fluoride with fluorides of alkaline metals. *Zh. Neorg. Khimii*, 1960, **5** (4), P. 925–929 (in Russian).
- [20] Cantor S. Freezing point depressions in sodium fluoride. Effect of alkaline earth fluorides. *J. Phys. Chem.*, 1961, **65**, P. 2208–2210.
- [21] Delbove F. Application de la method cryometrique a haute temperature a letude de la formation de solutions solides dans les fluorures alcalino-terreux, a la limite de dilution infinie. *Silicates Industriels*, 1967, **32**, P. 2659–2667.
- [22] Bollmann W., Görlich P., Hauk W., Mothes H. Ionic conduction of pure and doped CaF₂ and SrF₂ crystals. *Phys. stat. sol. (a)*, 1970, **2**, P. 157–170.
- [23] Fedorov P.P., Kuznetsov S.V., et al. Coprecipitation from aqueous solutions to prepare binary fluorides. *Russian J. Inorg. Chem.*, 2011, **56** (10), P. 1525–1531.
- [24] Fedorov .P., Mayakova M.N., et al. Co-precipitation of yttrium and barium fluorides from aqueous solutions. *Mater. Res. Bull.*, 2012, **47**, P. 1794–1799.
- [25] Fedorov P.P., Mayakova M.N., et al. Synthesis of CaF₂–YF₃ nanopowders by co-precipitation from aqueous solutions. *Nanosystems: Physics, Chemistry, Mathematics*, 2017, **8** (4), P. 462–470.
- [26] Ivanov V.K., Fedorov P.P., Baranchikov A.Y., Osiko V.V. Oriented aggregation of particles: 100 years of investigations of non-classical crystal growth. *Russ. Chem. Rev.*, 2014, **83** (12), P. 1204–1222.
- [27] Fedorov P.P. Third law of thermodynamics as applied to phase diagrams. *Russ. J. Inorg. Chem.*, 2010, **55** (11), P. 1722–1739.
- [28] Fedorov P.P. Heterovalent isomorphism and solid solutions with a variable number of ions in the unit cell. *Russ. J. Inorg. Chem.*, 2000, **45** (3), P. 268–291.
- [29] Fedorov P.P., Kuznetsov S.V., Osiko V.V. Elaboration of nanofluorides and ceramics for optical and laser applications. *In Photonic & Electronic Properties of Fluoride Materials*, Elsevier, 2016, P. 7–31.

Phase diagram for $K_{(1-x)}(NH_4)_xH_2PO_4$ ($x = 0 - 0.15$) solid solutions embedded into magnetic glasses

P. Yu. Vanina¹, A. A. Naberezhnov^{1,2}, A. A. Sysoeva², V. I. Nizhankovskii³, B. Nacke⁴

¹Peter the Great Saint Petersburg Polytechnic University, Polytechnicheskaya, 29, St. Petersburg, 195251, Russia

²Ioffe Institute, Polytechnicheskaya, 26, St. Petersburg, 194021, Russia

³International Laboratory of High Magnetic Fields and Low Temperatures,
Gajowicka, 95, Wroclaw, 53-421, Poland

⁴Leibniz University of Hannover, ETP, Wilhelm-Busch-Street, 30167 Hannover, Germany

p.yu.vanina@gmail.com, alex.naberezhnov@mail.ioffe.ru, annasysoeva07@mail.ru,
nizhan@ml.pan.wroc.pl, nacke@etp.uni-hannover.de

DOI 10.17586/2220-8054-2017-8-6-835-838

Effect of magnetic field application on phase transition in nanostructured solid solutions $(1-x)KH_2PO_4 - x(NH_4)H_2PO_4$ at $x = 0, 0.05$ and 0.15 has been studied by dielectric spectroscopy at $B = 0 - 10T$. The samples have been prepared by impregnation of magnetic porous glasses by KDP-ADP solid solutions. The average pore diameter in glasses was $50(5)$ nm. The temperatures of the ferroelectric phase transition have been determined, and the phase diagrams for these nanocomposite materials (NCM) on cooling and heating (including at magnetic field application) were constructed. The interface “matrix-nanoparticles” was shown to play the principal role in phase diagram formation.

Keywords: ferroelectrics, antiferroelectrics, phase diagram, nanocomposite materials, magnetic porous glasses.

Received: 1 October 2017

Revised: 25 October 2017

1. Introduction

It is known that a restricted geometry drastically modifies the macroscopic properties of nanostructured materials, especially when the correlation length of corresponding interaction becomes comparable with a characteristic size of nanoparticles. In the majority of nanocomposite materials (NCM), the host matrices play a passive role forming the conditions of restricted geometry only, except the interface “embedded material – matrix”. At the Ioffe Institute (in cooperation with Leibniz University of Hannover – LUH) we have developed a procedure for preparing porous alkali borosilicate glasses with magnetic properties [1, 2]. These glasses have positive linear and volume magnetostriction coefficients [3] and can be named “active host matrix” as they can participate in modification of macroscopic properties of embedded materials due to the appearance of additional strains on the interface “matrix-nanoparticle” upon magnetic field application. The phase diagram for the bulk KH_2PO_4 (KDP) and $(NH_4)H_2PO_4$ (ADP) solid solutions (KADP) are known [4, 5] and it is shown that a small admixture of ADP leads to a drastic decreasing of the ferroelectric phase transition temperature T_C . In previous work [6] we studied the effect of restricted geometry on this phase transition for NCM based on conventional porous glasses (PG) with KADP at low ADP concentrations. It has been revealed that there are the shifts in the ferroelectric phase transition temperature, to higher temperature T_C , as a function of ADP concentration on cooling and heating in comparison with the bulk KADP at the same $(NH_4)H_2PO_4$ concentrations. So the effect of ADP admixture on T_C in confinement becomes less pronounced than in the bulk KADP. The principal goal of the present work was to study the influence of applied magnetic fields on T_C for NCM based on magnetic glasses with internal parameters similar to those of nonmagnetic alkali borosilicate glasses in the paper [6].

2. Experimental part

Magnetic glasses have been produced at LUH by induction melting process using convection and electromagnetic agitation [1, 2]. Rectangular plates of the size of $10 \times 10 \times 0.5$ mm³ were cut out from the original glass. Porous glasses were obtained by two-stages etching of magnetic glass after phase separation procedure. These glasses contained about 87 % of SiO_2 and about 6 % of magnetite into the matrix skeleton. The average pore diameter, which was determined by adsorption poroscopy, was about $50(5)$ nm (macroporous glasses – MAP). The total porosity of porous glasses was about 45 %. KDP-ADP (KADP) solid solutions were embedded into the pores from an aqueous solution with triple recrystallization. The pore filling achieved 35 % for the 5 % ADP sample and 38 % for the 15 % ADP sample. The dielectric response was studied using a capacitance bridge at 1 kHz in

the International Laboratory of High Magnetic Fields and Low Temperatures (Wroclaw, Poland). The temperature dependences of the samples' capacitances were measured from 40 – 200 K, but in all figures (for visibility), only the smaller diapasons in the vicinity of phase transitions are shown. “Cooling–heating” cycles were repeated twice for every sample during the experiment. The temperature stability was better than 0.1 K. The applied magnetic fields were varied from 0 – 10T. The nanoparticles' crystal structures were studied using X-ray diffractometry (Supernova, Agilent Technologies) using Cu $K\alpha$ line (in SPbPU) and corresponded to structure of the bulk KDP-ADP solid solutions at low ADP concentrations. The average size of nanoparticles, which was estimated from broadening of elastic peaks, was ~ 40 nm.

3. Results and discussion

The typical temperature dependence $C(T)$ of sample capacitance at magnetic field 10 T is presented in Fig. 1 for NCM 0.95KDP-0.05ADP on cooling and heating.

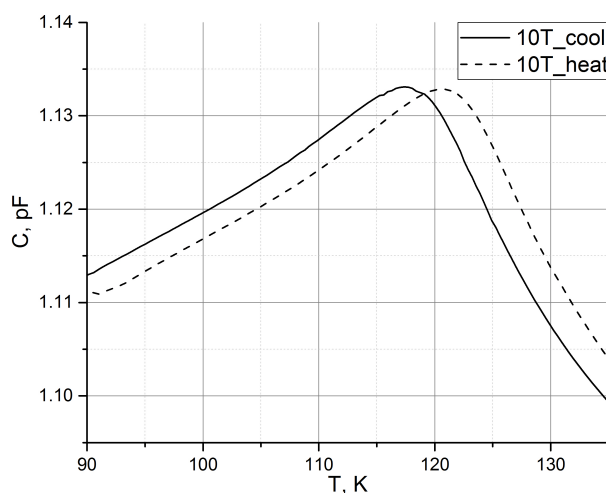


FIG. 1. Temperature dependence of capacity of NCM 0.95KDP – 0.05ADP on cooling and heating at magnetic field $B = 10T$

The principle feature of all dependences $C(T)$ is the presence of a shift in the maximum position on cooling and heating. We have observed a similar hysteresis for NCM based on conventional PG [6] with embedded KADP. Temperatures of ferroelectric phase transition (T_C) on cooling and heating have been determined from the maximum positions for every sample, with an accuracy in the determination of T_C of better than 0.1 K. In Fig. 2 the dependences of T_C on cooling as a function of the ADP admixture are presented for PG and magnetic MAP glasses.

It is easy to see that on cooling, the T_C for MAP glasses decreases at higher ADP concentration, as for PG-based NCM, but for MAP glasses, this curve follows a little bit higher. This may occur due to different nanoparticle sizes in these glass types: in PG-type glasses the nanoparticle size was about 50 nm. Upon magnetic field application, the behavior of T_C as a function of ADP concentration changes essentially. Upon cooling, (Fig. 3a) the shift of T_C is practically independent of magnetic field.

On heating, we have observed the reliably identifiable difference in the T_C values in magnetic field and without it (Fig. 3b). It can be explained by multidirectional effects of glass volume thermal expansion (or compression on cooling) α_3 and magnetostriction. Indeed, on heating, both coefficients are positive, but on cooling, the α_3 coefficient of KDP changes sign while the coefficient of volume magnetostriction remains positive. In this manner, on cooling, both mechanisms compensate each other and the decrease of T_C at higher ADP concentrations is an internal feature of these solid solution nanoparticles. The final results for nonmagnetic and magnetic glasses are presented for comparison in Table 1.

4. Conclusion

Introduction of ADP admixture into KDP nanoparticles leads to a decrease in the ferroelectric phase transition temperature T_C in NCM on base of magnetic MAP glasses, but this decrease is essentially smaller than in the case of bulk solid solutions at the relevant concentrations. Application of an internal magnetic field does not practically change T_C on cooling. It is most likely that this effect relates to the multidirectional influences of

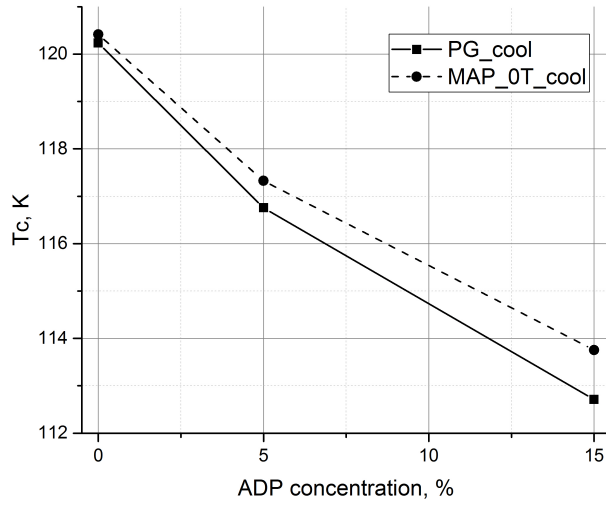


FIG. 2. Dependence of T_C as a function of ADP concentration for conventional PG [6] and magnetic MAP glasses on cooling without magnetic field

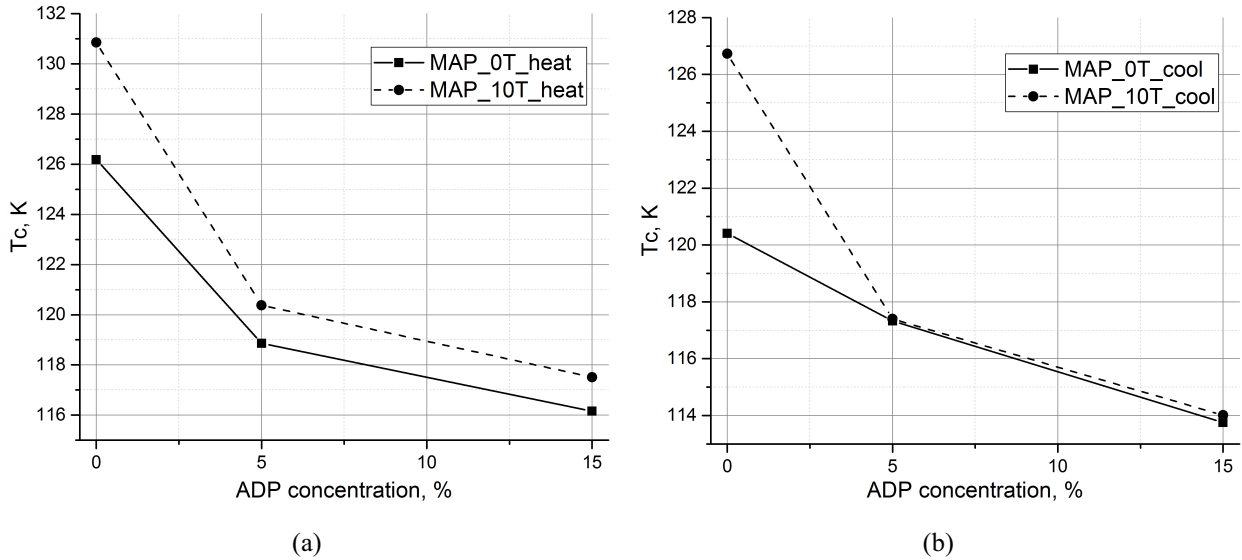


FIG. 3. Dependences of T_C as a function of ADP concentration for magnetic MAP glasses on cooling (a) and on heating (b) without magnetic field (black squares) and at magnetic field $B = 10T$ (black circles)

thermal compression and positive magnetostriction of MAP glasses at temperature decreasing: the both mechanisms compensate each other. On heating, they act in one direction and in this case T_C becomes slightly higher. As a result, we have observed the temperature hysteresis between T_C on cooling and on heating. It is worth noting that the effect of restricted geometry on ΔT_C in NCM on base of magnetic glasses for the pure KDP is larger than in NCM with embedded KADP solid solutions. The explanation is the temperature dependence of the volume expansion coefficient α_3 for the pure KDP. According to literature data [13] α_3 on heating from 90 to 130 K (in the vicinity of phase transition) decreases from $25 \cdot 10^{-6}$ to $(-57) \cdot 10^{-6}$, i.e. this coefficient changes the sign and becomes a positive again above ~ 126 K only. In this manner, on heating, the properties of NCM is determined by competition on interface “host matrix – embedded material” of thermal compression of KDP itself and thermal expansion of glass, including the additional input due to positive magnetostriction. On cooling, the situation changes drastically: we have only one positive (magnetostriction) and two negative inputs (compression of KDP and glass). ADP has a positive and large ($\sim 45 \cdot 10^{-6}$ and more) coefficient α_3 in the whole temperature interval, including a vicinity of the ferroelectric phase transition in KDP. It is logical to suppose that the admixture of ADP modifies the coefficient α_3 and the effects on interface become less pronounced. In summary, one can

TABLE 1. T_C values for NCM with embedded KADP solid solutions on base of PG and MAP glasses on cooling and heating and at applied magnetic fields

		ADP concentration, %		0	5	15	
Bulk samples [7–12]		T_C , K		~ 122	104.2	~ 73	
Present work KDP-ADP nanoparticles	Nonmagnetic glass		$T_{C(\text{cooling})}$, K	120.2 ± 0.1 [5]	116.7 ± 0.1	112.7 ± 0.1	
			$T_{C(\text{heating})}$, K	126.2 ± 0.1	119.8 ± 0.1	114.8 ± 0.1	
			$\Delta T_C = T_{C(\text{cooling})} - T_{C(\text{heating})}$, K	6	3.1	2.1	
	Magnetic glass		$B = 0$		$T_{C(\text{cooling})}$, K	120.4 ± 0.1	117.3 ± 0.1
					$T_{C(\text{heating})}$, K	126.2 ± 0.1	118.9 ± 0.1
					$\Delta T_C = T_{C(\text{cooling})} - T_{C(\text{heating})}$, K	5.8	1.6
			$B = 10$		$T_{C(\text{cooling})}$, K	126.7 ± 0.1	117.4 ± 0.1
					$T_{C(\text{heating})}$, K	130.9 ± 0.1	120.4 ± 0.1
					$\Delta T_C = T_{C(\text{cooling})} - T_{C(\text{heating})}$, K	4.2	3.0

conclude that the phenomena on interface “host matrix- embedded KADP solution” play the principle role in the formation of the phase diagram for KADP in a restricted geometry.

Acknowledgements

A. A. Sysoeva and A. A. Naberezhnov thank the Russian Foundation for Basic Researches (grant 15-02-01413) for financial support. In Peter the Great Saint Petersburg Polytechnic University the studies were carried out in the framework of the grant of Ministry of Education and Science of Russian Federation, No. 3.1150.2017/4.6. B. Nacke acknowledges DAAD program “Strategic Partnership with St. Petersburg State Polytechnical University and Leibniz Universitt Hannover”.

References

- [1] Naberezhnov A., Porechnaya N., et al. Morphology and Magnetic Properties of Ferriferous Two-Phase Sodium Borosilicate Glasses. *The Scientific World Journal*, 2014, **2014**, 320451 (7 p.).
- [2] Andreeva N., Tomkovich M., et al. SEM and AFM Studies of Two-Phase Magnetic Alkali Borosilicate Glasses. *The Scientific World Journal*, 2017, **2017**, 9078152 (9 p.).
- [3] Naberezhnov A., Rudskoy A., et al. Nanoporous Glasses with Magnetic Properties as a Base of High-frequency Multifunctional Device Making. *Lecture Notes in Computer Science*, 2014, **8638**, P. 459–466.
- [4] Gridnev S.A., Korotkov L.N., et al. Dielectric properties and x-T phase diagram of $K_{1-x}(NH_4)_xH_2PO_4$ crystals. *Ferroelectrics Letters*, 1991, **13** (3), P. 67–72.
- [5] Korotkov L.N., Shuvalov L.A. Transitions to the relaxor and dipole glass states in mixed crystals of the potassium dihydrogen phosphate family. *Crystallography reports*, 2004, **49** (5), P. 832–842.
- [6] Vanina P.Yu., Naberezhnov A.A., et al. Phase transitions in nanostructured $K_{1-x}(NH_4)_xH_2PO_4$ ($x = 0 - 0.15$) solid solutions. *Nanosystems: physics, chemistry, mathematics*, 2017, **8** (4), P. 535–539.
- [7] Koroleva E., Naberezhnov A., et al. The effect of magnetic field on the ferroelectric phase transition in KH_2PO_4 nanoparticles embedded in magnetic porous glass. *Technical Physics Letters*, 2015, **41** (10), P. 981–983.
- [8] Ravi G., Haja Hameed A.S., Ramasamy P. Effect of temperature and deuterium concentration on the growth of deuterated potassium dihydrogen phosphate (DKDP) single crystals. *J. Cryst. Growth*, 1999, **207**, P. 319.
- [9] Trybua Z., Kaszyski J. Phases Coexistence of Hydrogen-Bonded Mixed Ferroelectric and Antiferroelectric Crystals. *Ferroelectrics*, 2004, **298**, P. 347–351.
- [10] Kwon Oh.J., Kim J.-J. Proton glass behavior and phase diagram of the $K_{1-x}(NH_4)_xH_2PO_4$ system. *Physical Review B*, 1993, **48** (9), P. 6639–6642.
- [11] Ono Y., Hikita T., Ikeda T. Phase-transitions in mixed-crystal system $K_{1-x}(NH_4)_xH_2PO_4$. *J. Phys. Soc. Jpn.*, 1987, **56** (2), P. 577–588.
- [12] Korotkov L.N., Shuvalov L.A. Transitions to the relaxor and dipole-glass states in mixed crystals of the potassium dihydrogen phosphate family. *Crystallography reports*, 2004, **49** (5), P. 832–842.
- [13] Shaskolskaya M.P. *Acoustic crystals*. Moscow, Nauka, 1982, 633 p. (in Russian).



NANOSYSTEMS:

PHYSICS, CHEMISTRY, MATHEMATICS

INFORMATION FOR AUTHORS

The journal publishes research articles and reviews, and also short scientific papers (letters) which are unpublished and have not been accepted for publication in other magazines. Articles should be submitted in English. All articles are reviewed, then if necessary come back to the author to completion.

The journal is indexed in Web of Science Core Collection (Emerging Sources Citation Index), Chemical Abstract Service of the American Chemical Society, Zentralblatt MATH and in Russian Scientific Citation Index.

Author should submit the following materials:

1. Article file in English, containing article title, the initials and the surname of the authors, Institute (University), postal address, the electronic address, the summary, keywords, MSC or PACS index, article text, the list of references.
2. Files with illustrations, files with tables.
3. The covering letter in English containing the article information (article name, MSC or PACS index, keywords, the summary, the literature) and about all authors (the surname, names, the full name of places of work, the mailing address with the postal code, contact phone number with a city code, the electronic address).
4. The expert judgement on possibility of publication of the article in open press (for authors from Russia).

Authors can submit a paper and the corresponding files to the following addresses: nanojournal.ifmo@gmail.com, popov1955@gmail.com.

Text requirements

Articles should be prepared with using of text editors MS Word or LaTeX (preferable). It is necessary to submit source file (LaTeX) and a pdf copy. In the name of files the English alphabet is used. The recommended size of short communications (letters) is 4-6 pages, research articles– 6-15 pages, reviews – 30 pages.

Recommendations for text in MS Word:

Formulas should be written using Math Type. Figures and tables with captions should be inserted in the text. Additionally, authors present separate files for all figures and Word files of tables.

Recommendations for text in LaTeX:

Please, use standard LaTeX without macros and additional style files. The list of references should be included in the main LaTeX file. Source LaTeX file of the paper with the corresponding pdf file and files of figures should be submitted.

References in the article text are given in square brackets. The list of references should be prepared in accordance with the following samples:

- [1] Surname N. *Book Title*. Nauka Publishing House, Saint Petersburg, 2000, 281 pp.
- [2] Surname N., Surname N. Paper title. *Journal Name*, 2010, **1** (5), P. 17-23.
- [3] Surname N., Surname N. Lecture title. In: Abstracts/Proceedings of the Conference, Place and Date, 2000, P. 17-23.
- [4] Surname N., Surname N. Paper title, 2000, URL: <http://books.ifmo.ru/ntv>.
- [5] Surname N., Surname N. Patent Name. Patent No. 11111, 2010, Bul. No. 33, 5 pp.
- [6] Surname N., Surname N. Thesis Title. Thesis for full doctor degree in math. and physics, Saint Petersburg, 2000, 105 pp.

Requirements to illustrations

Illustrations should be submitted as separate black-and-white files. Formats of files – jpeg, eps, tiff.



NANOSYSTEMS:

PHYSICS, CHEMISTRY, MATHEMATICS

Журнал зарегистрирован

Федеральной службой по надзору в сфере связи, информационных технологий и массовых коммуникаций

(свидетельство ПИ № ФС 77 - 49048 от 22.03.2012 г.)

ISSN 2220-8054

Учредитель: федеральное государственное автономное образовательное учреждение высшего образования

«Санкт-Петербургский национальный исследовательский университет информационных технологий, механики и оптики»

Издатель: федеральное государственное автономное образовательное учреждение высшего образования

«Санкт-Петербургский национальный исследовательский университет информационных технологий, механики и оптики»

Отпечатано в Учреждении «Университетские телекоммуникации»

Адрес: 197101, Санкт-Петербург, Кронверкский пр., 49

Подписка на журнал НФХМ

На второе полугодие 2018 года подписка осуществляется через

ОАО Агентство «Роспечать»

Подписной индекс 57385 в каталоге «Издания органов научно-технической информации»